

# การวิเคราะห์เชิงตัวเลขของฮอโลแกรมอนุภาค

นายศิริวัช สุนทรานนท์

วิทยานิพนธ์นี้เป็นส่วนหนึ่งของการศึกษาตามหลักสูตรปริญญาวิทยาศาสตรดุษฎีบัณฑิต

สาขาวิชาเทคโนโลยีเลเซอร์

มหาวิทยาลัยเทคโนโลยีสุรนารี

ปีการศึกษา 2549

ISBN 974-533-599-1

# **DIGITAL ANALYSIS OF PARTICLE HOLOGRAMS**

**Siriwat Soontaranon**

**A Thesis Submitted in Partial Fulfillment of the Requirements for  
the Degree of Doctor of Philosophy in Laser Technology**

**Suranaree University of Technology**

**Academic Year 2006**

**ISBN 974-533-599-1**

# DIGITAL ANALYSIS OF PARTICLE HOLOGRAMS

Suranaree University of Technology has approved this thesis submitted in partial fulfillment of the requirements for the Degree of Doctor of Philosophy.

Thesis Examining Committee

---

(Assoc. Prof. Dr. Prapun Manyum)

Chairperson

---

(Assoc. Prof. Dr. Joewono Widjaja)

Member (Thesis Advisor)

---

(Assoc. Prof. Dr. Pichet Limsuwan)

Member

---

(Asst. Prof. Dr. Eckart Schulz)

Member

---

(Dr. Rangsang Tongta)

Member

---

(Assoc. Prof. Dr. Saowanee Rattanaphani)

Vice Rector for Academic Affairs

---

(Assoc. Prof. Dr. Sompong Thammathaworn)

Dean of Institute of Science

ศิริวิษ สุทรานนท์ : การวิเคราะห์เชิงตัวเลขของฮอโลแกรมอนุภาค (DIGITAL ANALYSIS OF PARTICLE HOLOGRAMS) อาจารย์ที่ปรึกษา : รองศาสตราจารย์ ดร. ยูวโน วิดจายา, 179 หน้า. ISBN 974-533-599-1

งานวิทยานิพนธ์นี้ได้ทำการศึกษาวิธีการเชิงตัวเลขชนิดใหม่ เพื่อหาขนาดและตำแหน่งของอนุภาคจากฮอโลแกรมอนุภาคด้วยการแปลงเวฟเล็ท โดยสร้างฮอโลแกรมด้วยวิธีการจับภาพรูปแบบการแทรกสอดด้วยเครื่องรับรู้ออปติคัล ในการศึกษาครั้งนี้ ระบุขั้นตอนที่จะหาได้โดยการคำนวณการแปลงเวฟเล็ทของฮอโลแกรม ผลจากการแปลงเวฟเล็ททำให้ได้ข้อมูลด้านตำแหน่งและความถี่ของรูปแบบการแทรกสอด ซึ่งถูกกำหนดโดยระบุขั้นตอน ในการคำนวณขนาดของอนุภาค ใช้วิธีการเชิงตัวเลขสองวิธีด้วยกัน วิธีการแรกหาตำแหน่งมินิมาในโดเมนของตำแหน่งโดยใช้วิธีเอ็นเวโลปริคอนสตรัคชัน วิธีที่สองหาความถี่ของสัญญาณพาหะที่ตำแหน่งมินิมาโดยคำนวณค่าสัมบูรณ์ของการแปลงเวฟเล็ท ได้ทำการศึกษาเพื่อยืนยันความสามารถนำไปใช้งานจริงของวิธีการดังกล่าว โดยทำการวิเคราะห์ฮอโลแกรมของวัตถุที่มีลักษณะเป็นเส้นและทรงกลม ซึ่งสร้างขึ้นมาจากการจำลองด้วยคอมพิวเตอร์และจากการทดลองจริง จากนั้นจึงทำการวิเคราะห์ประสิทธิภาพระบบของวิธีการที่นำเสนอ ทั้งในกรณีฮอโลแกรมของวัตถุจำนวนชิ้นเดียวและหลายชิ้น การวิเคราะห์สำหรับกรณีฮอโลแกรมของวัตถุชิ้นเดียว ทำได้โดยการพิจารณาขนาดและความละเอียดอันจำกัดของเครื่องรับรู้ออปติคัล ส่วนในกรณีวัตถุจำนวนหลายชิ้น สามารถประมาณฮอโลแกรมที่ได้จากผลรวมของรูปแบบการแทรกสอดจากวัตถุแต่ละชิ้น ดังนั้นประสิทธิภาพระบบจึงขึ้นอยู่กับระยะห่างระหว่างผลการแปลงเวฟเล็ทของแต่ละรูปแบบการแทรกสอดในโดเมนของการแปลงเวฟเล็ท ได้ทำการสร้างสมการซึ่งเป็นตัวกำหนดระยะห่างที่ต้องการระหว่างแต่ละฮอโลแกรม และทำการยืนยันด้วยการวิเคราะห์ฮอโลแกรมที่จำลองวัตถุจำนวนหลายชิ้น ทั้งวัตถุที่มีลักษณะเป็นเส้นและทรงกลม

สาขาวิชาเทคโนโลยีเลเซอร์และโฟตอนิกส์  
ปีการศึกษา 2549

ลายมือชื่อนักศึกษา \_\_\_\_\_  
ลายมือชื่ออาจารย์ที่ปรึกษา \_\_\_\_\_  
ลายมือชื่ออาจารย์ที่ปรึกษาร่วม \_\_\_\_\_

SIRIWAT SOONTARANON : DIGITAL ANALYSIS OF PARTICLE  
HOLOGRAMS. THESIS ADVISOR : ASSOC. PROF. JOEWONO  
WIDJAJA, Ph.D. 179 PP. ISBN 974-533-599-1

PARTICLE HOLOGRAMS/IN-LINE HOLOGRAPHY/WAVELET  
TRANSFORM/DIGITAL ANALYSIS

New digital methods for sizing and tracking particles from in-line particle holograms by using wavelet transform (WT) are studied. The holograms are obtained by capturing the interference pattern with a charge-couple device (CCD) sensor. In the study, the recording distance is extracted by computing the WT of the holograms. The WT output gives the space-frequency information of the interference pattern which are determined by the recording distance. As for the particle size, two digital methods are studied. The first method is based on the determination of the minima positions in the space domain by using the envelope function reconstruction method. The second method extracts the frequency of the carrier signal at the minima positions by computing absolute values of the WT. The feasibility of the methods is verified by analyzing the simulated and the experimentally generated holograms of line and spherical objects. Analysis of the system performance of the methods for the case of the holograms of the single and the multiple objects are discussed. The analysis for the hologram of the single object is based on the finite size and finite resolution of the employed CCD sensor. As for the case of multiple objects, the hologram can be approximately represented by summation of the interference patterns of the individual objects. Thus, the system performance depends on the separation between the WT of each interference pattern in the WT domain. The equations that determine the

required separation between each hologram are derived and are verified by analyzing the simulated holograms of the multiple line and spherical objects.

School of Laser Technology and Photonics

Academic Year 2006

Student's Signature \_\_\_\_\_

Advisor's Signature \_\_\_\_\_

Co-advisor's Signature \_\_\_\_\_

## **ACKNOWLEDGEMENTS**

First of all, I would like to express my gratitude to my advisor, Assoc. Prof. Dr. Joewono Widjaja for his continued guidance, help and encouragement throughout the course of this study. I am indebted to his valuable insights and constructive comments on my work. This dissertation would not have reached completion without his constant encouragement and support.

I would like to thank Prof. Dr. Toshimitsu Asakura, my co-advisor, for his advice and guidance throughout my research study. I also want to express my appreciation to Prof. Dr. Jun Uozumi for his technical assistance and encouragement during my stay at the Faculty of Engineering, Hokkai-Gakuen University.

I wish to express my special thanks to the Thailand Research Fund for financial support through the Royal Golden Jubilee scholarship (Grant No. PHD/0188/2542).

Finally, I am indebted to my family for their love and encouragement throughout my studies.

Siriwat Soontaranon

# CONTENTS

	<b>Page</b>
ABSTRACT IN THAI .....	I
ABSTRACT IN ENGLISH .....	II
ACKNOWLEDGEMENTS .....	IV
CONTENTS .....	V
LIST OF TABLES .....	VII
LIST OF FIGURES .....	VII
<b>CHAPTER</b>	
<b>I INTRODUCTION .....</b>	<b>1</b>
1.1 Background .....	1
1.2 Significant of the study .....	3
1.3 Research objective .....	4
1.4 Scope and limitation of the study .....	4
1.5 Organization .....	5
<b>II THEORY .....</b>	<b>6</b>
2.1 In-line Fraunhofer holography .....	7
2.1.1 Line object .....	8
2.1.2 Spherical object .....	10
2.2 The wavelet transform .....	12
<b>III HOLOGRAM FORMATION .....</b>	<b>19</b>
3.1 Single object .....	20

## CONTENTS (Continued)

	<b>Page</b>
3.1.1 Line object .....	20
3.1.2 Spherical object .....	26
3.2 Multiple objects .....	35
<b>IV EXTRACTION OF OBJECT POSITION FROM IN-LINE HOLOGRAM .....</b>	<b>42</b>
4.1 Position of line objects .....	53
4.2 Position of spherical objects .....	56
<b>V EXTRACTION OF OBJECT SIZE FROM IN-LINE HOLOGRAM .....</b>	<b>59</b>
5.1 Object sizing by using reconstruction of envelope function .....	59
5.2 Object sizing by using absolute value of the WT .....	69
5.2.1 Absolute values of wavelet transform .....	71
<b>VI SYSTEM PERFORMANCE .....</b>	<b>83</b>
6.1 Single object .....	83
6.1.1 Line object .....	84
6.1.2 Spherical object .....	86
6.2 Multiple objects .....	89
6.2.1 Extraction of the object size .....	90
6.2.2 Extraction of the axial position of objects .....	98
<b>VII CONCLUSIONS .....</b>	<b>119</b>
<b>REFERENCES .....</b>	<b>124</b>
<b>APPENDIX .....</b>	<b>127</b>
<b>CURRICULUM VITAE .....</b>	<b>179</b>

## LIST OF TABLES

Table	Page
6.1 Measurement of the critical separation $d_x$ and the frequency ratio $p$ from the WT of the simulated holograms of two line objects .....	96
6.2 Measurement of the critical separation $d_x$ and the frequency ratio $p$ from the WT of the simulated holograms of two spherical objects .....	99
6.3 Measurement of the spatial separation $d_x$ and $w$ from the WT of the simulated holograms of the line objects .....	115
6.4 Measurement of the spatial separation $d_r$ and $w$ from the WT of the simulated holograms of the spherical objects .....	116

## LIST OF FIGURES

Figure	Page
2.1 Formation of an in-line hologram. ....	6
2.2 Reconstruction of the in-line hologram. ....	8
2.3 Simulated in-line hologram of a line object. ....	10
2.4 Simulated in-line hologram of a spherical object. ....	11
2.5 Morlet wavelet and its spectrum for different dilation values. ....	14
2.6 Plot of real value of the continuous wavelet coefficients of the simulated hologram in Fig. 2.3. ....	15
2.7 Single level decomposition of the signal $s$ . ....	17
2.8 Plot of the discrete wavelet coefficients of the simulated hologram in Fig. 2.3. ....	17
3.1 Simulated in-line hologram of the line object with $a = 62.48 \mu\text{m}$ and $z = 20 \text{ cm}$ . ....	21
3.2 Experimental setup for generating the in-line hologram of the optical fiber. ....	22
3.3 Optical fiber mounted on the holder. ....	22
3.4 In-line hologram of the optical fiber recorded at $z = 20 \text{ cm}$ . ....	23
3.5 Recorded intensity of the reference beam at $z = 20 \text{ cm}$ . ....	24
3.6 In-line hologram of the optical fiber recorded at $z = 20 \text{ cm}$ with the background removed. ....	24
3.7 1-D intensity profile of the 240 <sup>th</sup> row of the hologram shown in Fig. 3.6. ....	25

## LIST OF FIGURES (Continued)

Figure	Page
3.8 1-D averaged intensity profile of the middle 400 rows of the hologram shown in Fig. 3.6. ....	26
3.9 Mach-Zehnder interferometer setup for recording the in-line hologram of the pinhole. ....	27
3.10 Simulated in-line hologram of a pinhole. ....	28
3.11 Simulated in-line hologram of a circular aperture with the radius $77.78 \mu\text{m}$ and distance $z = 20 \text{ cm}$ . ....	29
3.12 The pinhole mounted on the slide holder. ....	30
3.13 Experimental setup for generating the in-line hologram of the pinhole. ....	30
3.14 Recorded intensity of the reference beam at $z = 20 \text{ cm}$ . ....	31
3.15 Recorded intensity of the object beam at $z = 20 \text{ cm}$ . ....	32
3.16 In-line hologram of the pinhole recorded at $z = 20 \text{ cm}$ . ....	33
3.17 In-line hologram of the pinhole recorded at $z = 20 \text{ cm}$ with the background removal. ....	33
3.18 1-D intensity profile of the 229 <sup>th</sup> row of the hologram shown in Fig. 3.17. ....	34
3.19 1-D angular averaged intensity profile of the desired interference pattern shown in Fig. 3.17. ....	35
3.20 Hologram of two optical fibers separated by 5 mm distance in both $x$ and $z$ direction. ....	38
3.21 1-D intensity profile of the hologram shown in Fig. 3.20. ....	38

## LIST OF FIGURES (Continued)

Figure	Page
3.22 Hologram of two spherical objects separated by 5 mm distance in both $x$ and $z$ direction. ....	40
3.23 1-D intensity profile of the hologram shown in Fig. 3.22. ....	40
4.1 Block diagram for calculating the WT of the signal $s$ . ....	44
4.2 $M \times N$ matrix of wavelet coefficients. ....	46
4.3 Block diagram for determining the local maxima and minima of the WT coefficients. ....	47
4.4 The resultant WT coefficients with maximum and minimum amplitudes generated from the real value of the WT of the hologram shown in Fig. 2.3. ....	48
4.5 A glass container with embedded micro-objects used in the recording setup. ....	49
4.6 Theoretical space varying frequencies correspond to the shortest and the longest recording distances defined by the thickness of the glass container. ....	50
4.7 The desired wavelet coefficient after discarding the unwanted information. ....	50
4.8 Enlarged version of Fig. 4.7 shows some maxima and minima of different translation having the same dilation values. ....	52
4.9 The desired maxima and minima of the Fig. 4.8 after discarding those with the same dilation denoted by circle sign. ....	52

## LIST OF FIGURES (Continued)

Figure	Page
4.10 Errors in measurement of $z$ from simulated holograms of line object by using the WT. ....	54
4.11 In-line hologram of the optical fiber recorded at $z = 10$ cm. ....	54
4.12 In-line hologram of the optical fiber recorded at $z = 20$ cm. ....	55
4.13 Errors in measurement of $z$ from the optically generated holograms of the optical fiber by using the WT. ....	55
4.14 Errors in measurements of $z$ from simulated holograms of spherical objects by using the WT. ....	56
4.15 In-line hologram of the pinhole recorded at $z = 12$ cm. ....	57
4.16 In-line hologram of the pinhole recorded at $z = 24$ cm. ....	57
4.17 Errors in measurement of $z$ from the optically generated hologram of the pinhole by using the WT. ....	58
5.1 A block diagram for reconstructing the envelope function by determining the local maxima and minima of the analyzed signal $s$ . ....	61
5.2 Reconstructed envelope function of the hologram in Fig. 2.3. ....	62
5.3 Block diagram for determining the local maxima and minima whose their amplitude different are smaller than a threshold value. ....	63
5.4 Maxima and minima whose amplitude difference are smaller than a threshold value. ....	64
5.5 Block diagram for determining the minimum position of the interference pattern ....	65

## LIST OF FIGURES (Continued)

Figure	Page
5.6 Detected minima positions. ....	66
5.7 Errors in measurement of $a$ from the simulated holograms of the line objects by using the envelope reconstruction method. ....	67
5.8 Errors in measurement of $a$ from the holograms of the optical fiber by using the envelope reconstruction method. ....	67
5.9 Errors in measurement of $a$ from the simulated holograms of the spherical objects by using the envelope reconstruction method. ....	68
5.10 Errors in measurement of $a$ from the holograms of pinhole by using the envelope reconstruction method. ....	67
5.11 Modulated signal $s(x)$ of Eq. (5.8) and the normalized absolute value of the WT given by Eq. (5.12) ....	74
5.12 Simulated in-line hologram of the line object and the normalized absolute value of its WT which is retrieved along the dilation $d = f_g/f_l$ . ....	74
5.13 The 3-D plot of the absolute value of the WT which is cut along the dilation $d = f_g/f_l$ . ....	75
5.14 Block diagram for calculating the object size from $ WT $ . ....	76
5.15 Approximated frequency $f_c = 1/d_c$ obtained from the detected minimum in the absolute values of the first WT. ....	77
5.16 Errors in measurement of $a$ as a function of the frequency interval $\Delta f$ .....	78

## LIST OF FIGURES (Continued)

Figure	Page
5.17 Errors in measurement of $a$ from the simulated holograms of line object by using the envelope reconstruction method and the absolute value of WT. ....	79
5.18 Errors in measurement of $a$ from the experimentally generated holograms of the optical fiber by using the envelope reconstruction method and the absolute value of the WT. ....	80
5.19 Errors in measurement of $a$ from the simulated holograms of 2D object by using the envelope reconstruction method and the absolute value of WT. ....	81
5.20 Errors in measurement of $a$ from the experimentally generated holograms of the pinhole by using the envelope reconstruction method and the absolute value of the WT. ....	82
6.1 Measurable size of objects and their recording distances. ....	88
6.3 Hologram of two optical fibers. ....	91
6.4 Local maxima and minima of the real values of the WT of the hologram shown in Fig. 6.3. ....	91
6.5 Errors of measurement of $a_1$ as a function of $d_x$ for $a_1 = 25 \mu\text{m}$ , $z_1 = 30 \text{ cm}$ and $a_2 = 50 \text{ mm}$ , $z_2 = 29 \text{ cm}$ . ....	94
6.6 $d_x$ calculated by using Eqs. (6.15) for different values of $p$ in comparison with the simulation results. ....	97
6.7 The WT of the hologram shown in Fig. 6.3. ....	100

## LIST OF FIGURES (Continued)

Figure	Page
6.8 Hologram of a line object and the chirp function (left column) versus their WT (right column). .....	102
6.9 The wavelet coefficients at the translation $t = 0$ is plotted by using the Eq. 6.19. ....	104
6.10 Hologram of a line object and the modulating signal of Eq. (6.21) (left column) and their real value of the WT scanned along the dilation $d = d_0$ (right column). ....	106
6.11 Plot of the real value of the WT along the dilation $d = d_0$ together with the four Gaussian functions of Eq. (6.22) and their summation results. ....	109
6.12 The Gaussian function and its width $W_G$ which is determined by the parameter $w$ . ....	110
6.13 Gaussians function determined the envelope function of the real value of the WT of the hologram of two line objects separated by $d_x$ . ....	112
6.14 Errors in detecting the center position of the object $P_1$ from the WT of the holograms of two line objects having $a_1 = 25 \mu\text{m}$ , $z_1 = 30 \text{ cm}$ , $a_2 = 50 \mu\text{m}$ , $z_2 = 29 \text{ cm}$ as a function of $d_x$ . ....	114
6.15 Plot of Eqs. (6.15a), (6.15b) and (6.32). ....	117

# CHAPTER I

## INTRODUCTION

### 1.1 Background

Holography is a technique to store three-dimensional (3-D) optical information on a light-sensitive medium such as a photographic film. In in-line particle holography, coherent illumination of opaque or semi-transparent particles illuminated produces an interference pattern between light waves diffracted from the particles and a directly transmitted light wave. After development, the recorded pattern is referred to as a hologram. As for micrometer size of particles, the diffraction caused by particles at a few tens of centimeters of recording distance can be categorized as a Fraunhofer diffraction. Thus, this type of hologram can be referred to as an in-line Fraunhofer hologram.

The interference pattern of the hologram contains information about both the 3-D spatial position and size of the particles. In a conventional analyzing method, this information is extracted by illuminating the hologram with the same coherent light. The transmitted light reconstructs images of the particles at the same distance as the recording distance. By analyzing this reconstructed image, the desired information can be obtained.

Particle sizing and tracking is one of potential applications of in-line Fraunhofer holography. The in-line holography was not only used for measurement of spherical objects such as fog and marine plankton (Thompson, 1974), its application

to the characterization of thermal insulator fibers has also been found to be very promising (Belaid, Lebrun and Özkul, 1997). Although the desired information can be obtained by analyzing the optically reconstructed image, we may deal with a huge number of particles in real applications. As a consequence, the conventional reconstruction process is very tedious and time consuming.

In order to overcome this problem, Murakami employed a microscope to observe directly the transmittance of the developed in-line hologram (Murakami, 1987). He established a relation between the density and the diameter of interference fringes in the hologram which could provide the desired information. However, his method is applicable only to a small far-field number that corresponds to either a very big diameter of particles or a very short recording distance. As for a large far-field number, the density of fringes does not vary significantly. This leads to inaccuracy of the method. An alternative solution for all-optical analysis of particle holograms using a wavelet transform (WT)-based correlator was proposed (Widjaja, 1998). In the method, the optically reconstructed image of a target particle is compared to the image of a reference particle by using a joint transform correlator technique. The interesting feature of this method is that the WT is used to enhance edge features of both images by imaging an image of a wavelet filter onto the joint Fourier spectrum of the images of the target and the reference particles. By correlating these two edge-enhanced images, the position and the size of particles can be accurately determined. Although the method is indeed useful for analyzing irregularly shaped particles, the problem in the method is that the optical system becomes complicated. Recently, the WT has also been used to extract information about the 3-D position of particles from digitally-recorded in-line holograms (Lefebvre, Coëtmellec and Özkul, 2000). This

method is based on an interpretation of the diffraction process as a wavelet transformation with a spherical wave for the wavelet and an axial distance of the wave propagation for its dilation (scale change). To determine the position of particles, the digital hologram is wavelet transformed by using a spherical wave-based analyzing wavelet. The position of particles can be obtained if the resultant WT gives a maximum value. In fact, this approach is equivalent to searching the in-focus image plane of particles reconstructed from the hologram. However, since the dilation factor is determined by the axial recording distance, this method is useful only for the short axial distance. For the longer distance, the dilation increases. As a result, the admissibility condition of the wavelet is so violated that this method becomes invalid.

## **1.2 Significant of the study**

In this thesis, a new digital method for extracting the information about the size and the recording distance of the object directly from the in-line Fraunhofer holograms is proposed. Instead of treating the diffraction process from the viewpoint of the WT, the proposed method is based on the signal processing approach applied directly to the holograms. This obviates the need for searching all depth planes. In this thesis, the WT is used to extract the axial position of particles. Here, the dilation factor is an independent variable whose value is not determined by the axial distance. The size of particles is determined by using either a reconstruction of the envelope function or an absolute values of the WT methods. In comparison with the previous methods, the proposed method has the following advantages. First, since the hologram is used to extract the above information, the method is free from unwanted virtual and out-of-focus images appearing in the reconstruction process from the hologram.

Second, it gives information about the spatial position and the size of particles. Third, since the method is independent of the fringe density, a wider dynamic range of measurement is expected. Fourth, a longer depth can be measured because the dilation factor does not depend on the axial distance. Finally, the accuracy of measurements can be maximized by taking advantage of a multi-resolution property of the WT.

### **1.3 Research objective**

The purpose of this research is first to invent a new digital method for measuring the size and position of particles from the digital in-line holograms. The position information is extracted from the hologram by using the WT, while the size can be obtained from either the combination of the WT and the envelope construction method or the absolute values of the WT method. The feasibility of the method will be verified by calculating error of measurement. Second, the system performance of the method will be studied.

### **1.4 Scope and limitation of the study**

In this dissertation, the in-line holograms of 1-D and 2-D objects are studied. An optical fiber is used as the 1-D specimen, while for the 2-D object it is a circular pinhole. The in-line holograms of a single object are simulated and experimentally generated. The generated holograms are analyzed by using the WT, the envelope reconstruction and the absolute values of the WT methods.

Since a charge-coupled device (CCD) sensor is used to capture the interference pattern of the holograms, the finite resolution and finite aperture of the CCD sensor determine the information quality of the captured holograms. In order to sample correctly the interference pattern, the spatial resolution of the sensor must

satisfy the Nyquist sampling theorem (Oppenheim and Schaffer, 1989). Whereas the aperture size of the sensor must be wide enough to record the interference pattern. Thus, these conditions limit the allowable recording distance and size of the objects. Furthermore in real world applications, analysis of the in-line holograms of multiple objects may have to be done. In this case, the hologram may contain multiple interference patterns which overlap each other. Therefore, it is important to study these effects on the performance of the analyzing method.

## **1.5 Organization**

The organization of this dissertation is divided into seven chapters. This is the first chapter which gives an introduction of the dissertation. The principles of in-line Fraunhofer holography and the WT are given in Chapter II which includes the mathematical discussions of the holograms of the 1-D line and the 2-D spherical objects. In Chapter III, an algorithm for simulating holograms of single and multiple objects and an optical setup used for generating the holograms are discussed. The extraction of the recording distance from the simulated and the optically generated holograms by using the WT is discussed in Chapter IV. Chapter V discusses the methods for extracting the object size from the holograms by using the envelope reconstruction and the absolute values of the WT. The measurement results by using these methods are given and discussed. In Chapter VI, the system performance of the proposed method for the case of single and multiple objects are analyzed. Finally, the conclusions of the dissertation are provided in Chapter VII. All rigorous mathematical derivations used in this dissertation are given in Appendix.

## CHAPTER II

### THEORY

#### 2.1 In-line Fraunhofer holography

Holography is a lensless imaging method proposed by Dennis Gabor in 1948 (Goodman, 1996). In this method, both the amplitude and phase of the light field diffracted of the object being studied is recorded into light-sensitive media such as a photographic-film through interference with a coherent reference wave. Although in general the phase of the light field cannot be recorded by intensity-sensitive media, the recorded intensity encodes the amplitude and phase information of the object wave into the interference pattern.

In in-line holography, the object and the light source are located in-line along an axis normal to the recording plane as shown in Fig. 2.1.

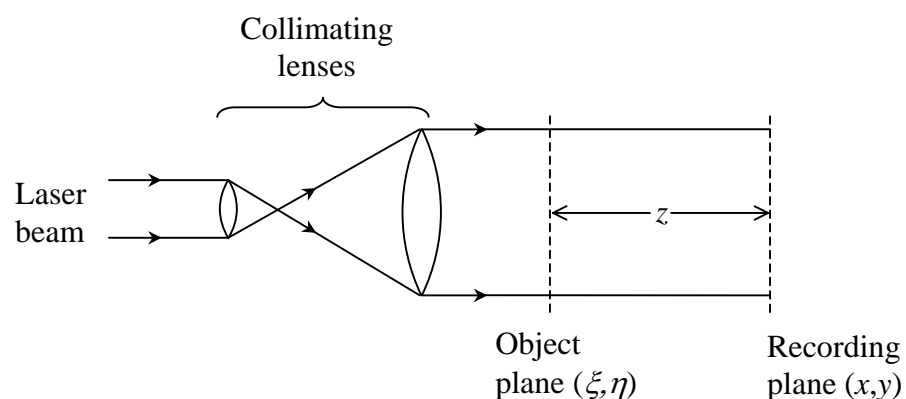


**Figure 2.1** Formation of an in-line hologram.

When the object located at plane  $(\xi, \eta)$  is illuminated with the collimated coherent plane wave, the intensity of the light incident on the recording medium placed a distance  $z$  behind the object is

$$\begin{aligned} I(x, y) &= |R + o(x, y)|^2 \\ &= |R|^2 + |o(x, y)|^2 + R^* o(x, y) + R o^*(x, y), \end{aligned} \quad (2.1)$$

where  $R$  is the amplitude of the reference plane wave and  $o(x, y)$  represents the complex amplitude of the scattered light at the recording plane. Here, the object plane is assumed to be highly transmissive such that the amplitude of the reference wave is greater than the object wave  $R \gg o(x, y)$ . After development, the recorded interference pattern is called a hologram. The existence of  $o(x, y)$  in the third term of Eq. (2.1) ensures that both the amplitude and the phase of the diffracted light are preserved into the intensity of the hologram.

In the reconstruction process, the developed hologram is illuminated with the uniform plane wave as shown in Fig. 2.2. Assume that the exposure is controlled such that the amplitude transmittance of the hologram is linearly proportional to the incident intensity, the reconstructed field immediately behind the hologram can be written as

$$U(x, y) = \beta C \left\{ |R|^2 + |o(x, y)|^2 + R^* o(x, y) + R o^*(x, y) \right\}, \quad (2.2)$$

where  $\beta$  is the constant of proportionality introduced in the developing process, while  $C$  is the amplitude of the illuminating light. Since the amplitude transmittance of the film is always less than one, the first term can be considered as an attenuated plane

wave passes directly through the hologram without scattering. Due to a highly transmissive object plane, the field of the second term is very small compared to the first term so that it is negligible. The third term represents the field that is proportional to the original scattered wave  $o(x, y)$ . Since this wave field appears from the original position of the object, it forms a virtual image of the object. The fourth term is proportional to  $o^*(x, y)$ , which leads to the formation of real image at the distance  $z$  behind the hologram.

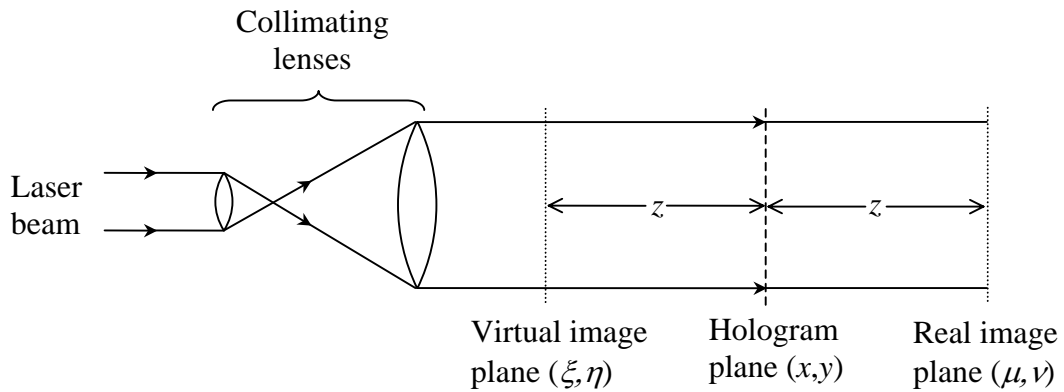


**Figure 2.2** Reconstruction of the in-line hologram.

### 2.1.1 Line object

In case of a small line-shaped object such as a vertical wire placed at the  $y$ -axis having the amplitude distribution function described by

$$A(\xi) = \begin{cases} 1 & \text{for } |\xi| \leq a \\ 0 & \text{for } |\xi| > a, \end{cases} \quad (2.3)$$

the amplitude transmittance of its hologram at the recording plane  $(x, y)$  a distance  $z$  behind the object plane can be mathematically expressed as (Tyler and Thompson, 1976)

$$I(x, y) = 1 - \frac{4a}{\sqrt{\lambda z}} \cos\left(\frac{\pi x^2}{\lambda z} - \frac{\pi}{4}\right) \left[ \frac{\sin \frac{2\pi ax}{\lambda z}}{\frac{2\pi ax}{\lambda z}} \right] + \frac{4a^2}{\lambda z} \left[ \frac{\sin \frac{2\pi ax}{\lambda z}}{\frac{2\pi ax}{\lambda z}} \right]^2. \quad (2.4)$$

Here,  $a$  represents the radius of the object while  $\lambda$  is the wavelength of illuminating light. The rigorous mathematical derivation of Eq. (2.4) is done by assuming that the illuminating wave is a unit amplitude plane wave (see Appendix). It can be seen from Eq. (2.4) that the hologram consists of three mathematical terms. The constant in the first term caused by the directly transmitted light corresponds to the uniform background in the hologram. This term is equivalent to the first term of Eq. (2.1). The second term is a modulation of a chirp signal by a sinc function that corresponds to the summation of the third and the fourth terms of the Eq. (2.1). Since the frequency of the sinc function is much lower than that of the chirp signal, the amplitude of the chirp signal is modulated by the sinc function. The third term of Eq. (2.4) associated with the second term of Eq. (2.1) is a square of the sinc function whose the amplitude is much smaller compared with the other terms. Thus, the hologram is mainly constructed by the first and the second term with the sinc function representing the envelope function and the chirp signal is the carrier signal. Note that the second term becomes very important for particle analysis because the frequency of the chirp signal is inversely proportional to the recording distance  $z$ , while the minima positions which are the zero-crossing positions of the sinc function are determined by the size of the particles. Plot of the Eq. (2.4) is shown as a solid line in Fig. 2.3, where the broken line represents the envelope function. From this figure, the above properties of the three terms can be obviously observed.

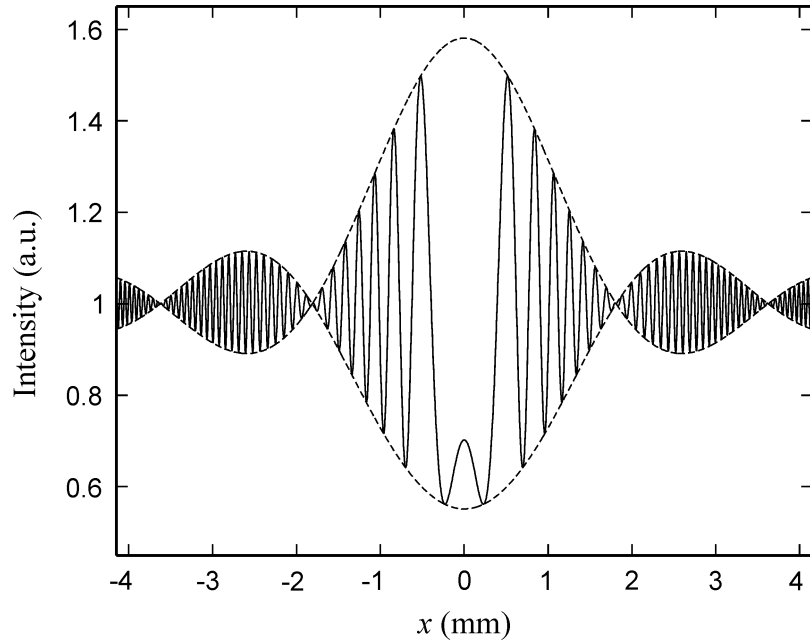


**Figure 2.3** Simulated in-line hologram of a line object.

### 2.1.2 Spherical object

For a circular cross-section spherical object with the amplitude distribution function defined by

$$A(\xi, \eta) = \begin{cases} 1 & \text{for } \sqrt{\xi^2 + \eta^2} \leq a \\ 0 & \text{for } \sqrt{\xi^2 + \eta^2} > a, \end{cases} \quad (2.5)$$

where  $a$  is the radius of the object, the amplitude transmittance of its hologram at the recording plane  $(x, y)$  a distance  $z$  behind the object plane can be mathematically expressed as (Tyler and Thompson, 1976)

$$I(r) = 1 - \frac{2\pi a^2}{\lambda z} \sin\left(\frac{\pi r^2}{\lambda z}\right) \left[ \frac{2J_1\left(\frac{2\pi ar}{\lambda z}\right)}{\frac{2\pi ar}{\lambda z}} \right] + \frac{\pi^2 a^4}{\lambda^2 z^2} \left[ \frac{2J_1\left(\frac{2\pi ar}{\lambda z}\right)}{\frac{2\pi ar}{\lambda z}} \right]^2. \quad (2.6)$$

$J_1$  denotes the first-order Bessel function, while  $r$  is the radius coordinate in the hologram plane which is defined by

$$r = \sqrt{x^2 + y^2}. \quad (2.7)$$

As in the case of the line object, the illuminating light is assumed to be of unit amplitude. The derivation of Eq. (2.6) is given in Appendix. The interpretation of Eq. (2.6) is similar to that of the Eq. (2.4). However, in case of a spherical object, the envelope function is now represented by the Bessel function instead of the sinc function. Plot of Eq. (2.6) by using the same parameters as the ones used for plotting of Eq. (2.4) is shown in Fig. 2.4, where the broken line represents the envelope function. It can be seen that, because of the Bessel function, the envelope function of the 2-D spherical object is wider than that of the 1-D case.

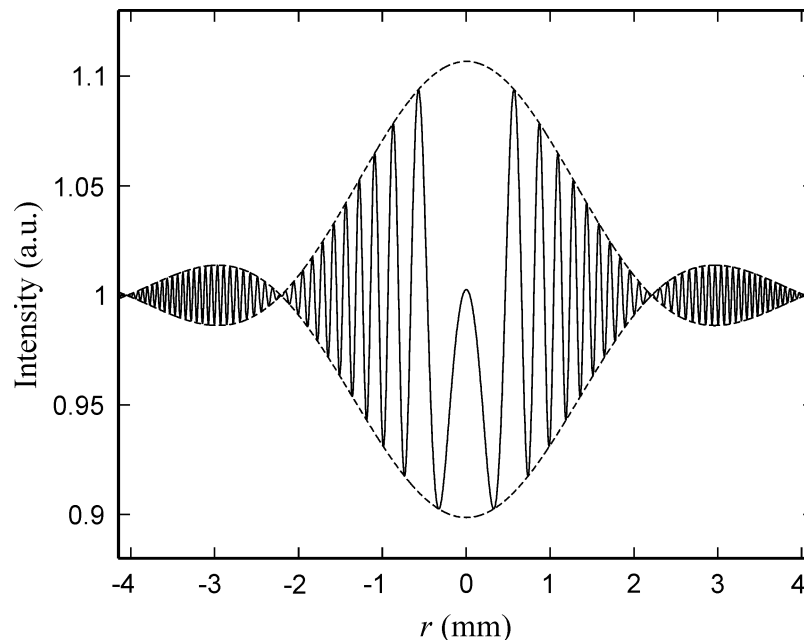


**Figure 2.4** Simulated in-line hologram of a spherical object.

## 2.2 The wavelet transform

The wavelet transform (WT) is a mathematical technique which has been introduced in signal analysis to overcome the inability of Fourier analysis in providing local frequency spectra. The WT of a signal pattern  $s(r)$  is defined as (Kronland-Martinet, Morlet and Grossmann, 1987)

$$W(t, d) = \frac{1}{\sqrt{d}} \int_{-\infty}^{\infty} g^* \left( \frac{r-t}{d} \right) s(r) dr, \quad (2.8)$$

where  $g(r)$  is the analyzing wavelet function with  $d$  and  $t$  being the dilation (scale) and the translation (shift) parameters, respectively. According to Eq. (2.8), the WT is computed by correlating the analyzed signal with a set of dilated wavelets whose frequency contents are inversely proportional to the dilation values. When the signal  $s(r)$  has the same frequency content as that of the dilated analyzing wavelet  $g(r/d)$  in the region subtended by  $g^* [(r-t)/d]$ , a correlation peak is generated in the WT domain. Thus, the WT of the signal  $s(r)$  is a description of the signal across a range of frequencies. The resultant WT gives many wavelet coefficients  $W$  which are a function of scale and position. Since the WT is computed at given continuous values of the dilation and the translation, this type of WT is called the continuous WT. By using a correlation property, Eq. (2.8) can be computed by using a Fourier transform (FT)

$$\begin{aligned} W(t, d) &= \mathcal{F}^{-1} \left\{ \frac{1}{\sqrt{d}} \mathcal{F} \left\{ g^* \left( \frac{r}{d} \right) \right\} \mathcal{F} \{ s(r) \} \right\} (t) \\ &= \mathcal{F}^{-1} \left\{ \sqrt{d} G^* (-df) S(f) \right\} (t), \end{aligned} \quad (2.9)$$

where  $\mathcal{F}$  and  $\mathcal{F}^{-1}$  denote the forward and the inverse FTs which are defined by (Goodman, 1996)

$$\mathcal{F}\{s(r)\} = \int_{-\infty}^{\infty} s(r)e^{-j2\pi fr} dr \quad (2.10)$$

and

$$\mathcal{F}^{-1}\{S(f)\} = \int_{-\infty}^{\infty} S(f)e^{j2\pi fr} df, \quad (2.11)$$

respectively.

In this thesis, the Morlet wavelet defined as (Kronland-Martinet et al., 1987)

$$g(r) = e^{i2\pi f_g r} e^{-r^2/2} \quad (2.12)$$

is used as the analyzing wavelet with  $f_g$  denoting the frequency of the wavelet. Plots of the real value of the dilated Morlet wavelet with  $f_g = 0.001$  lines/mm versus its spectrum for different dilations are shown in the left column of Fig. 2.5. When the scale value is high, the wavelet is dilated. While it is compressed for small value of the scale. The inverse proportional relationship between the dilation and the frequency response of the wavelet can be obviously observed from the right column of the figure. When the wavelet is dilated in the space domain, its center frequency and bandwidth decrease. However, the compressed wavelet gives higher center frequency and broader bandwidth. It can also be seen from Eq. (2.9) and Fig. 2.5 that the computation of the wavelet coefficients equivalent to the filtering operation of the analyzed signal by the set of band pass filters having center frequency of  $f_g/d$ . The filtered signal is the wavelet coefficients at the corresponding dilation value  $d$ .

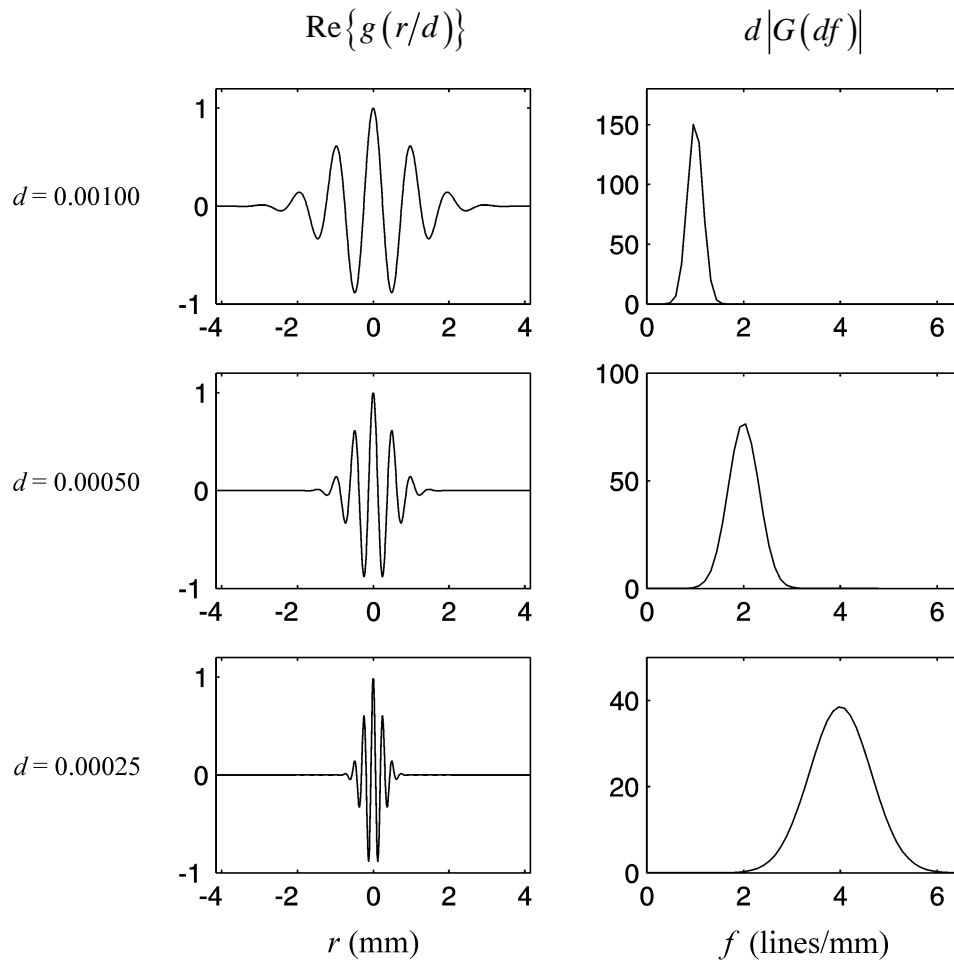


**Figure 2.5** Morlet wavelet and its spectrum for different dilation values.

If the spatial width and the bandwidth of the wavelet are regarded as the spatial and the frequency resolutions respectively, the small scale gives a wavelet analysis with high spatial resolution and low frequency resolution. In contrast, the high scale corresponds to wavelet coefficients with low spatial resolution and high frequency resolution. This is known as the multi-resolution property of the WT. This property is suitable for analyzing non-stationary signals whose high-frequency components occur in short period, while its low-frequency components exist for a longer period. Therefore, analysis of single-shot signals such as spikes must be done by using the

compressed wavelet because its spatial width is narrow and its center frequency is high. However, the decomposition of the low-frequency components of signals which occur in a longer period requires the dilated wavelets. This yields wavelet coefficients with higher frequency resolution.

Figure 2.6 illustrates the real value of the resultant wavelet coefficients of the hologram shown in Fig. 2.3. The horizontal axis corresponds to the spatial translation of the interference pattern, while the vertical axis indicates the dilation parameter plotted in a logarithmic scale. The black and white colors represent the minimum and the maximum values of the wavelet coefficients, respectively. The solid lines represent the theoretical value of the space varying spatial frequency of the chirp signal. Since the frequency of the chirp signal becomes higher as the position  $x$

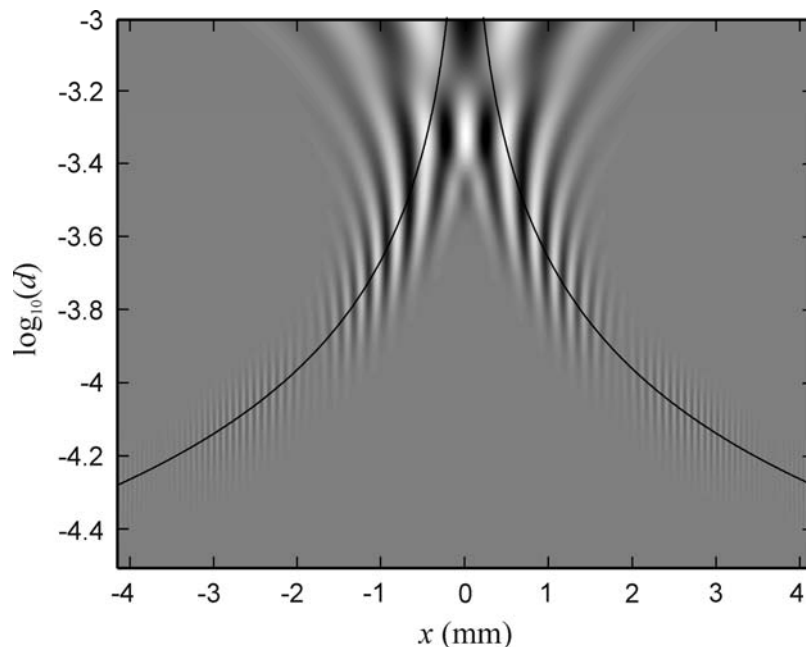


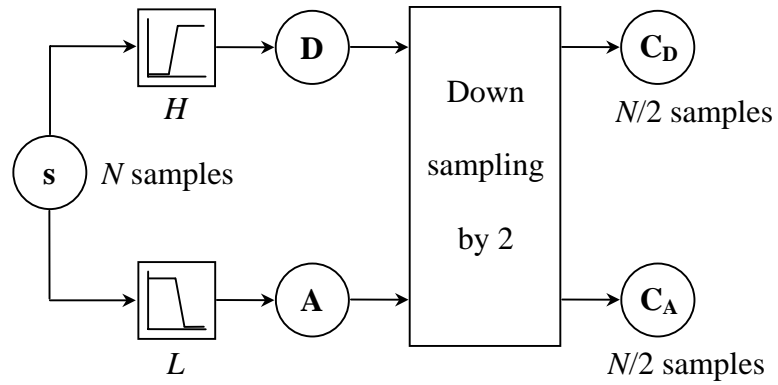
**Figure 2.6** Plot of the real value of the continuous wavelet coefficients of the simulated hologram in Fig. 2.3.

increases, the dilation values decreases. It can be seen from the Fig. 2.6 that the resultant continuous WT of the interference pattern agree well with the predicted theoretical values.

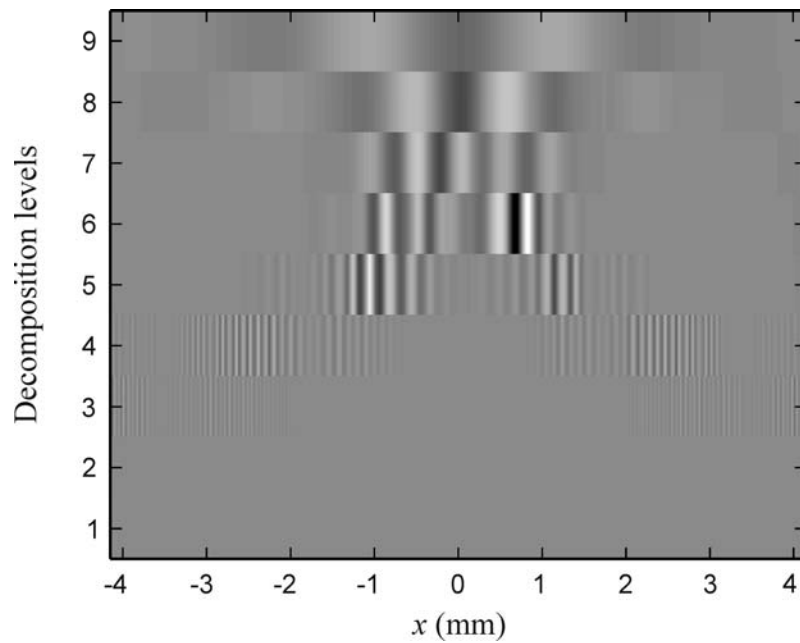
Unlike the continuous WT which is computed at any given continuous values of the translation and the dilation, a discrete WT computes the wavelet coefficients only in a dyadic interval of the translation  $t = 2^j$  and the dilation  $d = 2^j$  (Misiti, Misiti, Oppenheim and Poggi, 2001). The discrete WT coefficients are obtained by means of a series of filtering and subsampling operations. As for the discrete signal  $\mathbf{s}$  having  $N$  samples, these operations are done by passing the signal through high-pass and low-pass filters whose cutoff frequencies are half of the maximum frequency of the analyzed signal  $\mathbf{s}$ . The output of the high-pass filter contains detail information  $\mathbf{D}$  of the signal with frequencies that are higher than its cut off frequency, while the low-pass filter produces coarse information  $\mathbf{A}$ . Since the frequency contents of the filtered signals are reduced by half, they can be faithfully described by only  $N/2$  samples. This allows the information  $\mathbf{A}$  and  $\mathbf{D}$  to be down-sampled by a factor of 2 without loss of frequency resolution. The results after down sampling are the detail coefficients and the approximation coefficients which are represented by  $\mathbf{C}_D$  and  $\mathbf{C}_A$ , respectively. Fig. 2.7 shows a block diagram of a single level decomposition process, where  $H$  and  $L$  denote the high-pass and low-pass filters, respectively. This process is repeatedly applied to the detail coefficient  $\mathbf{C}_A$  until it consists of single sample. The detail coefficients resulting from these processes are the WT coefficients in the corresponding level of decomposition.

Figure 2.8 plots the discrete wavelet coefficients of the interference signal shown in Fig. 2.3. The first level decomposition gives the discrete wavelet

coefficients that corresponds to the high frequency content of the interference pattern,



**Figure 2.7** Single level decomposition of the signal  $s$  (Misiti, Misiti, Oppenheim and Poggi, 2001).



**Figure 2.8** Plot of the discrete wavelet coefficients of the simulated hologram in Fig. 2.3.

while the ninth level decomposition represents the low frequency information. Although the discrete WT could reveal the space-varying frequency of the analyzed signal, the accuracy of this information is much lower than that of the continuous WT. This is because the discrete WT is computed only at the dyadic intervals. Therefore, in order to analyze accurately the particle holograms, this thesis employs the continuous WT. For the sake of simplicity, the term WT will henceforth be used in regard to the continuous WT.

## **CHAPTER III**

### **HOLOGRAM FORMATION**

In order to study feasibility of the proposed method, the holograms of line and spherical objects are both digitally and optically generated. The study also takes into account the presence of multiple objects in the object plane. In the simulation all parameters used to generate holograms are based on technical specifications of instruments employed in the experiment. All digital computations are conducted by using the Matlab 6.1 software run on the Windows XP based computer IBM NetVista 6578-TBT with the 966 MHz Intel Pentium III processor and 256 MB of RAM.

In the experimental verification, the CCD sensor HAMAMATSU C5948 having the resolution of 640×480 pixels in the area of 8.3×6.3 mm was employed to capture the hologram. However, since this type of CCD has analog output, the pixel size in the stored hologram depends on the image-captured board used. In order to calibrate the pixel size of the sensor, a small spot of a laser beam was used to illuminate the CCD sensor mounted on a micrometer stage. The average pixel size of the sensor was obtained by dividing a measured distance between two different positions illuminated by the beam by the number of pixels contained by this distance. By doing this calibration, the average pixel sizes in the horizontal and the vertical directions are found to be 12.99  $\mu\text{m}$  and 11.03  $\mu\text{m}$ , respectively.

### 3.1 Single object

The holograms of single line and spherical objects were generated for different object sizes and recording distances. The holograms are simulated with the same recording distances as those used in the experiment. However, due to the different experimental setup and the limited experimental space, the range of the recording distances for the line and the spherical objects are different.

#### 3.1.1 Line object

The holograms of line objects having the radius  $a$  of 20  $\mu\text{m}$  and 62.48  $\mu\text{m}$  are simulated by using Eq. (2.4) for the recording distances of  $10\text{ cm} < z < 20\text{ cm}$ . According to the resolution of the CCD sensor, the number of samples  $N$  used for simulating the hologram is 640 pixels with the sampling interval  $\Delta x$  of 12.99  $\mu\text{m}$ , and the wavelength of illuminating light  $\lambda$  is 543.5 nm.

According to Eq. (6.3) in Chapter VI, the length  $x$  measured from the center of the interference pattern that can be correctly sampled must less than  $\lambda z/2\Delta x$ . In the case of the line object recorded at the distance 20 cm the maximum length is 4.2 mm. Fig. 3.1 shows the simulated hologram of the line object with a radius of 62.48  $\mu\text{m}$  recorded at the distance  $z = 20\text{ cm}$ . Although the simulated hologram satisfies this condition, some distortions can still be observed at the higher-order lobes of the signal. This is because the frequency of the chirp signal increases as a function of the position  $x$  while the sampling frequency is fixed at  $1/\Delta x$  lines/mm. As a result, large amount of distortion will be introduced to the portion of the signal having higher frequencies than the Nyquist frequency,  $1/2\Delta x$  lines/mm, such that the contents of

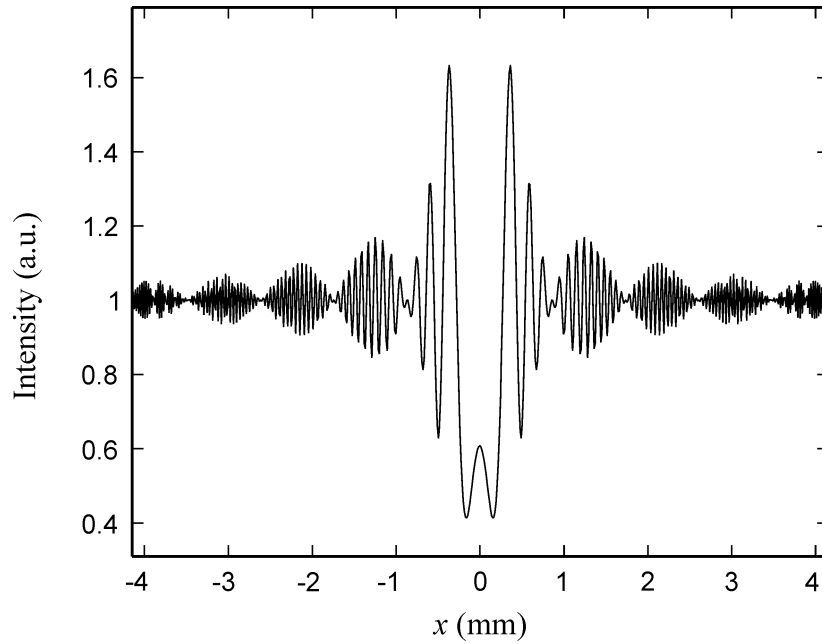


**Figure 3.1** Simulated in-line hologram of the line object  
with  $a = 62.48 \mu\text{m}$  and  $z = 20 \text{ cm}$ .

those frequencies is loss. When the frequencies of the digitized signal are lower than the Nyquist frequency, their frequencies content is preserved. However, smaller distortion still exists in the 3<sup>rd</sup> and 4<sup>th</sup> lobes of the digitized hologram.

For the optical generation of the holograms, an optical fiber having a radius of  $62.48 \mu\text{m}$  was employed as the line object. This size was obtained by measuring the fiber using a microscope OLYMPUS CH30RF200. The optical setup used to generate the holograms is shown in Fig. 3.2. It consisted of a He-Ne laser source Melles Griot 05-LGR-193 with a wavelength of  $543.5 \text{ nm}$ , a spatial filter, a collimating lens with a focal length of  $300 \text{ mm}$  and a CCD sensor. The spatial filter was constructed by using a microscope objective lens with focal length of  $14.8 \text{ mm}$  and the pinhole having a diameter of  $25 \mu\text{m}$ . The laser beam was expanded by using a combination of the spatial filter and the collimating lens to generate a uniform plane wave. Next, the

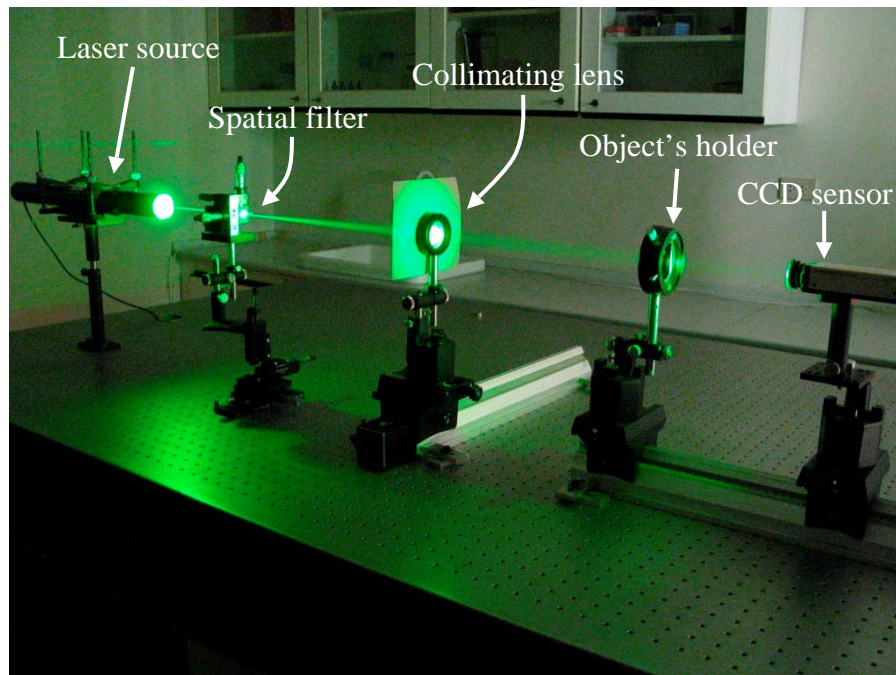


**Figure 3.2** Experimental setup for generating the in-line hologram of the optical fiber.

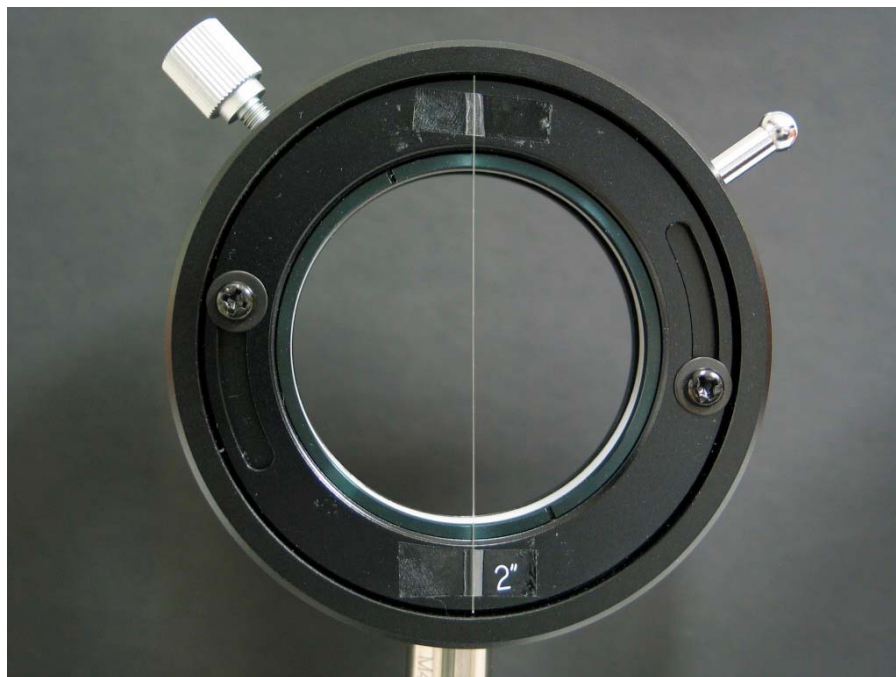


**Figure 3.3** Optical fiber mounted on the holder.

generated plane wave was used to illuminate the optical fiber mounted on the holder as shown in Fig. 3.3. Figure 3.4 illustrates the resultant interference pattern captured by the CCD sensor at the recording distance  $z = 20$  cm. It can be seen that the captured interference pattern has non uniform background. This may be caused by an imperfect collimation of the laser beam. In order to eliminate this background noise, a recorded holograms was digitally subtracted with the intensity of the illuminating beam recorded without the object depicted in Fig. 3.5. The subtraction of these two patterns resulted in modified holograms with significantly less background noise (Lai and Lin, 1996). Figure 3.6 shows that the subtraction of Fig. 3.5 from Fig. 3.4 entirely removes the noise. However, although the background noise can be removed, the hologram is still corrupted by a speckle noise. This is because the recorded speckle patterns caused by the scattered illuminating beam without and with the object are different. As a result, the subtraction cannot remove the speckle noise.

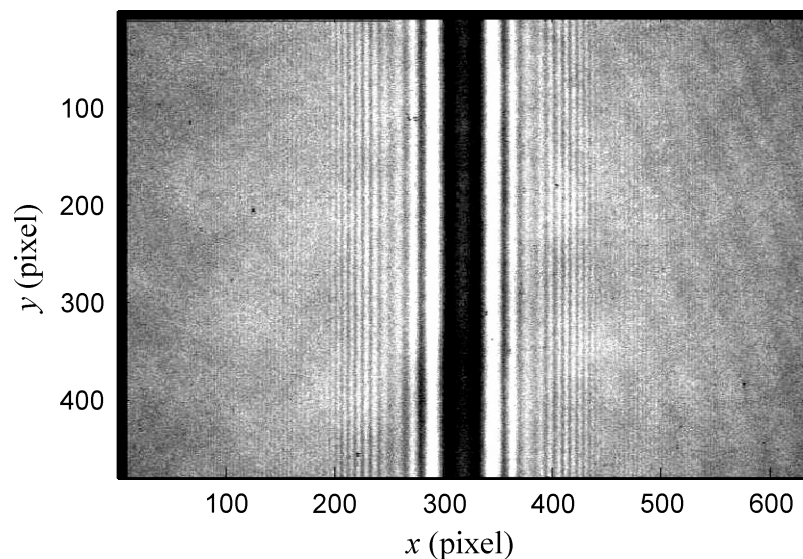


**Figure 3.4** In-line hologram of the optical fiber recorded at  $z = 20$  cm.

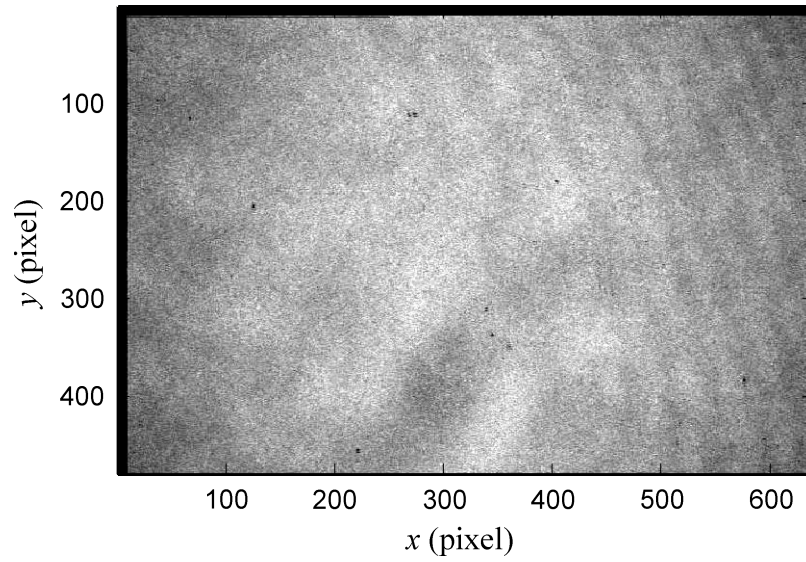


**Figure 3.5** Recorded intensity of the reference beam at  $z = 20$  cm.

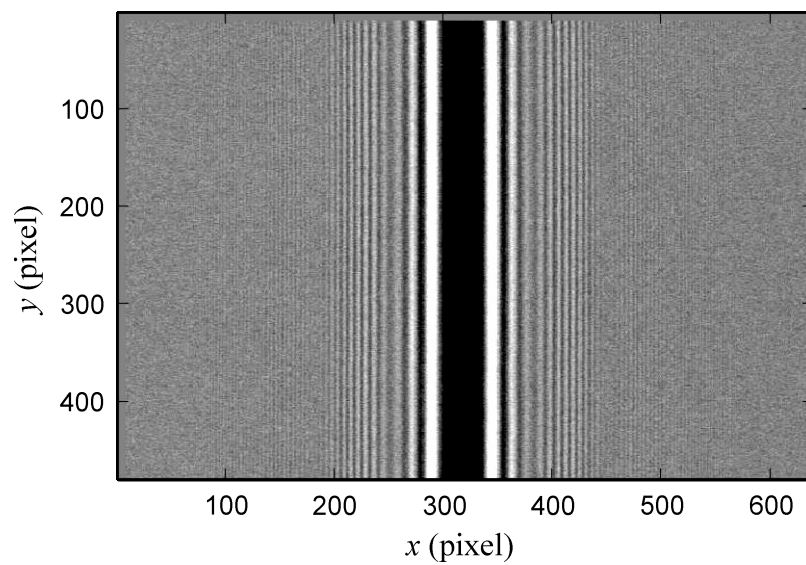


**Figure 3.6** In-line hologram of the optical fiber recorded at  $z = 20$  cm with the background removed.

Figure 3.7 shows the 1-D profile of the hologram obtained by scanning the intensity at the 240<sup>th</sup> row of Fig. 3.6. In comparison with Fig. 3.1, it is understood that the speckle noise appears as random intensity fluctuation of the hologram. In order to reduce the speckle noise, intensities of all pixels are averaged along the vertical direction. The effectiveness of this averaging process is shown in Fig. 3.8 which is computed from the middle four hundred lines of the Fig. 3.6, because the first few lines shown as a thick black line on top row of Fig. 3.5 have no information.

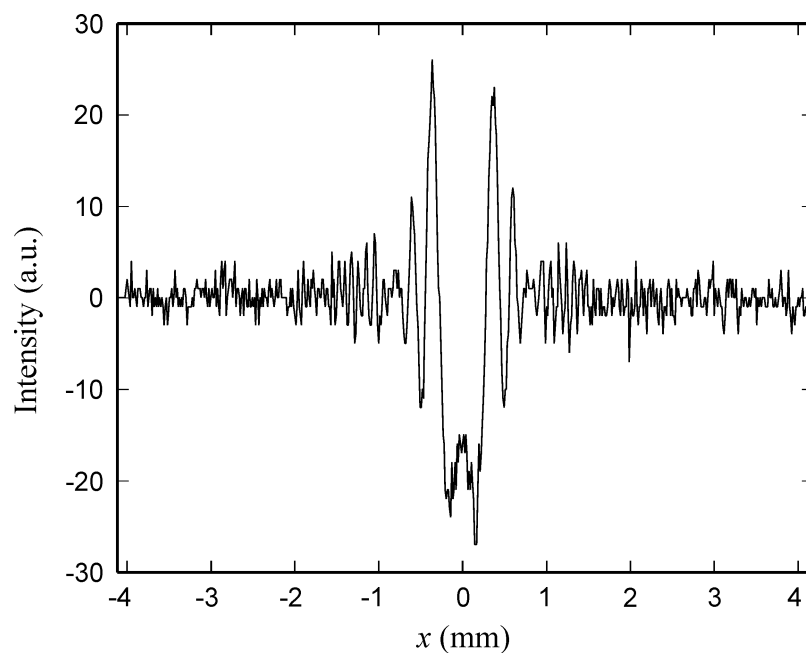


**Figure 3.7** 1-D intensity profile of the 240<sup>th</sup> row of the hologram shown in Fig. 3.6.

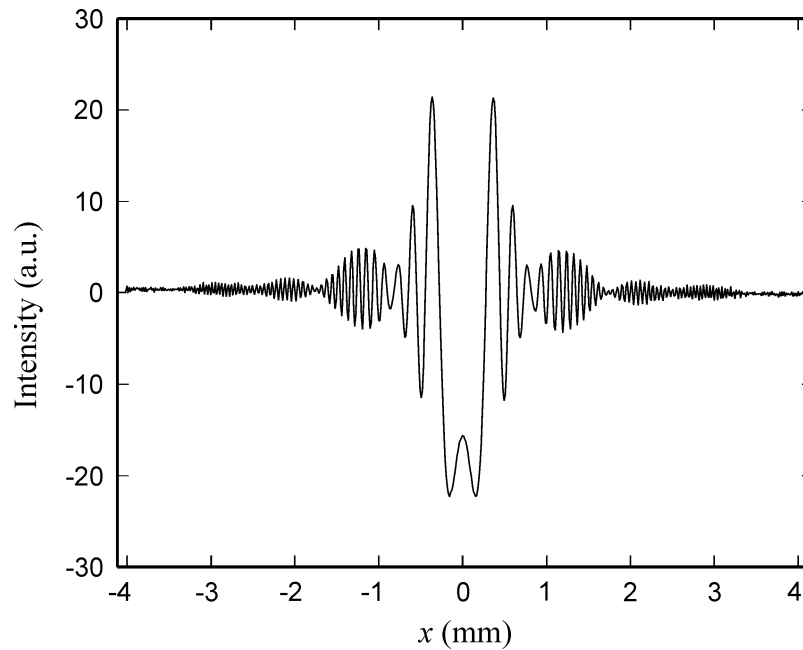


**Figure 3.8** 1-D averaged intensity profile of the middle 400 rows of the hologram shown in Fig. 3.6.

### 3.1.2 Spherical object

Although a spherical particle is the most common 2-D object found in the applications of particle holography, the size of the available standard spherical objects is very small. As a result, the generated interference pattern is very broad so that the CCD sensor could not record faithfully the pattern. For this reason, instead, the pinhole with larger diameter was used as the 2-D test object, because it has the same circular cross-sectional shape as the spherical opaque particle. However, the amplitude distribution function of the pinhole is the reversal of that of an opaque spherical object, since the incident light is blocked from passing the pinhole outer area. Since this light should constitute the reference beam, the hologram of the pinhole could not be generated by using the optical setup of the in-line holography

shown in Fig. 2.1. In order to overcome this problem, the Mach-Zehnder interferometer shown in Fig. 3.9 is employed. The interferometer consists of two optical paths separated by the beam splitter BS1. The first path is the object path that contains the mirror M1 and the object to be studied. The second one is the reference path that contains the mirror M2. The mirrors M1 and M2 are used for beam steering purpose. After being diffracted by the object located at the input plane  $(\xi, \eta)$  the object beam is recombined with the reference beam by the BS2. Finally, the interference pattern of these two waves at a distance  $z$  behind the object plane is captured by the CCD sensor.

Due to the different optical setup, Eq. (2.6) is not valid mathematical expression for the generated hologram of the pinhole. The hologram is now the interference of the diffraction of the pinhole and the reference plane wave which can be mathematically expressed as

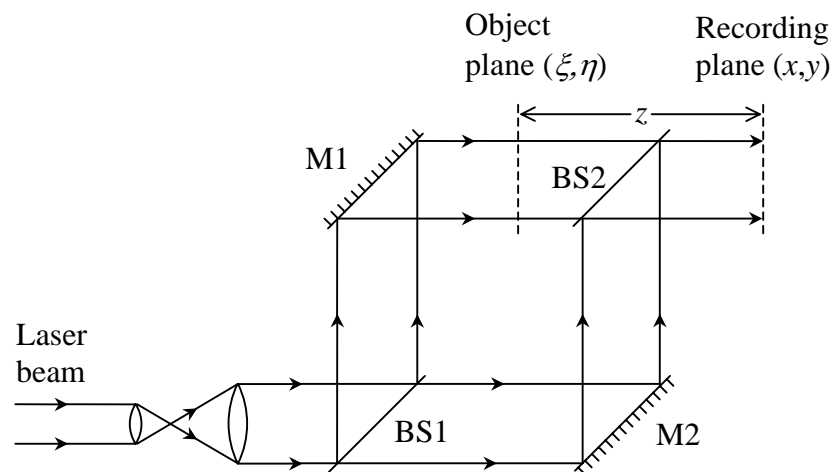


**Figure 3.9** Mach-Zehnder interferometer setup for recording the in-line hologram of the pinhole.

$$I(r) = 1 - \frac{2\pi a^2}{\lambda z} \sin\left(\frac{\pi r^2}{\lambda z} + \pi\right) \left[ \frac{2J_1\left(\frac{2\pi ar}{\lambda z}\right)}{\frac{2\pi ar}{\lambda z}} \right] + \frac{\pi^2 a^4}{\lambda^2 z^2} \left[ \frac{2J_1\left(\frac{2\pi ar}{\lambda z}\right)}{\frac{2\pi ar}{\lambda z}} \right]^2. \quad (3.1)$$

The proof of Eq. (3.1) is provided in Appendix. The difference between Eq. (3.1) and Eq. (2.6) is that the chirp function has an additional phase factor  $\pi$ . However, since the information of the recording distance and the object size are still encoded into the interference pattern in a similar manner as the hologram of the opaque spherical object, the in-line holograms of pinhole can be used for verifying the proposed digital analyzing method. The plot of Eq. (3.1) by using the same parameters as the ones used for plotting Fig. 2.4 is shown in Fig. 3.10. From these two figures, the initial phase different of  $\pi$  can be noticed.

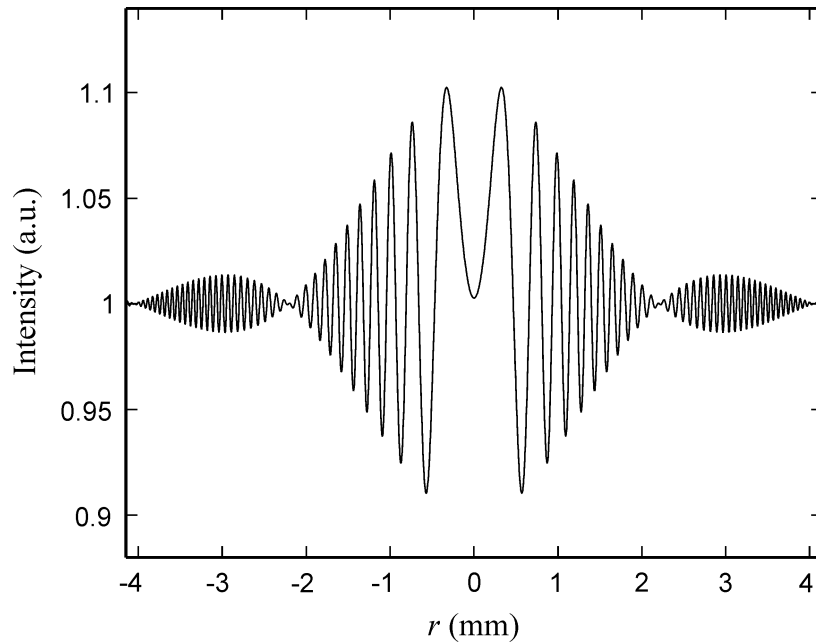


**Figure 3.10** Simulated in-line hologram of a pinhole.

In this study, the in-line holograms were simulated by using pinholes having the radius  $a$  of  $20\ \mu\text{m}$  and  $77.78\ \mu\text{m}$  at the recording distance of  $12\ \text{cm} < z < 24\ \text{cm}$ . Figure 3.11 shows the simulated hologram of the circular aperture having a radius of  $77.78\ \mu\text{m}$  recorded at the distance of  $20\ \text{cm}$ .

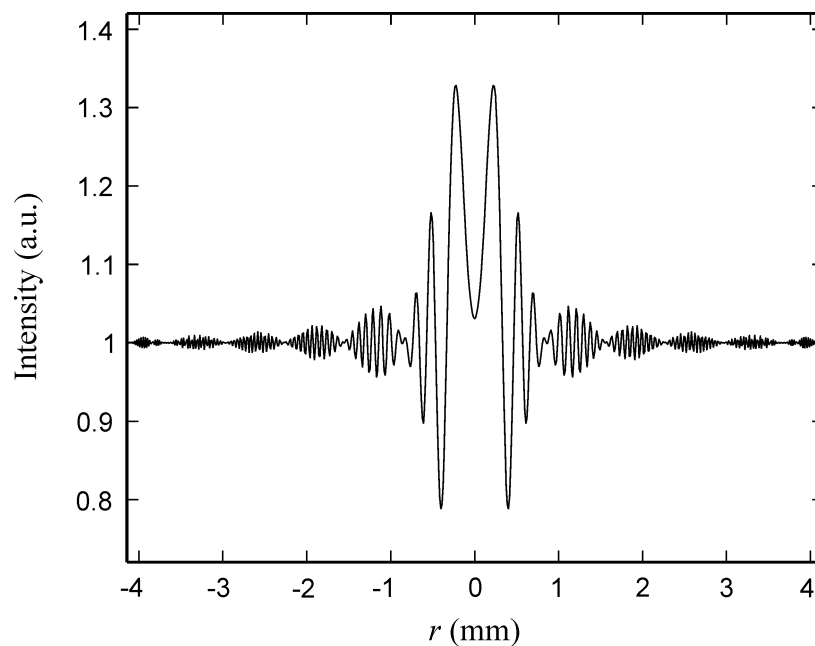


**Figure 3.11** Simulated in-line hologram of a circular aperture with the radius  $77.78\ \mu\text{m}$  and distance  $z = 20\ \text{cm}$ .

In the optical generation of the holograms of spherical objects, a pinhole having a radius of  $77.78\ \mu\text{m}$  was employed as the test object. This size was obtained by measuring the pinhole using the microscope OLYMPUS CH30RF200. Figure 3.12 shows the picture of the pinhole mounted on the slide holder. The Mach-Zehnder interferometer shown in Fig. 3.13 was used to generate the holograms of the pinhole. The same coherent light source and the spatial filter were used for providing light



**Figure 3.12** The pinhole mounted on the slide holder.

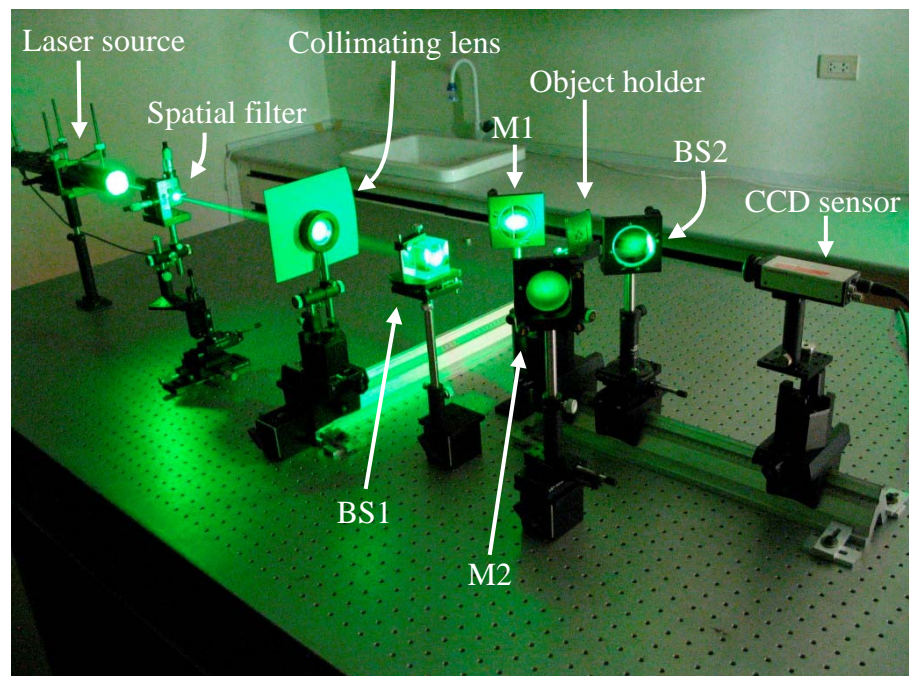


**Figure 3.13** Experimental setup for generating the in-line hologram of the pinhole.

wave to be expanded. The beam was expanded by using a collimating lens with a focal length of 400 mm. A cube beam splitter Melles Griot 03BSC013 with a thickness of 40 mm which was used as a BS1 produced the reference and the object beams. The mirrors M1 and M2, Melles Griot 02MFG019/023, were used for steering the object and the reference beams, respectively. After passing through the pinhole, the diffracted wave was recombined with the reference wave by the beam splitter BS2. In order to prevent aberration of the diffracted object wave caused by thickness of the beam splitter, the optical flat glass Sigma OFBP-50C05-10-5 having a thickness of 5 mm was employed as the BS2. However, since the surfaces of the flat glass do not have anti-reflection coating, the beam passing through the glass may undergo multiple reflection. As for the collimated reference beam, the multiple reflected beams produced interference fringes which could be seen as a periodic diagonal pattern shown in Fig. 3.14. In the object path, the multiple reflection of the

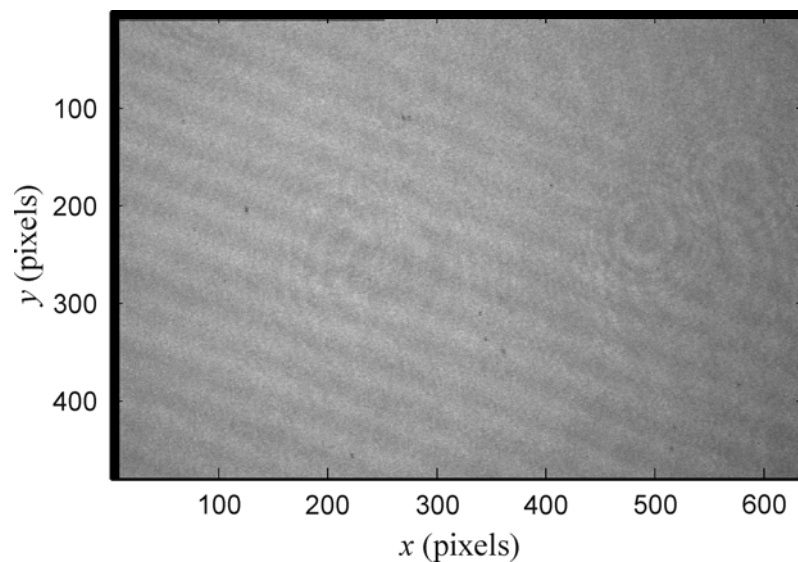


**Figure 3.14** Recorded intensity of the reference beam at  $z = 20$  cm.

object beam produces a weak Airy pattern on the left side of the desired Airy pattern as shown in Fig. 3.15. Figure 3.16 shows the hologram of the pinhole recorded at the distance  $z = 20$  cm with the unwanted diagonal interference pattern appearing as background. According to the background removal technique discussed in the preceding section, the unwanted background can be removed by subtracting digitally the generated hologram shown in Fig. 3.16 with the intensity of the reference beam shown in Fig. 3.14. The resultant subtraction is depicted in Fig. 3.17. It is clear that the unwanted background can be successfully removed. The unwanted interference pattern on the left side of Fig. 3.17 may be generated by the multiple reflections of the object beam inside the flat glass. It is very weak and does not overlap with the desired interference pattern. Thus, the distortion of the hologram from this interference pattern is minimal.

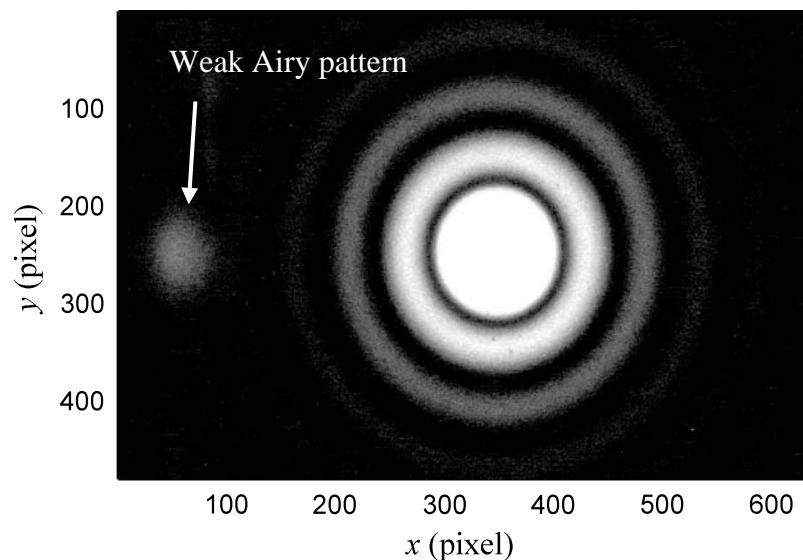


**Figure 3.15** Recorded intensity of the object beam at  $z = 20$  cm

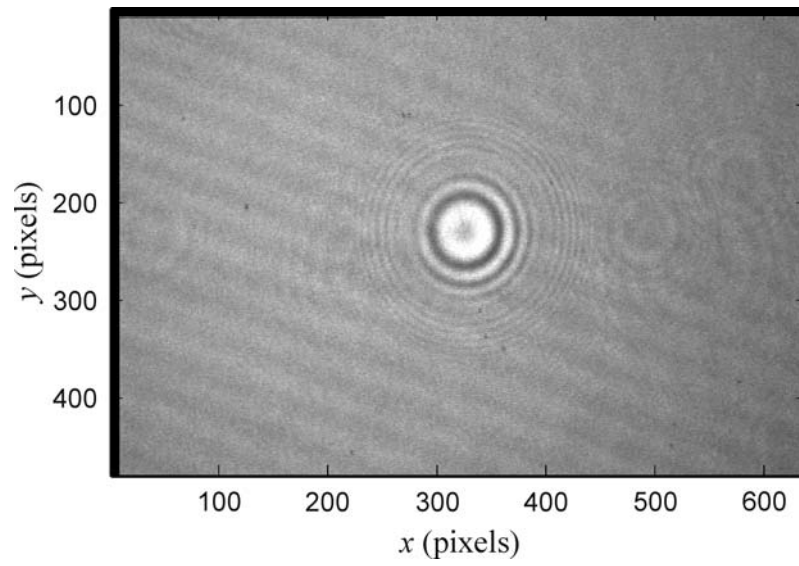


**Figure 3.16** In-line hologram of the pinhole recorded at  $z = 20$  cm.

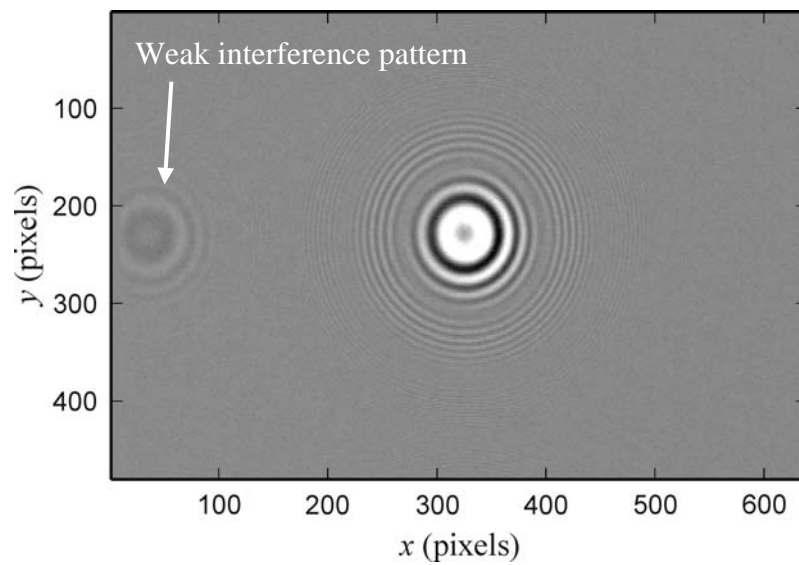


**Figure 3.17** In-line hologram of the pinhole recorded at  $z = 20$  cm with the background removal.

As in the case of the hologram of the optical fiber, the generated holograms are also distorted by speckle noise. This can be seen from the 1-D intensity profile of the hologram depicted in Fig. 3.18. This profile was obtained by scanning the intensity variation along the 229<sup>th</sup> row which is the center row of the interference pattern. In order to remove this speckle noise, an angular averaging of the intensities of the corresponding pixels of the interference pattern was used. Due to the circular symmetry of the pattern, the outer most pixel that can be averaged is determined by its position in the vertical direction. Figure 3.19 shows the 1-D intensity profile of the angular averaged interference pattern with 1-degree angular increment. The reduction of the speckle noise can be clearly seen from this figure and this result agrees with the simulated hologram illustrated in Fig. 3.11.

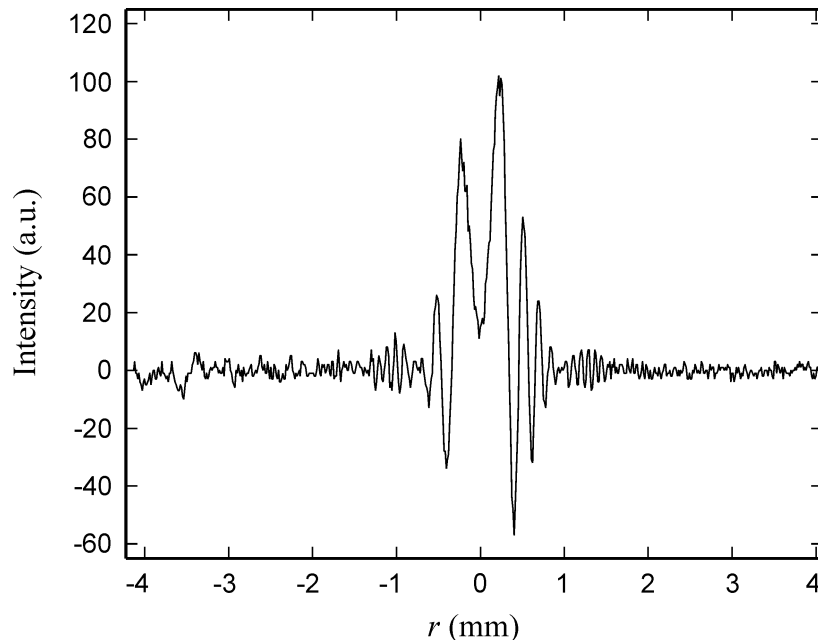


**Figure 3.18** 1-D intensity profile of the 229<sup>th</sup> row of the hologram shown in Fig. 3.17.

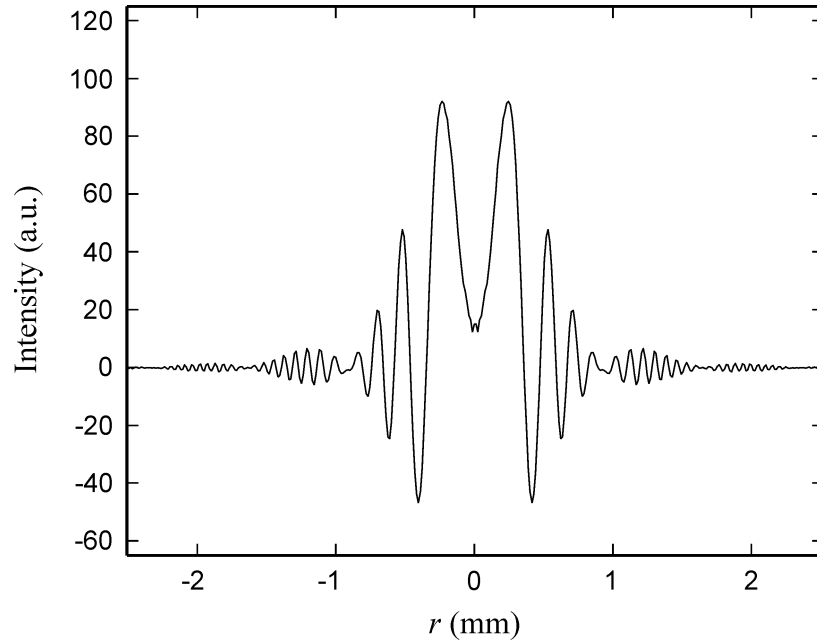


**Figure 3.19** 1-D angular averaged intensity profile of the desired interference pattern shown in Fig. 3.17.

### 3.2 Multiple objects

In real situation, the particle field may consists of many particles. In this case, the complex field incident on the recording plane becomes the interference between the reference plane wave and the object wave which is a summation of the waves scattered from the individual object. Thus, the recorded intensity at the hologram plane can be mathematically expressed as

$$I(x, y) = |R + O(x, y)|^2, \quad (3.2)$$

where  $R$  is the complex amplitude of the reference plane wave and  $O(x, y)$  represents the scattered light defined by

$$O(x, y) = \sum_{k=1}^K o_k(x, y). \quad (3.3)$$

Here,  $o_k(x, y)$  is the wave scattered from the  $k^{\text{th}}$  object while  $K$  represents the number of the objects. Thus, the amplitude transmittance of the hologram becomes

$$I(x, y) = |R|^2 + |O(x, y)|^2 + R^*O(x, y) + RO^*(x, y), \quad (3.4)$$

where the interference among the object waves denoted by the second term of Eq. (3.4) can be found from

$$|O(x, y)|^2 = \sum_{k=1}^K \sum_{l=1}^K o_k(x, y) o_l^*(x, y). \quad (3.5)$$

For the sake of consistency with the hologram of a single object, the interference of the object waves from the same and different objects are separately written from each other. As a result, Eq. (3.5) becomes

$$|O(x, y)|^2 = \sum_{k=1}^K o_k(x, y) o_k^*(x, y) + \sum_{k=1}^K \sum_{\substack{l=1 \\ l \neq k}}^K o_k(x, y) o_l^*(x, y). \quad (3.6)$$

Substitution of the Eqs. (3.6) and (3.3) into the Eq. (3.4) resulted in

$$\begin{aligned} I(x, y) = & |R|^2 + \sum_{k=1}^K o_k(x, y) o_k^*(x, y) + R^* \sum_{k=1}^K o_k(x, y) \\ & + R \sum_{k=1}^K o_k^*(x, y) + \sum_{k=1}^K \sum_{\substack{l=1 \\ l \neq k}}^K o_k(x, y) o_l^*(x, y). \end{aligned} \quad (3.7)$$

In comparison with the Eq. (2.1), aside from the constant term  $|R|^2$ , the hologram of multiple objects is simply a linear summation of the hologram from the individual

object with the extra addition of the interference among the object waves from different objects denoted by the fifth terms of the Eq. (3.7).

In case of multiple-line objects, the intensity of the recorded hologram can be mathematically expressed as

$$\begin{aligned}
 I(x, y) = 1 - \sum_{k=1}^K & \left\{ \frac{4a_k}{\sqrt{\lambda z_k}} \cos \left( \frac{\pi |x - x_k|^2}{\lambda z_k} - \frac{\pi}{4} \right) \left[ \frac{\sin \frac{2\pi a_k |x - x_k|}{\lambda z_k}}{\frac{2\pi a_k |x - x_k|}{\lambda z_k}} \right] \right. \\
 & + \frac{4a_k^2}{\lambda z_k} \left. \left[ \frac{\sin \frac{2\pi a_k |x - x_k|}{\lambda z_k}}{\frac{2\pi a_k |x - x_k|}{\lambda z_k}} \right]^2 \right\} + \sum_{k=1}^K \sum_{\substack{l=1 \\ l \neq k}}^K \left\{ \frac{4a_k a_l}{\lambda \sqrt{z_k z_l}} \left[ \frac{\sin \frac{2\pi a_k |x - x_k|}{\lambda z_k}}{\frac{2\pi a_k |x - x_k|}{\lambda z_k}} \right] \right. \\
 & \times \left. \left[ \frac{\sin \frac{2\pi a_l |x - x_l|}{\lambda z_l}}{\frac{2\pi a_l |x - x_l|}{\lambda z_l}} \right] \exp \left[ j \left( \frac{\pi |x - x_k|^2}{\lambda z_k} - \frac{\pi |x - x_l|^2}{\lambda z_l} \right) \right] \right\}, \quad (3.8)
 \end{aligned}$$

where  $a_k$ ,  $z_k$  and  $x_k$  are the radius, the recording distance, and the translation position of the  $k^{\text{th}}$  object, respectively. Figure 3.20 shows the simulated hologram of two optical fibers with the same radius of 62.48  $\mu\text{m}$  which are separated by 5 mm distance in both the  $x$  and the  $z$  directions. Its 1-D intensity profile plotted in Fig. 3.21 shows that the interference pattern of one of the fibers is distorted by the interference pattern of the other fiber.

Similarly, the hologram of multiple spherical objects can be mathematically written as

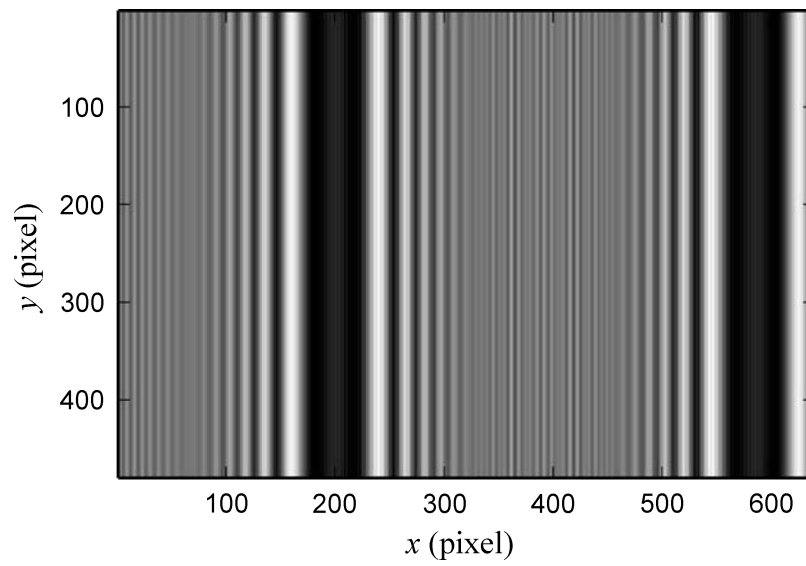


**Figure 3.20** Hologram of two optical fibers separated by 5 mm distance in both  $x$  and  $z$  direction.

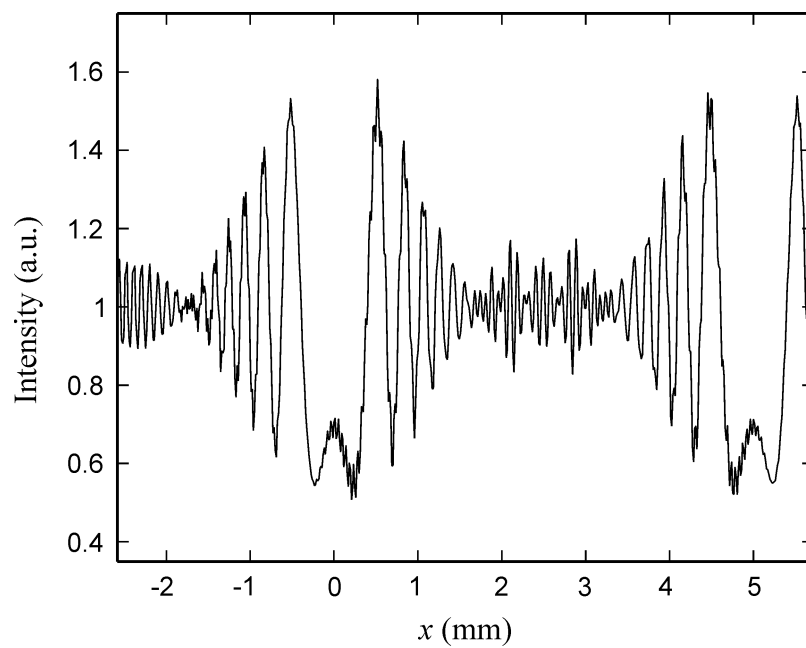


**Figure 3.21** 1-D intensity profile of the hologram shown in Fig. 3.20.

$$\begin{aligned}
I(r) = & 1 - \sum_{k=1}^K \left\{ \frac{2\pi a_k^2}{\lambda z_k} \sin\left(\frac{\pi |r-r_k|^2}{\lambda z_k}\right) \left[ \frac{2J_1\left(\frac{2\pi a_k |r-r_k|}{\lambda z_k}\right)}{\frac{2\pi a_k |r-r_k|}{\lambda z_k}} \right] \right. \\
& + \frac{\pi^2 a_k^4}{\lambda^2 z_k^2} \left. \left[ \frac{2J_1\left(\frac{2\pi a_k |r-r_k|}{\lambda z_k}\right)}{\frac{2\pi a_k |r-r_k|}{\lambda z_k}} \right]^2 \right\} + \sum_{k=1}^K \sum_{\substack{l=1 \\ l \neq k}}^K \left\{ \frac{\pi^2 a_k^2 a_l^2}{\lambda^2 z_k z_l} \left[ \frac{2J_1\left(\frac{2\pi a_k |r-r_k|}{\lambda z_k}\right)}{\frac{2\pi a_k |r-r_k|}{\lambda z_k}} \right] \right. \\
& \times \left. \left[ \frac{2J_1\left(\frac{2\pi a_l |r-r_l|}{\lambda z_l}\right)}{\frac{2\pi a_l |r-r_l|}{\lambda z_l}} \right] \exp\left[ j \left( \frac{\pi |r-r_k|^2}{\lambda z_k} - \frac{\pi |r-r_l|^2}{\lambda z_l} \right) \right] \right\}. \quad (3.9)
\end{aligned}$$

The rigorous mathematical derivation of the Eqs. (3.8) and (3.9) is given in Appendix.

The hologram of two identical spherical objects having the radius of 77.78  $\mu\text{m}$  which are separated by 5 mm distance in the  $r$  and the  $z$  directions is shown in Fig. 3.22, and its 1-D intensity profile is plotted in Fig. 3.23. In comparison with Fig. 3.21, the distortion of the hologram shown in Fig. 3.23 is smaller. This is because firstly the amplitude of the side lobe of the Bessel function in the second term of Eq. (3.9) is smaller than that of the Sinc function of the Eq. (3.8). Secondly, the multiplicative factor of the second term of Eq. (3.9) is smaller than that of Eq. (3.8).

Furthermore, it is found from Eqs. (3.8) and (3.9) that the amplitude of the third term is much smaller than that of the second term so that the third term does not affect significantly the resultant interference pattern. As for the fourth terms of both equations, their amplitudes are determined by the multiplication of two envelope functions centered at different positions. Therefore they are smaller than the third term. As a consequence when the separation between the two objects decreases, this

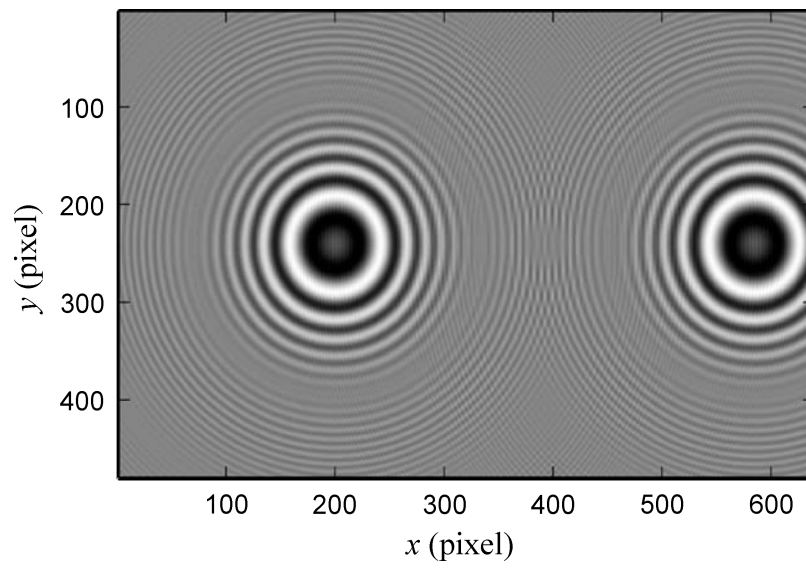


**Figure 3.22** Hologram of two spherical objects separated by 5 mm distance in both  $x$  and  $z$  direction.

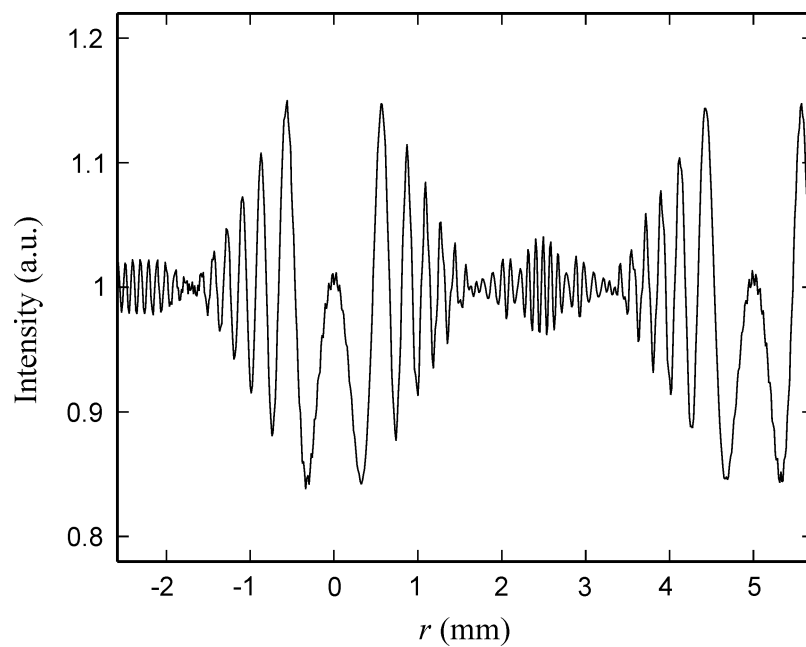


**Figure 3.23** 1-D intensity profile of the hologram shown in Fig. 3.22.

amplitude increases. The value of the amplitude of the fourth term becomes maximum when one of the object overlaps another. Since this maximum amplitude is comparable to the amplitude of the third term, the effect of the fourth term on the resultant interference pattern is also not significant.

# CHAPTER IV

## EXTRACTION OF OBJECT POSITION FROM IN-LINE HOLOGRAMS

In order to extract the 3-D position of the object from the digital hologram, the numerical method can be used to reconstruct the image of the object from the hologram by solving Fresnel diffraction integral (Schnars and Jüptner, 1994). The object position is obtained by searching for the best focus plane of the reconstructed image. However, as the number of object increases, the analysis by using the numerical reconstruction requires considerable computational time. In this thesis, a new method for extracting the object position through a direct analysis of the in-line hologram by using the WT is proposed. The method has advantages in that the information of the position can be directly obtained without searching for the best focus plane.

In Chapter II, Eqs. (2.4) and (2.6) reveal that the axial position of the objects is encoded as

$$z = \frac{x}{\lambda f_{\text{chirp}}}, \quad (4.1)$$

where  $f_{\text{chirp}}$  represents the frequency of the chirp signal at position  $x$ . Thus, the extraction of the axial position  $z$  from the hologram can be performed, provided that the space-varying frequency  $f_{\text{chirp}}$  of the interference pattern is known. Since the WT can represent simultaneously the space-spatial frequency information of the analyzed

signal, this Chapter discusses the use of the WT for extracting the axial positions of the objects from the holograms.

The WT of the 1-D intensity profile of the hologram can be calculated by using Eq. (2.9). Although the WT can be theoretically calculated at any given continuous values of dilation and translation, the digital computation of the continuous WT is accomplished by using the discretized dilation and translation. The accuracy of the resultant WT is determined by the dilation interval of the discretized dilation and the spatial resolution of the CCD sensor used to capture the hologram. Since the reduction of the dilation interval increases the dilation resolution as well as the computation time, the WT must be computed with sufficient number of dilation in short computation time. In the case of the chirp signal with wide bandwidth, the discretized dilation used in the WT computation must be chosen to cover this bandwidth. In order to maintain short computation time and good accuracy, the dilation is discretized as exponentiation with base 10 (Lewalle, 1995). If the first dilation is defined as  $10^{b_1}$ , then the  $n^{\text{th}}$  discretized dilation is mathematically expressed as

$$d_n = 10^{\{b_1 + (n-1)\Delta b\}}, \quad (4.2)$$

where  $\Delta b$  is a logarithmic interval given by  $\Delta b = \log_{10}(d_{n+1}) - \log_{10}(d_n)$ . For given  $M$  dilations the interval  $\Delta b$  can be found from

$$\Delta b = \frac{b_M - b_1}{M - 1}, \quad (4.3)$$

where  $b_1$  and  $b_M$  are the predefined exponents. Since the WT is in fact a correlation operation, its computation done in the frequency domain will be faster than that in the space domain. This is because the spectrum of the signal can be obtained by employing the fast FT algorithm. Figure 4.1 shows the flow chart for computing the

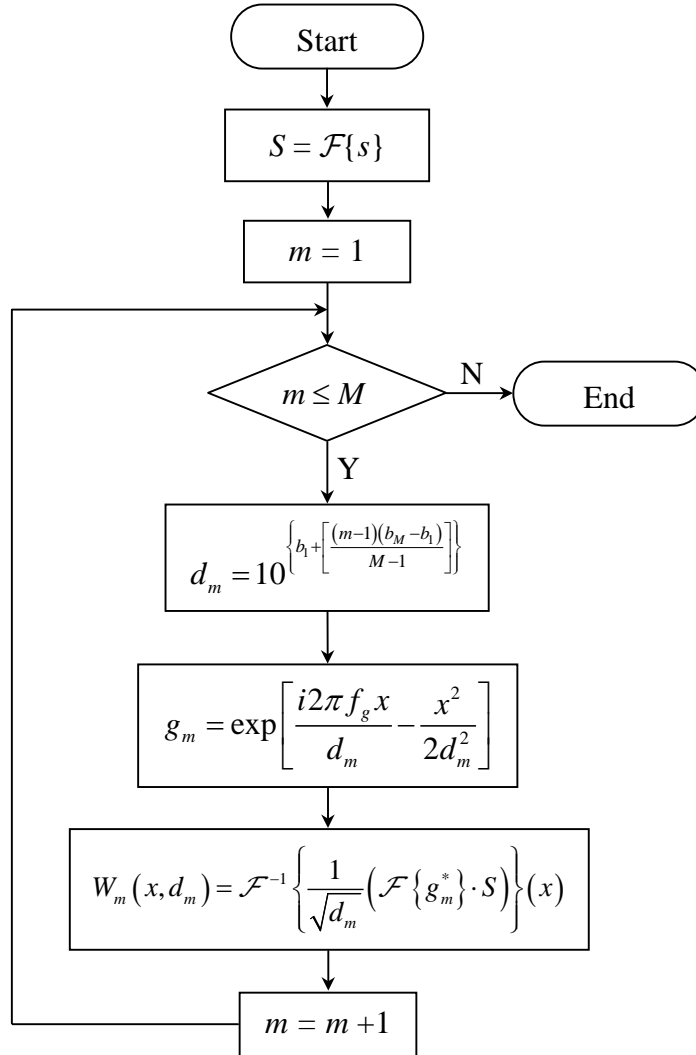


**Figure 4.1** Block diagram for calculating the WT of the signal  $s$ .

WT in the frequency domain by using the Eq. (2.9). First, the analyzed signal  $s$  is Fourier transformed. Then, the first dilation  $d_1$  is generated. The parameter  $b_1$  and  $b_M$  must be defined such that the lowest dilation value  $10^{b_1}$  gives the dilated wavelet with

higher frequency than the highest frequency content of the analyzed signal  $s$  while the highest dilation value  $10^{b_M}$  gives the frequency of the wavelet that is lower than the lowest frequency of the signal. As this condition is achieved, the resultant WT will be confined within the range of the calculated dilations as shown in Fig. 2.6. If the selected range of dilations is not suitable, the resultant WT will appear in the lower or the upper part of the Fig. 2.6 and may be cut by either the top or the bottom horizontal axis. In this case, the WT must be recalculated using a wider range of dilations. It is found that by using  $b_1$  and  $b_M$  as  $-5$  and  $-3$ , respectively, the frequency range of the dilated wavelet covers the frequency band of the interference pattern used in this study. Here, the number of dilations  $M$  are 256 samples. Next, the generation of the dilated Morlet wavelet  $g(x/d)$  is started with the dilation  $d = d_1$ . In this computation, the frequency of the mother wavelet  $f_g$  is 1 lines/mm, while the spatial position  $x$  is generated with the same number of samples and sampling interval as those of the analyzed signal  $s$ . The wavelet coefficients corresponding to the dilation  $d_1$  are then calculated by using Eq. (2.9). The computations of the dilated wavelet and the wavelet coefficients are then repeated for every values of the generated  $d_m$ . By concatenating these resultant wavelet coefficients, the 2-D function of the wavelet coefficients such as the one shown in Fig. 2.6 can be formed.

The next step is to extract the information of the recording distances  $z$  from the resultant WT coefficients. Since the WT is a correlation operation, the highest amplitude of the wavelet coefficients is generated when the frequency content of the wavelet matches with that of the signal. Thus, the positions of the maximum and minimum values of the wavelet coefficients give the space varying frequency

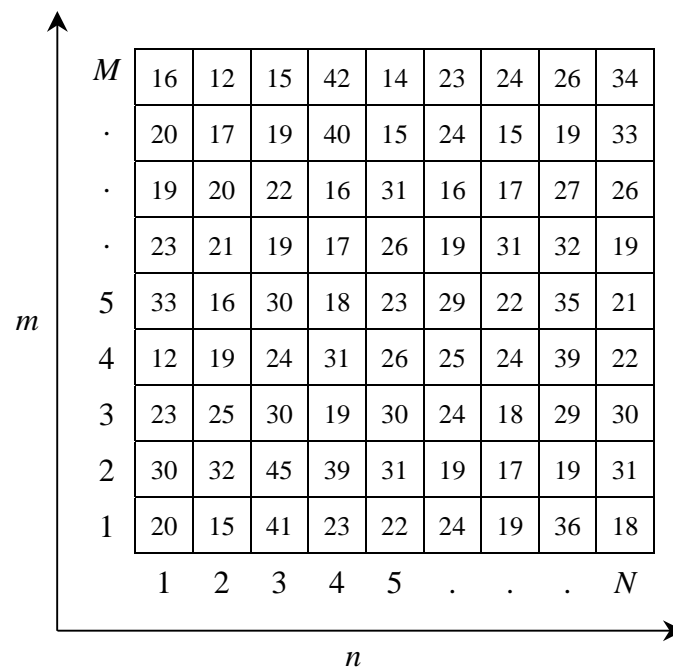


**Figure 4.2**  $M \times N$  matrix of wavelet coefficients.

information of the analyzed signal. In order to extract this information, these positions must be determined. In the numerical computation of the WT, the resultant real value of the WT  $W(x,d)$  is obtained as a 2-D matrix. Figure 4.2 shows the  $M \times N$  matrix of the wavelet coefficients, where the horizontal and the vertical axes correspond to the translation  $x$  and the dilation  $d$ , respectively. The number in each entry of the matrix corresponds to the value of the wavelet coefficient. The value of the wavelet coefficient  $W_{mn}$  is maximum or minimum if it is greater or smaller than the values of its 8 neighboring coefficients, ie.  $W_{m-1,n-1}$ ,  $W_{m-1,n}$ ,  $W_{m-1,n+1}$ ,  $W_{m,n-1}$ ,  $W_{m,n+1}$ ,  $W_{m+1,n-1}$ ,  $W_{m+1,n}$ ,  $W_{m+1,n+1}$ , respectively. In Fig. 4.2, the value of  $W_{23} = 45$  is maximum, while  $W_{34} = 19$  is minimum. However, although the amplitude of  $W_{41} = 12$  is minimum compared to its neighboring coefficients, this coefficient cannot be considered as having minimum value because it is compared to only 5 neighboring coefficients.

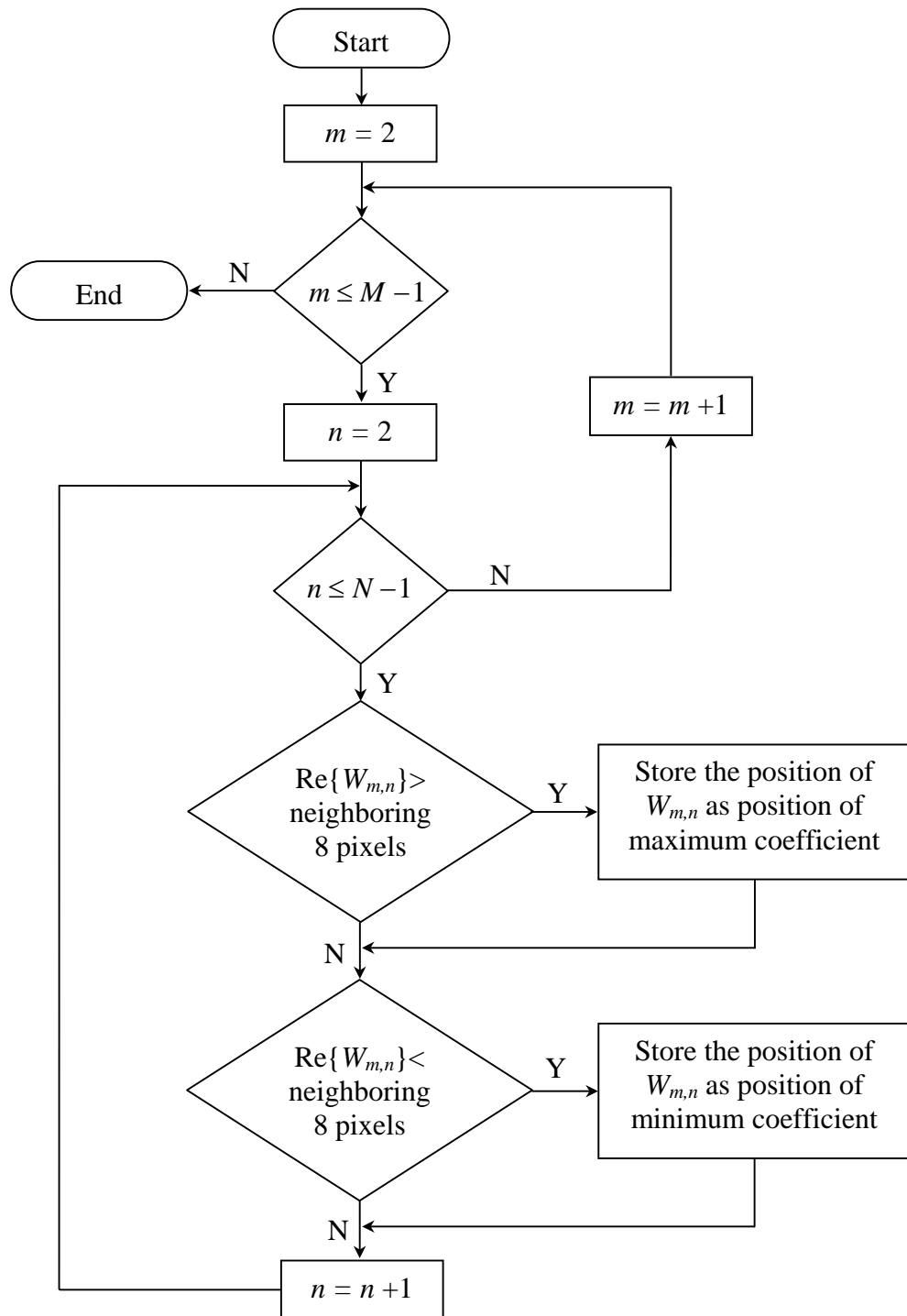


**Figure 4.3** Block diagram for determining the local maxima and minima of the WT coefficients.

Therefore, in order to solve this problem, the wavelet coefficients along the outermost rows and columns of the matrix, i.e.  $W_{1n}$ ,  $W_{m1}$ ,  $W_{Mn}$ , and  $W_{mN}$ , are not included in searching the local maxima and minima.

Figure 4.3 shows the algorithm for determining the maximum and minimum amplitudes of the resultant wavelet coefficients  $W(x,d)$ . First, the amplitude of  $W_{22}$  is compared to the values of the 8 neighboring wavelet coefficients that are  $W_{11}$ ,  $W_{12}$ ,  $W_{13}$ ,  $W_{21}$ ,  $W_{23}$ ,  $W_{31}$ ,  $W_{32}$ , and  $W_{33}$ . If it is larger or smaller than the amplitude of all these positions, the position of  $W_{22}$  is stored as the coefficient with maximum or minimum values. This process of amplitude detection is repeated for every coefficient except those located along the outermost rows and columns. Figure 4.4 illustrates a plot of the resultant wavelet coefficients with maximum and minimum amplitudes

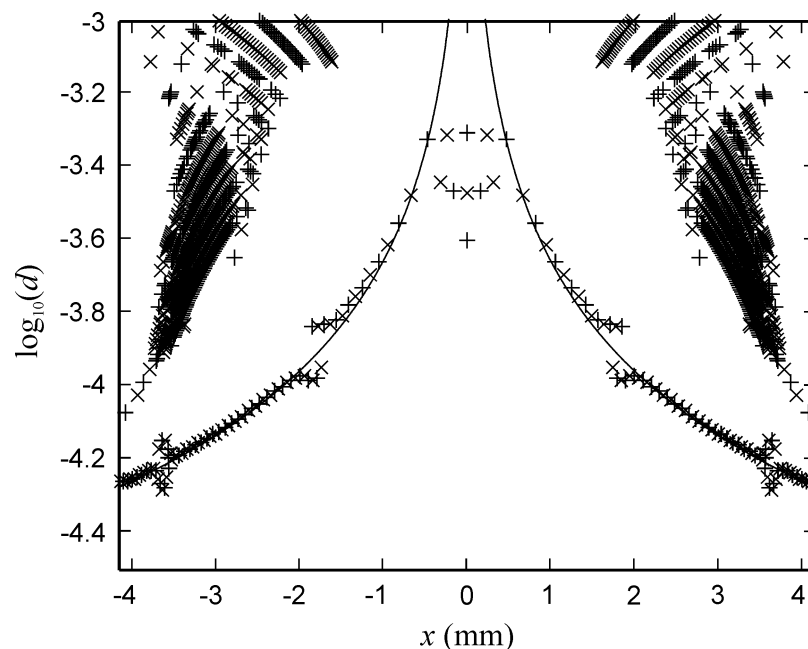


**Figure 4.4** The resultant WT coefficients with maximum and minimum amplitudes generated from the real value of the WT of the hologram shown in Fig. 2.3.

generated from the real value of the WT of the hologram shown in Fig. 2.3. The maximum and the minimum amplitudes are represented by the plus and the cross symbols, respectively. In this example, instead of  $b_1 = -5$ , the WT is calculated by using the dilation parameter with the first exponent  $b_1 = -4.5$  which corresponds to the frequency  $= 1/d_1 = 10^{4.5} = 31.6$  lines/mm. This is because the recording distance  $z$  of the hologram which is equal to 40 cm yields the highest frequency of the chirp signal  $x_{\max}/\lambda z = 19.1$  lines/mm. It is obvious that the predicted theoretical space-varying frequency denoted by the solid line coincides with several wavelet coefficients with maximum and minimum amplitudes. The remaining wavelet coefficients which do not coincide with the theoretical spatial frequency variation cannot be used for the calculation of the axial position  $z$ . They can be considered as the unwanted information. Thus, in order to extract the recording distance with high accuracy, this unwanted information must be eliminated.

However in most real situations, the micro-objects being studied may be embedded in a test volume constructed from a glass container with a known thickness as shown in Fig. 4.5. If the glass container is located at a distance  $z_c$  in front of the

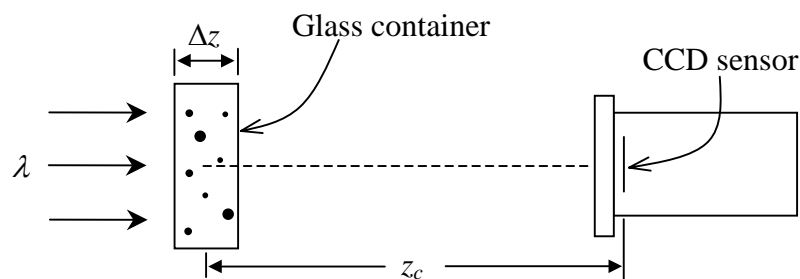


**Figure 4.5** A glass container with embedded micro-objects used in the recording setup.

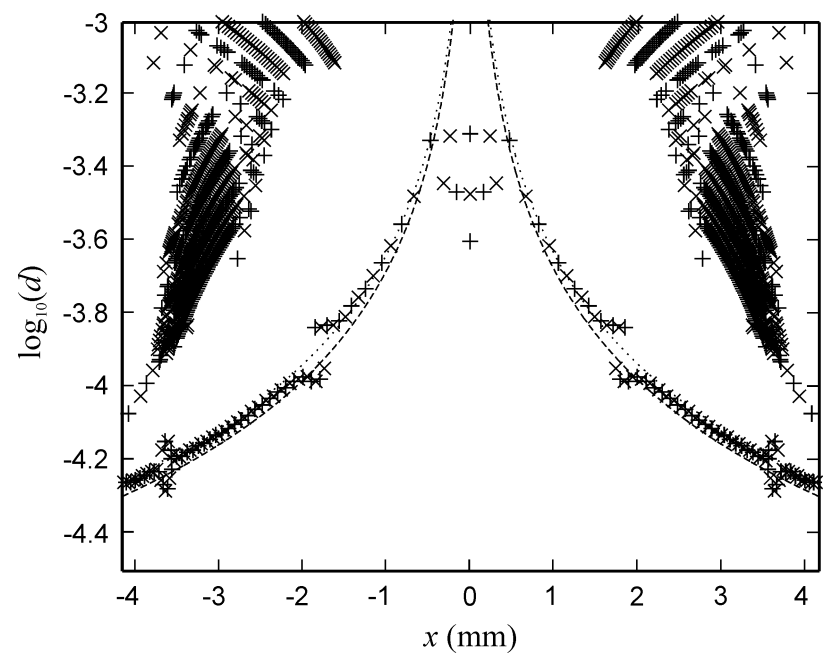


**Figure 4.6** Theoretical space varying frequencies correspond to the shortest and the longest recording distances defined by the thickness of the glass container.

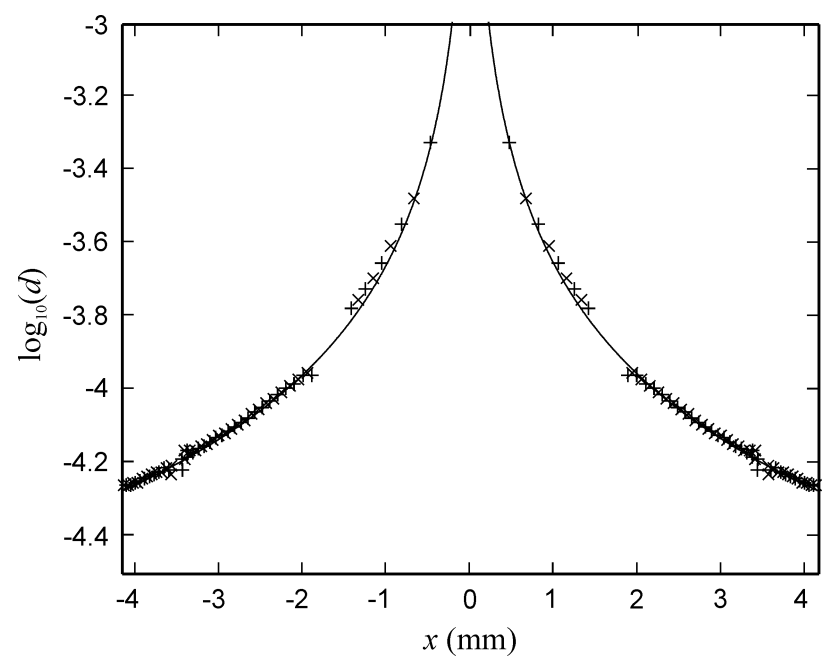


**Figure 4.7** The desired wavelet coefficient after discarding the unwanted information.

CCD sensor and its thickness is  $\Delta z$ , the possible positions of the micro-objects inside the container will be confined to a distance  $z_c - \Delta z/2 \leq z \leq z_c + \Delta z/2$ . Figure 4.6 shows the theoretical spatial-frequency variations correspond to the shortest and the longest recording distances,  $z_c - \Delta z/2$  and  $z_c + \Delta z/2$ , represented by using the dash and the dot lines, respectively. For the sake of clearness of the graph, the lines are drawn by using  $\Delta z = 6$  cm. However in this dissertation, the thickness  $\Delta z = 2$  cm is employed. It is obvious that the desired wavelet coefficients are in the region confined by these two lines. Therefore, the unwanted coefficients located outside the two lines can be discarded. Figure 4.7 shows the resultant wavelet coefficients after discarding the unwanted information.

Due to the discretization, the wavelet computation by using the discretized dilations may not always yield the desired wavelet coefficients. Since the correct wavelet coefficients may not be produced, the determination of the maximum and the minimum amplitudes of the wavelet coefficients may give wrong space-varying frequency information. This can be seen from Fig. 4.8 which is the enlargement of Fig. 4.7. In this figure, several maxima and minima appeared at different translations have the same dilations. Since the frequency of the interference pattern is a function of position, it is not possible that the same value of frequencies occur at different position of the signal. It can be seen from the Fig. 4.8 that if there are more than one translations with the same dilation value, the maximum or the minimum amplitude corresponds to the first translation appear closer to the theoretical value than the others. Therefore, the wavelet coefficient of the first translation is used in the calculation of the recording distance. Figure 4.9 shows the desired maxima and

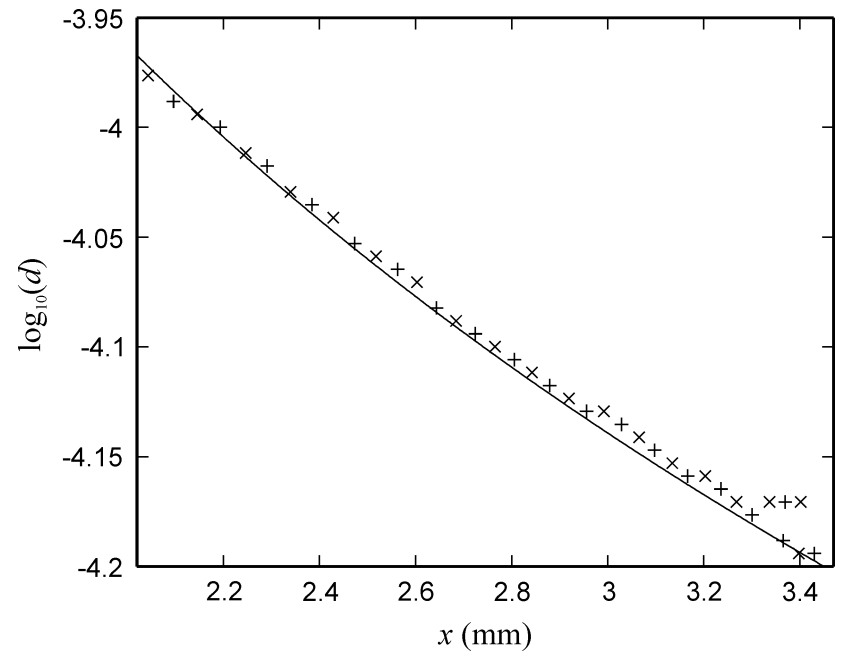


**Figure 4.8** Enlarged version of Fig. 4.7 shows some maxima and minima of different translation having the same dilation values.

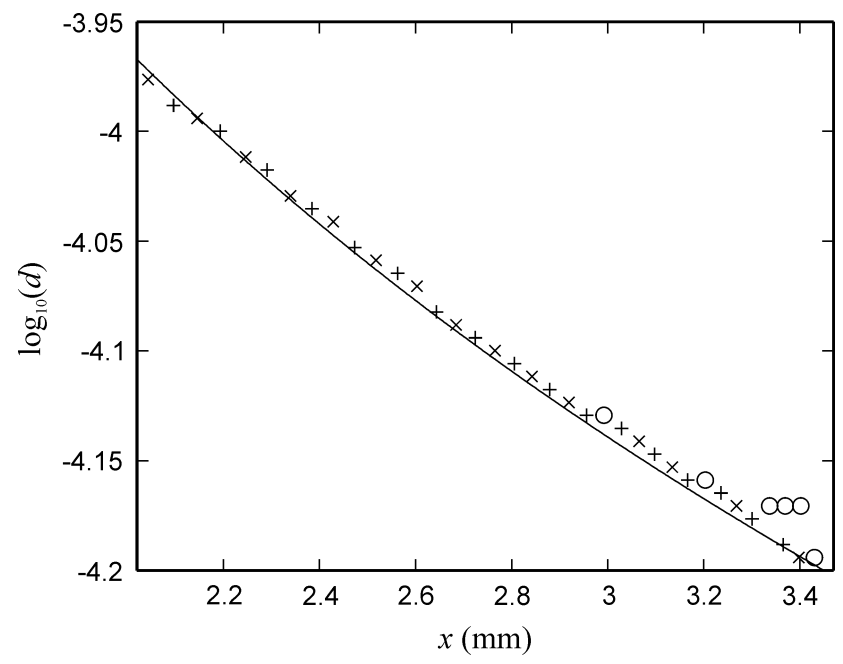


**Figure 4.9** The desired maxima and minima of the Fig. 4.8 after discarding those with the same dilation denoted by circle sign.

minima after discarding those having the same dilation values denoted by the circle signs.

After discarding the unwanted maxima and minima in the WT domain, the recording distance of the object given by

$$z = \frac{xd}{\lambda}. \quad (4.4)$$

is calculated from the desired maxima and minima. However, since each maximum and minimum may give slightly different value of  $z$ , the resultant recording distance extracted by the WT is obtained by averaging of those values.

#### 4.1 Position of line objects

The errors in measurement of the recording distance from the simulated holograms of line objects having the radius of 20  $\mu\text{m}$  and 62.48  $\mu\text{m}$  are shown in Fig. 4.10 as the cross and the circle signs, respectively. The simulation results show that the WT could extract the axial position of both objects recorded at several recording distances with the small error of less than 1 percent. Figures 4.11 and 4.12 show the 1-D scan of the optically generated holograms of the optical fiber recorded at the distance  $z = 10$  cm and 20 cm, respectively. As discussed in Chapter III, these signals are obtained by averaging along the vertical direction the middle four hundred lines of the captured 2-D interference pattern. Due to the limited resolution of the employed CCD sensor, a part of the signals with high frequency components cannot be correctly sampled. This effect can be clearly seen in the Fig. 4.11, because the shorter the recording distance the higher the chirp frequency. The effect of the CCD size and resolution on the captured hologram is rigorously discussed in Chapter VI.

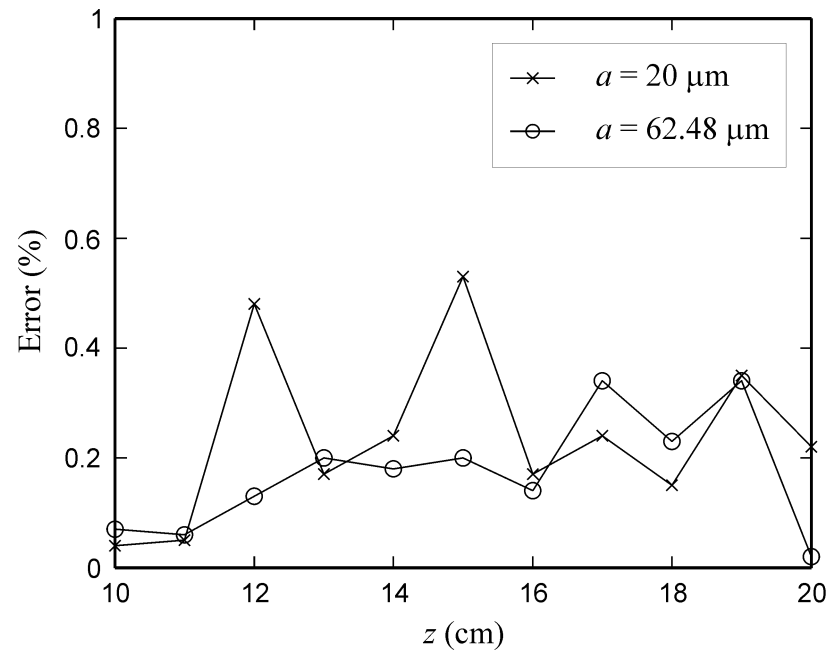


**Figure 4.10** Errors in measurement of  $z$  from simulated holograms of line objects by using the WT.

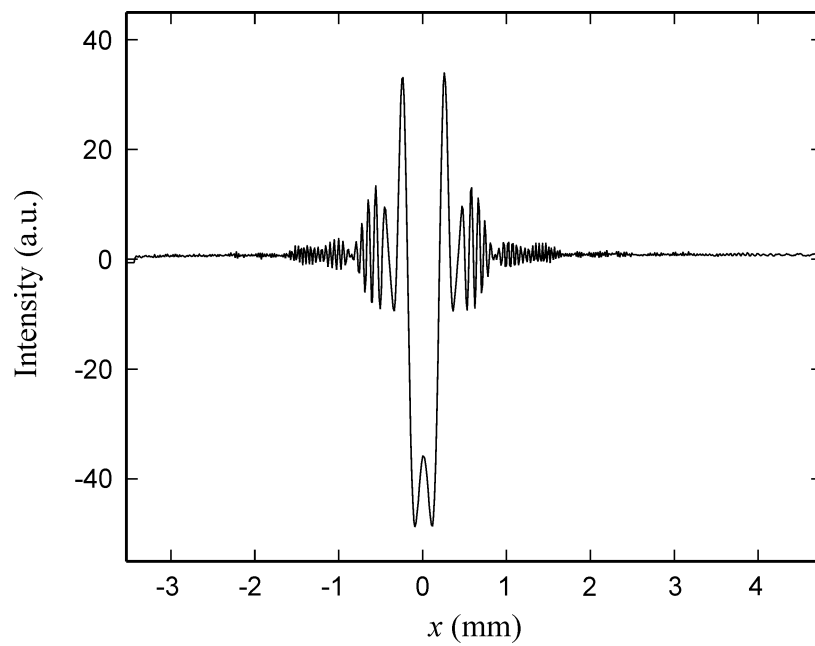


**Figure 4.11** In-line hologram of the optical fiber recorded at  $z = 10$  cm.

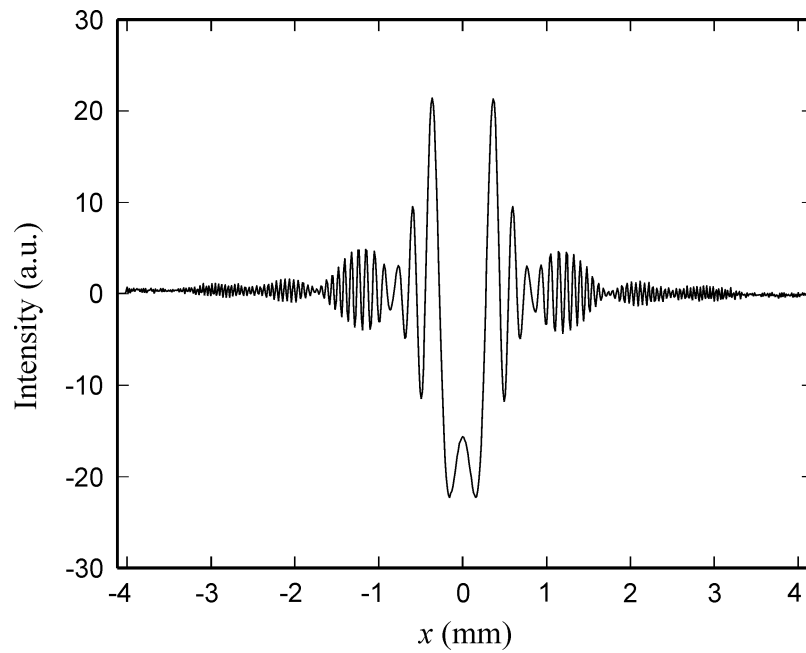


**Figure 4.12** In-line hologram of the optical fiber recorded at  $z = 20$  cm.

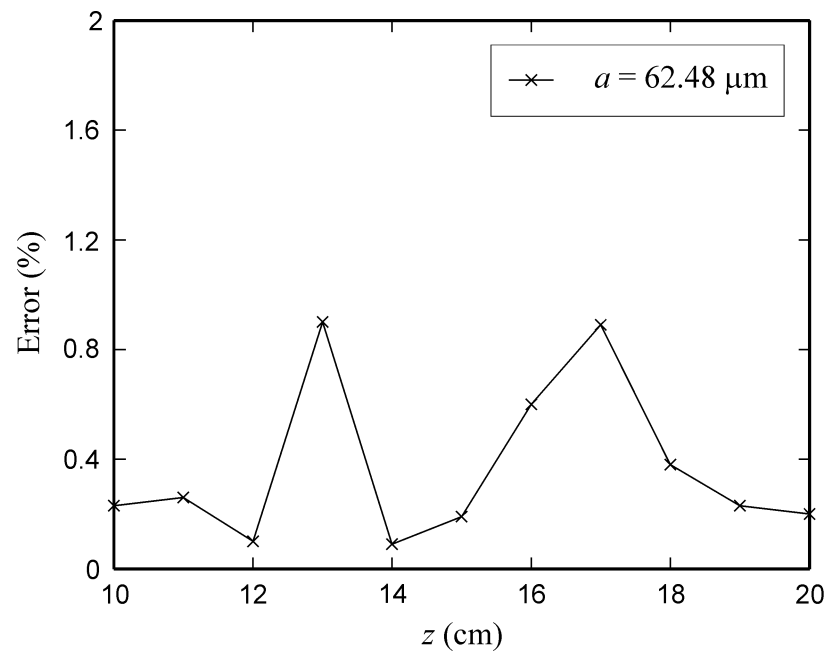


**Figure 4.13** Errors in measurement of  $z$  from the optically generated holograms of the optical fiber by using the WT.

Figure 4.13 shows the errors of the recording distances measured from the optically generated holograms of the optical fiber. In the experiment, the errors are about 1 percent. This is slightly higher than those of the simulation, because the imperfection of the holograms which are resulted from the optical noises generated by the employed equipment during the experiment, the speckle noises that overlap the hologram, etc.

## 4.2 Position of spherical objects

In the case of the spherical object, the errors in measurement of the recording distance from the simulated holograms are shown in Fig. 4.14, where the cross and the circle signs represent the measurement errors of the objects having the radius of  $20\ \mu\text{m}$  and  $77.78\ \mu\text{m}$ , respectively. It can be seen that the errors of the measurement

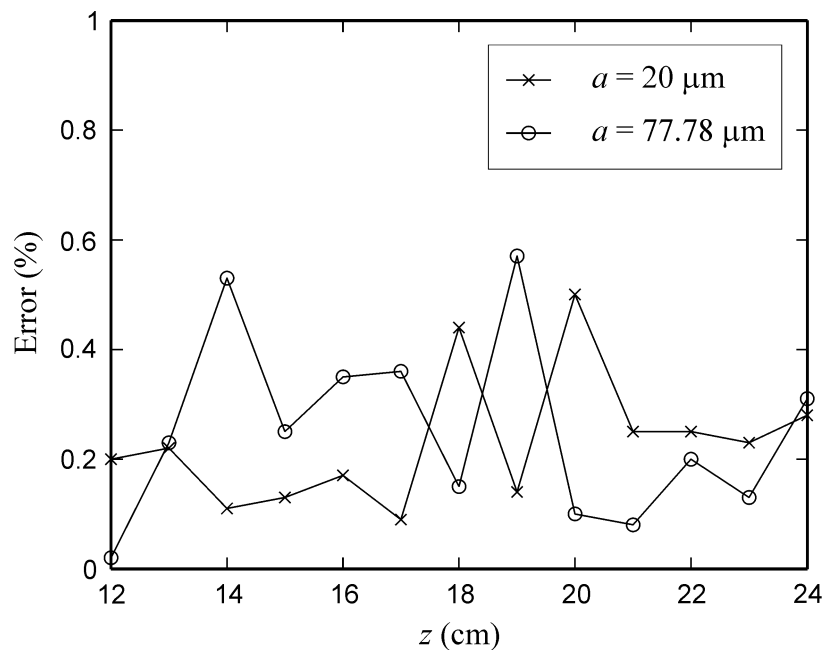


**Figure 4.14** Errors in measurement of  $z$  from simulated holograms of spherical objects by using the WT.

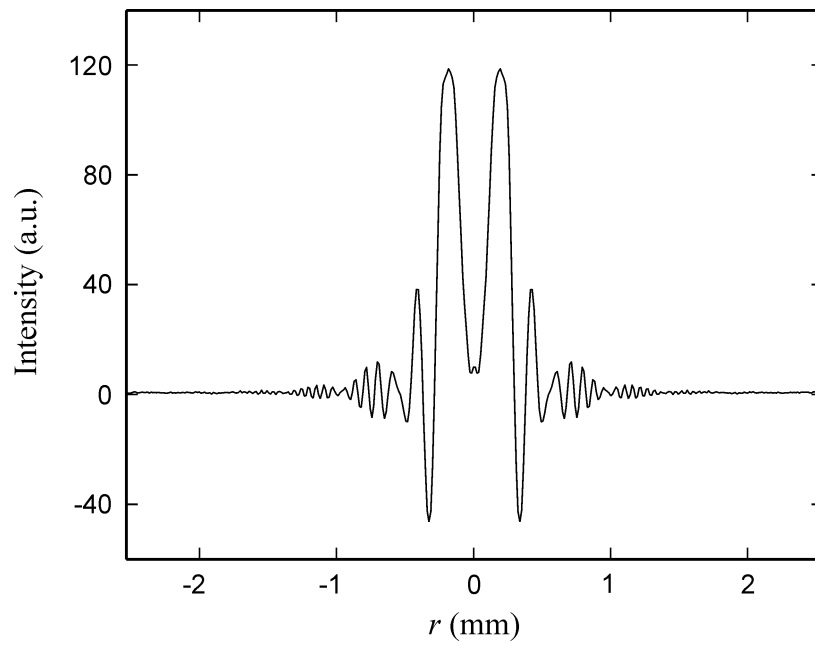


**Figure 4.15** In-line hologram of the pinhole recorded at  $z = 12$  cm.

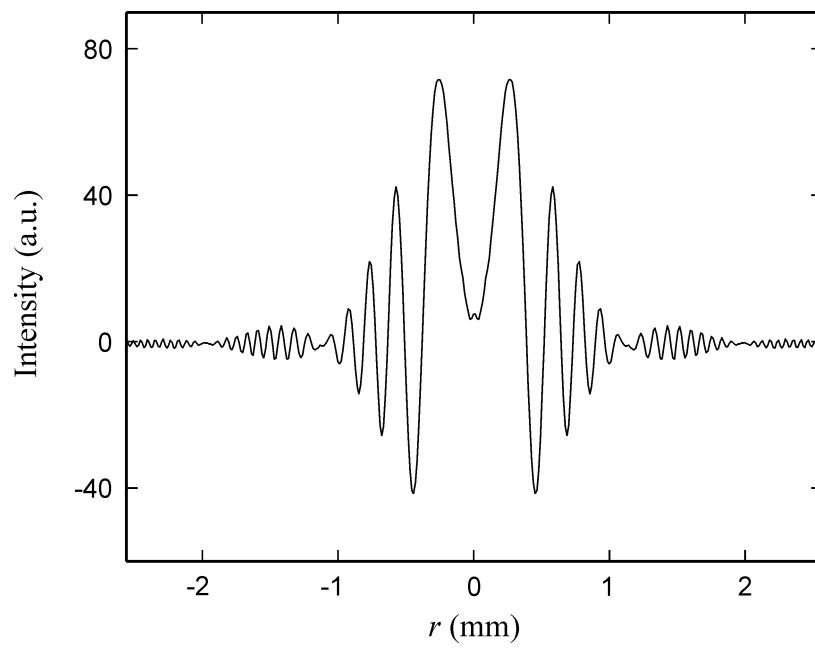


**Figure 4.16** In-line hologram of the pinhole recorded at  $z = 24$  cm.

are less than 1 percent as in the case of the line objects. The 1-D intensity profile of the optically generated holograms of a pinhole recorded at the distance  $z = 12$  and  $24$  cm are shown in Figs. 4.15 and 4.16, respectively. Figure 4.17 shows the errors obtained from the holograms of pinhole which are slightly higher than those of the simulation with the maximum value of around 1.1 percent.

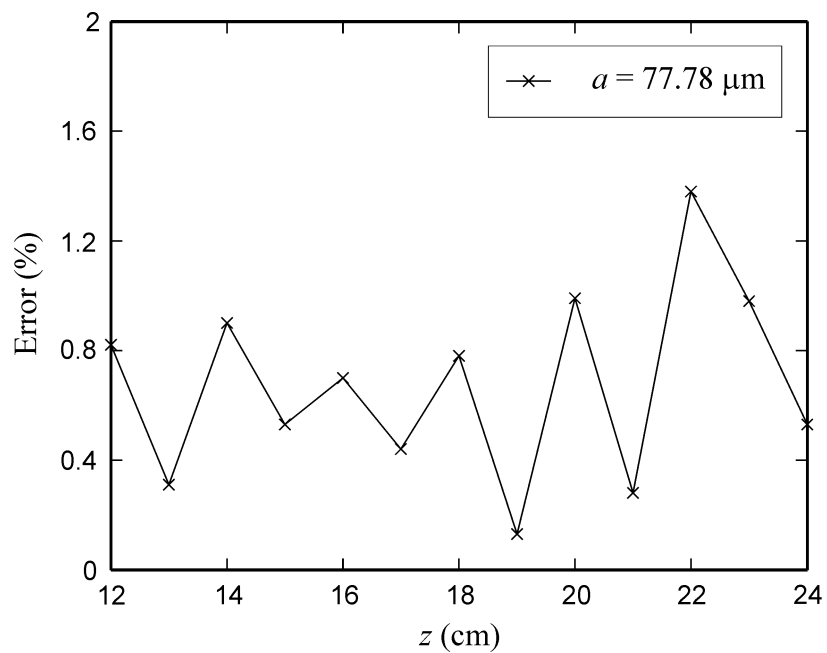


**Figure 4.17** Errors in measurement of  $z$  from the optically generated holograms of the pinhole by using the WT.

The simulation and the experimental results confirm that the WT can be used to extract accurately the axial position of the line and spherical micro-objects from the in-line Fraunhofer holograms.

# CHAPTER V

## EXTRACTION OF OBJECT SIZE FROM IN-LINE HOLOGRAMS

Object size is one of the desired information encoded into the in-line holograms. It is obvious from Eqs. (2.4) and (2.6) that the minima positions of the interference pattern can be used to determine the object size. In this chapter, two methods for extracting the object size are discussed. The first method discussed in Section 5.1 is accomplished by reconstructing the envelope function. The second one is done by computing the absolute values of the wavelet transformation of the interference pattern. The reason for this is that the frequency of the chirp signal at the minima positions also contains the information about the object size. Section 5.2 discusses the second method. It is found that the second proposed method could extract the information of the object size from the hologram with a higher accuracy than the first one.

### **5.1 Object sizing by using reconstruction of the envelope function**

According to Eq. (2.4), the minima positions of the in-line hologram of the line object appear when the argument of the sinc function equal to  $n\pi$ , where  $n$  is an integer number which represents the order of the minimum. Thus, the radius of the line object can be determined from

$$a_{\text{line}} = \frac{n\lambda z}{2x_n}, \quad (5.1)$$

with  $x_n$  denotes the position of the  $n^{\text{th}}$  minimum. In analogy, the radius of a spherical object can be determined from Eq. (2.6)

$$a_{\text{sphere}} = \frac{c_n \lambda z}{2\pi r_n}, \quad (5.2)$$

where  $r_n$  is the position of the  $n^{\text{th}}$  minimum measured in radius coordinate and  $c_n$  is a constant factor corresponds to the  $n^{\text{th}}$  root of the Bessel function. For the first three minima, these constant factors are equal to  $c_1 = 3.83$ ,  $c_2 = 7.02$ , and  $c_3 = 10.17$  (Gradshteyn and Ryzhik, 1994).

From Eq. (5.1) and Eq. (5.2), the object size can be calculated if the minima positions, the wavelength of the illuminating light, and the recording distance are known. Since the wavelength of the illuminating light is known and the recording distance can be obtained by using the WT discussed in Chapter IV, the minima positions are the only unknown parameter to be obtained. In the first proposed method, these positions are obtained through the reconstruction of the envelope function.

In order to reconstruct the envelope function, the pixels of the hologram having maximum and minimum amplitudes compared to its neighboring pixels must be determined. Let us consider that the 1-D intensity profile of the digitized hologram  $s$  consists of  $N$  pixels. The amplitude of the pixel  $s_n$  can be maximum or minimum if it is larger or smaller than the pixels  $s_{n-1}$  and  $s_{n+1}$ , respectively. However, since the first and the last pixels, i.e.  $s_1$  and  $s_N$ , have only one neighboring pixel, they are not included in the reconstruction of the envelope function. A block diagram of an algorithm for reconstructing the envelope function of the signal  $s$  is shown in Fig. 5.1. First,  $s_2$  is compared to its neighboring elements, i.e.  $s_1$  and  $s_3$ . If its amplitude is

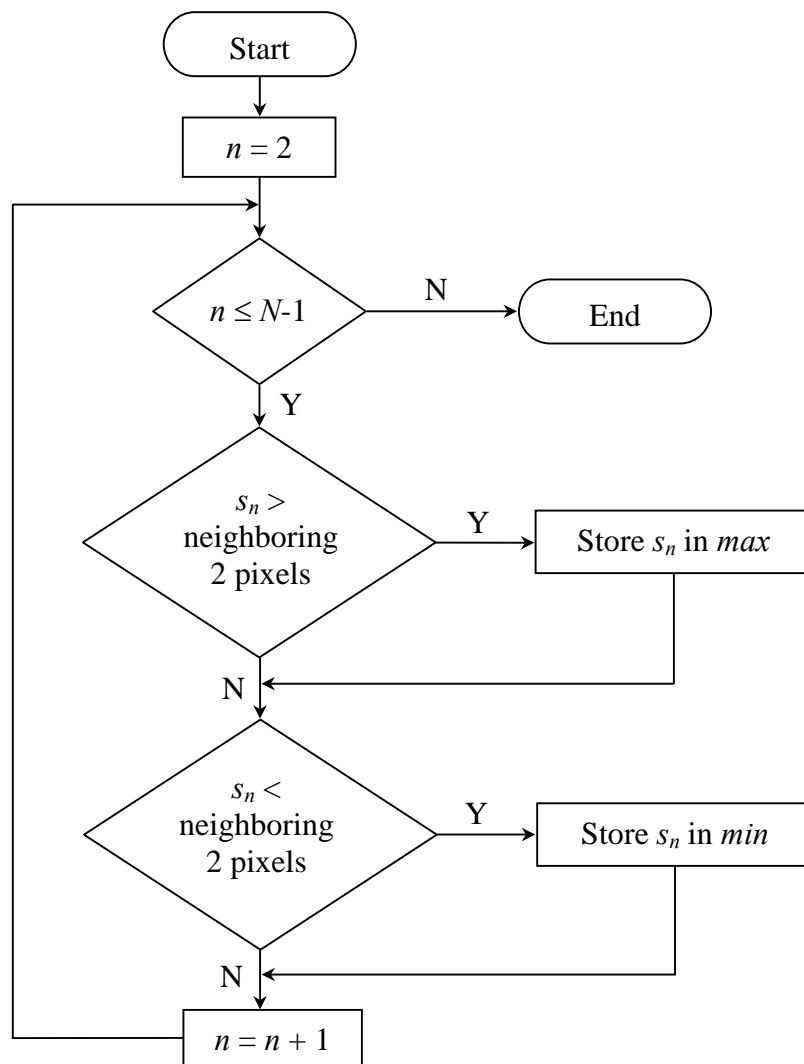


**Figure 5.1** A block diagram for reconstructing the envelope function by determining the local maxima and minima of the analyzed signal  $s$ .

larger or smaller than that of the neighboring pixels, a new variable *max* or *min* is used for storing the value of the amplitude and position of the pixel  $s_2$ . The process of searching for the maximum and the minimum amplitudes is repeated for other pixels until  $s_{N-1}$ . The resultant reconstructed envelope function of the hologram shown in Fig. 2.3 is depicted in Fig. 5.2, where the plus and the cross signs represent the

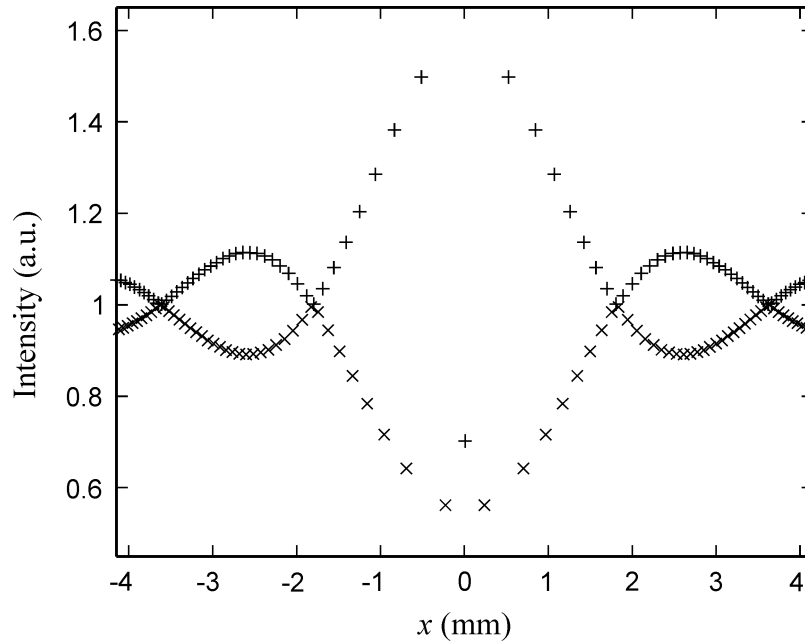


**Figure 5.2** Reconstructed envelope function of the hologram in Fig. 2.3.

maximum and the minimum amplitudes, respectively.

After the envelope is reconstructed, the minima positions of the interference pattern are determined by finding the pixels whose amplitudes give the smallest difference. Figure 5.3 shows an algorithm for finding the smallest difference between the maximum and the minimum amplitudes. First, the pixels with the maximum and the minimum amplitudes obtained from the previous step are sorted according to their horizontal positions as a new variable  $m$ . The percentage of the amplitude difference between  $m_1$  and  $m_2$  is calculated with respect to  $m_1$ . If it is smaller than a certain threshold value, the position of both  $m_1$  and  $m_2$  are stored in a new variable  $h$ . The threshold value is determined by the amplitude of the interference pattern. The interference pattern with larger amplitude requires a higher threshold value than that with smaller amplitude. In this dissertation, the threshold values of 0.1 to 3 percent are used. The process of finding the smallest amplitude difference is repeated for

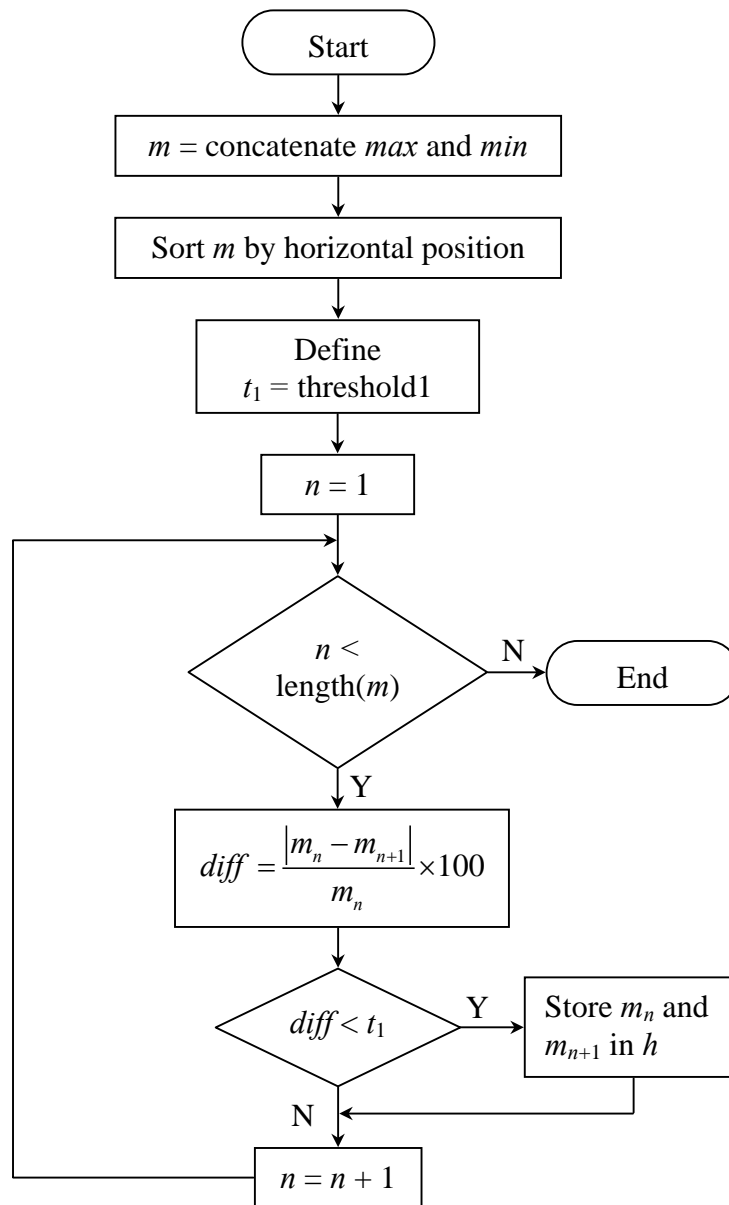


**Figure 5.3** Block diagram for determining the local maxima and minima whose their amplitude different are smaller than a threshold value.

every element of  $m$ . The resultant  $h$  contains information of the pixels with small amplitude differences located around the minima positions of the interference pattern. Figure 5.4 shows the enlargement of area around the first and the second minima of Fig. 5.2, where  $\oplus$  and  $\otimes$  represent the pixels having maximum and minimum values whose differences are small, respectively. The minima positions of the interference pattern are then determined by averaging the horizontal positions of  $h_n$  from the same minimum. The algorithm for accomplishing this task is shown in Fig. 5.5. First, the horizontal positions of  $h_1$  and  $h_2$  are compared. If the difference of their positions is less than 20 pixels, they are considered as from the same minimum position and then they will be stored in a new variable  $k$ . This process is repeated until the difference between the horizontal positions of  $h_n$  and  $h_{n+1}$  is larger than 20 pixels. At this state,  $k$  contains information of the pixels located around the same minimum position of the

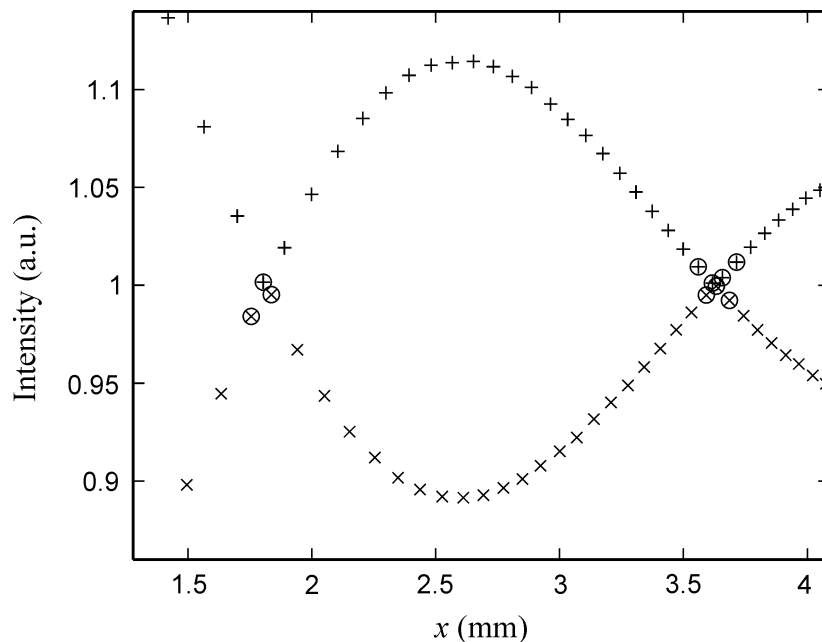


**Figure 5.4** Maxima and minima whose amplitude differences are smaller than a threshold value.

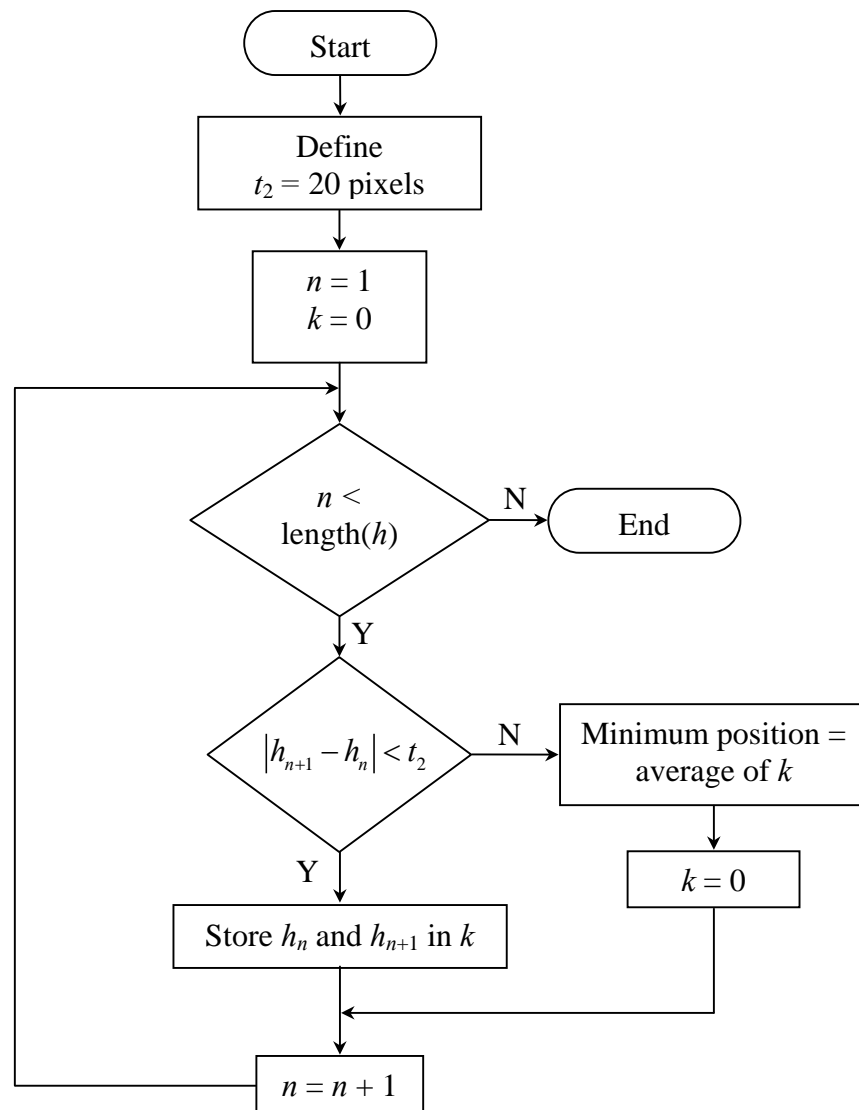


**Figure 5.5** Block diagram for determining the minimum position of the interference pattern.

interference pattern. Finally, the minimum position is simply determined by averaging the position of elements of  $k$ . This process can be further carried out for determining the next minimum. Figure 5.6 shows the resultant minima positions of the hologram denoted by the vertical lines which are obtained by using the envelope reconstruction method. After the minima of the interference pattern are obtained, the object size is

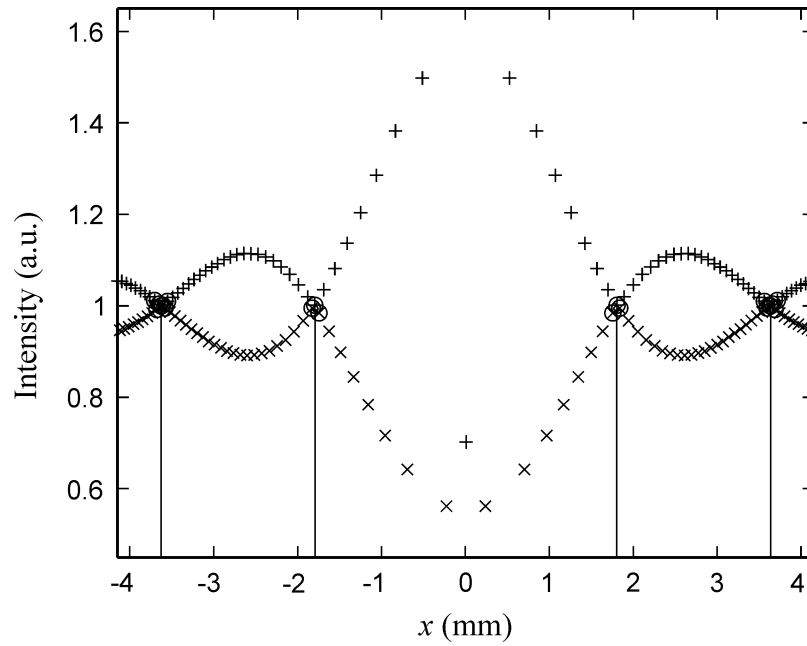


**Figure 5.6** Detected minima positions.

calculated by using either Eq. (5.1) or Eq. (5.2) for the line and the spherical objects, respectively.

The measurement results of the object size from the holograms of the line and the spherical objects by using the envelope function reconstruction method are shown in Figs. 5.7, 5.8, 5.9 and 5.10. In Fig. 5.7, the cross and the circle signs represent the measurement errors obtained from the simulated holograms of the line object having the radius of  $20\ \mu\text{m}$  and  $62.48\ \mu\text{m}$ , respectively. It is found that a small error of lower than 1 percent could be obtained from both sizes of the object. However, the experimental results depicted in Fig. 5.8 are slightly higher than that of the simulation. This may be caused by the remaining speckle noise that cannot be completely removed by the averaging technique discussed in Chapter III. Since the amplitude of the holograms around the minima is very small, it can be significantly disturbed by the speckle noise. As a result, the minima positions of the optically generated

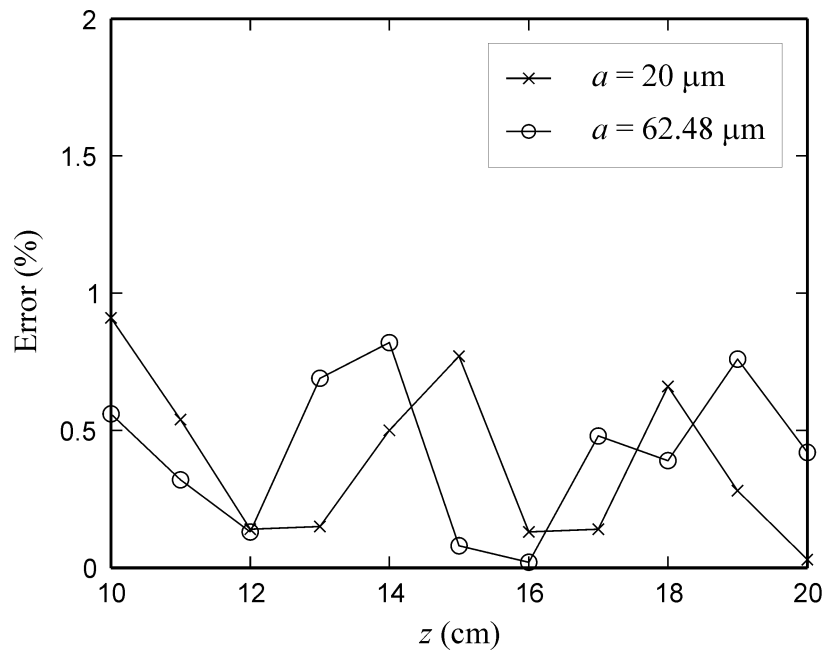


**Figure 5.7** Errors in measurement of  $a$  from the simulated holograms of the line objects by using the envelope reconstruction method.

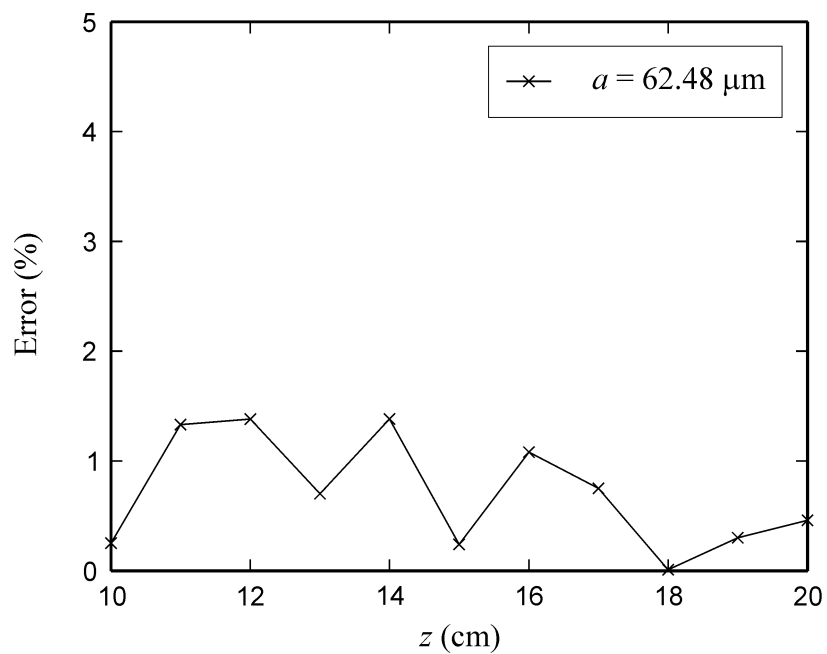


**Figure 5.8** Errors in measurement of  $a$  from the holograms of the optical fiber by using the envelope reconstruction method.

holograms cannot be accurately determined. Moreover, the calculation of the object size employs information of the recording distance extracted from the hologram by using the WT. The error of measurement of the recording distance reduces the accuracy of the measurement of the object size.

In the case of the spherical objects, the results are in agreement with those from the line objects. The simulation results depicted in Fig. 5.9 show that the errors are smaller than 1% for both sizes of  $20\ \mu\text{m}$  and  $77.78\ \mu\text{m}$ . However, as illustrated in Fig. 5.10, slightly higher errors are obtained from the experimental results.

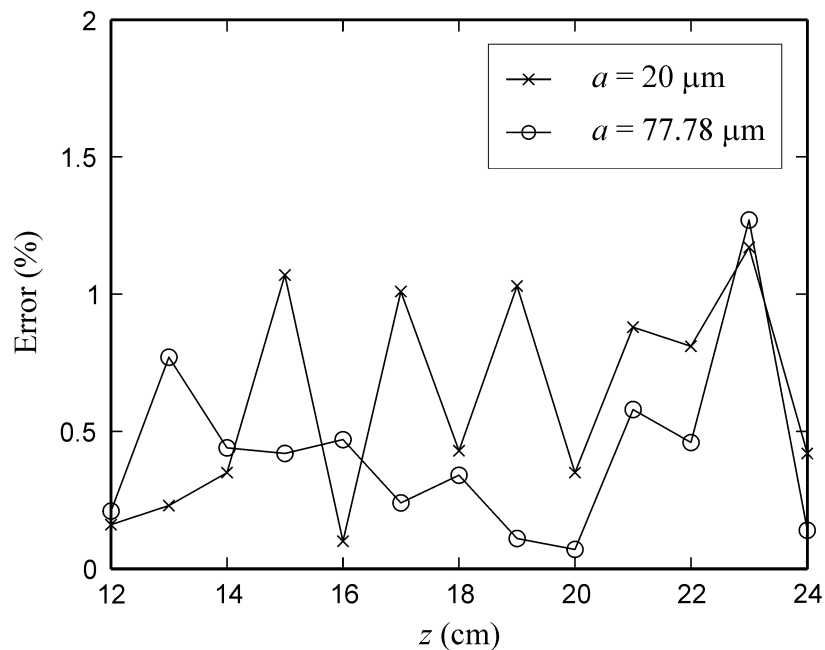


**Figure 5.9** Errors in measurement of  $a$  from the simulated holograms of spherical objects by using the envelope reconstruction method.

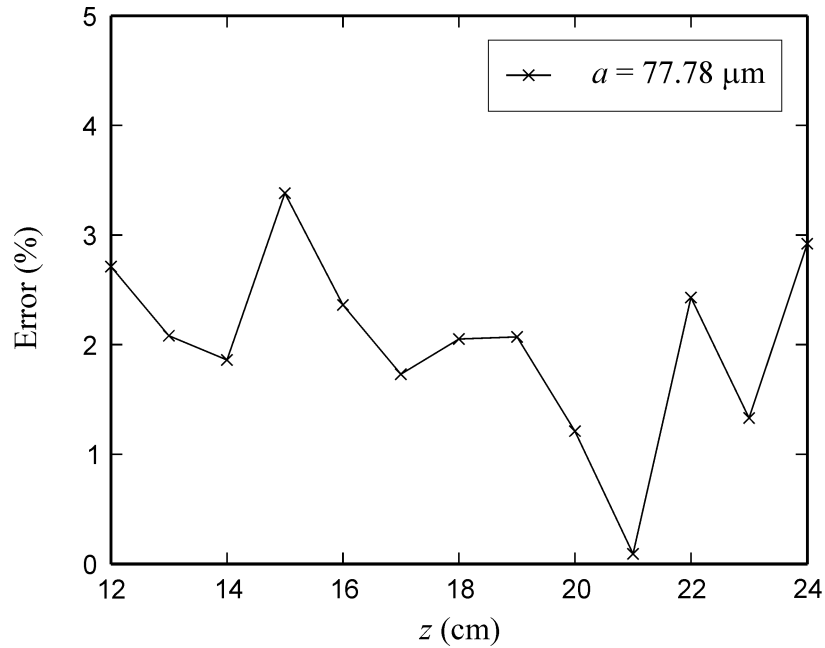


**Figure 5.10** Errors of measurement of  $a$  from the holograms of pinhole by using the envelope reconstruction method.

## 5.2 Object sizing by using absolute value of the WT

In order to improve the accuracy in the measurements of the object size obtained from the envelope reconstruction method, a novel method for sizing the objects by using the absolute value of the WT is proposed. This interest stems from the fact that the absolute value of the WT extracts the minima positions of the interference pattern. In the WT domain, these minima are functions of the dilation and the spatial translation. The frequencies of the fringes at the minima are directly obtained by using values of the dilation of the wavelet at the corresponding minima. Since the object size is inversely proportional to these frequencies, the object size can be measured.

The relationship between the object size and the frequency of the chirp signal can be derived by considering the frequency of the chirp signal given by

$$f_{\text{chirp}} = \frac{x}{\lambda z}, \quad (5.3)$$

while the minima positions appear at

$$x_n = \frac{n\lambda z}{2a_{\text{line}}}. \quad (5.4)$$

By substituting Eq. (5.4) into Eq. (5.3), the frequency of the chirp signal at the  $n^{\text{th}}$  minimum position is found to be

$$f_{\text{chirp@minima}} = \frac{n}{2a_{\text{line}}}. \quad (5.5)$$

Thus, the radius of a line object can be calculated from

$$a_{\text{line}} = \frac{n}{2f_{\text{chirp@minima}}}. \quad (5.6)$$

In a similar fashion, the radius of a spherical object is equal to

$$a_{\text{sphere}} = \frac{c_n}{2\pi f_{\text{chirp@minima}}}. \quad (5.7)$$

Unlike the Eqs. (5.1) and (5.2) in which two unknown parameters,  $x_n$  and  $z$ , are demanded for the calculation of the object size, the only required information depicted by the Eqs. (5.6) and (5.7) is the frequency of the chirp signal at the minima positions. In this dissertation, this frequency is extracted by computing the absolute values of the WT.

### 5.2.1 Absolute values of wavelet transform

The computation of the WT of the signal  $s(r)$  is actually a cross correlation between the analyzed signal and the dilated wavelet. In the general case of signals where  $s(r)$  is an amplitude-modulated signal, the amplitudes of the resultant correlation peaks are determined by the amplitude of the envelope function. Therefore, besides its excellent ability of providing the space-frequency information simultaneously, the WT extracts the modulating information of the signals being analyzed. A further insight into this property may be gained by analyzing mathematically the modulated signal on the use of the WT.

For the sake of simplicity, we consider that a modulated signal is given by

$$s(x) = \cos(2\pi f_1 x) \cos(2\pi f_0 x), \quad (5.8)$$

where the first cosine term corresponds to the carrier signal while the second one is the envelope signal. Here, the carrier frequency  $f_1$  is greater than the modulating frequency  $f_0$ . The wavelet transformation of the signal  $s(x)$  by using the Morlet wavelet as the analyzing wavelet is found to be

$$\begin{aligned} W(t, d) = \sqrt{\frac{\pi d}{8}} \left\{ \exp\left[-i2\pi(f_0 + f_1) t - 2\pi^2 d^2 \left(\frac{f_g}{d} + f_0 + f_1\right)^2\right] \right. \\ + \exp\left[-i2\pi(-f_0 + f_1) t - 2\pi^2 d^2 \left(\frac{f_g}{d} - f_0 + f_1\right)^2\right] \\ + \exp\left[-i2\pi(f_0 - f_1) t - 2\pi^2 d^2 \left(\frac{f_g}{d} + f_0 - f_1\right)^2\right] \\ \left. + \exp\left[-i2\pi(-f_0 - f_1) t - 2\pi^2 d^2 \left(\frac{f_g}{d} - f_0 - f_1\right)^2\right] \right\}, \quad (5.9) \end{aligned}$$

where  $f_g$  denotes the frequency of the wavelet. Since the first and second terms of Eq. (5.9) are much smaller than the other terms, the first two terms can be neglected.

Therefore, Eq. (5.9) may be approximated as

$$W(t, d) = \sqrt{\frac{\pi d}{8}} \left\{ \exp \left[ i2\pi (f_1 - f_0) t - 2\pi^2 d^2 \left( \frac{f_g}{d} + f_0 - f_1 \right)^2 \right] \right. \\ \left. + \exp \left[ i2\pi (f_1 + f_0) t - 2\pi^2 d^2 \left( \frac{f_g}{d} - f_0 - f_1 \right)^2 \right] \right\}. \quad (5.10)$$

The absolute value of the WT given by Eq. (5.10) results in

$$|W(t, d)| = \sqrt{\frac{\pi d}{8}} \left[ \exp \left\{ -4\pi^2 (f_0 - f_1)^2 \left[ d - \frac{f_g}{f_1 - f_0} \right]^2 \right\} \right. \\ \left. + \exp \left\{ -4\pi^2 (f_0 + f_1)^2 \left[ d - \frac{f_g}{f_1 + f_0} \right]^2 \right\} \right. \\ \left. + 2 \cos(4\pi f_0 t) \exp \left\{ -2\pi^2 (f_0 - f_1)^2 \left[ d - \frac{f_g}{f_1 - f_0} \right]^2 \right. \right. \\ \left. \left. - 2\pi^2 (f_0 + f_1)^2 \left[ d - \frac{f_g}{f_1 + f_0} \right]^2 \right\} \right]^{\frac{1}{2}}. \quad (5.11)$$

Equation (5.11) shows that the first two terms are the summation of two Gaussian functions while the third term is multiplication of the cosine function corresponding to the envelope function with a product of two other Gaussian functions. The first and third Gaussian functions have the same mean values, while the means of the second and fourth Gaussians are also the same. Since  $f_1 \gg f_0$ , the difference between the values of the two means is not significant, nor are their variances. As a result, either the summation or the multiplication of the two Gaussian functions produces a Gaussian-like function whose maximum peak appears at the same position of the average value of the two means,  $d = f_g/f_1$ . This can be mathematically verified by substituting this average value into the first and second derivatives of the summation and the multiplication of the Gaussian functions. The first derivative test yields zero

for the critical value  $d = f_g/f_1$ , while the second derivative test gives a negative result. These tests verify that the peak position of the Gaussian-like function is at  $d = f_g/f_1$ . This position is regarded as the one where the frequency of the dilated wavelet  $f_g/d$  matches the frequency of the modulating signal  $f_1$ . Therefore, the cosine function in the third term of Eq. (5.11) is confined by the Gaussian-like function centered at the dilation  $d = f_g/f_1$ .

When the dilation  $d = f_g/f_1$  is achieved, Eq. (5.11) reduces to approximately

$$|W(t, d)|_{d=\frac{f_g}{f_1}} = \sqrt{\frac{\pi f_g}{2f_1}} \exp\left[\frac{-2\pi^2 f_g^2 f_0^2}{f_1^2}\right] |\cos(2\pi f_0 t)|. \quad (5.12)$$

Equation (5.12) confirms that the absolute value of the WT gives the information about the envelope function with its absolute value  $|\cos(2\pi f_0 t)|$ . The rigorous mathematical derivation of Eq. (5.9) to Eq. (5.12) are given in Appendix. Figure 5.11 shows the modulated signal  $s(x)$  of Eq. (5.8) and the normalized absolute value of its WT given by Eq. (5.12), which are represented by the solid and broken lines, respectively. Here, the carrier frequency  $f_1$  is 5 times higher than the modulating frequency  $f_0$ . It is clear from the figure that the minima of the absolute value of the resultant WT output coincide with the zero-crossing points of the carrier signal of Eq. (5.8).

Since the modulus of the envelope function appears along the dilation corresponding to the frequency of the carrier signal in the absolute of the WT, the holographic interference pattern is analyzed by computing the absolute value of its wavelet transformation. Figure 5.12 shows the simulated in-line hologram of the line object equivalent to Fig. 2.3 and the absolute value of its WT which is obtained by

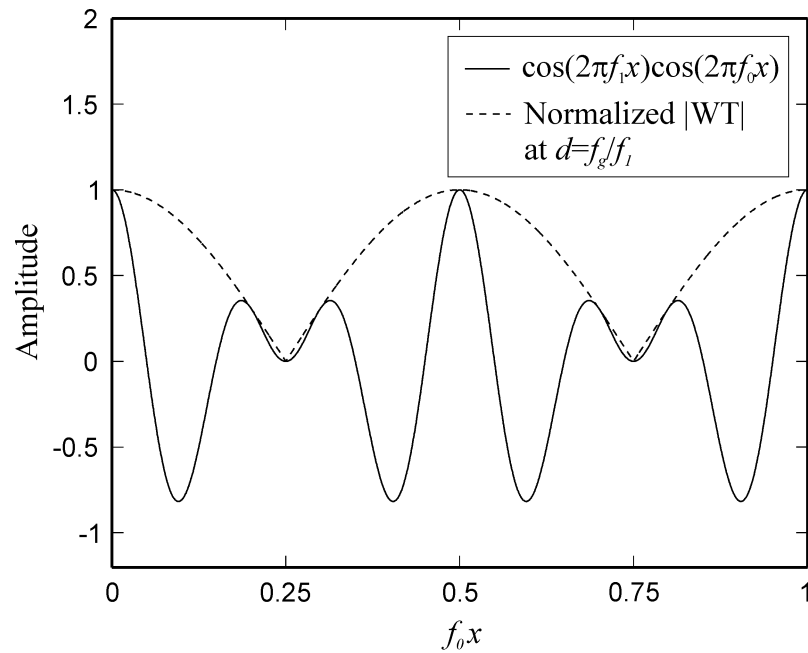


**Figure 5.11** Modulated signal  $s(x)$  of Eq. (5.8) and the normalized absolute value of its WT given by Eq. (5.12).

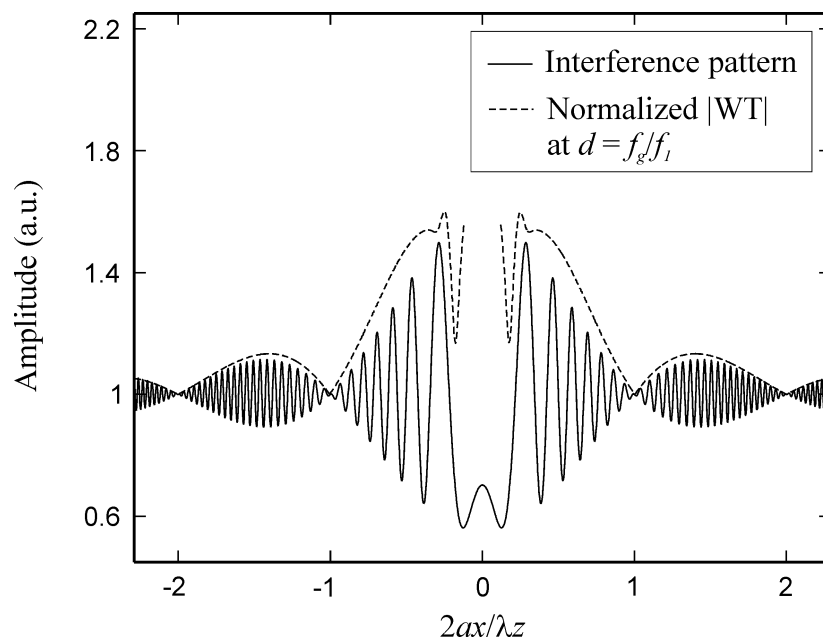


**Figure 5.12** Simulated in-line hologram of the line object and the normalized absolute value of its WT which is retrieved along the dilation  $d = f_g/f_1$ .

retrieving the amplitude of the resultant absolute value of the WT along the dilation  $d = f_g/f_1$ . In the case of in-line holograms,  $f_1$  stands for the frequency of the chirp signal determined by  $r/\lambda z$ . As a function of dilation  $2a/d$ , Fig. 5.13 illustrates a 3-D plot for the absolute value of the WT of the fringe which is cut along the dilation  $d = f_g/f_1$  represented by the dashed line. In the WT domain, the path of the dilation is nonlinear, because it is inversely proportional to the space-varying frequency  $f_1$  of the chirp signal. Evidently, the minima of the absolute value of the resultant WT output appear at the correct zero-crossing points of the chirp signal. By determining the frequencies of the chirp function at these minima, the object size can then be calculated.

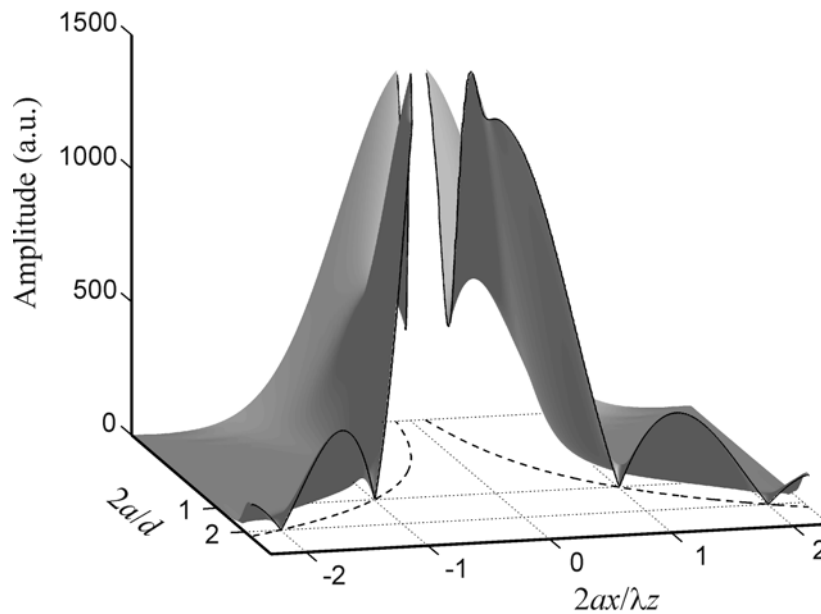


**Figure 5.13** The 3-D plot of the absolute value of the WT which is cut along the dilation  $d = f_g/f_1$ .

In order to obtain accurately the object size by using the proposed method, the frequency of the chirp signal at the minimum position must be accurately determined.

This can be achieved by computing the WT with fine dilation intervals. However, since the computation of the WT with fine dilation interval requires long computation time, the WT of the interference pattern is computed twice as shown in the block diagram of Fig. 5.14. The first computation of the WT uses coarse and logarithmic dilation interval. This gives coarse WT output. By computing the absolute value of

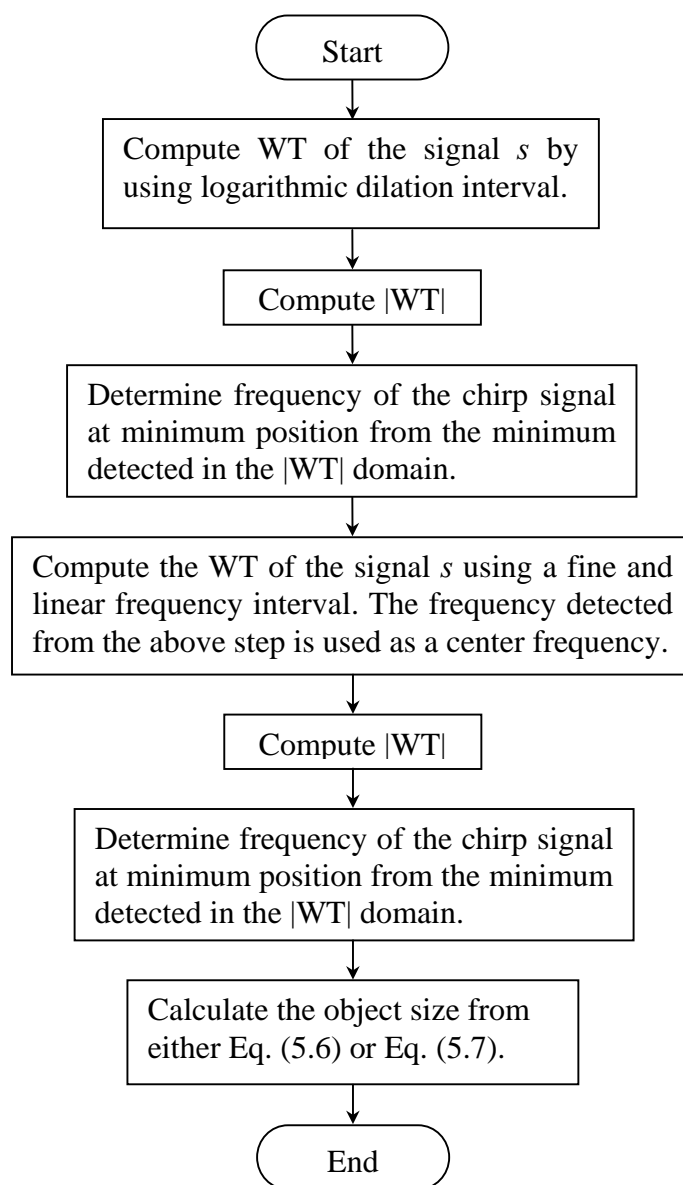


**Figure 5.14** Block diagram for calculating the object size from  $|WT|$ .

the resultant WT the rough estimate of the chirp frequency at the minimum position  $f_c = 1/d_c$  can be obtained. Figure 5.15 show the top-view plot of the absolute values of the WT of the hologram shown in Fig. 2.3. In this example, its first minimum position gives  $f_c = 10^{3.92} = 8.32$  lines/mm. The interference pattern is next analyzed by the second WT with the analyzing wavelets generated at the frequencies  $f_1 < f < f_{M_2}$ , where  $M_2$  is the number of dilations used in the second WT. Here, the first dilation  $d_1 = 1/f_1$  and the last dilation  $d_{M_2} = 1/f_{M_2}$  are selected with respect to the center value of dilation  $d_{M_2/2} = d_c$ . In order to obtain accurate frequency information at the minimum position, the dilation interval is set to produce a frequency interval that is always constant and linear. Thus, for a desired frequency interval of  $\Delta f$ , the generated frequency  $f_n$  must satisfy

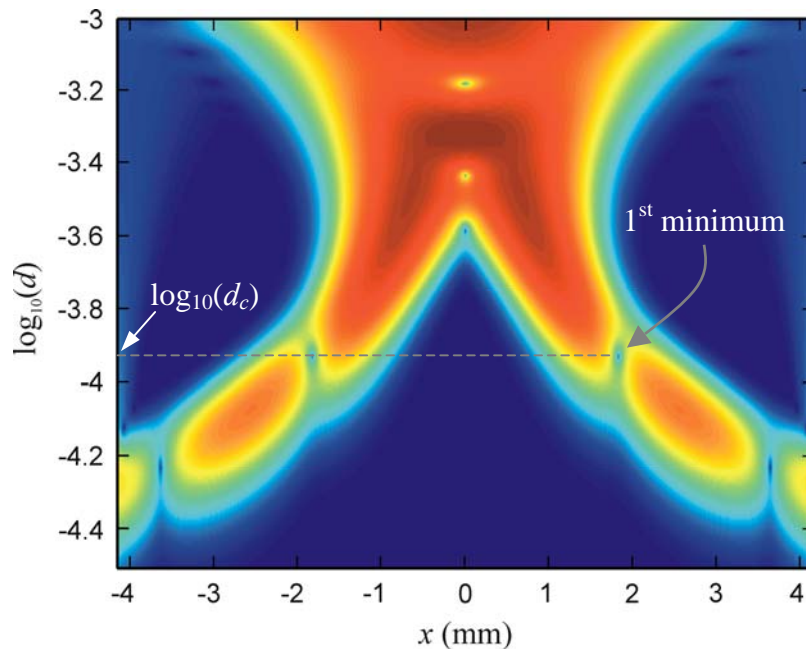


**Figure 5.15** Approximated frequency  $f_c = 1/d_c$  obtained from the detected minimum in the absolute values of the first WT.

$$f_n = f_1 - (n-1)\Delta f, \quad (5.13)$$

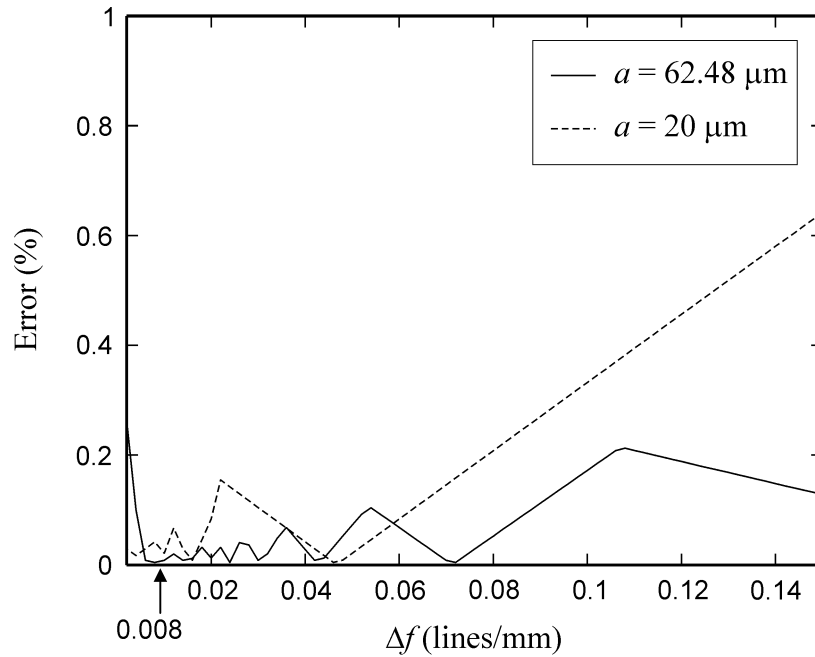
For given dilations  $d_1$  and  $d_{M_2}$ , the frequency interval  $\Delta f$  can be calculated from

$$\Delta f = \frac{1}{M_2 - 1} \left( \frac{1}{d_1} - \frac{1}{d_{M_2}} \right). \quad (5.14)$$

By substituting Eq. (5.14) into Eq. (5.13) and taking the inverse of the result, the dilations used in the second WT are found to be

$$d_n = \left\{ \frac{1}{d_1} - \left( \frac{n-1}{M_2 - 1} \right) \left( \frac{1}{d_1} - \frac{1}{d_{M_2}} \right) \right\}^{-1}. \quad (5.15)$$

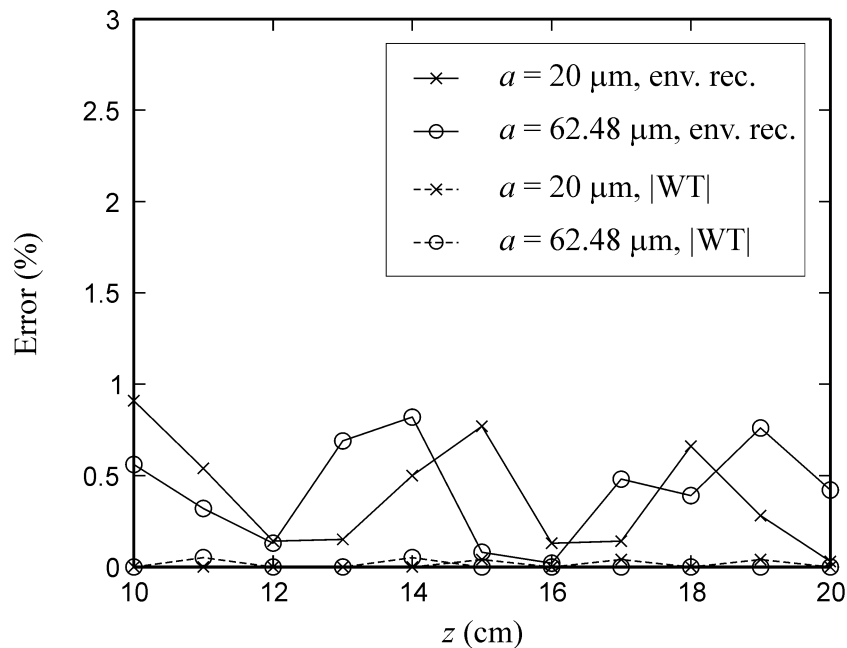
As a function of  $\Delta f$ , Fig. 5.16 shows the errors in measurement of the object size from the holograms of a line object having the radius of  $62.48 \mu\text{m}$  and  $20 \mu\text{m}$  represented



**Figure 5.16** Errors in measurement of  $a$  as a function of the frequency interval  $\Delta f$ .

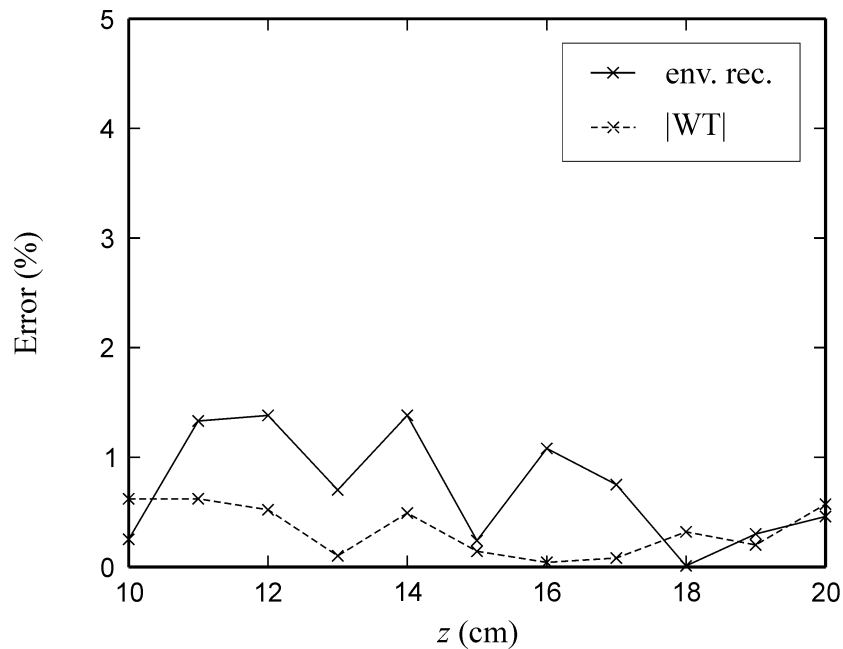
by using the solid and the dash lines, respectively. Here, the recording distance of both holograms are  $z = 20$  cm. It is found that at large frequency interval, the fluctuation of the errors is higher than that of the smaller interval. Thus, in order to obtain a small error of measurement, the small frequency interval of  $\Delta f = 0.008$  lines/mm is employed for the computation of the second WT. Here, the computation is performed with the number of dilations  $M_2 = 64$ .

Figure 5.17 to Fig. 5.20 show the comparison of the errors in measurement of the object size by using the absolute values of the WT and the envelope reconstruction method which are represented by the broken and the solid lines, respectively. In Fig. 5.17, the errors in measurement of  $a$  from the simulated holograms of the line object having the diameter of  $20 \mu\text{m}$  and  $62.48 \mu\text{m}$  are represented by the cross and the



**Figure 5.17** Errors in measurement of  $a$  from the simulated holograms of line object by using the envelope reconstruction method and the absolute value of WT.

circle sign, respectively. It is obvious from the figure that, in comparison with the envelope reconstruction method, the errors in measurements by using the absolute value of the WT are significantly reduced for both sizes of the object. The reason of this reduction is that this method employs only the frequency of the chirp signal at the minimum position of the envelope function for evaluating the object size. By analyzing the hologram with fine frequency interval, the high accuracy frequency information at the minima positions of the interference pattern can be obtained. Since the information of the recording distance is not required, its measurement errors do not affect the measurements in the size of the object. The improvement of the accuracy of the measurement is verified by applying this method to the experimentally generated holograms of the optical fiber as shown in Fig. 5.18.



**Figure 5.18** Errors in measurement of  $a$  from the experimentally generated holograms of the optical fiber by using the envelope reconstruction method and the absolute value of the WT.

Similarly, significant reduction of the errors is obtained from the measurements of the size of the spherical objects by using the absolute values of the WT. The errors in measurement of the simulated holograms of spherical object are shown in Fig. 5.19. Here, the cross sign represents the error in measurement of the size of the spherical object having the radius of  $20\ \mu\text{m}$ , while the circle sign corresponds to those of the radius  $77.78\ \mu\text{m}$ . The experimental results illustrated in Fig. 5.20 agree well with the simulation. Therefore, the results confirm the effectiveness of the method on improving the accuracy in measurement of the object size from the in-line holograms.

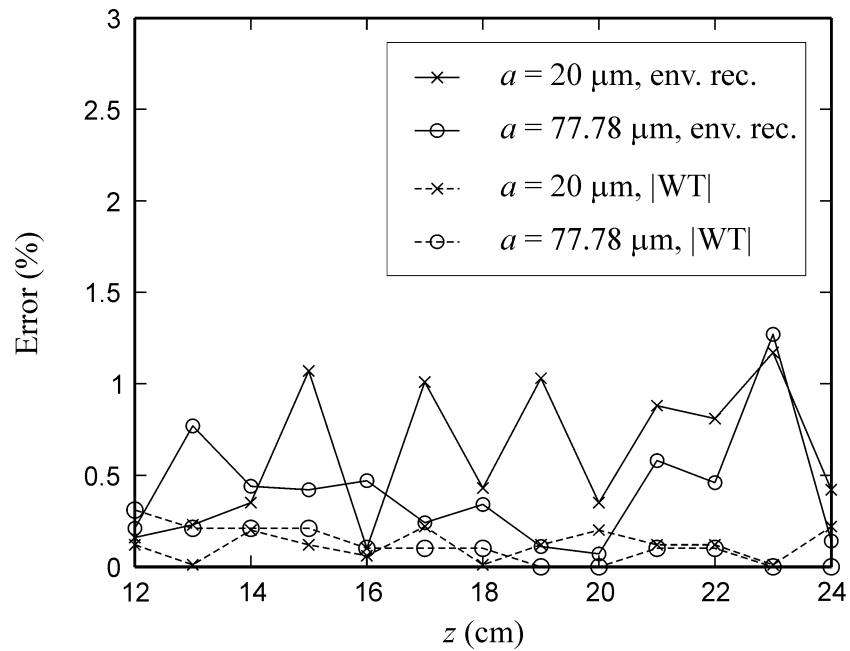


**Figure 5.19** Errors in measurement of  $a$  from the simulated holograms of 2D object by using the envelope reconstruction method and the absolute value of WT.

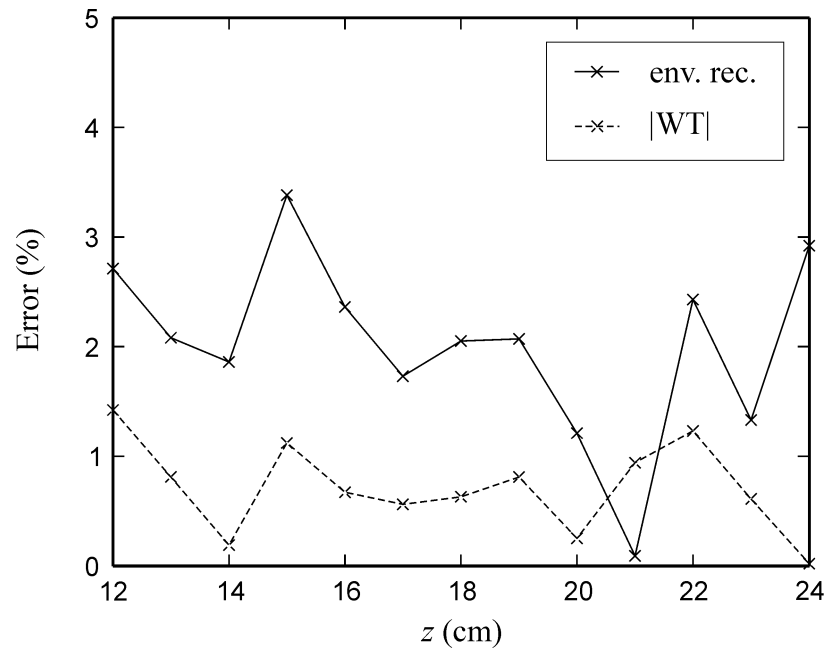


**Figure 5.20** Errors in measurement of  $a$  from the experimentally generated holograms of the pinhole by using the envelope reconstruction method and the absolute value of the WT.

# **CHAPTER VI**

## **SYSTEM PERFORMANCE**

In the proposed digital analysis method, the CCD sensor is employed for capturing the in-line holograms. As a consequence, the finite size and the finite resolution of the CCD sensor become the factors that determine the amount of information which can be faithfully recorded. For this reason, it is important to study the system performance of our proposed method. In the case of holograms of single objects, the analysis of the system performance is based on these two limiting factors of the employed CCD sensor. As for the case of the holograms of multiple objects, the analysis is done by using information in the wavelet domain, because the desired wavelet coefficient from one object is not always distorted by the others. Thus, the feasibility of the proposed method depends on the separation of the wavelet coefficients.

### **6.1 Single object**

The interference pattern recorded on the CCD sensor is a modulation between the chirp signal and the envelope function. The frequency of the chirp signal is determined by the recording distance, while the minima positions of the envelope function depend on the object size. As discussed in Chapter IV, the recording distance of the object is extracted by determining the frequency of the chirp signal using the WT. In order to achieve this, the interference pattern must be correctly sampled by the CCD sensor or the spatial resolution of the sensor must satisfy the Nyquist sampling

theorem (Oppenheim and Schaffer, 1989). Moreover, in order to determine the object size, the area of the CCD must be wide enough to record the minima positions. In the following discussion the CCD sensor is assumed to have a square-shaped aperture with the size of  $X \times X$  and the pixel size of  $\Delta x \times \Delta x$ . The sampling spatial frequency in either the horizontal or the vertical directions of the CCD can be mathematically expressed as

$$f_{\text{CCD}} = \frac{1}{\Delta x}. \quad (6.1)$$

### 6.1.1 Line object

Since the spatial resolution of the sensor must satisfy the Nyquist sampling theorem, the relationship between the frequency of the chirp signal and the sampling frequency  $f_{\text{CCD}}$  can be expressed as

$$f_{\text{CCD}} > 2f_{\text{chirp}}. \quad (6.2)$$

Substitutions of the chirp frequency  $f_{\text{chirp}}$  by  $x/\lambda z$  and Eq. (6.1) into Eq. (6.2) give

$$x < \frac{\lambda z}{2\Delta x}, \quad (6.3)$$

which describes the length of the interference pattern that can be correctly sampled by the CCD sensor placed at the distance  $z$ . Therefore, for a given recording distance  $z$ , the analyzable area on the CCD is confined in the region of  $0 < x < \lambda z/2\Delta x$ . When the recording distance becomes longer, the size of the analyzable area increases, because the longer recording distance causes the smaller frequency of the chirp signal. As a consequence, when the right term in the inequality of Eq. (6.3) is bigger than the CCD

aperture size, the range of the recorded hologram that can be analyzed becomes  $0 < x \leq X$ . This condition is achieved if the recording distance  $z$  is bigger than  $2X\Delta x / \lambda$ . We define this factor as a critical distance. Therefore, the analyzable area is determined as follows

$$x < \frac{\lambda z}{2\Delta x} \quad \text{if} \quad 0 < z \leq \frac{2X\Delta x}{\lambda} \quad (6.4a)$$

and

$$x \leq X \quad \text{if} \quad z > \frac{2X\Delta x}{\lambda} \quad (6.4b)$$

On the other hand, in order to measure the size of the object, a minimum number of the minima  $n_{\min}$  of the envelope Sinc function must be recorded by the CCD. As a result, the following relationship

$$\frac{2ax}{\lambda z} \geq n_{\min} \quad (6.5)$$

is obtained. By substituting Eqs. (6.4a) and (6.4b) into Eq. (6.5), the smallest size of the line object that can be measured is found to be

$$a \geq \begin{cases} n_{\min} \Delta x & \text{if } 0 < z \leq \frac{2X\Delta x}{\lambda} \\ \frac{\lambda z n_{\min}}{2X} & \text{if } z > \frac{2X\Delta x}{\lambda} \end{cases} . \quad (6.6)$$

Furthermore, in order to reconstruct faithfully the envelope function, a large number of interference fringes must be present within the first minimum of the sinc function at  $x = \lambda z / 2a$ . Since the zero of the chirp function occurs at  $x = \sqrt{\lambda z (n - 1/4)}$

where  $n$  is the number of fringes, the number of interference fringes within the first minimum is found to be

$$n = \frac{\lambda z}{(2a)^2} + \frac{1}{4}. \quad (6.7)$$

By using the far-field condition  $z \gg \pi(2a)^2/\lambda$  (Goodman, 1996) Eq. (6.7) reduces to  $n \gg \pi + 1/4$  or

$$a \ll \frac{1}{2} \sqrt{\frac{\lambda z}{\pi}} \quad (6.8)$$

Equation (6.8) describes the upper limit of the measurable object size as a function of the recording distance.

### 6.1.2 Spherical object

Since the chirp signal is solely determined by the axial position of the object, the analyzable area of the interference pattern for spherical objects can also be described by Eqs. (6.4a) and (6.4b) with the replacement of the variable  $x$  by  $r$ . However, the positions of the minima for the Bessel function and the sinc function are different. The absolute value of the Bessel function becomes minimum when the argument is  $1.22\pi$ ,  $2.23\pi$ ,  $3.24\pi$ , etc. (Gradshteyn and Ryzhik, 1994). By taking this consideration into account, a minimum number of the minima  $n_{\min}$  of the envelope function can be approximately described by

$$\frac{2ar}{\lambda z} \geq (n_{\min} + 0.23). \quad (6.9)$$

To find the smallest measurable size of the spherical particle, the finite extent of the analyzable area of the interference pattern is applied. This gives

$$a \geq \begin{cases} (n_{\min} + 0.23) \Delta x & \text{if } 0 < z \leq \frac{2X \Delta x}{\lambda} \\ \frac{\lambda z (n_{\min} + 0.23)}{2X} & \text{if } z > \frac{2X \Delta x}{\lambda} \end{cases} \quad (6.10)$$

By using the far-field condition to account for the number of fringes within the first minimum of the Airy function, the biggest size of the measurable particle becomes

$$a \ll \frac{1}{2} \sqrt{\frac{\lambda z}{\pi}}. \quad (6.11)$$

In summary, the lower limit of the measurable size for spherical objects is higher than that for line objects, while the upper limits for both objects are the same. This is due to the fact that the width between the two minima of the Airy function is wider than that of the sinc function. Figure 6.1 shows the ranges of the object size and the recording distance in a logarithmic scale that can be measured. The ranges of measurements for line and spherical objects are confined by the triangles drawn with the solid and the broken lines, respectively. The base and the right side of the triangle correspond to the lower limits of the measurable size of the object for the recording distances being smaller and bigger than the critical value, respectively. The left side of the triangle associates with the upper limit of the measurable size. Since the upper limits of the measurable size for both objects are the same, the two lines coincide. The maximum measurable size of the object must have a smaller value than the upper limit as described by Eqs. (6.8) and (6.11). At the recording distance which is greater

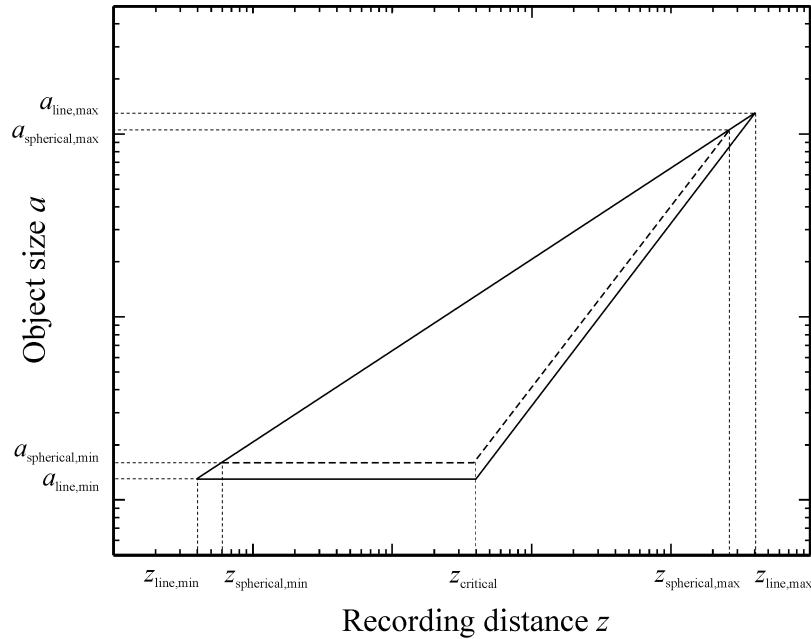


**Figure 6.1** Measurable size of objects and their recording distances.

than the critical value, the longest recording distance and the largest size of particle could be mathematically determined by equating the maximum and the minimum values of the particle size  $a$ . In the case of line objects, this yields  $z_{\text{line,max}} = X^2/\pi\lambda n_{\text{min}}^2$  and  $a_{\text{line,max}} = X/2\pi n_{\text{min}}$ , while for spherical particles the maximum recording distance and the maximum size are given by  $z_{\text{spherical,max}} = X^2/\pi\lambda(n_{\text{min}}+0.23)^2$  and  $a_{\text{spherical,max}} = X/2\pi(n_{\text{min}}+0.23)$ , respectively. In a similar fashion, when the recording distance is smaller than the critical value, the shortest recording distance and the smallest size of line objects that can be measured becomes  $z_{\text{line,min}} = 4\pi\Delta x^2 n_{\text{min}}^2/\lambda$  and  $a_{\text{line,min}} = \Delta x n_{\text{min}}$ , respectively. In the case of spherical objects we obtain  $z_{\text{spherical,min}} = 4\pi\Delta x^2 (n_{\text{min}}+0.23)^2/\lambda$  and  $a_{\text{spherical,min}} = \Delta x(n_{\text{min}}+0.23)$ .

## 6.2 Multiple objects

In the case where the object field consists of multiple objects, Eqs. (3.8) and (3.9) show that the in-line holograms can be mathematically described by the summation of the holograms from the individual object and the interference pattern between the object waves diffracted from the different objects. Since the hologram of the object being studied may be overlapped by the hologram from the other objects, the proposed analysis method may not be able to accurately extract the required information from the hologram. In this section, the feasibility of the proposed method for analyzing the holograms of multiple objects is studied through the computer simulation.

Since the WT is a linear operation, the resultant WT of the hologram of multiple objects can be determined by a linear summation of the WT of each term of Eqs. (3.8) or (3.9). However, the amplitudes of the interference between the object waves corresponding to the third and the fourth terms are very small compared to the second term, that is the interference between the object and the reference waves. As a consequence, the resultant amplitudes of the WTs of the third and the fourth terms are also very small compared to the WT of the second term. Thus, they can be neglected. This is verified by taking the WT of the holograms of two objects simulated with and without both the third and the fourth terms. It is found that the errors in measurements of the object size and its recording distance obtained from both holograms are not different significantly. Although the holograms of multiple objects are generated by using Eqs. (3.8) and (3.9), for the sake of simplicity, the following mathematical analysis uses the first and the second terms of those equations.

### 6.2.1 Extraction of the object size

As discussed in Section 5.2, the absolute values of the WT can be used to extract the size of the object from the holograms by determining the frequency of the chirp signal at the minima positions of the interference pattern. However, in the case of the multiple objects, the desired interference pattern may be overlapped by the interference pattern of the other objects. This overlap may distort the positions of the minima. As a result, the accuracy of measuring the object size by using the absolute values of the WT is reduced. In order to keep the high accuracy of the measurement, the minimum separation between the objects is mathematically derived and verified through the computer simulation.

Figure 6.2 shows the top-view of the recording setup of the hologram of two-line objects,  $P_1$  and  $P_2$ , placed at distances  $z_1$  and  $z_2$  in front of the recording plane, respectively. Here,  $d_x$  represents the separation between the objects along the horizontal direction. Figure 6.3 illustrates the 1-D intensity profile of the simulated hologram of two optical fibers having the radius  $a_1 = a_2 = 62.48 \mu\text{m}$  recorded at the recording distance  $z_1 = 40 \text{ cm}$  and  $z_2 = 35 \text{ cm}$  with the separation  $d_x = 5 \text{ mm}$  and the

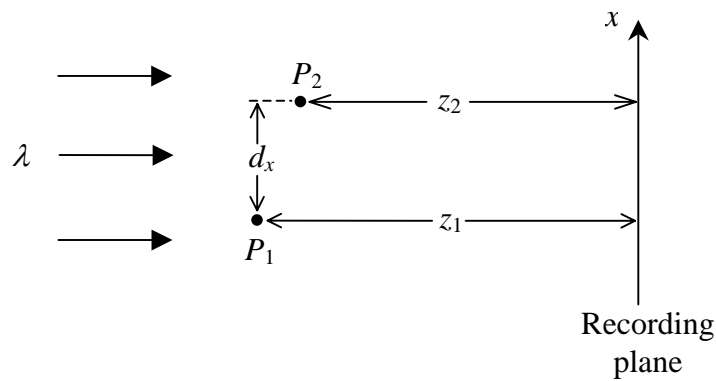


**Figure 6.2** Recording of in-line hologram of 2 line objects.

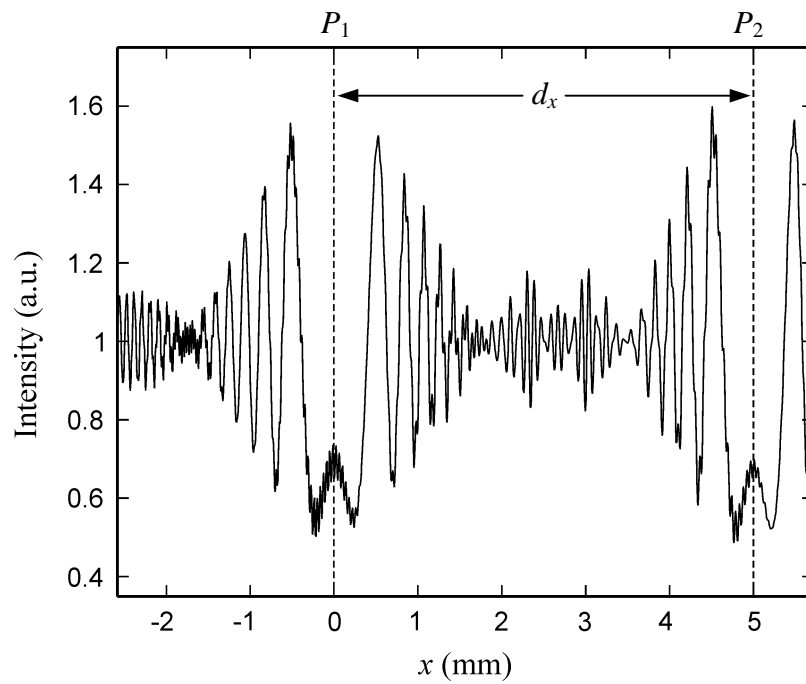


**Figure 6.3** Hologram of two optical fibers.

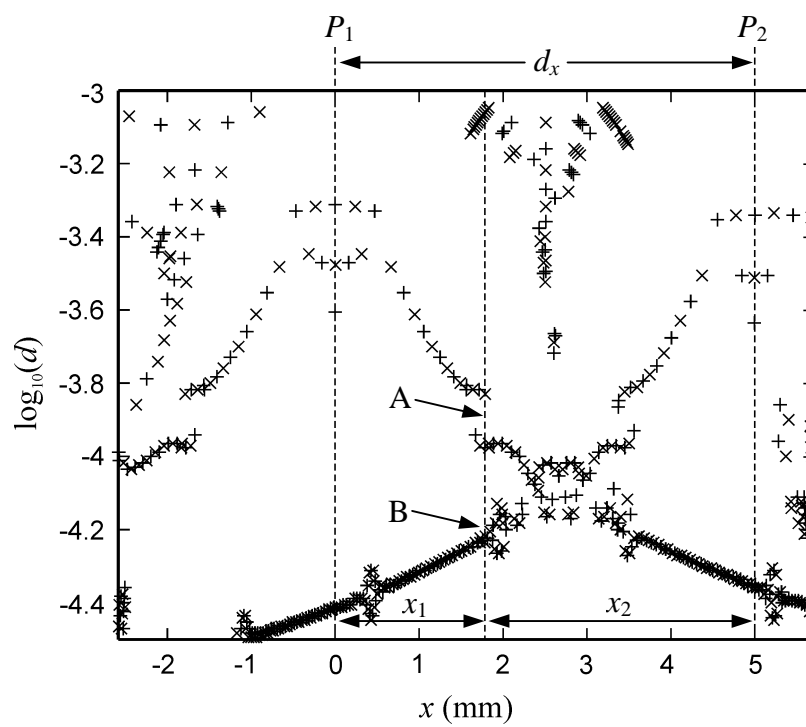


**Figure 6.4** Local maxima and minima of the real values of the WT of the hologram shown in Fig. 6.3.

wavelength  $\lambda = 543.5$  nm. Figure 6.4 illustrates the maximum and minimum amplitudes of the real values of the resultant WT of the hologram shown in Fig. 6.3 which are denoted by the plus and the cross signs, respectively. For the sake of better visualization of the frequency variation of the interference pattern, the real values of the WT is chosen in this figure. In Fig. 6.4, point A corresponds to the first minimum of the interference patterns of the first fiber  $P_1$ ,  $x_1$  and  $x_2$  are the distances between the first minimum A and the centers of the resultant WT of the fiber  $P_1$  and  $P_2$ , respectively. Point B is the wavelet coefficient of the resultant WT of the second fiber  $P_2$  which appears at  $x_1$ . In order to extract the size of the fiber  $P_1$ , the resultant WT at the minimum point A is required and must not be corrupted by any wavelet coefficient of the interference pattern of the fiber  $P_2$ . This is achieved if the wavelet coefficient B is well separated from the point A. In the frequency domain, the separation of two wavelet coefficients with respect to the frequency at the point A can be mathematically written as

$$\frac{|f_B - f_A|}{f_A} > p, \quad (6.12)$$

where  $p$  is the ratio of the frequency difference to the frequency at the point A. By rewriting Eq. (6.12), the frequency  $f_B$  corresponding to the wavelet coefficient B can be expressed as

$$f_B > f_A(1 + p) \quad (6.13a)$$

or

$$f_B < f_A(1 - p). \quad (6.13b)$$

Substitutions of the frequency at the points A and B,  $f_A = x_1/\lambda z_1$  and  $f_B = x_2/\lambda z_2$ , into Eq. (6.13) give

$$\frac{x_2}{\lambda z_2} > \frac{x_1}{\lambda z_1}(1+p) \quad (6.14a)$$

or

$$\frac{x_2}{\lambda z_2} < \frac{x_1}{\lambda z_1}(1-p). \quad (6.14b)$$

Since the distance  $x_1$  is equivalent to  $n\lambda z_1/2a_1$ , the distance  $x_2$  can be calculated from  $|d_x - n\lambda z_1/2a_1|$ . Substitutions of the values of  $x_1$  and  $x_2$  into Eq. (6.14a) yield

$$d_x > \frac{n\lambda}{2a_1} [z_2(1+p) + z_1] \quad (6.15a)$$

or

$$d_x < -\frac{n\lambda}{2a_1} [z_2(1+p) - z_1], \quad (6.15b)$$

while the same substitutions into Eq. (6.14b) give

$$-\frac{n\lambda}{2a_1} [z_2(1-p) - z_1] < d_x < \frac{n\lambda}{2a_1} [z_2(1-p) + z_1]. \quad (6.15c)$$

Equation (6.15) define the allowable separation  $d_x$  between the fibers  $P_1$  and  $P_2$  that the radius  $a_1$  of the fiber  $P_1$  can still be extracted from the hologram by using the absolute values of the WT.

In order to obtain the practical value of the factor  $p$ , the error of measurement of the radius  $a_1$  from the simulated holograms of two line objects  $P_1$  and  $P_2$  with  $a_1 =$

25  $\mu\text{m}$ ,  $z_1 = 30$  cm and  $a_2 = 50$   $\mu\text{m}$ ,  $z_2 = 29$  cm is plotted in Fig. 6.5 as a function of the separation  $d_x$ . Here, the holograms are generated with the separation interval  $\Delta d_x = 0.1$  mm. The negative and positive values of  $d_x$  represent the situation that  $P_2$  is located on the left and on the right side of  $P_1$ , respectively. In this computation, the radius  $a_1$  is measured from the first minimum of the interference pattern ( $n = 1$ ). It can be seen from Fig. 6.5 that there are three ranges of  $d_x$  where the errors in finding  $a_1$  are small. The most right region corresponds to the condition defined by Eq. (6.15a), while the most left region is associated with Eq. (6.15b). Equation (6.15c) gives the allowable  $d_x$  in the middle region of the graph. However, the errors obtained from the region defined by the Eq (6.15c) are higher than that of the Eqs. (6.15a) and (6.15b). Thus, the region of  $d_x$  defined by the Eq. (6.15c) cannot be used and is neglected. By

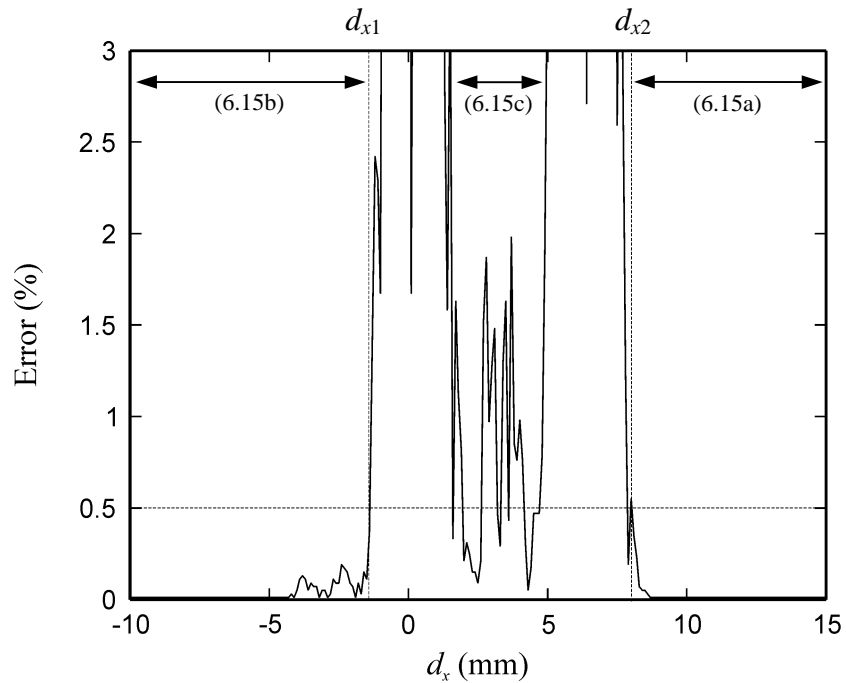


**Figure 6.5** Errors of measurement of  $a_1$  as a function of  $d_x$  for  $a_1 = 25$   $\mu\text{m}$ ,

$z_1 = 30$  cm and  $a_2 = 50$   $\mu\text{m}$ ,  $z_2 = 29$  cm.

defining the critical separation  $d_{x1}$  and  $d_{x2}$  as the value of  $d_x$  at the boundary between the regions with low and high errors, the small errors of measurement of  $a_1$  are obtained when  $d_x < d_{x1}$  or  $d_x > d_{x2}$ . If the maximum error is set to be 0.5 percent the critical separations found from Fig. 6.5 are  $d_{x1} = -1.4$  mm and  $d_{x2} = 8.1$  mm. Substitutions of these values of  $d_{x1}$  and  $d_{x2}$  into their corresponding Eqs. (6.15b) and (6.15a) give the values  $p_1 = 0.48$  and  $p_2 = 0.53$ , respectively.

The measurement of the spatial separation  $d_x$  obtained by analyzing the simulated holograms generated from different conditions of the object size and the recording distance are summarized in Table 6.1. Two object sizes of 25  $\mu\text{m}$  and 50  $\mu\text{m}$  are used in the simulation with the recording distances  $z_1$  of the object  $P_1$  are 10 cm and 30 cm. As for the object  $P_2$ , the recording distance  $z_2$  is varied from 9, 10 to 11 cm for  $z_1 = 10$  cm, while  $z_2 = 29, 30$  and 31 cm for  $z_1 = 30$  cm. It is found that although the critical separation distances  $d_{x1}$  and  $d_{x2}$  are different significantly for different objects, their corresponding values of  $p$  are still in the range of 0.4 to 0.8. These results confirm the feasibility of Eqs. (6.15) for determining the required separation  $d_x$  between the objects in order to extract its size by using the absolute values of the WT method. However, in order to employ Eqs. (6.15) for determining the range of the allowable  $d_x$ , the value of  $p$  must be selected such that the resultant values of  $d_x$  are consistent with the simulation results depicted in the Table 6.1. If a small value of  $p$  is substituted into Eqs. (6.15), the resultant separation between the object is shorter than that obtained from the simulation. As for an example, a substitution of  $p = 0.4$ ,  $a_1 = 25$   $\mu\text{m}$ ,  $z_1 = 30$  cm,  $a_2 = 25$  and  $z_2 = 30$  cm into Eqs. (6.15)

**Table 6.1** Measurement of the critical separation  $d_x$  and the frequency ratio  $p$  from the WT of the simulated holograms of two line objects.

$a_1$	$z_1$	$a_2$	$z_2$	$d_{x1}$	$d_{x2}$	$p_1$	$p_2$
25	10	25	9	-0.4	2.7	0.52	0.65
25	10	25	10	-0.6	2.8	0.55	0.58
25	10	25	11	-0.8	2.9	0.58	0.52
25	10	50	9	-0.5	2.6	0.62	0.55
25	10	50	10	-0.5	2.8	0.46	0.58
25	10	50	11	-0.7	2.9	0.49	0.52
25	30	25	29	-1.7	7.8	0.57	0.44
25	30	25	30	-1.8	8.3	0.55	0.55
25	30	25	31	-2	8.6	0.56	0.58
25	30	50	29	-1.4	8.1	0.48	0.54
25	30	50	30	-1.6	8	0.49	0.45
25	30	50	31	-1.8	8.3	0.50	0.50
50	10	25	9	-0.3	1.4	0.72	0.75
50	10	25	10	-0.4	1.5	0.74	0.76
50	10	25	11	-0.4	1.6	0.58	0.77
50	10	50	9	-0.3	1.4	0.72	0.75
50	10	50	10	-0.4	1.4	0.74	0.58
50	10	50	11	-0.5	1.6	0.75	0.77
50	30	25	29	-0.8	4	0.54	0.50
50	30	25	30	-0.9	4.1	0.55	0.51
50	30	25	31	-0.9	4.2	0.50	0.53
50	30	50	29	-0.9	4	0.61	0.50
50	30	50	30	-0.9	4	0.55	0.45
50	30	50	31	-0.9	4.3	0.50	0.58

gives  $d_x < -1.3$  mm and  $d_x > 7.8$  mm, while the results obtained from the simulation are  $d_x < -1.8$  mm and  $d_x > 8.3$  mm. On the other hand, when the value of  $p$  is too high, the separation between the object will be wider than from the simulation result. This can be easily obtained if  $p = 0.8$  are substituted into Eqs. (6.15) which gives  $d_x < -2.6$  mm and  $d_x > 9.1$  mm. Figure 6.6 illustrates the region of allowable  $d_x$  for different conditions of  $p$ . The solid line represents the real allowable  $d_x$  which is obtained from the simulation, while the broken lines are those calculated by using Eqs. (6.15). It can be seen that in the case of small  $p$ , the calculated  $d_x$  exceeds the allowable  $d_x$  from the simulation results. However,  $d_x$  calculated by using high value of  $p$  agrees with the simulation results. For this reason, it is better to use the highest value of  $p = 0.8$  obtained from the simulation for calculating the allowable  $d_x$  given by Eqs. (6.15).

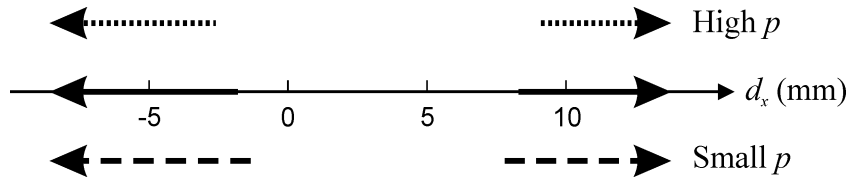


**Figure 6.6**  $d_x$  calculated by using Eqs. (6.15) for different values of  $p$  in comparison with the simulation result.

The analysis for the separation between the spherical objects is in analogy with those of the line objects. Since the minima positions of the hologram of spherical object appear at  $r_n = (n+0.23)\lambda z/2a$  while those of the line object can be found at  $x_n = n\lambda z/2a$ , the criteria for the separation  $d_r$  between the spherical objects can be simply obtained by substituting  $n$  in Eqs. (6.15) with  $n+0.23$ . This yields

$$d_r > \frac{(n+0.23)\lambda}{2a_1} [z_2(1+p) + z_1], \quad (6.16a)$$

and

$$d_r < -\frac{(n+0.23)\lambda}{2a_1} [z_2(1+p) - z_1]. \quad (6.16b)$$

As in the case of the line objects, the hologram of two spherical objects are generated by using the Eq. (3.9) with the same object sizes and recording distances. The measurement results of the analysis of these holograms are summarized in Table 6.2. It can be seen from these results that the values of the parameter  $p$  in Eqs. (6.16) are varied from 0.4 to 0.7. In analogy with the analysis of the line objects, the smallest value of  $p$  cannot be used since its may give inconsistent results. For example, by substituting  $p = 0.4$ ,  $a_1 = 25 \mu\text{m}$ ,  $z_1 = 30 \text{ cm}$ ,  $a_2 = 50 \mu\text{m}$  and  $z_2 = 30 \text{ cm}$  into Eqs. (6.16), the allowable  $d_r$  are found to be  $d_r < -1.6 \text{ mm}$  and  $d_r > 9.6 \text{ mm}$  which is inconsistent with the simulation results which are  $d_r < -2.4$  and  $d_r > 10.3 \text{ mm}$ . Thus, the highest value of  $p = 0.7$  is used for determining the required separation between the spherical objects from Eq. (6.16).

### 6.2.2 Extraction of the axial position of objects

As discussed in Chapter IV, the recording distance is extracted from the hologram by determining the space-varying frequency of the interference pattern. These frequencies and their corresponding spatial positions are determined from the dilation and the translation of all wavelet coefficients with maximum or minimum amplitudes, respectively. However, since the determined spatial position corresponds to the horizontal distance measured from the center position of the interference pattern, the exact information of the center position of the interference pattern is required. In the case of the single object, this center position can be easily determined

**Table 6.2** Measurement of the critical separation  $d_x$  and the frequency ration  $p$  from the WT of the simulated holograms of two spherical objects.

$a_1$	$z_1$	$a_2$	$z_2$	$d_{r1}$	$d_{r2}$	$p_1$	$p_2$
25	10	25	9	-0.5	3.2	0.53	0.55
25	10	25	10	-0.7	3.4	0.52	0.54
25	10	25	11	-0.8	3.6	0.45	0.54
25	10	50	9	-0.5	3.2	0.53	0.55
25	10	50	10	-0.7	3.4	0.52	0.54
25	10	50	11	-0.9	3.6	0.52	0.54
25	30	25	29	-1.9	10	0.52	0.54
25	30	25	30	-2.2	10.3	0.55	0.57
25	30	25	31	-2.5	10.4	0.57	0.54
25	30	50	29	-2.1	10.2	0.58	0.60
25	30	50	30	-2.4	10.3	0.60	0.57
25	30	50	31	-2.5	10.5	0.57	0.57
50	10	25	9	-0.3	1.6	0.61	0.55
50	10	25	10	-0.4	1.7	0.60	0.54
50	10	25	11	-0.4	1.8	0.45	0.54
50	10	50	9	-0.3	1.7	0.61	0.71
50	10	50	10	-0.4	1.7	0.60	0.54
50	10	50	11	-0.4	1.8	0.45	0.54
50	30	25	29	-0.9	4.8	0.50	0.44
50	30	25	30	-1	5.1	0.50	0.54
50	30	25	31	-1.1	5.1	0.50	0.49
50	30	50	29	-1	5	0.55	0.54
50	30	50	30	-1	5.1	0.50	0.54
50	30	50	31	-1.1	5.2	0.50	0.54

by detecting the pixel around the symmetrical axis of the hologram. However, for the holograms of multiple objects, the interference pattern of particular interest may be distorted by the others. For example, the center position of the interference pattern of the fiber  $P_1$  shown in Fig. 6.3 is difficult to detect. Thus, the feasibility of the method for extracting the recording distance from the hologram of multiple objects is mainly determined by the accuracy of detecting the center position of the interference pattern.

On the other hand, due to shift-invariant nature of the WT, the analysis of the holograms by the WT gives symmetrical wavelet coefficients. Figure 6.7 shows the maximum and minimum amplitudes of the real values of the wavelet coefficients obtained from the hologram shown in Fig. 6.3. It is found that the wavelet coefficients with the maximum amplitudes which are pointed to by the arrow signs appear at the

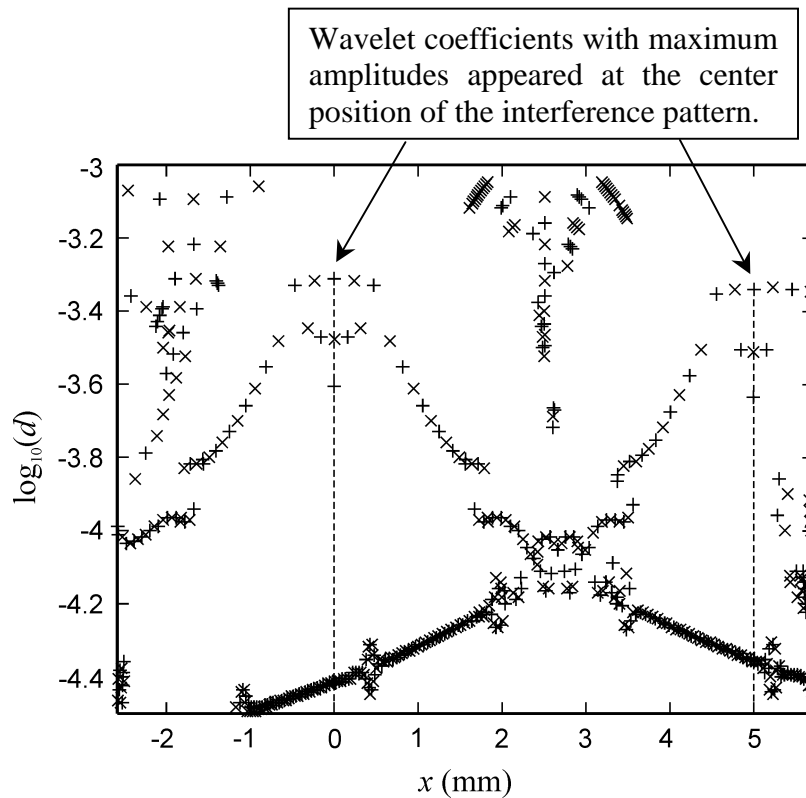


**Figure 6.7** The WT of the hologram shown in Fig. 6.3.

center positions of both objects. The disturbance from the hologram of the other objects in the WT domain is minimum because of their frequency difference. Since the frequency of the chirp signal at the center position of the interference pattern is low, its wavelet coefficient appears at high scale, while the high-frequency components appear at lower scales. As a consequence, in the WT domain, the disturbance at the center position by the hologram of the other object is very small provided the two objects do not exactly overlap. Thus, the detection of the center position of the object being studied can be discussed by using the maximum real value of the wavelet coefficients.

Although the dilation corresponding to the maximum value of the wavelet coefficient at the center of the object is not required for determining the recording distance, the position of this wavelet coefficient as a function of both the dilation and the translation is needed for analyzing mathematically the allowable separation distance  $d_x$ . In order to obtain the dilation value at this maximum wavelet coefficient, the WT of the hologram around its center position is mathematically investigated. However, since the modulation effect of envelope function at this center position is not significant, the envelope function can be neglected. The first column of Fig. 6.8 shows the original hologram of a line object  $s(x)$  and its approximation  $u_1(x)$ . The mathematical expression of the simplified holograms of line and spherical objects can be mathematically written as

$$u_1(x) = 1 - A \cos(Bx^2 - C), \quad (6.17)$$

where  $A = 4a/\sqrt{\lambda z}$ ,  $B = \pi/\lambda z$  and  $C = \pi/4$  for the line object while  $A = 2\pi a^2/\lambda z$ ,  $B = \pi/\lambda z$  and  $C = \pi/2$  are for the spherical object. The second column of Fig. 6.8

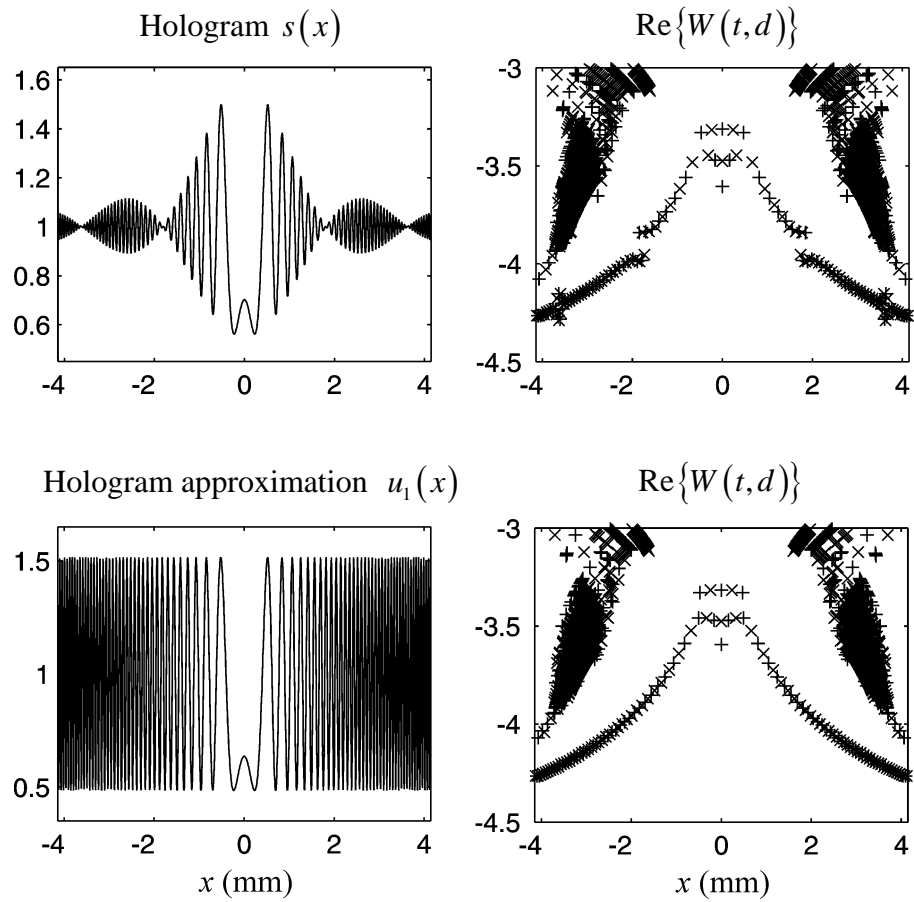


**Figure 6.8** Hologram of a line object and the chirp function (left column) versus their WT (right column).

are their resultant WTs. It is obvious that the center position and the wavelet coefficient at this center obtained from the hologram approximation appear at the same positions as those of the original hologram. This is because, around the center position the amplitude and the frequency content of the signal of both holograms are the same. Therefore the approximation of the hologram can be justified. By using the Morlet wavelet, the WT of the Eq. (6.17) can be mathematically written as

$$W(t, d) = \sqrt{2\pi d} \exp(-2\pi^2 f_g^2)$$

$$\begin{aligned}
& -A(1+4B^2d^4)^{-\frac{1}{4}}\sqrt{\frac{\pi d}{2}}\exp\left[\frac{4\pi f_g t B d - 2\pi^2 f_g^2 - 2B^2 t^2 d^2}{1+4B^2d^4}\right] \\
& + j\left\{\frac{Bt^2 + 8\pi f_g t B^2 d^3 - 4\pi^2 f_g^2 B d^2}{1+4B^2d^4} + \frac{\tan^{-1}(2Bd^2)}{2} - C\right\} \\
& -A(1+4B^2d^4)^{-\frac{1}{4}}\sqrt{\frac{\pi d}{2}}\exp\left[\frac{-4\pi f_g t B d - 2\pi^2 f_g^2 - 2B^2 t^2 d^2}{1+4B^2d^4}\right] \\
& - j\left\{\frac{Bt^2 - 8\pi f_g t B^2 d^3 - 4\pi^2 f_g^2 B d^2}{1+4B^2d^4} + \frac{\tan^{-1}(2Bd^2)}{2} - C\right\} \quad (6.18)
\end{aligned}$$

In order to obtain the maximum value of the wavelet coefficient at the center position of the interference pattern, Eq. (6.18) is evaluated at the translation  $t = 0$ . This yields

$$\begin{aligned}
W(0, d) &= \sqrt{2\pi d} \exp(-2\pi^2 f_g^2) \\
& -A(1+4B^2d^4)^{-\frac{1}{4}}\sqrt{\frac{\pi d}{2}}\exp\left[\frac{-2\pi^2 f_g^2}{1+4B^2d^4}\right] \\
& + j\left\{\frac{-4\pi^2 f_g^2 B d^2}{1+4B^2d^4} + \frac{\tan^{-1}(2Bd^2)}{2} - C\right\} \\
& -A(1+4B^2d^4)^{-\frac{1}{4}}\sqrt{\frac{\pi d}{2}}\exp\left[\frac{-2\pi^2 f_g^2}{1+4B^2d^4}\right] \\
& - j\left\{\frac{-4\pi^2 f_g^2 B d^2}{1+4B^2d^4} + \frac{\tan^{-1}(2Bd^2)}{2} - C\right\} \\
& = \sqrt{2\pi d} \exp(-2\pi^2 f_g^2) - \frac{A\sqrt{2\pi d}}{(1+4B^2d^4)^{\frac{1}{4}}}\exp\left(\frac{-2\pi^2 f_g^2}{1+4B^2d^4}\right) \\
& \quad \times \cos\left\{\frac{4\pi^2 f_g^2 B d^2}{1+4B^2d^4} - \frac{\tan^{-1}(2Bd^2)}{2} + C\right\}. \quad (6.19)
\end{aligned}$$

Plot of Eq. (6.19) for the line object with the parameters  $a = 60 \mu\text{m}$ ,  $z = 40 \text{ cm}$  and  $\lambda = 543.5 \text{ nm}$  is shown in Fig. 6.9. From this figure, the maximum value of the wavelet

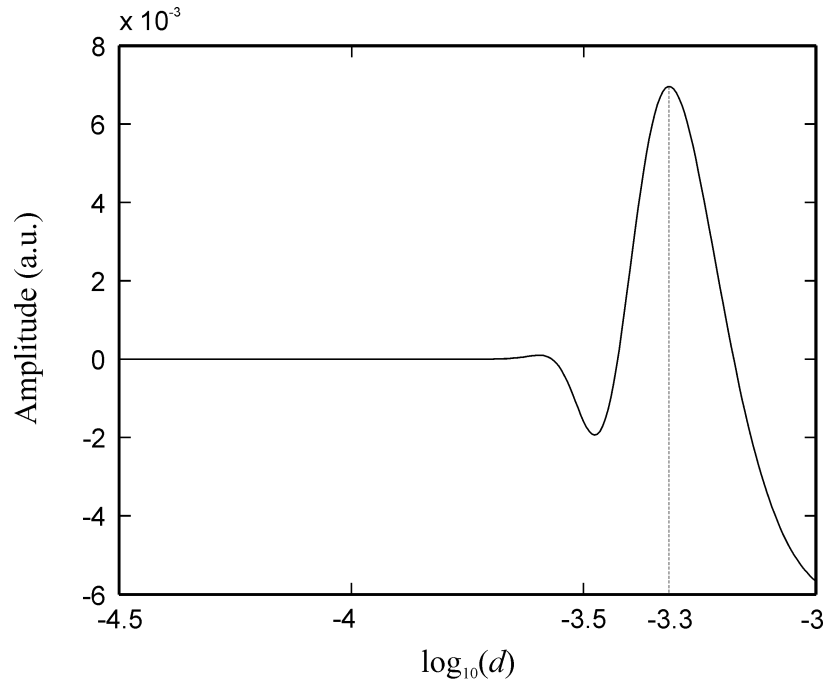


**Figure 6.9** The wavelet coefficients at the translation  $t = 0$  is plotted by using the Eq. (6.19).

coefficient which appears at  $\log_{10}(d_0) = -3.3$  can be clearly observed.

In order to determine mathematically the dilation that gives this maximum value, the derivative of the Eq. (6.19) with respect to the dilation is performed. The value of the dilation  $d_0$  that gives the first derivative equals to zero corresponds to either the minimum or the maximum value of the wavelet coefficient  $W(0,d)$ . It is found that the dilation  $d_0$  is approximately equal to  $1.05\sqrt{\lambda z}$  and  $1.22\sqrt{\lambda z}$  for the line and the spherical objects, respectively. The mathematical proof of this result is given in Appendix. It can be seen that the mathematical expression of dilation  $d_0$  is in the form of  $c\sqrt{\lambda z}$  where  $c$  is a constant factor. Since the derived  $d_0$  is obtained from the hologram approximation  $u_1(x)$ , some mathematical approximations are done during the derivation, the resultant constant  $c$  obtained in the derivation may contain

an error. In order to minimize this error, the value of  $c$  is verified by computing the WT of the holograms  $s(x)$  simulated at various recording distances. By detecting the dilation  $d_0$  from the maximum value of the wavelet coefficients along the translation  $t = 0$ , the constant  $c$  can be calculated from  $c = d_0 / \sqrt{\lambda z}$ . From these computations, the maximum positions  $d_0$  are found to be

$$d_0 = 1.0439\sqrt{\lambda z} \quad (6.20a)$$

and

$$d_0 = 1.1902\sqrt{\lambda z}, \quad (6.20b)$$

for the line object and the spherical object, respectively.

In the case of multiple objects, this maximum value may be disturbed when the WT of the hologram of the other objects overlaps with the hologram of the object being studied along the dilation  $d_0$ . Thus it is necessary to know the range of significant wavelet coefficient of the other object at any given dilation  $d_0$ .

In order to obtain the range of significant wavelet coefficient at any given dilation, the analytical WT of the hologram must be investigated. However, since the desired dilation  $d_0$  corresponds to the low-frequency content of the interference pattern at the center position, the study of the WT of the signal having the same low frequency component as those from the hologram can provide the required information. The effect of high frequency information of the signal along the dilation  $d_0$  can be neglected. Thus, for the sake of simplicity, the hologram is approximately expressed as

$$u_2(x) = 1 - A \cos(Bx^2 - C) \cos(Dx), \quad (6.21)$$

where the cosine function is used as the envelope function, instead of the sinc and the Bessel functions. Here,  $A$ ,  $B$  and  $C$  are the same parameters used in the derivation of Eq. (6.17). The parameter  $D$  is chosen such that the first minimum position  $x = \pi/2D$  of the simplified hologram coincides with that of the original hologram. The first minimum of the hologram of a line object appears at  $x = \lambda z/2a$ , while that of the spherical object is at  $r = 3.83\lambda z/2\pi a$ . By substituting this  $x$  into the first

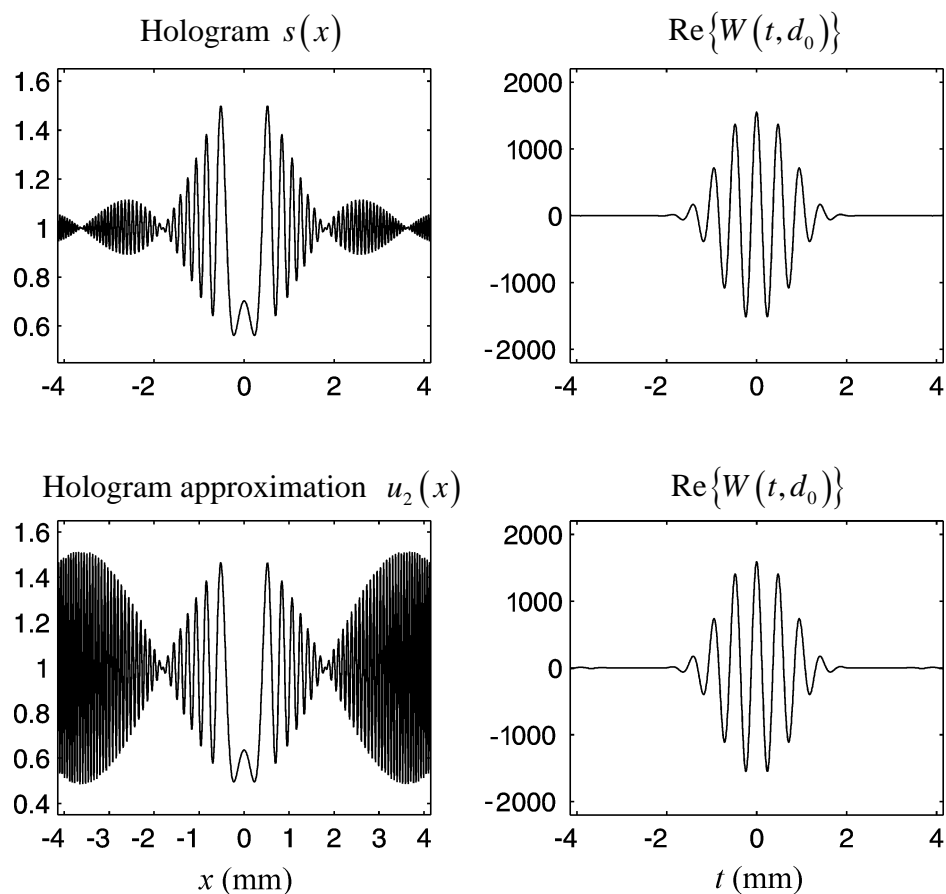


**Figure 6.10** Hologram of a line object and the modulating signal of Eq. (6.21) (left column) and their real value of the WT scanned along the dilation  $d = d_0$  (right column).

minimum position, the parameter  $D$  for the line and the spherical objects are found to be  $D = \pi a / \lambda z$  and  $D = \pi^2 a / 3.83 \lambda z$ , respectively. The top row of Fig. 6.10 shows the original hologram generated by using Eq. (2.3) and the real value of its resultant WT which is scanned along the dilation  $d = d_0$ , while those obtained from Eq. (6.21) are depicted in the bottom row. It can be seen from the left column of this figure that both signals confined by the main lobes are similar. The real value of the wavelet coefficients at  $d = d_0$  shown in the right column of Fig. 6.10 for both signals are also identical. This is because the wavelet coefficients at dilation  $d = d_0$  represent the low-frequency component of the analyzed signal. Since the low-frequency information of the signal given by Eq. (6.21) is the same as those of the Eqs. (2.3) and (2.4), the hologram approximation of Eq. (6.21) can be employed for studying the width of the wavelet coefficient at dilation  $d = d_0$ .

Analysis of Eq. (6.21) by using the Morlet wavelet along the dilation  $d_0$  gives

$$\begin{aligned}
W(t, d_0) = & -\frac{A \exp(-jC)}{4} \sqrt{\frac{2\pi d_0}{1-i2Bd_0^2}} \exp \left[ \frac{1}{1+4B^2d_0^4} \left\{ -\left[ \sqrt{2}Bd_0t - \left( \sqrt{2}\pi f_g - \frac{Dd_0}{\sqrt{2}} \right) \right]^2 \right. \right. \\
& \left. \left. + j \left( Bt^2 + Dt + 8\pi f_g B^2 d_0^3 t - 4\pi^2 f_g^2 B d_0^2 - BD^2 d_0^4 + 4\pi f_g B D d_0^3 \right) \right\} \right] \\
& -\frac{A \exp(jC)}{4} \sqrt{\frac{2\pi d_0}{1+i2Bd_0^2}} \exp \left[ \frac{1}{1+4B^2d_0^4} \left\{ -\left[ \sqrt{2}Bd_0t + \left( \sqrt{2}\pi f_g - \frac{Dd_0}{\sqrt{2}} \right) \right]^2 \right. \right. \\
& \left. \left. + j \left( -Bt^2 + Dt + 8\pi f_g B^2 d_0^3 t + 4\pi^2 f_g^2 B d_0^2 + BD^2 d_0^4 - 4\pi f_g B D d_0^3 \right) \right\} \right] \\
& -\frac{A \exp(-jC)}{4} \sqrt{\frac{2\pi d_0}{1-i2Bd_0^2}} \exp \left[ \frac{1}{1+4B^2d_0^4} \left\{ -\left[ \sqrt{2}Bd_0t - \left( \sqrt{2}\pi f_g + \frac{Dd_0}{\sqrt{2}} \right) \right]^2 \right. \right. \\
& \left. \left. + j \left( Bt^2 - Dt + 8\pi f_g B^2 d_0^3 t - 4\pi^2 f_g^2 B d_0^2 - BD^2 d_0^4 - 4\pi f_g B D d_0^3 \right) \right\} \right] \\
& -\frac{A \exp(jC)}{4} \sqrt{\frac{2\pi d_0}{1+i2Bd_0^2}} \exp \left[ \frac{1}{1+4B^2d_0^4} \left\{ -\left[ \sqrt{2}Bd_0t + \left( \sqrt{2}\pi f_g + \frac{Dd_0}{\sqrt{2}} \right) \right]^2 \right. \right.
\end{aligned}$$

$$+ j(-Bt^2 - Dt + 8\pi f_g B^2 d_0^3 t + 4\pi^2 f_g^2 B d_0^2 + B D^2 d_0^4 + 4\pi f_g B D d_0^3) \} \Big]. \quad (6.22)$$

Equation (6.22) is a summation of four terms. Each term is a multiplication between a Gaussian and a complex exponential function. The slowly varying Gaussian function acts as an envelope function, while the complex exponential with high-frequency components represents a carrier signal. Since the width of the resultant WT is determined by the width of the summation of these envelope functions, the multiplicative complex exponential functions can be neglected in the following analysis.

The first and the second Gaussian functions of the Eq. (6.22) are centered at  $\pi f_g / B d_0 - D/2B$  and  $-\pi f_g / B d_0 + D/2B$ , while those of the third and the fourth terms are at  $\pi f_g / B d_0 + D/2B$  and  $-\pi f_g / B d_0 - D/2B$ , respectively. Figure 6.11 shows these four Gaussian functions and their summation result which are represented by the dot and the dash lines, respectively. The solid line represents the plot of the real value of Eq. (6.22). In comparison with Fig. 6.10, the amplitude of this wavelet output is smaller, because it is computed from the analytical derivation of the wavelet transformation, instead of the numerical calculation. Moreover, it can be seen from Fig. 6.11 that the summation of these four Gaussian functions corresponds to the envelope function of the WT output at  $d = d_0$ . Equation (6.22) shows that the separation between the center positions of the second and the fourth Gaussian functions and between the first and the third Gaussians are equal to  $D/B$ . By substituting the mathematical definitions of the parameters  $D$  and  $B$ , the separation between the Gaussians are equal to  $a$  and  $\pi a/3.83$  for the line and the spherical objects, respectively. However, the value of the object radius  $a$  is very small. Thus,

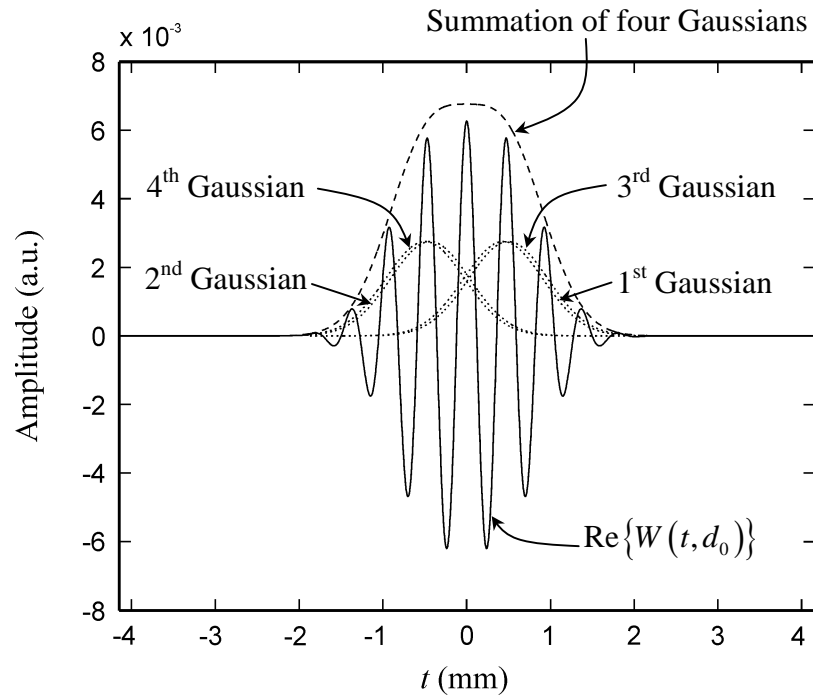


**Figure 6.11** Plot of the real value of the WT along the dilation  $d = d_0$  together with the four Gaussian functions of Eq. (6.22) and their summation result.

the center position of the first and the third Gaussian functions are approximately the same. This approximation is also valid for second and the fourth Gaussians. By taking this approximation into consideration and neglecting the constant complex phase factor, the envelope function defined as  $E(t)$  reduces to the summation of two Gaussian functions

$$\begin{aligned}
 E(t) \propto & 2 \exp \left[ \frac{1}{1+4B^2d_0^4} \left\{ - \left[ \sqrt{2}Bd_0t - \left( \sqrt{2}\pi f_g + \frac{Dd_0}{\sqrt{2}} \right) \right]^2 \right\} \right] \\
 & + 2 \exp \left[ \frac{1}{1+4B^2d_0^4} \left\{ - \left[ \sqrt{2}Bd_0t + \left( \sqrt{2}\pi f_g + \frac{Dd_0}{\sqrt{2}} \right) \right]^2 \right\} \right]. \quad (6.23)
 \end{aligned}$$

In order to determine the width occupied by the envelope function  $E(t)$ , the width of a Gaussian function

$$f(t) = \exp\left\{-\frac{(\alpha t - \beta)^2}{\gamma}\right\}, \quad (6.24)$$

shown in Fig. 6.12 is determined. When its amplitude is equal to  $1/w$ , Eq. (6.24) becomes

$$\frac{1}{w} = \exp\left\{-\frac{(\alpha t - \beta)^2}{\gamma}\right\}. \quad (6.25)$$

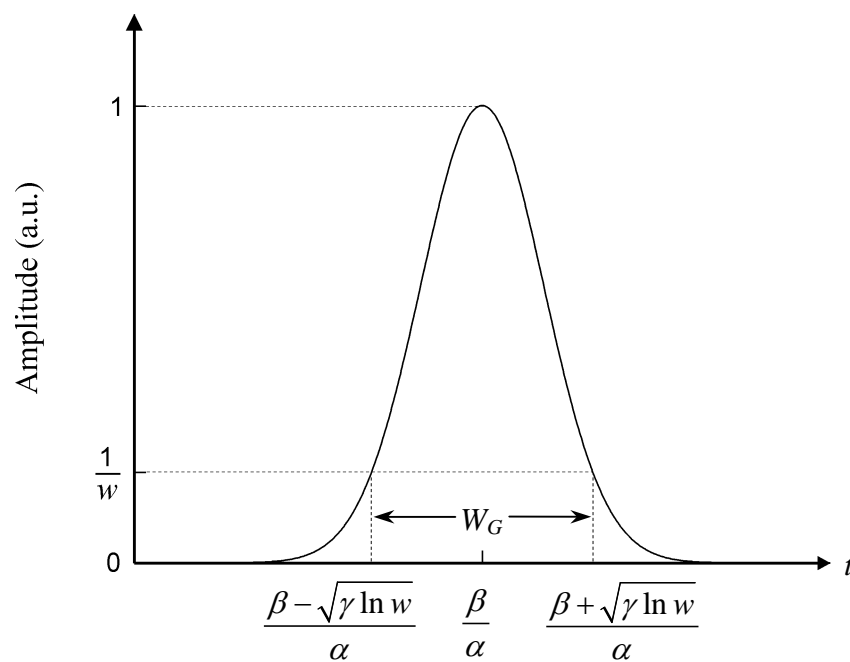


**Figure 6.12** The Gaussian function and its width  $W_G$  which is determined by the parameter  $w$ .

This amplitude appears at the translation

$$t = \frac{\beta \pm \sqrt{\gamma \ln w}}{\alpha}. \quad (6.26)$$

As a result, the width  $W_G$  of the Gaussian function measured from the position where its amplitude is equal to  $1/w$  can be expressed as

$$W_G = \frac{2\sqrt{\gamma \ln w}}{\alpha}. \quad (6.27)$$

As  $w$  increases, the width  $W_G$  of the Gaussian becomes wider.

By taking Eq. (6.27) into account, the width of the Gaussian functions  $E_1(t)$  and  $E_2(t)$  which correspond to the first and the second terms of Eq. (6.23) can be mathematically determined as

$$W_G = \frac{2\sqrt{(1+4B^2d_0^4)\ln(w)}}{\sqrt{2B}d_0}. \quad (6.28)$$

Figure 6.13 plots the envelope Gaussian functions  $E(t)$  of two line objects  $P_1$  and  $P_2$  from Eq. (6.23) by using the solid and the broken lines, respectively. Here, the amplitude of each Gaussian function is normalized by the factor 2 in order to obtain the maximum amplitude of 1. The separation between the objects is  $d_x$ . The value of  $t_1$  corresponds to the center of the Gaussian function in the second term of Eq. (6.23) is

$$t_1 = \frac{\pi f_g}{Bd_0} + \frac{D}{2B}, \quad (6.29)$$

while  $t_2$  can be determined from the half width of that Gaussian function

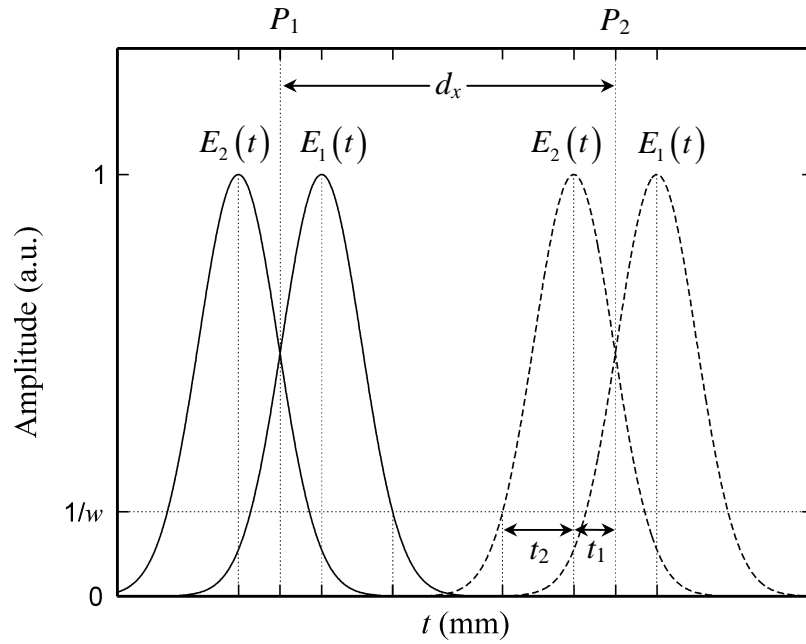


**Figure 6.13** Gaussians function determined the envelope function of the real value of the WT of the hologram of two line objects separated by  $d_x$ .

$$t_2 = \frac{\sqrt{(1 + 4B^2d_0^4) \ln(w)}}{\sqrt{2}Bd_0}, \quad (6.30)$$

where the parameters  $B$  and  $D$  are defined for the object  $P_2$ . In order to extract accurately the center position of the object  $P_1$ , the envelope Gaussian function from the other object  $P_2$  must not disturb this position. This condition can be mathematically expressed as

$$d_x > t_1 + t_2. \quad (6.31)$$

Substitutions of Eqs. (6.29) and (6.30) into Eq. (6.31) and taking the possibility of negative value of  $d_x$  into account gives

$$|d_x| > \frac{\pi f_g}{Bd_0} + \frac{D}{2B} + \frac{\sqrt{(1+4B^2d_0^4)\ln(w)}}{\sqrt{2}Bd_0}. \quad (6.32)$$

Equation (6.32) defines the separation between two objects where the center position of the WT output at the dilation  $d = d_0$  can be extracted in order to obtain the recording distance of the object  $P_1$ . By substituting the mathematical definitions of  $d_0$ ,  $B$  and  $D$  into the Eq. (6.32), the separation  $d_x$  can be rewritten as

$$|d_x| > \frac{f_g z_2}{1.0439} \sqrt{\frac{\lambda}{z_1}} + \frac{a_2}{2} + \frac{\sqrt{\lambda(z_2^2 + 4.75\pi^2 z_1^2)\ln(w)}}{1.0439\pi\sqrt{2}z_1} \quad (6.33)$$

and

$$|d_r| > \frac{f_g z_2}{1.1902} \sqrt{\frac{\lambda}{z_1}} + \frac{a_2}{2.44} + \frac{\sqrt{\lambda(z_2^2 + 8.03\pi^2 z_1^2)\ln(w)}}{1.1902\pi\sqrt{2}z_1}, \quad (6.34)$$

for the line and the spherical objects, respectively. In this derivation, the width of the Gaussian function is measured at the position where its amplitude is equal to  $1/w$ . In order to determine the suitable value for the parameter  $w$ , the center position of the object  $P_1$  is determined from the WT of simulated holograms of two objects.

Figure 6.14 shows the errors of detecting the center position from the holograms of two line objects  $P_1$  and  $P_2$  having the radius  $a_1 = 25 \mu\text{m}$  and  $a_2 = 50 \mu\text{m}$  while their recording distance are  $z_1 = 30 \text{ cm}$  and  $z_2 = 29 \text{ cm}$ , respectively. It is found that this error becomes higher than 1 pixel when  $-1.2 < d_x < 1.2 \text{ mm}$ . In this figure,  $d_{x3} = -1.2 \text{ mm}$  and  $d_{x4} = 1.2 \text{ mm}$  are defined as the critical separations of the objects that cause high error. By substituting these values of the critical separation  $d_x$ , the object size  $a$  and the recording distance  $z$  into the Eq. (6.33), the value of  $w$  can be

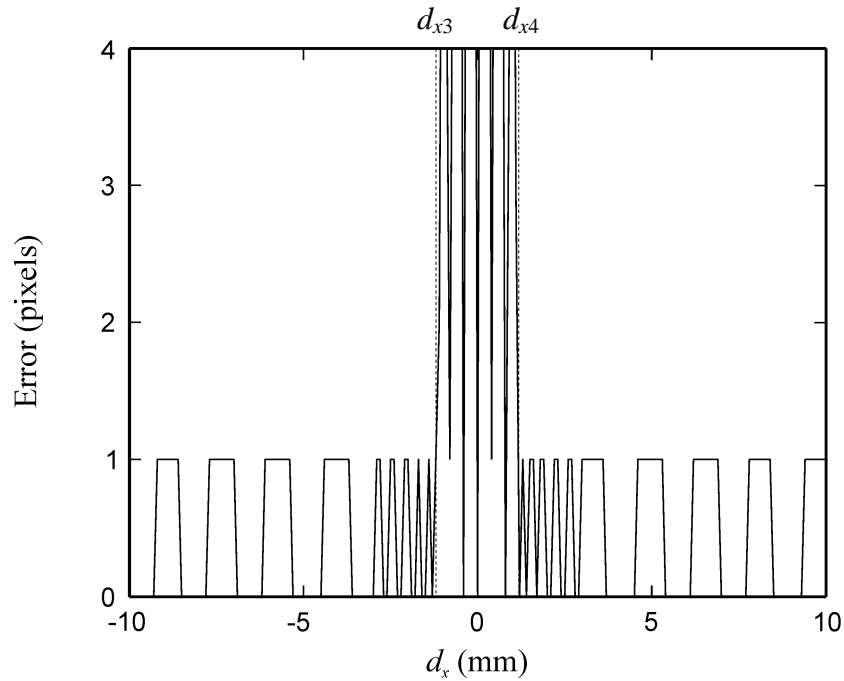


**Figure 6.14** Errors of detecting the center position of the object  $P_1$  from the WT of the holograms of two line objects having  $a_1 = 25 \mu\text{m}$ ,  $z_1 = 30 \text{ cm}$ ,  $a_2 = 50 \mu\text{m}$ ,  $z_2 = 29 \text{ cm}$  as a function of  $d_x$ .

obtained. In this case,  $d_{x3}$  and  $d_{x4}$  yield  $w_3$  and  $w_4$  that are equal to 6.32. Tables 6.3 and 6.4 summarize the results of measuring the center position of the object  $P_1$  in the present of the other object  $P_2$  for the line and the spherical objects, respectively. It can be seen from these results that the maximum desired values of  $w$  are 7.0 and 9.9 for the line and the spherical object, respectively. Thus, in order to ensure the feasibility of the method for measuring the recording distance from the hologram of multiple objects, the object separation must satisfy Eq. (6.33) or (6.34) with the large value of the parameter, i.e.  $w > 7.0$  and  $w > 9.9$ , for the line and the spherical object, respectively.

**Table 6.3** Measurement of the spatial separation  $d_x$  and  $w$  from the WT of the simulated holograms of the line objects.

$a_1$	$z_1$	$a_2$	$z_2$	$d_{x3}$	$d_{x4}$	$w_3$	$w_4$
25	10	25	9	-0.6	0.7	3.43	7.04
25	10	25	10	-0.6	0.7	2.98	5.88
25	10	25	11	-0.7	0.6	4.95	2.61
25	10	50	9	-0.7	0.7	6.38	6.38
25	10	50	10	-0.7	0.7	5.35	5.35
25	10	50	11	-0.7	0.7	4.53	4.53
25	30	25	29	-1.1	1.2	4.05	6.14
25	30	25	30	-1.1	1.2	3.84	5.79
25	30	25	31	-1.1	1.2	3.65	5.47
25	30	50	29	-1.2	1.2	5.81	5.81
25	30	50	30	-1.2	1.2	5.49	5.49
25	30	50	31	-1.2	1.2	5.18	5.18
50	10	25	9	-0.5	0.5	1.97	1.97
50	10	25	10	-0.6	0.6	2.98	2.98
50	10	25	11	-0.6	0.6	2.61	2.61
50	10	50	9	-0.6	0.7	3.17	6.38
50	10	50	10	-0.6	0.6	2.77	2.77
50	10	50	11	-0.7	0.7	4.53	4.53
50	30	25	29	-1	0.9	2.81	2.07
50	30	25	30	-1.1	1.2	3.84	5.79
50	30	25	31	-1.1	1.2	3.65	5.47
50	30	50	29	-1.1	1.2	3.85	5.81
50	30	50	30	-1.1	1.2	3.67	5.49
50	30	50	31	-1.2	1.2	5.18	5.18

**Table 6.4** Measurement of the spatial separation  $d_r$  and  $w$  from the WT of the simulated holograms of the spherical objects.

$a_1$	$z_1$	$a_2$	$z_2$	$d_{r3}$	$d_{r4}$	$w_3$	$w_4$
25	10	25	9	-0.7	0.6	5.16	2.91
25	10	25	10	-0.7	0.6	4.57	2.64
25	10	25	11	-0.6	0.6	2.41	2.41
25	10	50	9	-0.7	0.8	4.84	9.59
25	10	50	10	-0.8	0.8	8.30	8.30
25	10	50	11	-0.8	0.8	7.21	7.21
25	30	25	29	-1.2	1.3	4.68	6.80
25	30	25	30	-1.2	1.3	4.49	6.50
25	30	25	31	-1.2	1.3	4.32	6.22
25	30	50	29	-1.4	1.4	9.86	9.86
25	30	50	30	-1.3	1.4	6.25	9.39
25	30	50	31	-1.3	1.3	5.98	5.98
50	10	25	9	-0.6	0.6	2.91	2.91
50	10	25	10	-0.6	0.6	2.64	2.64
50	10	25	11	-0.6	0.6	2.41	2.41
50	10	50	9	-0.7	0.6	4.84	2.77
50	10	50	10	-0.6	0.6	2.51	2.51
50	10	50	11	-0.6	0.6	2.30	2.30
50	30	25	29	-0.9	0.9	1.94	1.94
50	30	25	30	-1	1	2.42	2.42
50	30	25	31	-1	1	2.35	2.35
50	30	50	29	-1.2	1.3	4.51	6.53
50	30	50	30	-1.2	1.3	4.33	6.25
50	30	50	31	-1.2	1.3	4.17	5.98

In order to extract both information of size and recording distance from the hologram of multiple objects, the object separation  $d_x$  must satisfy all three conditions defined by Eqs. (6.15a), (6.15b) and (6.33) or Eqs. (6.16a), (6.16b) and (6.34) for the line and the spherical objects, respectively. Figure 6.15 shows the plots of Eqs. (6.15a), (6.15b) and (6.32) represented by the solid, the dot and the dash lines, respectively, for  $a_1 = 50 \mu\text{m}$ ,  $z_1 = 10 \text{ cm}$  and  $a_2 = 25 \mu\text{m}$  as a function of  $z_2$ . The figure is plotted with the value of the parameter  $p = 0.8$  and  $w = 7$ . For positive value of  $d_x$ , which mean that  $P_2$  is located on the right side of  $P_1$ , the WT can be used to extract the size and the position of the object  $P_1$  provided  $d_x$  satisfy the condition defined by Eq. (6.15a). In this case, the value of  $d_x$  and  $z_2$  must be inside the shaded area above the solid line. In the case of  $d_x$  having negative value, both conditions of Eqs. (6.15b) and (6.32) must be satisfied. This can be achieved if the value of  $d_x$  and  $z_2$  are

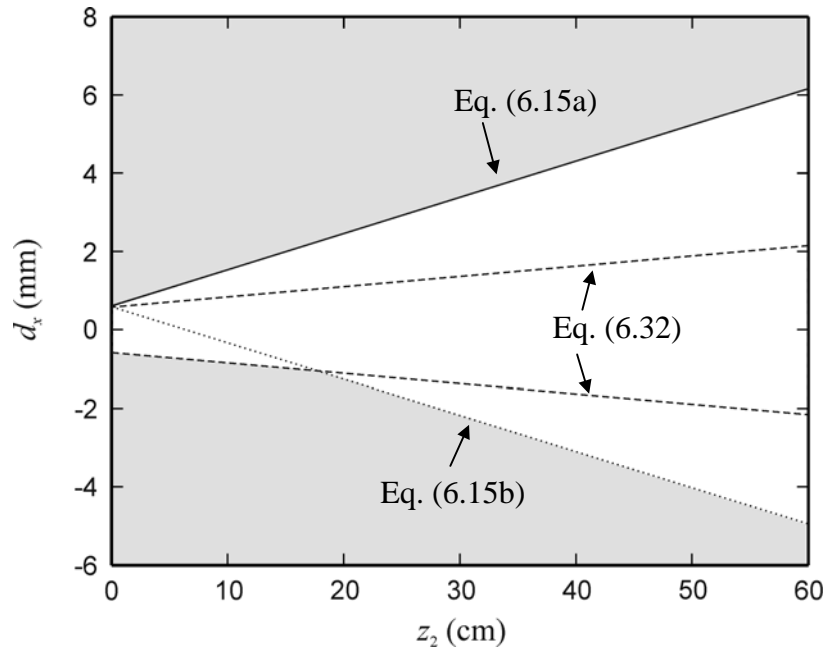


**Figure 6.15** Plot of the Eqs. (6.15a), (6.15b) and (6.32).

confined within the lower shaded area. It can be seen that the required separation  $|d_x|$  is larger for positive value of  $d_x$  than that of the negative one. This is because the information about the object size is extracted from the frequency of the chirp signal at the first minimum position which is located on the right side of the axis of symmetry of the hologram ( $n = 1$ ). If the first minimum in the left side is used ( $n = -1$ ), the graph will be flipped along the axis  $d_x = 0$ . This gives shorter allowable  $|d_x|$  for the positive  $d_x$  in comparison with the negative one. However, for the same value of  $z_2$ , the condition given by Eqs. (6.15b) and (6.33) give a shorter allowable separation  $|d_x|$  than that of the Eq. (6.15a). Since in real situation the sign of  $d_x$  cannot be controlled, the condition of the Eq. (6.15a) is used for both positive and negative values of  $d_x$ . By taking this consideration into account, Eq. (6.15a) can be rewritten as

$$|d_x| > \frac{n\lambda}{2a_1} [z_2(1+p) + z_1]. \quad (6.35)$$

As  $d_x$  satisfy Eq. (6.35), all of the conditions in the Eqs. (6.15a), (6.15b) and (6.33) are also satisfied. In analogy, the condition for the separation of the spherical object is

$$|d_r| > \frac{(n+0.23)\lambda}{2a_1} [z_2(1+p) + z_1]. \quad (6.36)$$

It can be seen that the separation is proportional to a combination of the recording distance and is inverse proportional to the object size. The hologram of a larger object recorded at a shorter recording distance gives the shorter allowable separation. As for a fixed size of the objects, the hologram must be recorded at a shorter distance in order to be able to analyze the higher concentration of the objects. However, higher resolution of the recording material is required for recording such a hologram.

## **CHAPTER VII**

### **CONCLUSIONS**

In this dissertation, new methods for extracting size and recording distance of small objects directly from the in-line Fraunhofer holograms by using the WT are studied. The proposed method obviates the conventional optical image reconstruction which is very tedious and time consuming process. The recording distance of the object being studied is obtained from the space-varying frequency of the holograms provided by the WT, while the size is extracted by either reconstructing the envelope function or taking the absolute values of the resultant WT output. The feasibility of the methods is verified by determining error of measurements from the digitally and experimentally generated holograms of the line and the spherical objects. The system performance of the proposed method for the case of holograms of the single and the multiple objects are analyzed.

In Chapter III, the algorithm for simulating and the optical setup for generating the holograms of the line and the spherical objects are discussed. In the simulation, the holograms are digitally generated by computing the Fraunhofer diffraction integral via the Matlab software. In the experiments, the holograms of the line object are generated by using the optical fiber as a test object with the CCD sensor is used to capture the generated interference pattern. As for the spherical object, because its available size is too small the generated interference pattern contains high frequency signal which cannot be faithfully captured by the CCD

sensor. In order to solve this problem, the holograms of the circular pinhole having a larger diameter are generated by employing the Mach-Zehnder interferometer. In the final discussion, the mathematical expressions of the holograms of the multiple line and spherical objects are presented.

The extraction of the recording distance from the holograms by using the WT is discussed in Chapter IV. Since the WT gives the spatial-varying frequency information of the analyzed signal, it is employed to extract the recording distance which is encoded into the frequency of the chirp signal. By determining the maximum and minimum positions of the wavelet output, the recording distance can be calculated. The simulation results show that the method can be accurately extract the recording distance information with small errors of less than 1 percent for both line and spherical objects. As for the experimental results, the errors are slightly higher, because the speckle noise cannot be completely removed from the holograms.

In Chapter V, two methods for extracting the object size from the digitized holograms are discussed. Since the object size is encoded into the minima positions of the interference pattern, the first method determines these positions in space domain by reconstructing the envelope function. By determining the minima positions and the recording distance obtained from the WT, the object size can be calculated. The simulation results show that the errors in measurement of the object size is smaller than 1 percent for the line object, while it is slightly higher for the spherical object. This may be caused by the fact that the envelope signal of the spherical object which is the Bessel function has minima with slower varying amplitude than the sinc function of the line object. As a consequence, the accuracy in detecting the minima of

the Bessel function is smaller than that of the sinc function. Furthermore, the experimental results give the slightly higher errors than the simulation.

The second proposed method determines the minima of the envelope function in the wavelet domain by computing absolute values of the WT. Beside the positions of minima, this method provides the frequency of the chirp signal at those minima positions. The object size which is solely a function of this frequency can then be determined. In this method, the accuracy of determining the object size depends on the accuracy of detecting the frequency at the minima positions. By increasing the resolution of the dilation interval in the WT computation, the frequency information at the minima can be obtained with high accuracy. The simulation and experimental results show the improvement of the accuracy in measuring the object size from the absolute values of the WT over the envelope reconstruction method.

In Chapter VI, the system performance for analyzing the holograms of single and multiple objects are discussed. Since the CCD sensor is employed for capturing the interference pattern, its finite size and finite resolution limit the amount of information that can be captured. By taking these limitations into account, the relationship between the object size, the recording distance, the wavelength of the illuminating light and the resolution and size of the CCD can be obtained. It is found that the largest size of the object is proportional to the CCD size and inverse proportional to the minimum position used for the calculation, while the smallest size is proportional to the multiplication between the minimum position and the pixel size of the employed CCD sensor. Thus, it can be concluded that the radius of the object cannot be smaller than the pixel size of the employed CCD sensor. As for the recording distance, the longest value is proportional to the square of CCD size and is

inverse proportional to the product of the square of the minimum position and the wavelength of the illuminating light, while the smallest value is proportional to the multiplication between a square of pixel size and a square of the minimum position and is inverse proportional to the wavelength. Since the Bessel function has wider main lobe than that of the sinc function, the shortest recording distance and smallest size of spherical object is larger than that of the line object, while its largest size and longest recording distance are smaller.

In the case of multiple objects, the hologram can be approximated by the summation of the interference pattern from the individual object. As a result, the resultant WT of the hologram is proportional to a linear summation of the WT from the individual interference pattern. Since the measurements of the size and the recording distance are done by computing the WT of the hologram, the feasibility of the method depends on a degree of distortion of the resultant WT. In order to extract the object size from the frequency at minimum position of the interference pattern, a certain frequency difference from the object being studied along its minimum position and that from the other objects is required. This criterion is employed for the mathematical derivation of the required separation between the objects. As for the recording distance, the accuracy in measurement is mainly determined by the accuracy of detecting the center position of the interference pattern. This study found that the WT coefficient at this center position is always maximum. In order to utilize this maximum position, its WT coefficient must not be disturbed by the WT of the other interference patterns. By taking this consideration into account, the required separation between the object is mathematically derived. The obtained separation is then confirmed by comparing with the allowable separations of the objects obtained

from the simulation. The comparison shows that the derived separations are in a good agreement with those of the simulations. It is found that the extraction of the object size requires a larger separation than that of the recording distance. Thus, in order to extract both the size and the recording distance from the holograms of multiple objects, the separation between the objects must satisfy the most severe conditions of the separation which are found to be proportional to a linear combination of the recording distances and are inverse proportional to the object size. Therefore, either the shorter the recording distance or the bigger the object size, the higher the concentration of objects that can be analyzed.

## **REFERENCES**

## REFERENCES

- Belaid, S., Lebrun, D. and Özkul, C. (1997). Application of two-dimensional wavelet transform to hologram analysis: visualization of glass fibers in a turbulent flame. **Optical Engineering**. 36(7): 1947-1951.
- Buraga-Lefebvre, B.C., Coëtmellec, S., Lebrun, D. and Özkul, C. (2000). Application of wavelet transform to hologram analysis: three-dimensional location of particles. **Optics and Lasers Engineering**. 33: 409-421.
- Goodman, J.W. (1996). **Introduction to Fourier optics** (2<sup>nd</sup> ed.). New York: McGraw-Hill.
- Gradshteyn, I.S., and Ryzhik, I.M. (1994). In A. Jeffrey (ed.). **Table of Integrals series and products** (5<sup>th</sup> ed., pp. 355). Translated by Scripta Technica. USA: Academic Press.
- Kronland-Martinet, R., Morlet, J. and Grossmann, A. (1987). Analysis of sound patterns through wavelet transforms. **International Journal of Pattern Recognition and Artificial Intelligence**. 1(2): 273-302.
- Lai, T. and Lin, W. (1996). Effective implementation of subtraction holography for noise suppression in particle fields. **Applied Optics**. 35(22): 4334-4336.
- Misiti, M., Misiti, Y., Oppenheim, G. and Poggi, J.M. (2001). Wavelet toolbox for use with Matlab (version 2.1) [Computer user's guide]. The MathWorks, Inc.
- Murakami, T. (1987). A New Direct Analysis Method for Measuring Particle Size and Location by Inline Hologram. in **Laser Diagnostics and Modeling of Combustion**. 71-76.

Oppenheim, A.V. and Schaffer, R. W. (1989). **Discrete-Time Signal Processing**. New Jersey: Prentice-Hall.

Thompson, B. J. (1974). Holographic particle sizing technique. **Journal of Physics E: Scientific Instruments**. 7: 781-788.

Tyler, G. A. and Thompson, B. J. (1976). Fraunhofer holography applied to particle size analysis: a reassessment. **Optica Acta**. 23(9): 685-700.

Widjaja, J. (1998). Automatic holographic particle sizing using wavelet-based joint transform correlator. **Optik**. 107(3): 132-134.

## **APPENDIX**

# APPENDIX

## MATHEMATICAL DERIVATION

### A1. In-line Fraunhofer holograms of single object

The amplitude transmittance of the in-line hologram is proportional to the intensity incident at the recording plane  $(x, y)$ . This intensity can be mathematically written as

$$\begin{aligned} I(x, y) &= |U(x, y)|^2 \\ &= |R + o(x, y)|^2, \end{aligned} \quad (\text{A1.1})$$

where  $U(x, y)$  is the complex amplitude of the light field incident at the recording plane. Here,  $R$  represents the directly transmitted reference plane wave, while  $o(x, y)$  is the wave diffracted from the object.

#### A1.1 Hologram of opaque line object

Let us consider a 1-D opaque object with the amplitude distribution  $A(\xi)$  located in the object plane of the optical setup shown in the Fig. 2.1. The light field at the recording plane can be derived from the Fresnel diffraction integral (Goodman, 1996)

$$U(x, y) = \frac{\exp[jkz/2]}{\sqrt{j\lambda z}} \int_{-\infty}^{\infty} [1 - A(\xi)] \exp\left\{\frac{jk}{2z}(x - \xi)^2\right\} d\xi, \quad (\text{A1.2})$$

where  $k$ ,  $z$  and  $\lambda$  are the wave number defined by  $k = 2\pi/\lambda$ , the recording distance of

the object and the wavelength of the illuminating light, respectively. By separating the integrals, Eq. (A1.2) can be rewritten as

$$U(x, y) = \frac{\exp[jkz/2]}{\sqrt{j\lambda z}} \left\{ \int_{-\infty}^{\infty} \exp\left\{\frac{jk}{2z}(x-\xi)^2\right\} d\xi - \int_{-\infty}^{\infty} A(\xi) \exp\left\{\frac{jk}{2z}(x-\xi)^2\right\} d\xi \right\}. \quad (\text{A1.3})$$

The first integral of Eq. (A1.3) is

$$\int_{-\infty}^{\infty} \exp\left\{\frac{jk}{2z}(x-\xi)^2\right\} d\xi = \exp\left(\frac{jkx^2}{2z}\right) \int_{-\infty}^{\infty} \exp\left\{\frac{jk\xi^2}{2z} - \frac{jkx\xi}{z}\right\} d\xi. \quad (\text{A1.4})$$

By using the identity (Gradshteyn and Ryzhik, 1994)

$$\int_{-\infty}^{\infty} \exp(-p^2x^2 \pm qx) dx = \frac{\sqrt{\pi}}{|p|} \exp\left(\frac{q^2}{4p^2}\right), \quad (\text{A1.5})$$

the integral on the right side of Eq. (A1.4) becomes

$$\begin{aligned} \int_{-\infty}^{\infty} \exp\left\{\frac{jk\xi^2}{2z} - \frac{jkx\xi}{z}\right\} d\xi &= \frac{\sqrt{\pi}}{\sqrt{-jk/2z}} \exp\left\{\left(\frac{jkx}{z}\right)^2 / 4 \left(\sqrt{\frac{-jk}{2z}}\right)^2\right\} \\ &= \sqrt{j\lambda z} \exp\left(\frac{-jkx^2}{2z}\right) \end{aligned}$$

$$\therefore \int_{-\infty}^{\infty} \exp\left\{\frac{jk}{2z}(x-\xi)^2\right\} d\xi = \sqrt{j\lambda z}. \quad (\text{A1.6})$$

The second integral of the Eq. (A1.3) is

$$\int_{-\infty}^{\infty} A(\xi) \exp\left\{\frac{jk}{2z}(x-\xi)^2\right\} d\xi$$

$$= \exp\left(\frac{jkx^2}{2z}\right) \int_{-\infty}^{\infty} A(\xi) \exp\left(\frac{jk\xi^2}{2z}\right) \exp\left(-\frac{j2\pi x\xi}{\lambda z}\right) d\xi$$

Under the far-field (Fraunhofer) condition (Goodman, 1996)

$$z \gg \frac{k\xi_{\max}^2}{2}, \quad (\text{A1.7})$$

the quadratic phase exponential term  $\exp(jk\xi^2/\lambda z)$  can be neglected. This yields,

$$\int_{-\infty}^{\infty} A(\xi) \exp\left\{\frac{jk}{2z}(x-\xi)^2\right\} d\xi = \exp\left(\frac{jkx^2}{2z}\right) \tilde{A}\left(\frac{x}{\lambda z}\right), \quad (\text{A1.8})$$

where  $\tilde{A}\left(\frac{x}{\lambda z}\right)$  is the 1-D Fourier transform of  $A(\xi)$  defined by

$$\tilde{A}\left(\frac{x}{\lambda z}\right) = \int_{-\infty}^{\infty} A(\xi) \exp\left(-\frac{j2\pi x\xi}{\lambda z}\right) d\xi. \quad (\text{A1.9})$$

Substituting the Eqs. (A1.6) and (A1.8) into Eq. (A1.3) results in

$$U(x, y) = \exp\left(\frac{jkz}{2}\right) \left\{ 1 - \frac{\exp(jkx^2/2z)}{\sqrt{j\lambda z}} \tilde{A}\left(\frac{x}{\lambda z}\right) \right\}$$

Since the intensity is the information being recorded on the recording medium, the constant complex exponential can be neglected. As a result, the complex field at the recording plane becomes

$$U(x, y) = 1 - \frac{\exp(jkx^2/2z)}{\sqrt{j\lambda z}} \tilde{A}\left(\frac{x}{\lambda z}\right). \quad (\text{A1.10})$$

Thus, in the case of a 1-D object, the reference wave  $R$  can be regarded as a plane wave with unity amplitude, while the object wave is

$$o_{1-D}(x, y) = -\frac{1}{\sqrt{\lambda z}} \exp \left[ j \left( \frac{\pi x^2}{\lambda z} - \frac{\pi}{4} \right) \right] \tilde{A} \left( \frac{x}{\lambda z} \right). \quad (\text{A1.11})$$

For a line object whose amplitude distribution function is

$$\begin{aligned} A(\xi) &= 1 \quad \text{for } |\xi| \leq a \\ &= 0 \quad \text{for } |\xi| > a, \end{aligned} \quad (\text{A1.12})$$

its Fourier transform becomes

$$\begin{aligned} \tilde{A} \left( \frac{x}{\lambda z} \right) &= \int_{-\infty}^{\infty} A(\xi) \exp \left( -\frac{i2\pi\xi x}{\lambda z} \right) d\xi \\ &= \int_{-a}^a \exp \left( -\frac{i2\pi\xi x}{\lambda z} \right) d\xi \\ &= -\frac{\lambda z}{i2\pi x} \exp \left( -\frac{i2\pi\xi x}{\lambda z} \right) \Big|_{\xi=-a}^{\xi=a} \\ &= -\frac{\lambda z}{i2\pi x} \left\{ \exp \left( -\frac{i2\pi a x}{\lambda z} \right) - \exp \left( \frac{i2\pi a x}{\lambda z} \right) \right\} \\ &= \frac{\lambda z}{\pi x} \sin \left( \frac{2\pi a x}{\lambda z} \right) \end{aligned}$$

$$\therefore \tilde{A} \left( \frac{x}{\lambda z} \right) = 2a \left[ \frac{\sin \left( \frac{2\pi a x}{\lambda z} \right)}{\frac{2\pi a x}{\lambda z}} \right]. \quad (\text{A1.13})$$

By substituting Eq. (A1.13) into Eq. (A1.11), the diffracted wave from the line object is found to be

$$o_L(x, y) = -\frac{2a}{\sqrt{\lambda z}} \left[ \frac{\sin \left( \frac{2\pi a x}{\lambda z} \right)}{\frac{2\pi a x}{\lambda z}} \right] \exp \left[ j \left( \frac{\pi x^2}{\lambda z} - \frac{\pi}{4} \right) \right] \quad (\text{A1.14})$$

Let us define

$$C_L = -\frac{2a}{\sqrt{\lambda z}}, \quad (\text{A1.15a})$$

$$Q_L = \left[ \frac{\sin\left(\frac{2\pi ax}{\lambda z}\right)}{\frac{2\pi ax}{\lambda z}} \right], \quad (\text{A1.15b})$$

and

$$\Phi_L = \frac{\pi x^2}{\lambda z} - \frac{\pi}{4}, \quad (\text{A1.15c})$$

Eq. (A1.14) can be rewritten as

$$o_L(x, y) = C_L Q_L \exp(j\Phi_L). \quad (\text{A1.16})$$

Thus, the intensity recorded at the hologram plane is

$$\begin{aligned} I(x, y) &= |R + o_L(x, y)|^2 \\ &= |1 + C_L Q_L \exp(j\Phi_L)|^2 \\ &= 1 + 2C_L Q_L \cos \Phi_L + C_L^2 Q_L^2. \end{aligned} \quad (\text{A1.17})$$

Substituting Eqs. (A1.15) into Eq. (A1.17) results in

$$I(x, y) = 1 - \frac{4a}{\sqrt{\lambda z}} \cos\left(\frac{\pi x^2}{\lambda z} - \frac{\pi}{4}\right) \left[ \frac{\sin\left(\frac{2\pi ax}{\lambda z}\right)}{\frac{2\pi ax}{\lambda z}} \right] + \frac{4a^2}{\lambda z} \left[ \frac{\sin\left(\frac{2\pi ax}{\lambda z}\right)}{\frac{2\pi ax}{\lambda z}} \right]^2. \quad (\text{A1.18})$$

### A1.2 Hologram of opaque spherical object

In the case of recording the hologram of an opaque 2-D object by using the in-line optical setup depicted in the Fig. 2.1, the field at the recording plane can be calculated by using the Fresnel diffraction integral as

$$\begin{aligned}
 U(x, y) &= \frac{\exp[jkz]}{j\lambda z} \int_{-\infty}^{\infty} \int_{-\infty}^{\infty} [1 - A(\xi, \eta)] \\
 &\quad \times \exp\left\{\frac{jk}{2z}[(x - \xi)^2 + (y - \eta)^2]\right\} d\xi d\eta \\
 &= \frac{\exp[jkz]}{j\lambda z} \left\{ \int_{-\infty}^{\infty} \int_{-\infty}^{\infty} \exp\left\{\frac{jk}{2z}[(x - \xi)^2 + (y - \eta)^2]\right\} d\xi d\eta \right. \\
 &\quad \left. - \int_{-\infty}^{\infty} \int_{-\infty}^{\infty} A(\xi, \eta) \exp\left\{\frac{jk}{2z}[(x - \xi)^2 + (y - \eta)^2]\right\} d\xi d\eta \right\}. \quad (\text{A1.19})
 \end{aligned}$$

Under the far-field condition, Eq. (A1.19) becomes

$$U(x, y) = \exp(jkz) \left[ 1 + \frac{j \exp(jkr^2/2z)}{\lambda z} \tilde{A}\left(\frac{x}{\lambda z}, \frac{y}{\lambda z}\right) \right], \quad (\text{A1.20})$$

where  $r^2 = x^2 + y^2$ , while  $\tilde{A}\left(\frac{x}{\lambda z}, \frac{y}{\lambda z}\right)$  represents the 2-D Fourier transform of

$A(\xi, \eta)$  defined by

$$\tilde{A}\left(\frac{x}{\lambda z}, \frac{y}{\lambda z}\right) = \int_{-\infty}^{\infty} \int_{-\infty}^{\infty} A(\xi, \eta) \exp\left(-j2\pi \left\{ \left(\frac{x}{\lambda z}\right)\xi + \left(\frac{y}{\lambda z}\right)\eta \right\}\right) d\xi d\eta. \quad (\text{A1.21})$$

By neglecting the constant phase exponential in Eq. (A1.20), the diffracted wave from the opaque 2-D object can be mathematically expressed as

$$o_{2-D}(x, y) = \frac{1}{\lambda z} \exp\left[j\left(\frac{\pi r^2}{\lambda z} + \frac{\pi}{2}\right)\right] \tilde{A}\left(\frac{x}{\lambda z}, \frac{y}{\lambda z}\right). \quad (\text{A1.22})$$

In the case of a spherical object, its amplitude transmittance function is defined by

$$\begin{aligned} A(\xi, \eta) &= 1 \quad \text{for } \sqrt{\xi^2 + \eta^2} \leq a \\ &= 0 \quad \sqrt{\xi^2 + \eta^2} > a. \end{aligned} \quad (\text{A1.23})$$

This can be rewritten in polar coordinate as

$$\begin{aligned} A(\rho) &= 1 \quad \text{for } \rho \leq a \\ &= 0 \quad \rho > a, \end{aligned}$$

where

$$\rho = \sqrt{\xi^2 + \eta^2}.$$

Since the function  $A(\xi, \eta)$  is circularly symmetric, its Fourier transform can be calculated by using the one-dimensional Fourier-Bessel transform (Goodman, 1996)

$$\tilde{A}(r) = 2\pi \int_0^{\infty} \rho A(\rho) J_0(2\pi\rho r) d\rho$$

$$\tilde{A}\left(\frac{r}{\lambda z}\right) = 2\pi \int_0^a \rho J_0\left(\frac{2\pi\rho r}{\lambda z}\right) d\rho.$$

By changing of the variables  $\rho' = \frac{2\pi\rho r}{\lambda z}$ ,

$$\tilde{A}\left(\frac{r}{\lambda z}\right) = \frac{1}{2\pi} \left(\frac{\lambda z}{r}\right)^2 \int_0^{2\pi a r / \lambda z} \rho' J_0(\rho') d\rho'.$$

Using the identity

$$\int_0^x \xi J_0(\xi) d\xi = x J_1(x), \quad (\text{A1.24})$$

the Fourier spectrum of the spherical object is

$$\tilde{A}\left(\frac{r}{\lambda z}\right) = \left(\frac{a\lambda z}{r}\right) J_1\left(\frac{2\pi ar}{\lambda z}\right).$$

$$\therefore \tilde{A}\left(\frac{r}{\lambda z}\right) = \pi a^2 \left[ \frac{2J_1\left(\frac{2\pi ar}{\lambda z}\right)}{\frac{2\pi ar}{\lambda z}} \right]. \quad (\text{A1.25})$$

Substitution of Eq. (A1.25) into Eq. (A1.22) gives the object wave of the spherical object

$$o_s(r) = \frac{\pi a^2}{\lambda z} \left[ \frac{2J_1\left(\frac{2\pi ar}{\lambda z}\right)}{\frac{2\pi ar}{\lambda z}} \right] \exp\left[ j\left(\frac{\pi r^2}{\lambda z} + \frac{\pi}{2}\right) \right]. \quad (\text{A1.26})$$

Define

$$C_s = \frac{\pi a^2}{\lambda z}, \quad (\text{A1.27a})$$

$$Q_s = \left[ \frac{2J_1\left(\frac{2\pi ar}{\lambda z}\right)}{\frac{2\pi ar}{\lambda z}} \right], \quad (\text{A1.27b})$$

and

$$\Phi_s = \frac{\pi r^2}{\lambda z} + \frac{\pi}{2}, \quad (\text{A1.27c})$$

the object wave in Eq. (A1.26) can be rewritten as

$$o_s(r) = C_s Q_s \exp(j\Phi_s). \quad (\text{A1.28})$$

The intensity at the hologram plane can be calculated from

$$\begin{aligned}
I(r) &= |R + o_s(r)|^2 \\
&= |1 + C_s Q_s \exp(j\Phi_s)|^2 \\
&= 1 + 2C_s Q_s \cos \Phi_s + C_s^2 Q_s^2.
\end{aligned} \tag{A1.29}$$

Substitution of Eq. (A1.27) into Eq. (A1.29) gives the intensity of the hologram of the opaque spherical object as

$$I(r) = 1 + \frac{2\pi a^2}{\lambda z} \cos\left(\frac{\pi r^2}{\lambda z} + \frac{\pi}{2}\right) \left[ \frac{2J_1\left(\frac{2\pi ar}{\lambda z}\right)}{\frac{2\pi ar}{\lambda z}} \right] + \frac{\pi^2 a^4}{\lambda^2 z^2} \left[ \frac{2J_1\left(\frac{2\pi ar}{\lambda z}\right)}{\frac{2\pi ar}{\lambda z}} \right]^2. \tag{A1.30}$$

By using the identity

$$\cos\left(\theta + \frac{\pi}{2}\right) = -\sin(\theta), \tag{A1.31}$$

Eq. (A1.30) becomes

$$I(r) = 1 - \frac{2\pi a^2}{\lambda z} \sin\left(\frac{\pi r^2}{\lambda z}\right) \left[ \frac{2J_1\left(\frac{2\pi ar}{\lambda z}\right)}{\frac{2\pi ar}{\lambda z}} \right] + \frac{\pi^2 a^4}{\lambda^2 z^2} \left[ \frac{2J_1\left(\frac{2\pi ar}{\lambda z}\right)}{\frac{2\pi ar}{\lambda z}} \right]^2. \tag{A1.32}$$

### A1.3 Hologram of circular aperture

In the case of recording a hologram of a 2-D circular aperture by using the Mach-Zehnder interferometer shown in the Fig. 3.9, the complex field incident on the recording plane can be mathematically expressed by

$$\begin{aligned}
U(x, y) &= \exp(jkz) + \frac{\exp(jkz)}{j\lambda z} \int_{-\infty}^{\infty} \int_{-\infty}^{\infty} t(\xi, \eta) \\
&\quad \times \exp\left\{ \frac{jk}{2z} [(x - \xi)^2 + (y - \eta)^2] \right\} d\xi d\eta.
\end{aligned} \tag{A1.33}$$

Here,  $t(\xi, \eta)$  is the amplitude transmittance function at the object plane. The first term of the Eq. (A1.33) represents the reference wave, while the second term is the diffracted wave from the object. Under the far-field condition, Eq. (A1.33) becomes

$$U(x, y) = \exp(jkz) \left[ 1 + \frac{\exp(jkr^2/2z)}{j\lambda z} \tilde{T}\left(\frac{x}{\lambda z}, \frac{y}{\lambda z}\right) \right], \quad (\text{A1.34})$$

where  $\tilde{T}\left(\frac{x}{\lambda z}, \frac{y}{\lambda z}\right)$  is the 2-D Fourier transform of  $t(\xi, \eta)$ . Thus, by neglecting the phase exponential, the object wave is equivalent to

$$\hat{o}_{2\text{-D}}(x, y) = \frac{1}{\lambda z} \exp\left[ j\left(\frac{\pi r^2}{\lambda z} - \frac{\pi}{2}\right) \right] \tilde{T}\left(\frac{x}{\lambda z}, \frac{y}{\lambda z}\right). \quad (\text{A1.35})$$

For a pinhole having a radius of  $a$ , the amplitude transmittance function at the object plane can be mathematically expressed by

$$\begin{aligned} t(\xi, \eta) &= 1 \quad \text{for } \sqrt{\xi^2 + \eta^2} \leq a \\ &= 0 \quad \sqrt{\xi^2 + \eta^2} > a. \end{aligned} \quad (\text{A1.36})$$

Its Fourier transform is given by

$$\tilde{T}\left(\frac{r}{\lambda z}\right) = \pi a^2 \left[ \frac{2J_1\left(\frac{2\pi ar}{\lambda z}\right)}{\frac{2\pi ar}{\lambda z}} \right]. \quad (\text{A1.37})$$

Substitution of Eq. (A1.37) into Eq. (A1.35) gives the diffracted wave from the pinhole as

$$o_p(r) = \frac{\pi a^2}{\lambda z} \left[ \frac{2J_1\left(\frac{2\pi ar}{\lambda z}\right)}{\frac{2\pi ar}{\lambda z}} \right] \exp\left[ j\left(\frac{\pi r^2}{\lambda z} - \frac{\pi}{2}\right) \right]. \quad (\text{A1.38})$$

Thus, in analogy with the derivation of the hologram of an opaque spherical object, the hologram of the pinhole becomes

$$I(r) = 1 + \frac{2\pi a^2}{\lambda z} \cos\left(\frac{\pi r^2}{\lambda z} - \frac{\pi}{2}\right) \left[ \frac{2J_1\left(\frac{2\pi ar}{\lambda z}\right)}{\frac{2\pi ar}{\lambda z}} \right] + \frac{\pi^2 a^4}{\lambda^2 z^2} \left[ \frac{2J_1\left(\frac{2\pi ar}{\lambda z}\right)}{\frac{2\pi ar}{\lambda z}} \right]^2. \quad (\text{A1.39})$$

Since

$$\cos\left(\theta - \frac{\pi}{2}\right) = \sin(\theta) \quad (\text{A1.40})$$

and

$$\sin(\theta + \pi) = -\sin(\theta), \quad (\text{A1.41})$$

as a result

$$\cos\left(\theta - \frac{\pi}{2}\right) = -\sin(\theta + \pi). \quad (\text{A1.42})$$

By using the identity in Eq. (A1.42), the hologram of the pinhole in Eq. (A1.39) is found to be

$$I(r) = 1 - \frac{2\pi a^2}{\lambda z} \sin\left(\frac{\pi r^2}{\lambda z} + \pi\right) \left[ \frac{2J_1\left(\frac{2\pi ar}{\lambda z}\right)}{\frac{2\pi ar}{\lambda z}} \right] + \frac{\pi^2 a^4}{\lambda^2 z^2} \left[ \frac{2J_1\left(\frac{2\pi ar}{\lambda z}\right)}{\frac{2\pi ar}{\lambda z}} \right]^2. \quad (\text{A1.43})$$

## A2. In-line Fraunhofer holograms of multiple objects

In the case where there are multiple objects in the object field, the optical field at the hologram plane can be found from

$$U(x, y) = R + O(x, y), \quad (\text{A2.1})$$

where  $O(x, y)$  is the summation of the object waves scattered from the individual objects

$$O(x, y) = \sum_{k=1}^K o_k(x, y), \quad (\text{A2.2})$$

with  $K$  representing the number of objects in the object field. The intensity at the hologram plane can be calculated from

$$\begin{aligned} I(x, y) &= |U(x, y)|^2 \\ &= |1 + O(x, y)|^2 \\ &= 1 + O(x, y) + O^*(x, y) + |O(x, y)|^2. \end{aligned} \quad (\text{A2.3})$$

Here, the reference wave is assumed to be a constant 1. For a  $k^{\text{th}}$  line object that is centered at the position  $\xi = x_k$  on the  $(\xi, \eta)$  plane, the object wave scattered from this line object can be mathematically expressed as

$$o_{L_k}(x, y) = -\frac{2a_k}{\sqrt{\lambda z_k}} \left[ \frac{\sin\left(\frac{2\pi a_k |x - x_k|}{\lambda z_k}\right)}{\frac{2\pi a_k |x - x_k|}{\lambda z_k}} \right] \exp\left[ j \left( \frac{\pi |x - x_k|^2}{\lambda z_k} - \frac{\pi}{4} \right) \right]. \quad (\text{A2.4})$$

In analogy, the object wave of the  $k^{\text{th}}$  spherical object centered at  $\rho = r_k$  is

$$o_{S_k}(r) = \frac{\pi a_k^2}{\lambda z_k} \left[ \frac{2J_1\left(\frac{2\pi a_k |r - r_k|}{\lambda z_k}\right)}{\frac{2\pi a_k |r - r_k|}{\lambda z_k}} \right] \exp\left[ j\left(\frac{\pi |r - r_k|^2}{\lambda z_k} + \frac{\pi}{2}\right) \right]. \quad (\text{A2.5})$$

The object wave of the line object can be written in the form

$$o_k(x, y) = C_k Q_k \exp(j\Phi_k), \quad (\text{A2.6})$$

where

$$C_k = -\frac{2a_k}{\sqrt{\lambda z_k}}, \quad (\text{A2.7a})$$

$$Q_k = \left[ \frac{\sin\left(\frac{2\pi a_k |x - x_k|}{\lambda z_k}\right)}{\frac{2\pi a_k |x - x_k|}{\lambda z_k}} \right], \quad (\text{A2.7b})$$

and

$$\Phi_k = \frac{\pi |x - x_k|^2}{\lambda z_k} - \frac{\pi}{4}, \quad (\text{A2.7c})$$

while

$$C_k = \frac{\pi a_k^2}{\lambda z_k}, \quad (\text{A2.8a})$$

$$Q_k = \left[ \frac{2J_1\left(\frac{2\pi a_k |r - r_k|}{\lambda z_k}\right)}{\frac{2\pi a_k |r - r_k|}{\lambda z_k}} \right], \quad (\text{A2.8b})$$

$$\Phi_k = \frac{\pi |r - r_k|^2}{\lambda z_k} - \frac{\pi}{2} \quad (\text{A2.8c})$$

for spherical objects. Substitution of Eq. (A2.6) into Eq. (A2.2) gives

$$O(x, y) = \sum_{k=1}^K C_k Q_k \exp(j\Phi_k). \quad (\text{A2.9})$$

Thus, the interference between the reference and the object waves is

$$O(x, y) + O^*(x, y) = 2 \sum_{k=1}^K C_k Q_k \cos(\Phi_k), \quad (\text{A2.10})$$

while that between the object waves is

$$|O(x, y)|^2 = \sum_{k=1}^K \sum_{l=1}^K C_k C_l Q_k Q_l \exp[j(\Phi_k - \Phi_l)]. \quad (\text{A2.11})$$

By separating the interference between the same object waves from those between the different objects, Eq. (A2.11) can be rewritten as

$$|O(x, y)|^2 = \sum_{k=1}^K C_k^2 Q_k^2 + \sum_{k=1}^K \sum_{\substack{l=1 \\ l \neq k}}^K C_k C_l Q_k Q_l \exp[j(\Phi_k - \Phi_l)]. \quad (\text{A2.12})$$

Substitution of Eqs. (A2.10) and (A2.12) into Eq. (A2.3) gives

$$I(x, y) = 1 + 2 \sum_{k=1}^K C_k Q_k \cos(\Phi_k) + \sum_{k=1}^K C_k^2 Q_k^2 + \sum_{k=1}^K \sum_{\substack{l=1 \\ l \neq k}}^K C_k C_l Q_k Q_l \exp[j(\Phi_k - \Phi_l)] \quad (\text{A2.13})$$

Thus, by substituting Eqs. (A2.7) and (A2.8) into Eq. (A2.13), the intensity of the recorded hologram of multiple objects are found to be

$$I(x, y) = 1 - \sum_{k=1}^K \left\{ \frac{4a_k}{\sqrt{\lambda z_k}} \cos \left( \frac{\pi |x - x_k|^2}{\lambda z_k} - \frac{\pi}{4} \right) \left[ \frac{\sin \frac{2\pi a_k |x - x_k|}{\lambda z_k}}{\frac{2\pi a_k |x - x_k|}{\lambda z_k}} \right] \right\}$$

$$\begin{aligned}
& + \frac{4a_k^2}{\lambda z_k} \left[ \frac{\sin \frac{2\pi a_k |x-x_k|}{\lambda z_k}}{\frac{2\pi a_k |x-x_k|}{\lambda z_k}} \right]^2 \left\{ + \sum_{k=1}^K \sum_{\substack{l=1 \\ l \neq k}}^K \left[ \frac{4a_k a_l}{\lambda \sqrt{z_k z_l}} \left[ \frac{\sin \frac{2\pi a_k |x-x_k|}{\lambda z_k}}{\frac{2\pi a_k |x-x_k|}{\lambda z_k}} \right] \right. \right. \\
& \times \left. \left. \left[ \frac{\sin \frac{2\pi a_l |x-x_l|}{\lambda z_l}}{\frac{2\pi a_l |x-x_l|}{\lambda z_l}} \right] \exp \left[ j \left( \frac{\pi |x-x_k|^2}{\lambda z_k} - \frac{\pi |x-x_l|^2}{\lambda z_l} \right) \right] \right\}, \quad (\text{A2.14})
\end{aligned}$$

and

$$\begin{aligned}
I(r) = 1 - \sum_{k=1}^K \left\{ \frac{2\pi a_k^2}{\lambda z_k} \sin \left( \frac{\pi |r-r_k|^2}{\lambda z_k} \right) \left[ \frac{2J_1 \left( \frac{2\pi a_k |r-r_k|}{\lambda z_k} \right)}{\frac{2\pi a_k |r-r_k|}{\lambda z_k}} \right] \right. \\
+ \frac{\pi^2 a_k^4}{\lambda^2 z_k^2} \left[ \frac{2J_1 \left( \frac{2\pi a_k |r-r_k|}{\lambda z_k} \right)}{\frac{2\pi a_k |r-r_k|}{\lambda z_k}} \right]^2 \left\{ + \sum_{k=1}^K \sum_{\substack{l=1 \\ l \neq k}}^K \left[ \frac{\pi^2 a_k^2 a_l^2}{\lambda^2 z_k z_l} \left[ \frac{2J_1 \left( \frac{2\pi a_k |r-r_k|}{\lambda z_k} \right)}{\frac{2\pi a_k |r-r_k|}{\lambda z_k}} \right] \right. \right. \\
\times \left. \left. \left[ \frac{2J_1 \left( \frac{2\pi a_l |r-r_l|}{\lambda z_l} \right)}{\frac{2\pi a_l |r-r_l|}{\lambda z_l}} \right] \exp \left[ j \left( \frac{\pi |r-r_k|^2}{\lambda z_k} - \frac{\pi |r-r_l|^2}{\lambda z_l} \right) \right] \right\}, \quad (\text{A2.15})
\end{aligned}$$

for multiple line and multiple spherical objects, respectively.

## B. Wavelet Transformations

### B1. Absolute value of the WT

Consider a modulated signal

$$s(x) = \cos(2\pi f_0 x) \cos(2\pi f_1 x), \quad (\text{B1.1})$$

where  $f_1 > f_0$ . Its WT calculated by using the Morlet wavelet of Eq. (2.12) is

$$\begin{aligned}
 W(t, d) = & \frac{1}{\sqrt{d}} \int_{-\infty}^{\infty} \exp\left[-j2\pi f_g \left(\frac{x-t}{d}\right)\right] \exp\left[-\left(\frac{x-t}{d}\right)^2 / 2\right] \\
 & \times \left\{ \frac{\exp(j2\pi f_0 x) + \exp(-j2\pi f_0 x)}{2} \right\} \\
 & \times \left\{ \frac{\exp(j2\pi f_1 x) + \exp(-j2\pi f_1 x)}{2} \right\} dx. \quad (\text{B1.2})
 \end{aligned}$$

Here, the definition

$$\cos(\theta) = \frac{\exp(j\theta) + \exp(-j\theta)}{2} \quad (\text{B1.3})$$

is employed. Equation (B1.2) can be rewritten as

$$\begin{aligned}
 W(t, d) = & \frac{1}{4\sqrt{d}} \int_{-\infty}^{\infty} \exp\left(\frac{-j2\pi f_g x}{d} + \frac{j2\pi f_g t}{d}\right) \exp\left[-\left(\frac{x^2 - 2xt + t^2}{2d^2}\right)\right] \\
 & \times \left\{ \exp(j2\pi f_0 x + j2\pi f_1 x) + \exp(-j2\pi f_0 x + j2\pi f_1 x) \right. \\
 & \left. + \exp(j2\pi f_0 x - j2\pi f_1 x) + \exp(-j2\pi f_0 x - j2\pi f_1 x) \right\} dx \\
 = & \frac{1}{4\sqrt{d}} \exp\left(\frac{j2\pi f_g t}{d} - \frac{t^2}{2d^2}\right) \int_{-\infty}^{\infty} \exp\left[\left(-\frac{1}{2d^2}\right)x^2 + \left(\frac{t}{d^2} - \frac{j2\pi f_g}{d}\right)x\right] \\
 & \times \left\{ \exp[(j2\pi f_0 + j2\pi f_1)x] + \exp[(-j2\pi f_0 + j2\pi f_1)x] \right. \\
 & \left. + \exp[(j2\pi f_0 - j2\pi f_1)x] + \exp[(-j2\pi f_0 - j2\pi f_1)x] \right\} dx \\
 = & \frac{1}{4\sqrt{d}} \exp\left(\frac{j2\pi f_g t}{d} - \frac{t^2}{2d^2}\right) \left[ w_1(t, d) + w_2(t, d) \right. \\
 & \left. + w_3(t, d) + w_4(t, d) \right], \quad (\text{B1.4})
 \end{aligned}$$

where

$$w_1(t, d) = \int_{-\infty}^{\infty} \exp \left[ \left( -\frac{1}{2d^2} \right) x^2 + \left( \frac{t}{d^2} - \frac{j2\pi f_g}{d} + j2\pi f_0 + j2\pi f_1 \right) x \right] dx \quad (\text{B1.5a})$$

$$w_2(t, d) = \int_{-\infty}^{\infty} \exp \left[ \left( -\frac{1}{2d^2} \right) x^2 + \left( \frac{t}{d^2} - \frac{j2\pi f_g}{d} - j2\pi f_0 + j2\pi f_1 \right) x \right] dx \quad (\text{B1.5b})$$

$$w_3(t, d) = \int_{-\infty}^{\infty} \exp \left[ \left( -\frac{1}{2d^2} \right) x^2 + \left( \frac{t}{d^2} - \frac{j2\pi f_g}{d} + j2\pi f_0 - j2\pi f_1 \right) x \right] dx \quad (\text{B1.5c})$$

$$w_4(t, d) = \int_{-\infty}^{\infty} \exp \left[ \left( -\frac{1}{2d^2} \right) x^2 + \left( \frac{t}{d^2} - \frac{j2\pi f_g}{d} - j2\pi f_0 - j2\pi f_1 \right) x \right] dx. \quad (\text{B1.5d})$$

By using the identity

$$\int_{-\infty}^{\infty} \exp(Ax^2 + Bx) dx = \sqrt{\frac{-\pi}{A}} \exp\left(\frac{-B^2}{4A}\right) \quad (\text{B1.6})$$

$$\begin{aligned} w_1(t, d) &= \sqrt{\frac{-\pi}{-(1/2d^2)}} \exp \left\{ - \left( \frac{t}{d^2} - \frac{j2\pi f_g}{d} + j2\pi f_0 + j2\pi f_1 \right)^2 / 4 \left( \frac{-1}{2d^2} \right) \right\} \\ &= \sqrt{2\pi} d \exp \left\{ \frac{d^2}{2} \left[ \frac{t}{d^2} - j2\pi \left( \frac{f_g}{d} + f_0 + f_1 \right) \right]^2 \right\} \\ &= \sqrt{2\pi} d \exp \left\{ \frac{d^2}{2} \left[ \frac{t^2}{d^4} - j4\pi \left( \frac{f_g}{d} + f_0 + f_1 \right) \left( \frac{t}{d^2} \right) \right. \right. \\ &\quad \left. \left. - 4\pi^2 \left( \frac{f_g}{d} + f_0 + f_1 \right)^2 \right] \right\}, \\ &= \sqrt{2\pi} d \exp \left\{ \frac{t^2}{2d^2} - j2\pi \left( \frac{f_g}{d} + f_0 + f_1 \right) t - 2\pi^2 d^2 \left( \frac{f_g}{d} + f_0 + f_1 \right)^2 \right\}. \quad (\text{B1.7a}) \end{aligned}$$

In analogy, Eqs. (A1.5b), (A1.5c) and (A1.5d) become

$$w_2(t, d) = \sqrt{2\pi d} \exp \left\{ \frac{t^2}{2d^2} - j2\pi \left( \frac{f_g}{d} - f_0 + f_1 \right) t - 2\pi^2 d^2 \left( \frac{f_g}{d} - f_0 + f_1 \right)^2 \right\} \quad (\text{B1.7b})$$

$$w_3(t, d) = \sqrt{2\pi d} \exp \left\{ \frac{t^2}{2d^2} - j2\pi \left( \frac{f_g}{d} + f_0 - f_1 \right) t - 2\pi^2 d^2 \left( \frac{f_g}{d} + f_0 - f_1 \right)^2 \right\} \quad (\text{B1.7c})$$

$$w_4(t, d) = \sqrt{2\pi d} \exp \left\{ \frac{t^2}{2d^2} - j2\pi \left( \frac{f_g}{d} - f_0 - f_1 \right) t - 2\pi^2 d^2 \left( \frac{f_g}{d} - f_0 - f_1 \right)^2 \right\}. \quad (\text{B1.7d})$$

Substitution of Eq. (B1.7) into Eq. (B1.4) results in

$$\begin{aligned} W(t, d) = \sqrt{\frac{\pi d}{8}} \left\{ \exp \left[ -j2\pi (f_0 + f_1) t - 2\pi^2 d^2 \left( f_g/d + f_0 + f_1 \right)^2 \right] \right. \\ + \exp \left[ -j2\pi (-f_0 + f_1) t - 2\pi^2 d^2 \left( f_g/d - f_0 + f_1 \right)^2 \right] \\ + \exp \left[ -j2\pi (f_0 - f_1) t - 2\pi^2 d^2 \left( f_g/d + f_0 - f_1 \right)^2 \right] \\ \left. + \exp \left[ -j2\pi (-f_0 - f_1) t - 2\pi^2 d^2 \left( f_g/d - f_0 - f_1 \right)^2 \right] \right\}. \quad (\text{B1.8}) \end{aligned}$$

Equation (B1.8) is a summation of four terms which can be rewritten as

$$W(t, d) = W_1(t, d) + W_2(t, d) + W_3(t, d) + W_4(t, d), \quad (\text{B1.9})$$

where

$$W_1(t, d) = \sqrt{\frac{\pi d}{8}} \exp \left[ -j2\pi (f_0 + f_1) t - 2\pi^2 d^2 \left( f_g/d + f_0 + f_1 \right)^2 \right], \quad (\text{B1.10a})$$

$$W_2(t, d) = \sqrt{\frac{\pi d}{8}} \exp \left[ -j2\pi (-f_0 + f_1) t - 2\pi^2 d^2 \left( f_g/d - f_0 + f_1 \right)^2 \right], \quad (\text{B1.10b})$$

$$W_3(t, d) = \sqrt{\frac{\pi d}{8}} \exp\left[-j2\pi(f_0 - f_1)t - 2\pi^2 d^2 \left(\frac{f_g}{d} + f_0 - f_1\right)^2\right], \quad (\text{B1.10c})$$

$$W_4(t, d) = \sqrt{\frac{\pi d}{8}} \exp\left[-j2\pi(-f_0 - f_1)t - 2\pi^2 d^2 \left(\frac{f_g}{d} - f_0 - f_1\right)^2\right]. \quad (\text{B1.10d})$$

The amplitude of each component in Eqs. (B1.10) is determined by the last multiplicative exponential term which is

$$W_{13}(d) = \exp\left[-2\pi^2 d^2 \left(\frac{f_g}{d} + f_0 + f_1\right)^2\right], \quad (\text{B1.11a})$$

$$W_{23}(d) = \exp\left[-2\pi^2 d^2 \left(\frac{f_g}{d} - f_0 + f_1\right)^2\right], \quad (\text{B1.11b})$$

$$W_{33}(d) = \exp\left[-2\pi^2 d^2 \left(\frac{f_g}{d} + f_0 - f_1\right)^2\right], \quad (\text{B1.11c})$$

$$W_{43}(d) = \exp\left[-2\pi^2 d^2 \left(\frac{f_g}{d} - f_0 - f_1\right)^2\right], \quad (\text{B1.11d})$$

respectively. Since the range of dilated frequency used in the calculation of the WT corresponds to the frequency content of the analyzed signal, the argument of the above four exponential terms vary around the frequency  $f_1$ . In addition, by using the assumption that  $f_1 > f_0$ , the inequality

$$\left(\frac{f_g}{d} \pm f_0 + f_1\right)^2 \gg \left(\frac{f_g}{d} \pm f_0 - f_1\right)^2$$

or

$$\exp\left[-2\pi^2 d^2 \left(\frac{f_g}{d} \pm f_0 + f_1\right)^2\right] \ll \exp\left[-2\pi^2 d^2 \left(\frac{f_g}{d} \pm f_0 - f_1\right)^2\right] \quad (\text{B1.12})$$

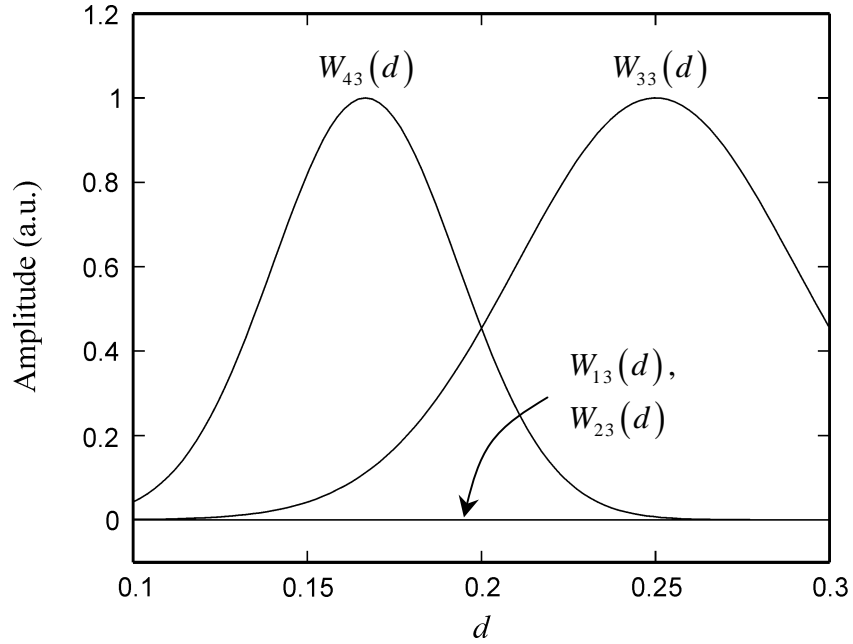


**Figure A1** Plot of Eqs. (B1.11) as a function of the dilation  $d$ .

is obtained. By taking this consideration into account, the first and the second terms of Eq. (B1.9) which are much smaller than the third and the fourth terms can be neglected. Plot of Eqs. (B1.11) by using the parameter  $f_g = f_0 = 1,000$  lines/mm and  $f_1 = 5,000$  lines/mm is shown in Fig. A1. Since the maximum amplitude of  $W_{13}(d)$  is in the order of  $10^{-22}$  and that of  $W_{23}(d)$  is  $10^{-17}$ , they appear as straight lines around the zero scale compared to  $W_{33}(d)$  and  $W_{43}(d)$  which have maximum amplitude of 1. These results ensure that the first and the second terms of Eq. (B1.8) can be neglected. After neglecting the first and the second terms, Eq. (B1.8) reduces to

$$\begin{aligned}
 W(t, d) &= \sqrt{\frac{\pi d}{8}} \left\{ \exp \left[ -j2\pi (f_0 - f_1) t - 2\pi^2 d^2 (f_g/d + f_0 - f_1)^2 \right] \right. \\
 &\quad \left. + \exp \left[ -j2\pi (-f_0 - f_1) t - 2\pi^2 d^2 (f_g/d - f_0 - f_1)^2 \right] \right\} \\
 &= \sqrt{\frac{\pi d}{8}} \left\{ \exp \left[ j2\pi (f_1 - f_0) t - 2\pi^2 \left\{ d (f_g/d + f_0 - f_1) \right\}^2 \right] \right\}
 \end{aligned}$$

$$\begin{aligned}
& + \exp \left[ j2\pi (f_1 + f_0) t - 2\pi^2 \left\{ d \left( f_g/d - f_0 - f_1 \right) \right\}^2 \right] \Big\} \\
& = \sqrt{\frac{\pi d}{8}} \left\{ \exp \left[ j2\pi (f_1 - f_0) t - 2\pi^2 \left\{ f_g + d(f_0 - f_1) \right\}^2 \right] \right. \\
& \quad \left. + \exp \left[ j2\pi (f_1 + f_0) t - 2\pi^2 \left\{ f_g - d(f_0 + f_1) \right\}^2 \right] \right\} \\
& = \sqrt{\frac{\pi d}{8}} \left\{ \exp \left[ j2\pi (f_1 - f_0) t - 2\pi^2 \left\{ (f_0 - f_1) \left[ f_g / (f_0 - f_1) + d \right] \right\}^2 \right] \right. \\
& \quad \left. + \exp \left[ j2\pi (f_1 + f_0) t - 2\pi^2 \left\{ (f_0 + f_1) \left[ f_g / (f_0 + f_1) - d \right] \right\}^2 \right] \right\} \\
& = \sqrt{\frac{\pi d}{8}} \left\{ \exp \left[ j2\pi (f_1 - f_0) t - 2\pi^2 (f_0 - f_1)^2 \left\{ d - f_g / (f_1 - f_0) \right\}^2 \right] \right. \\
& \quad \left. + \exp \left[ j2\pi (f_1 + f_0) t - 2\pi^2 (f_0 + f_1)^2 \left\{ d - f_g / (f_1 + f_0) \right\}^2 \right] \right\}. \quad (\text{B1.13})
\end{aligned}$$

The absolute value of  $W(t, d)$  can be calculated from

$$|W(t, d)| = \sqrt{W(t, d)W^*(t, d)}. \quad (\text{B1.14})$$

Substitution of Eq. (B1.13) into Eq. (B1.14) gives

$$\begin{aligned}
|W(t, d)| & = \left[ \sqrt{\frac{\pi d}{8}} \left\{ \exp \left[ j2\pi (f_1 - f_0) t - 2\pi^2 (f_0 - f_1)^2 \left\{ d - f_g / (f_1 - f_0) \right\}^2 \right] \right. \right. \\
& \quad \left. \left. + \exp \left[ j2\pi (f_1 + f_0) t - 2\pi^2 (f_0 + f_1)^2 \left\{ d - f_g / (f_1 + f_0) \right\}^2 \right] \right\} \right. \\
& \quad \left. \sqrt{\frac{\pi d}{8}} \left\{ \exp \left[ -j2\pi (f_1 - f_0) t - 2\pi^2 (f_0 - f_1)^2 \left\{ d - f_g / (f_1 - f_0) \right\}^2 \right] \right. \right. \\
& \quad \left. \left. + \exp \left[ -j2\pi (f_1 + f_0) t - 2\pi^2 (f_0 + f_1)^2 \left\{ d - f_g / (f_1 + f_0) \right\}^2 \right] \right\} \right]^{\frac{1}{2}}
\end{aligned}$$

$$\begin{aligned}
&= \sqrt{\frac{\pi d}{8}} \left\{ \exp \left[ j2\pi (f_1 - f_0) t - 2\pi^2 (f_0 - f_1)^2 \left\{ d - f_g / (f_1 - f_0) \right\}^2 \right. \right. \\
&\quad \left. \left. - j2\pi (f_1 - f_0) t - 2\pi^2 (f_0 - f_1)^2 \left\{ d - f_g / (f_1 - f_0) \right\}^2 \right] \right. \\
&\quad + \exp \left[ j2\pi (f_1 + f_0) t - 2\pi^2 (f_0 + f_1)^2 \left\{ d - f_g / (f_1 + f_0) \right\}^2 \right. \\
&\quad \left. \left. - j2\pi (f_1 - f_0) t - 2\pi^2 (f_0 - f_1)^2 \left\{ d - f_g / (f_1 - f_0) \right\}^2 \right] \right. \\
&\quad + \exp \left[ j2\pi (f_1 - f_0) t - 2\pi^2 (f_0 - f_1)^2 \left\{ d - f_g / (f_1 - f_0) \right\}^2 \right. \\
&\quad \left. \left. - j2\pi (f_1 + f_0) t - 2\pi^2 (f_0 + f_1)^2 \left\{ d - f_g / (f_1 + f_0) \right\}^2 \right] \right. \\
&\quad \left. + \exp \left[ j2\pi (f_1 + f_0) t - 2\pi^2 (f_0 + f_1)^2 \left\{ d - f_g / (f_1 + f_0) \right\}^2 \right. \right. \\
&\quad \left. \left. - j2\pi (f_1 + f_0) t - 2\pi^2 (f_0 + f_1)^2 \left\{ d - f_g / (f_1 + f_0) \right\}^2 \right] \right\}^{\frac{1}{2}}
\end{aligned}$$

$$\begin{aligned}
&= \sqrt{\frac{\pi d}{8}} \left\{ \exp \left[ -4\pi^2 (f_0 - f_1)^2 \left\{ d - f_g / (f_1 - f_0) \right\}^2 \right] \right. \\
&\quad + \exp \left[ j4\pi f_0 t - 2\pi^2 (f_0 + f_1)^2 \left\{ d - f_g / (f_1 + f_0) \right\}^2 \right. \\
&\quad \left. \left. - 2\pi^2 (f_0 - f_1)^2 \left\{ d - f_g / (f_1 - f_0) \right\}^2 \right] \right. \\
&\quad + \exp \left[ -j4\pi f_0 t - 2\pi^2 (f_0 - f_1)^2 \left\{ d - f_g / (f_1 - f_0) \right\}^2 \right. \\
&\quad \left. \left. - 2\pi^2 (f_0 + f_1)^2 \left\{ d - f_g / (f_1 + f_0) \right\}^2 \right] \right. \\
&\quad \left. + \exp \left[ -4\pi^2 (f_0 + f_1)^2 \left\{ d - f_g / (f_1 + f_0) \right\}^2 \right] \right\}^{\frac{1}{2}}
\end{aligned}$$

$$\begin{aligned}
&= \sqrt{\frac{\pi d}{8}} \left\{ \exp \left[ -4\pi^2 (f_0 - f_1)^2 \left\{ d - f_g / (f_1 - f_0) \right\}^2 \right] \right. \\
&\quad + \exp \left[ -4\pi^2 (f_0 + f_1)^2 \left\{ d - f_g / (f_1 + f_0) \right\}^2 \right] \\
&\quad + \left\{ \exp(j4\pi f_0 t) + \exp(-j4\pi f_0 t) \right\} \\
&\quad \times \exp \left[ -2\pi^2 (f_0 - f_1)^2 \left\{ d - f_g / (f_1 - f_0) \right\}^2 \right. \\
&\quad \left. \left. - 2\pi^2 (f_0 + f_1)^2 \left\{ d - f_g / (f_1 + f_0) \right\}^2 \right] \right\}^{\frac{1}{2}}
\end{aligned}$$

$$\begin{aligned}
|W(t, d)| = & \sqrt{\frac{\pi d}{8}} \left\{ \exp \left[ -4\pi^2 (f_0 - f_1)^2 \left\{ d - f_g / (f_1 - f_0) \right\}^2 \right] \right. \\
& + \exp \left[ -4\pi^2 (f_0 + f_1)^2 \left\{ d - f_g / (f_1 + f_0) \right\}^2 \right] \\
& + 2 \cos(4\pi f_0 t) \exp \left[ -2\pi^2 (f_0 - f_1)^2 \left\{ d - f_g / (f_1 - f_0) \right\}^2 \right. \\
& \left. \left. - 2\pi^2 (f_0 + f_1)^2 \left\{ d - f_g / (f_1 + f_0) \right\}^2 \right] \right\}^{\frac{1}{2}}. \tag{B1.15}
\end{aligned}$$

At  $d = f_g / f_1$ , Eq. (B1.15) becomes

$$\begin{aligned}
|W(t, d)|_{d=\frac{f_g}{f_1}} = & \sqrt{\frac{\pi (f_g / f_1)}{8}} \left\{ \exp \left[ -4\pi^2 (f_0 - f_1)^2 \left\{ (f_g / f_1) - f_g / (f_1 - f_0) \right\}^2 \right] \right. \\
& + \exp \left[ -4\pi^2 (f_0 + f_1)^2 \left\{ (f_g / f_1) - f_g / (f_1 + f_0) \right\}^2 \right] \\
& + 2 \cos(4\pi f_0 t) \exp \left[ -2\pi^2 (f_0 - f_1)^2 \left\{ (f_g / f_1) - f_g / (f_1 - f_0) \right\}^2 \right. \\
& \left. \left. - 2\pi^2 (f_0 + f_1)^2 \left\{ (f_g / f_1) - f_g / (f_1 + f_0) \right\}^2 \right] \right\}^{\frac{1}{2}} \\
= & \sqrt{\frac{\pi f_g}{8 f_1}} \left\{ \exp \left[ -4\pi^2 (f_0 - f_1)^2 \left\{ \frac{f_g (f_1 - f_0) - f_g f_1}{f_1 (f_1 - f_0)} \right\}^2 \right] \right. \\
& + \exp \left[ -4\pi^2 (f_0 + f_1)^2 \left\{ \frac{f_g (f_1 + f_0) - f_g f_1}{f_1 (f_1 + f_0)} \right\}^2 \right] \\
& + 2 \cos(4\pi f_0 t) \exp \left[ -2\pi^2 (f_0 - f_1)^2 \left\{ \frac{f_g (f_1 - f_0) - f_g f_1}{f_1 (f_1 - f_0)} \right\}^2 \right. \\
& \left. \left. - 2\pi^2 (f_0 + f_1)^2 \left\{ \frac{f_g (f_1 + f_0) - f_g f_1}{f_1 (f_1 + f_0)} \right\}^2 \right] \right\}^{\frac{1}{2}} \\
= & \sqrt{\frac{\pi f_g}{8 f_1}} \left\{ \exp \left[ -4\pi^2 (f_0 - f_1)^2 \left\{ \frac{-f_g f_0}{f_1 (f_1 - f_0)} \right\}^2 \right] \right.
\end{aligned}$$

$$\begin{aligned}
& + \exp \left[ -4\pi^2 (f_0 + f_1)^2 \left\{ \frac{f_g f_0}{f_1 (f_1 + f_0)} \right\}^2 \right] \\
& + 2 \cos(4\pi f_0 t) \exp \left[ -2\pi^2 (f_0 - f_1)^2 \left\{ \frac{-f_g f_0}{f_1 (f_1 - f_0)} \right\}^2 \right. \\
& \left. - 2\pi^2 (f_0 + f_1)^2 \left\{ \frac{f_g f_0}{f_1 (f_1 + f_0)} \right\}^2 \right] \Bigg]^{\frac{1}{2}} \\
& = \sqrt{\frac{\pi f_g}{8 f_1}} \left\{ \exp \left( -\frac{4\pi^2 f_g^2 f_0^2}{f_1^2} \right) + \exp \left( -\frac{4\pi^2 f_g^2 f_0^2}{f_1^2} \right) \right. \\
& \left. + 2 \cos(4\pi f_0 t) \exp \left( -\frac{2\pi^2 f_g^2 f_0^2}{f_1^2} - \frac{2\pi^2 f_g^2 f_0^2}{f_1^2} \right) \right\}^{\frac{1}{2}} \\
& = \sqrt{\frac{\pi f_g}{8 f_1}} \left\{ 2 \exp \left( -\frac{4\pi^2 f_g^2 f_0^2}{f_1^2} \right) + 2 \cos(4\pi f_0 t) \exp \left( -\frac{4\pi^2 f_g^2 f_0^2}{f_1^2} \right) \right\}^{\frac{1}{2}} \\
& = \sqrt{\frac{\pi f_g}{4 f_1}} \exp \left( -\frac{2\pi^2 f_g^2 f_0^2}{f_1^2} \right) \{1 + \cos(4\pi f_0 t)\}^{\frac{1}{2}} \tag{B1.16}
\end{aligned}$$

By using the identity

$$\cos(2\theta) = 2\cos^2(\theta) - 1$$

$$\sqrt{1 + \cos(2\theta)} = \sqrt{2} |\cos(\theta)|, \tag{B1.17}$$

Eq. (B1.16) reduces to

$$|W(t, d)|_{d=\frac{f_g}{f_1}} = \sqrt{\frac{\pi f_g}{2 f_1}} \exp \left[ \frac{-2\pi^2 f_g^2 f_0^2}{f_1^2} \right] |\cos(2\pi f_0 t)|. \tag{B1.18}$$

## B2. Determination of the dilation $d_0$

Consider the chirp signal described by

$$u_1(x) = 1 - A \cos(Bx^2 - C). \quad (\text{B2.1})$$

Its wavelet transform calculated by using the Morlet wavelet of Eq. (2.12) is

$$\begin{aligned} W(t, d) &= \frac{1}{\sqrt{d}} \int_{-\infty}^{\infty} \exp\left\{-j2\pi f_g \left(\frac{x-t}{d}\right)\right\} \exp\left\{\frac{-[(x-t)/d]^2}{2}\right\} \\ &\quad [1 - A \cos(Bx^2 - C)] dx \\ &= \frac{1}{\sqrt{d}} \int_{-\infty}^{\infty} \exp\left\{\frac{-j2\pi f_g x}{d} + \frac{j2\pi f_g t}{d} - \left(\frac{x^2 - 2xt + t^2}{2d^2}\right)\right\} \\ &\quad \left[1 - \frac{A}{2} (\exp[j(Bx^2 - C)] + \exp[-j(Bx^2 - C)])\right] dx \\ &= \frac{1}{\sqrt{d}} \exp\left(-\frac{t^2}{2d^2} + \frac{j2\pi f_g t}{d}\right) \int_{-\infty}^{\infty} \exp\left\{-\frac{x^2}{2d^2} + \left(\frac{t}{d^2} - \frac{j2\pi f_g}{d}\right)x\right\} \\ &\quad \left[1 - \frac{A}{2} \exp\{j(Bx^2 - C)\} - \frac{A}{2} \exp\{-j(Bx^2 - C)\}\right] dx \\ &= \frac{1}{\sqrt{d}} \exp\left(-\frac{t^2}{2d^2} + \frac{j2\pi f_g t}{d}\right) \left[ \int_{-\infty}^{\infty} \exp\left\{-\frac{x^2}{2d^2} + \left(\frac{t}{d^2} - \frac{j2\pi f_g}{d}\right)x\right\} dx \right. \\ &\quad \left. - \frac{A}{2} \exp(-jC) \int_{-\infty}^{\infty} \exp\left\{\left(jB - \frac{1}{2d^2}\right)x^2 + \left(\frac{t}{d^2} - \frac{j2\pi f_g}{d}\right)x\right\} dx \right. \\ &\quad \left. - \frac{A}{2} \exp(jC) \int_{-\infty}^{\infty} \exp\left\{\left(-jB - \frac{1}{2d^2}\right)x^2 + \left(\frac{t}{d^2} - \frac{j2\pi f_g}{d}\right)x\right\} dx \right] \quad (\text{B2.2}) \end{aligned}$$

By using Eq. (B1.6), the first integral of Eq. (B2.2) becomes

$$\begin{aligned}
\int_{-\infty}^{\infty} \exp\left\{-\frac{x^2}{2d^2} + \left(\frac{t}{d^2} - \frac{j2\pi f_g}{d}\right)x\right\} dx &= \sqrt{\frac{-\pi}{-1/2d^2}} \exp\left[\frac{-\left(\frac{t}{d^2} - \frac{j2\pi f_g}{d}\right)^2}{4\left(-\frac{1}{2d^2}\right)}\right] \\
&= \sqrt{2\pi d} \exp\left[\frac{d^2}{2}\left(\frac{t^2}{d^4} - \frac{j4\pi f_g t}{d^3} - \frac{4\pi^2 f_g^2}{d^2}\right)\right] \\
&= \sqrt{2\pi d} \exp\left(\frac{t^2}{2d^2} - \frac{j2\pi f_g t}{d} - 2\pi^2 f_g^2\right). \tag{B2.3}
\end{aligned}$$

The second term of Eq. (B2.2) becomes

$$\begin{aligned}
-\frac{A}{2} \exp(-jC) \int_{-\infty}^{\infty} \exp\left\{-\left(\frac{1}{2d^2} - jB\right)x^2 + \left(\frac{t}{d^2} - \frac{j2\pi f_g}{d}\right)x\right\} dx \\
&= -\frac{A}{2} \exp(-jC) \sqrt{\frac{-\pi}{-\left(\frac{1}{2d^2} - jB\right)}} \exp\left[\frac{-\left(\frac{t}{d^2} - \frac{j2\pi f_g}{d}\right)^2}{-4\left(\frac{1}{2d^2} - jB\right)}\right] \\
&= -\frac{A}{2} \exp(-jC) \sqrt{\frac{\pi}{1 - j2Bd^2}} \exp\left[\frac{\frac{t^2}{d^4} - \frac{j4\pi f_g t}{d^3} - \frac{4\pi^2 f_g^2}{d^2}}{4\left(\frac{1 - j2Bd^2}{2d^2}\right)}\right] \\
&= -\frac{A}{2} \exp(-jC) \sqrt{\frac{2\pi d^2}{1 - j2Bd^2}} \exp\left[\frac{d^2}{2(1 - j2Bd^2)}\right. \\
&\quad \left.\left(\frac{t^2}{d^4} - \frac{j4\pi f_g t}{d^3} - \frac{4\pi^2 f_g^2}{d^2}\right)\right]
\end{aligned}$$

$$\begin{aligned}
&= -\frac{Ad}{2} \exp(-jC) \sqrt{\frac{2\pi}{1-j2Bd^2}} \exp\left[\frac{1}{1-j2Bd^2}\right. \\
&\quad \left.\left(\frac{t^2}{2d^2} - \frac{j2\pi f_g t}{d} - 2\pi^2 f_g^2\right)\right] \tag{B2.4}
\end{aligned}$$

The third term of Eq. (B2.2) becomes

$$\begin{aligned}
&-\frac{A}{2} \exp(jC) \int_{-\infty}^{\infty} \exp\left\{-\left(\frac{1}{2d^2} + jB\right)x^2 + \left(\frac{t}{d^2} - \frac{j2\pi f_g}{d}\right)x\right\} dx \\
&= -\frac{A}{2} \exp(jC) \sqrt{\frac{-\pi}{-\left(\frac{1}{2d^2} + jB\right)}} \exp\left[\frac{-\left(\frac{t}{d^2} - \frac{j2\pi f_g}{d}\right)^2}{-4\left(\frac{1}{2d^2} + jB\right)}\right] \\
&= -\frac{A}{2} \exp(jC) \sqrt{\frac{\pi}{\frac{1+j2Bd^2}{2d^2}}} \exp\left[\frac{\frac{t^2}{d^4} - \frac{j4\pi f_g t}{d^3} - \frac{4\pi^2 f_g^2}{d^2}}{4\left(\frac{1+j2Bd^2}{2d^2}\right)}\right] \\
&= -\frac{A}{2} \exp(jC) \sqrt{\frac{2\pi d^2}{1+j2Bd^2}} \exp\left[\frac{d^2}{2(1+j2Bd^2)}\right. \\
&\quad \left.\left(\frac{t^2}{d^4} - \frac{j4\pi f_g t}{d^3} - \frac{4\pi^2 f_g^2}{d^2}\right)\right] \\
&= -\frac{Ad}{2} \exp(jC) \sqrt{\frac{2\pi}{1+j2Bd^2}} \exp\left[\frac{1}{1+j2Bd^2}\right. \\
&\quad \left.\left(\frac{t^2}{2d^2} - \frac{j2\pi f_g t}{d} - 2\pi^2 f_g^2\right)\right] \tag{B2.5}
\end{aligned}$$

Substitution of Eqs. (B2.3), (B2.4) and (B2.5) into Eq. (B2.2) gives

$$\begin{aligned}
W(t, d) &= \frac{1}{\sqrt{d}} \exp\left(-\frac{t^2}{2d^2} + \frac{j2\pi f_g t}{d}\right) \left[ \sqrt{2\pi d} \exp\left(\frac{t^2}{2d^2} - \frac{j2\pi f_g t}{d} - 2\pi^2 f_g^2\right) \right. \\
&\quad \left. - \frac{Ad}{2} \exp(-jC) \sqrt{\frac{2\pi}{1-j2Bd^2}} \exp\left\{\frac{1}{1-j2Bd^2} \left(\frac{t^2}{2d^2} - \frac{j2\pi f_g t}{d} - 2\pi^2 f_g^2\right)\right\} \right. \\
&\quad \left. - \frac{Ad}{2} \exp(jC) \sqrt{\frac{2\pi}{1+j2Bd^2}} \exp\left\{\frac{1}{1+j2Bd^2} \left(\frac{t^2}{2d^2} - \frac{j2\pi f_g t}{d} - 2\pi^2 f_g^2\right)\right\} \right] \\
&= \sqrt{2\pi d} \exp(-2\pi^2 f_g^2) \\
&\quad - \frac{A}{2} \exp(-jC) \sqrt{\frac{2\pi d}{1-j2Bd^2}} \\
&\quad \times \exp\left\{\left(\frac{1}{1-j2Bd^2} - 1\right) \frac{t^2}{2d^2} - \left(\frac{1}{1-j2Bd^2} - 1\right) \frac{j2\pi f_g t}{d} - \frac{2\pi^2 f_g^2}{1-j2Bd^2}\right\} \\
&\quad - \frac{A}{2} \exp(jC) \sqrt{\frac{2\pi d}{1+j2Bd^2}} \\
&\quad \times \exp\left\{\left(\frac{1}{1+j2Bd^2} - 1\right) \frac{t^2}{2d^2} - \left(\frac{1}{1+j2Bd^2} - 1\right) \frac{j2\pi f_g t}{d} - \frac{2\pi^2 f_g^2}{1+j2Bd^2}\right\} \\
&= \sqrt{2\pi d} \exp(-2\pi^2 f_g^2) \\
&\quad - A \exp(-jC) \sqrt{\frac{\pi d}{2(1-j2Bd^2)}} \\
&\quad \times \exp\left\{\left(\frac{j2Bd^2}{1-j2Bd^2}\right) \frac{t^2}{2d^2} - \left(\frac{j2Bd^2}{1-j2Bd^2}\right) \frac{j2\pi f_g t}{d} - \frac{2\pi^2 f_g^2}{1-j2Bd^2}\right\} \\
&\quad - A \exp(jC) \sqrt{\frac{\pi d}{2(1+j2Bd^2)}} \\
&\quad \times \exp\left\{\left(\frac{-j2Bd^2}{1+j2Bd^2}\right) \frac{t^2}{2d^2} - \left(\frac{-j2Bd^2}{1+j2Bd^2}\right) \frac{j2\pi f_g t}{d} - \frac{2\pi^2 f_g^2}{1+j2Bd^2}\right\} \\
&= \sqrt{2\pi d} \exp(-2\pi^2 f_g^2) \\
&\quad - A \exp(-jC) \sqrt{\frac{\pi d}{2(1-j2Bd^2)}} \exp\left(\frac{jBt^2 + 4\pi f_g t B d - 2\pi^2 f_g^2}{1-j2Bd^2}\right)
\end{aligned}$$

$$-A \exp(jC) \sqrt{\frac{\pi d}{2(1+j2Bd^2)}} \exp\left(\frac{-jBt^2 - 4\pi f_g t B d - 2\pi^2 f_g^2}{1+j2Bd^2}\right) \quad (\text{B2.6})$$

The second term of Eq. (B2.6) is

$$\begin{aligned} & -A \exp(-jC) \sqrt{\frac{\pi d}{2(1-j2Bd^2)}} \exp\left(\frac{jBt^2 + 4\pi f_g t B d - 2\pi^2 f_g^2}{1-j2Bd^2}\right) \\ &= -A \exp(-jC) \sqrt{\frac{\pi d}{2}} \frac{1}{\sqrt{1-j2Bd^2}} \times \frac{\sqrt{1-j2Bd^2}}{\sqrt{1-j2Bd^2}} \\ & \quad \exp\left(\frac{jBt^2 + 4\pi f_g t B d - 2\pi^2 f_g^2}{1-j2Bd^2} \times \frac{1+j2Bd^2}{1+j2Bd^2}\right) \\ &= -A \exp(-jC) \sqrt{\frac{\pi d}{2}} \left\{ \frac{\sqrt{1-j2Bd^2}}{1-j2Bd^2} \times \frac{1+j2Bd^2}{1+j2Bd^2} \right\} \\ & \quad \exp\left(\frac{jBt^2 + 4\pi f_g t B d - 2\pi^2 f_g^2 - 2B^2 t^2 d^2 + j8\pi f_g t B^2 d^3 - j4\pi^2 f_g^2 B d^2}{1+4B^2 d^4}\right) \\ &= -A \exp(-jC) \sqrt{\frac{\pi d}{2}} \left\{ \frac{\sqrt{(1-j2Bd^2)(1+j2Bd^2)(1+j2Bd^2)}}{1+4B^2 d^4} \right\} \\ & \quad \exp\left(\frac{jBt^2 + 4\pi f_g t B d - 2\pi^2 f_g^2 - 2B^2 t^2 d^2 + j8\pi f_g t B^2 d^3 - j4\pi^2 f_g^2 B d^2}{1+4B^2 d^4}\right) \\ &= -A \exp(-jC) \sqrt{\frac{\pi d}{2}} \left\{ \frac{\sqrt{1+j2Bd^2}}{\sqrt{1+4B^2 d^4}} \right\} \\ & \quad \exp\left(\frac{jBt^2 + 4\pi f_g t B d - 2\pi^2 f_g^2 - 2B^2 t^2 d^2 + j8\pi f_g t B^2 d^3 - j4\pi^2 f_g^2 B d^2}{1+4B^2 d^4}\right) \\ &= -A \exp(-jC) \sqrt{\frac{\pi d}{2}} \left\{ \frac{\left[ \sqrt{1+4B^2 d^4} \exp\{j \tan^{-1}(2Bd^2)\} \right]^{\frac{1}{2}}}{\sqrt{1+4B^2 d^4}} \right\} \end{aligned}$$

$$\begin{aligned}
& \exp\left(\frac{jBt^2 + 4\pi f_g tBd - 2\pi^2 f_g^2 - 2B^2 t^2 d^2 + j8\pi f_g tB^2 d^3 - j4\pi^2 f_g^2 B d^2}{1 + 4B^2 d^4}\right) \\
&= -A(1 + 4B^2 d^4)^{\frac{1}{4}} \sqrt{\frac{\pi d}{2}} \exp\left[j\left(\frac{\tan^{-1}(2Bd^2)}{2} - C\right)\right] \\
& \exp\left(\frac{jBt^2 + 4\pi f_g tBd - 2\pi^2 f_g^2 - 2B^2 t^2 d^2 + j8\pi f_g tB^2 d^3 - j4\pi^2 f_g^2 B d^2}{1 + 4B^2 d^4}\right)
\end{aligned}$$

The third term of Eq. (B2.6) is

$$\begin{aligned}
& -A \exp(jC) \sqrt{\frac{\pi d}{2(1 + j2Bd^2)}} \exp\left(\frac{-jBt^2 - 4\pi f_g tBd - 2\pi^2 f_g^2}{1 + j2Bd^2}\right) \\
&= -A \exp(jC) \sqrt{\frac{\pi d}{2}} \frac{1}{\sqrt{1 + j2Bd^2}} \times \frac{\sqrt{1 + j2Bd^2}}{\sqrt{1 + j2Bd^2}} \\
& \exp\left(\frac{-jBt^2 - 4\pi f_g tBd - 2\pi^2 f_g^2}{1 + j2Bd^2} \times \frac{1 - j2Bd^2}{1 - j2Bd^2}\right) \\
&= -A \exp(jC) \sqrt{\frac{\pi d}{2}} \left\{ \frac{\sqrt{1 + j2Bd^2}}{1 + j2Bd^2} \times \frac{1 - j2Bd^2}{1 - j2Bd^2} \right\} \\
& \exp\left(\frac{-jBt^2 - 4\pi f_g tBd - 2\pi^2 f_g^2 - 2B^2 t^2 d^2 + j8\pi f_g tB^2 d^3 + j4\pi^2 f_g^2 B d^2}{1 + 4B^2 d^4}\right) \\
&= -A \exp(jC) \sqrt{\frac{\pi d}{2}} \left\{ \frac{\sqrt{(1 + j2Bd^2)(1 - j2Bd^2)(1 - j2Bd^2)}}{1 + 4B^2 d^4} \right\} \\
& \exp\left(\frac{-jBt^2 - 4\pi f_g tBd - 2\pi^2 f_g^2 - 2B^2 t^2 d^2 + j8\pi f_g tB^2 d^3 + j4\pi^2 f_g^2 B d^2}{1 + 4B^2 d^4}\right)
\end{aligned}$$

$$\begin{aligned}
&= -A \exp(jC) \sqrt{\frac{\pi d}{2}} \left\{ \sqrt{\frac{1-j2Bd^2}{1+4B^2d^4}} \right\} \\
&\quad \exp\left( \frac{-jBt^2 - 4\pi f_g t B d - 2\pi^2 f_g^2 - 2B^2 t^2 d^2 + j8\pi f_g t B^2 d^3 + j4\pi^2 f_g^2 B d^2}{1+4B^2d^4} \right) \\
&= -A \exp(jC) \sqrt{\frac{\pi d}{2}} \left\{ \frac{\left[ \sqrt{1+4B^2d^4} \exp\{j \tan^{-1}(-2Bd^2)\} \right]^{\frac{1}{2}}}{\sqrt{1+4B^2d^4}} \right\} \\
&\quad \exp\left( \frac{-jBt^2 - 4\pi f_g t B d - 2\pi^2 f_g^2 - 2B^2 t^2 d^2 + j8\pi f_g t B^2 d^3 + j4\pi^2 f_g^2 B d^2}{1+4B^2d^4} \right) \\
&= -A(1+4B^2d^4)^{\frac{1}{4}} \sqrt{\frac{\pi d}{2}} \exp\left[ -j \left( \frac{\tan^{-1}(2Bd^2)}{2} - C \right) \right] \\
&\quad \exp\left( \frac{-jBt^2 - 4\pi f_g t B d - 2\pi^2 f_g^2 - 2B^2 t^2 d^2 + j8\pi f_g t B^2 d^3 + j4\pi^2 f_g^2 B d^2}{1+4B^2d^4} \right)
\end{aligned}$$

Thus, Eq. (B2.6) becomes

$$\begin{aligned}
W(t, d) &= \sqrt{2\pi d} \exp(-2\pi^2 f_g^2) \\
&\quad -A(1+4B^2d^4)^{\frac{1}{4}} \sqrt{\frac{\pi d}{2}} \exp\left[ j \left( \frac{\tan^{-1}(2Bd^2)}{2} - C \right) \right] \\
&\quad \exp\left( \frac{jBt^2 + 4\pi f_g t B d - 2\pi^2 f_g^2 - 2B^2 t^2 d^2 + j8\pi f_g t B^2 d^3 - j4\pi^2 f_g^2 B d^2}{1+4B^2d^4} \right) \\
&\quad -A(1+4B^2d^4)^{\frac{1}{4}} \sqrt{\frac{\pi d}{2}} \exp\left[ -j \left( \frac{\tan^{-1}(2Bd^2)}{2} - C \right) \right] \\
&\quad \exp\left( \frac{-jBt^2 - 4\pi f_g t B d - 2\pi^2 f_g^2 - 2B^2 t^2 d^2 + j8\pi f_g t B^2 d^3 + j4\pi^2 f_g^2 B d^2}{1+4B^2d^4} \right) \\
&= \sqrt{2\pi d} \exp(-2\pi^2 f_g^2)
\end{aligned}$$

$$\begin{aligned}
& -A(1+4B^2d^4)^{-\frac{1}{4}}\sqrt{\frac{\pi d}{2}}\exp\left[\frac{4\pi f_g t B d - 2\pi^2 f_g^2 - 2B^2 t^2 d^2}{1+4B^2d^4}\right] \\
& + j\left\{\frac{Bt^2 + 8\pi f_g t B^2 d^3 - 4\pi^2 f_g^2 B d^2}{1+4B^2d^4} + \frac{\tan^{-1}(2Bd^2)}{2} - C\right\} \\
& -A(1+4B^2d^4)^{-\frac{1}{4}}\sqrt{\frac{\pi d}{2}}\exp\left[\frac{-4\pi f_g t B d - 2\pi^2 f_g^2 - 2B^2 t^2 d^2}{1+4B^2d^4}\right] \\
& - j\left\{\frac{Bt^2 - 8\pi f_g t B^2 d^3 - 4\pi^2 f_g^2 B d^2}{1+4B^2d^4} + \frac{\tan^{-1}(2Bd^2)}{2} - C\right\}. \tag{B2.7}
\end{aligned}$$

At  $t = 0$ , Eq. (B2.7) becomes

$$\begin{aligned}
W(0, d) &= \sqrt{2\pi d} \exp(-2\pi^2 f_g^2) \\
& -A(1+4B^2d^4)^{-\frac{1}{4}}\sqrt{\frac{\pi d}{2}}\exp\left[\frac{-2\pi^2 f_g^2}{1+4B^2d^4}\right] \\
& + j\left\{\frac{-4\pi^2 f_g^2 B d^2}{1+4B^2d^4} + \frac{\tan^{-1}(2Bd^2)}{2} - C\right\} \\
& -A(1+4B^2d^4)^{-\frac{1}{4}}\sqrt{\frac{\pi d}{2}}\exp\left[\frac{-2\pi^2 f_g^2}{1+4B^2d^4}\right] \\
& - j\left\{\frac{-4\pi^2 f_g^2 B d^2}{1+4B^2d^4} + \frac{\tan^{-1}(2Bd^2)}{2} - C\right\} \\
& = \sqrt{2\pi d} \exp(-2\pi^2 f_g^2) - \frac{A\sqrt{2\pi d}}{(1+4B^2d^4)^{\frac{1}{4}}}\exp\left(\frac{-2\pi^2 f_g^2}{1+4B^2d^4}\right) \\
& \cos\left\{\frac{4\pi^2 f_g^2 B d^2}{1+4B^2d^4} - \frac{\tan^{-1}(2Bd^2)}{2} + C\right\}. \tag{B2.8}
\end{aligned}$$

Plots of the first and the second terms of Eq. (B2.8) are shown in Fig. 6.19, where its maximum value that corresponds to the center of the object appears at the dilation  $\log_{10}(d_0) = -3.3$ . In order to determine mathematically the dilation  $d_0$ , the derivative of

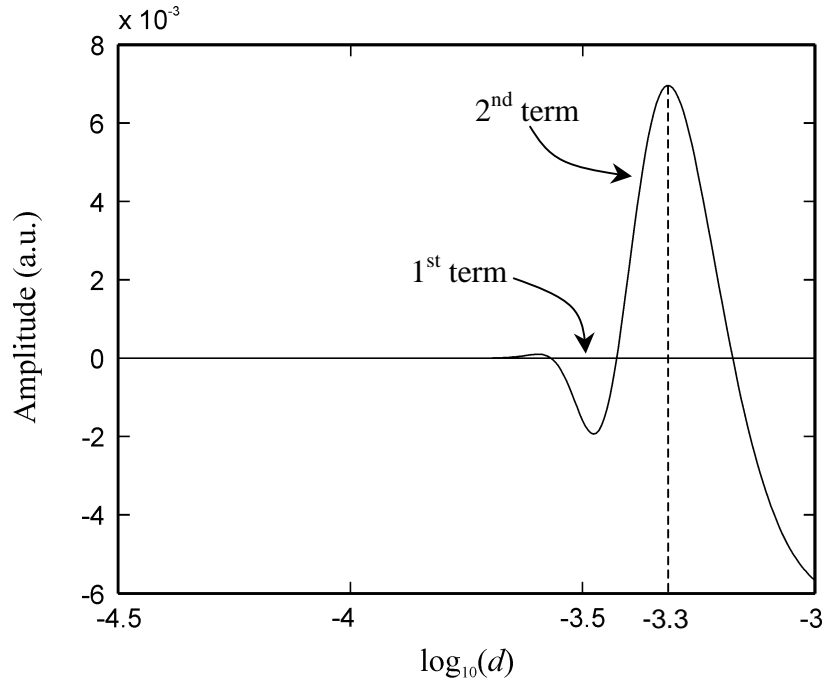


**Figure A2** Plot of each term in the Eq. (B2.8).

Eq. (B2.8) with respect to  $d$  is calculated. The value of the dilation that gives this resultant derivation equals to zero is equal to the dilation  $d_0$ . However, as illustrated in Fig. A2, plots of each term of the Eq. (B2.8) by using the same parameters as those used in Fig. 6.19 show that the first term is much smaller than the second term. Thus the first term can be neglected. In this figure, the first term appears as a straight line because its amplitude is in the order of  $10^{-10}$ , while that of the second term is  $10^{-3}$ . After neglecting the first term, Eq. (B2.8) reduces to

$$\begin{aligned}
 W(0, d) = & -\frac{A\sqrt{2\pi d}}{(1+4B^2d^4)^{\frac{1}{4}}} \exp\left(\frac{-2\pi^2 f_g^2}{1+4B^2d^4}\right) \\
 & \times \cos\left\{\frac{4\pi^2 f_g^2 B d^2}{1+4B^2d^4} - \frac{\tan^{-1}(2Bd^2)}{2} + C\right\} \quad (\text{B2.9})
 \end{aligned}$$

which is a multiplication of three terms. A plot of each term of Eq. (B2.9) is shown in Fig. A3. It can be seen that the first term varies slowly and can be approximately considered as a constant compared to the second and the third term. Thus, by neglecting the first term, Eq. (B2.9) reduces to

$$W(0, d) = -\exp\left(\frac{-2\pi^2 f_g^2}{1+4B^2 d^4}\right) \cos\left\{\frac{4\pi^2 f_g^2 B d^2}{1+4B^2 d^4} - \frac{\tan^{-1}(2B d^2)}{2} + C\right\}. \quad (\text{B2.10})$$

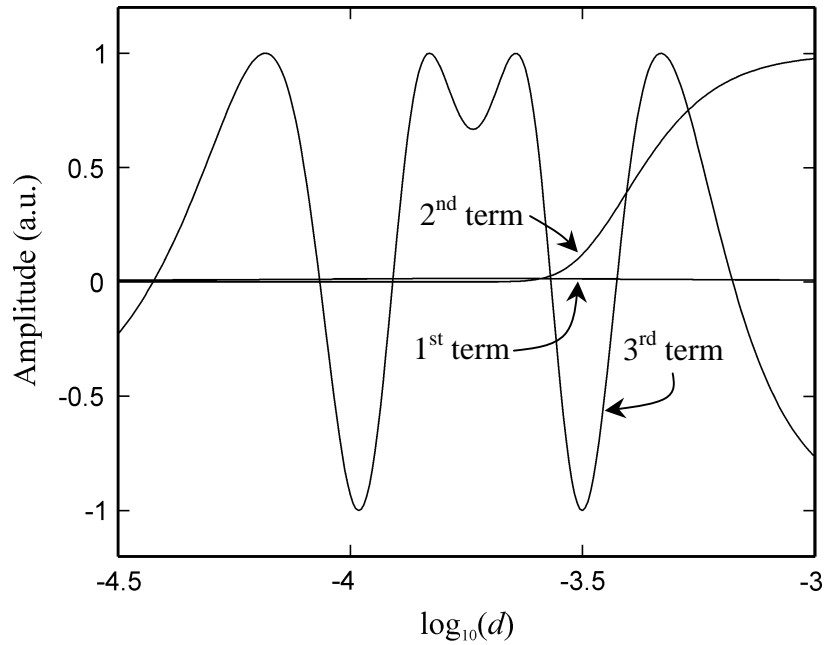


**Figure A3** Plot of each term in the Eq. (B2.9).

The derivative of the Eq. (B2.10) with respect to  $d$  is

$$W'(0, d) = \exp\left(\frac{-2\pi^2 f_g^2}{1+4B^2 d^4}\right) \left[ \frac{8\pi^2 f_g^2 B d^2 - 32\pi^2 f_g^2 B^3 d^5 - 2B d (1+4B^2 d^4)}{(1+4B^2 d^4)^2} \right] \sin\left\{\frac{4\pi^2 f_g^2 B d^2}{1+4B^2 d^4} - \frac{1}{2} \tan^{-1}(2B d^2) + C\right\} - \frac{32\pi^2 f_g^2 B^2 d^3}{(1+4B^2 d^4)^2}$$

$$\exp\left(\frac{-2\pi^2 f_g^2}{1+4B^2 d^4}\right) \cos\left\{\frac{4\pi^2 f_g^2 B d^2}{1+4B^2 d^4} - \frac{1}{2} \tan^{-1}(2B d^2) + C\right\} \quad (\text{B2.11})$$

The maximum position can be determined when Eq. (B2.11) is equal to zero. This yields

$$\begin{aligned} \tan\left\{\frac{4\pi^2 f_g^2 B d^2}{1+4B^2 d^4} - \frac{1}{2} \tan^{-1}(2B d^2) + C\right\} \\ = \frac{16\pi^2 f_g^2 B d^2}{4\pi^2 f_g^2 - 16\pi^2 f_g^2 B^2 d^4 - 1 - 4B^2 d^4}. \end{aligned} \quad (\text{B2.12})$$

Arctan of Eq. (B2.12) is

$$\begin{aligned} \frac{4\pi^2 f_g^2 B d^2}{1+4B^2 d^4} - \frac{1}{2} \tan^{-1}(2B d^2) + C + n\pi \\ = \tan^{-1}\left(\frac{16\pi^2 f_g^2 B d^2}{4\pi^2 f_g^2 - 16\pi^2 f_g^2 B^2 d^4 - 1 - 4B^2 d^4}\right), \end{aligned} \quad (\text{B2.13})$$

where  $n$  is an integer number which represents the periodicity of the tangent function.

By grouping the arctan functions, Eq. (B2.13) becomes

$$\begin{aligned} \frac{4\pi^2 f_g^2 B d^2}{1+4B^2 d^4} + C + n\pi = \tan^{-1}\left(\frac{16\pi^2 f_g^2 B d^2}{4\pi^2 f_g^2 - 16\pi^2 f_g^2 B^2 d^4 - 1 - 4B^2 d^4}\right) \\ + \frac{1}{2} \tan^{-1}(2B d^2) \end{aligned} \quad (\text{B2.14})$$

In order to determine the value of  $d$  that gives the desired maximum, the right hand side (RHS) and the left hand side (LHS) of Eq. (B2.14) are plotted as a function of dilation for different value of  $n$ . Figures A4.a and A4.b show the plots of Eq. (B2.10) and the RHS-LHS of Eq. (B2.14), respectively. The RHS is represented by using the dashed line, while the LHS by the solid line. The dilations at the crossing points of the

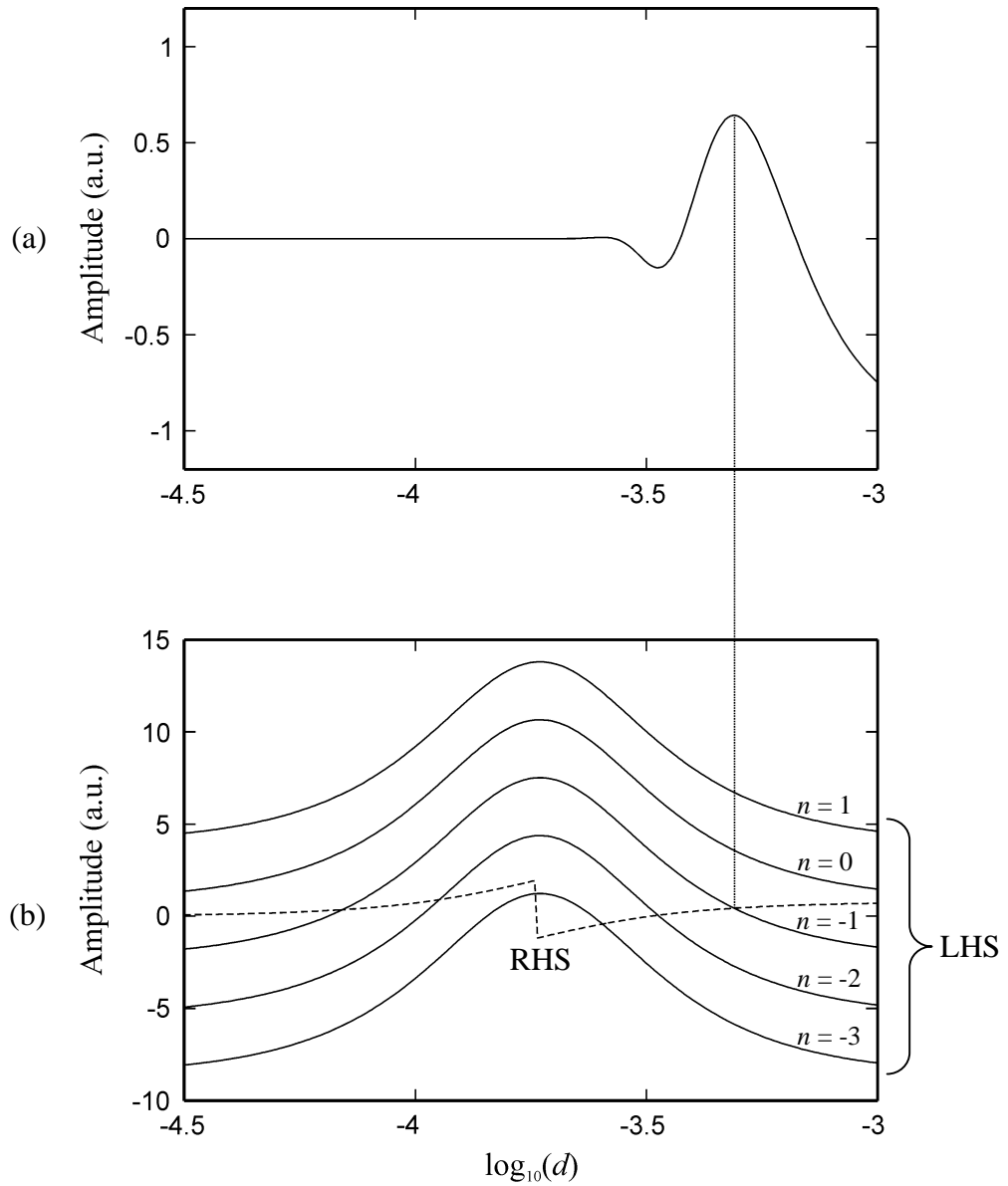


**Figure A4** Plot of Eq. (B2.10) (top) and the LHS and RHS of Eq. (B2.14) (bottom).

two lines are the solution of the Eq. (B2.14). It is clear that for  $n = -1$ , there are two crossing points one of which corresponds to the desired maximum. Let us assume that the solution of Eq. (B2.14) is in the form of

$$d = \frac{c}{\sqrt{B}} \quad (\text{B2.15})$$

with  $c$  is a constant. Substitution of Eq. (B2.15) and  $n = -1$  into Eq. (B2.14) gives

$$\begin{aligned} & \frac{4\pi^2 f_g^2 c^2}{1+4c^4} + C - \pi \\ &= \tan^{-1} \left\{ \frac{16\pi^2 f_g^2 c^2}{4\pi^2 f_g^2 - 16\pi^2 f_g^2 c^4 - 1 - 4c^4} \right\} + \frac{1}{2} \tan^{-1}(2c^2). \end{aligned} \quad (\text{B2.16})$$

Plots of the RHS and the LHS of Eq. (B2.16) as a function of  $c$  are shown in Fig. A5 by using the dash and the solid lines, respectively. Here, the parameter  $C = \pi/4$  is used for the line and  $C = \pi/2$  for the spherical object. It is found that there are two solutions for each type of the objects. However, from Fig. A4, the solution that gives the higher value of the dilation produces the desired maximum. Thus,  $c = 1.86$  and  $c = 2.16$  are used as the solutions of the Eq. (B2.16) for the line and the spherical objects, respectively. By substituting these values of  $c$  and the definition of the parameter  $B$

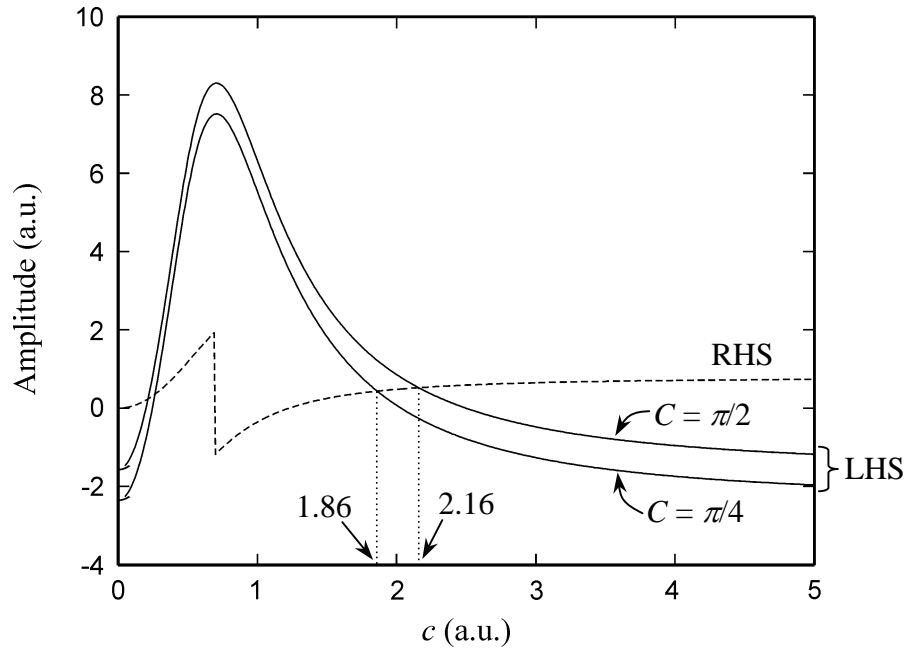


**Figure A5** Plots of the LHS and the RHS of Eq. (B2.16).

into Eq. (B2.15), the dilation  $d_0$  that gives the maximum is equal to

$$d_0 = 1.05\sqrt{\lambda z} \quad (\text{B2.17})$$

and

$$d_0 = 1.22\sqrt{\lambda z}, \quad (\text{B2.18})$$

for the line and the spherical objects, respectively.

### B3. WT of modulation of chirp signal by a cosine function

Consider a modulated signal

$$u_2(x) = 1 - A \cos(Bx^2 - C) \cos(Dx). \quad (\text{B3.1})$$

Its WT calculated by using the Morlet wavelet given by the Eq. (2.12) is

$$\begin{aligned} W(t, d) &= \frac{1}{\sqrt{d}} \int_{-\infty}^{\infty} \exp\left\{-j2\pi f_g \left(\frac{x-t}{d}\right)\right\} \exp\left\{-\frac{[(x-t)/d]^2}{2}\right\} \\ &\quad \left[1 - A \cos(Bx^2 - C) \cos(Dx)\right] dx \\ &= \frac{1}{\sqrt{d}} \int_{-\infty}^{\infty} \exp\left\{\frac{-j2\pi f_g x}{d} + \frac{j2\pi f_g t}{d} - \left(\frac{x^2 - 2xt + t^2}{2d^2}\right)\right\} \\ &\quad \left[1 - \frac{A}{2} \left(\exp[j(Bx^2 - C)] + \exp[-j(Bx^2 - C)]\right)\right] \\ &\quad \times \frac{1}{2} \left\{\exp(jDx) + \exp(-jDx)\right\} dx \\ &= \frac{1}{\sqrt{d}} \exp\left(\frac{-t^2}{2d^2} + \frac{j2\pi f_g t}{d}\right) \left\{ \int_{-\infty}^{\infty} \exp\left[\frac{-x^2}{2d^2} + \left(\frac{t}{d^2} - \frac{j2\pi f_g}{d}\right)x\right] dx \right. \\ &\quad \left. - \frac{A}{4} \int_{-\infty}^{\infty} \exp\left[\frac{-x^2}{2d^2} + \left(\frac{t}{d^2} - \frac{j2\pi f_g}{d}\right)x + j(Bx^2 + Dx - C)\right] dx \right. \\ &\quad \left. + \frac{A}{4} \int_{-\infty}^{\infty} \exp\left[\frac{-x^2}{2d^2} + \left(\frac{t}{d^2} - \frac{j2\pi f_g}{d}\right)x - j(Bx^2 + Dx - C)\right] dx \right\} \end{aligned}$$

$$\begin{aligned}
& -\frac{A}{4} \int_{-\infty}^{\infty} \exp \left[ \frac{-x^2}{2d^2} + \left( \frac{t}{d^2} - \frac{j2\pi f_g}{d} \right) x - j(Bx^2 - Dx - C) \right] dx \\
& -\frac{A}{4} \int_{-\infty}^{\infty} \exp \left[ \frac{-x^2}{2d^2} + \left( \frac{t}{d^2} - \frac{j2\pi f_g}{d} \right) x + j(Bx^2 - Dx - C) \right] dx \\
& -\frac{A}{4} \int_{-\infty}^{\infty} \exp \left[ \frac{-x^2}{2d^2} + \left( \frac{t}{d^2} - \frac{j2\pi f_g}{d} \right) x - j(Bx^2 + Dx - C) \right] dx \Big\}. \quad (\text{B3.2})
\end{aligned}$$

By taking Eq. (B2.3) into account, the first integral of Eq. (B3.2) is equal to

$$\begin{aligned}
& \int_{-\infty}^{\infty} \exp \left\{ -\frac{x^2}{2d^2} + \left( \frac{t}{d^2} - \frac{j2\pi f_g}{d} \right) x \right\} dx \\
& = \sqrt{2\pi} d \exp \left( \frac{t^2}{2d^2} - \frac{j2\pi f_g t}{d} - 2\pi^2 f_g^2 \right). \quad (\text{B3.3a})
\end{aligned}$$

By using the definition of Eq. (B1.6), the second integral of Eq. (B3.2) becomes

$$\begin{aligned}
& \int_{-\infty}^{\infty} \exp \left[ \frac{-x^2}{2d^2} + \left( \frac{t}{d^2} - \frac{j2\pi f_g}{d} \right) x + j(Bx^2 + Dx - C) \right] dx \\
& = \exp(-jC) \int_{-\infty}^{\infty} \exp \left\{ -\left[ \frac{1}{2d^2} - jB \right] x^2 + \left( \frac{t}{d^2} - \frac{j2\pi f_g}{d} + jD \right) x \right\} dx \\
& = \exp(-jC) \sqrt{\frac{-\pi}{-(1/2d^2 - jB)}} \exp \left\{ \frac{-(t/d^2 - j2\pi f_g/d + jD)^2}{-4(1/2d^2 - jB)} \right\} \\
& = \exp(-jC) \sqrt{\frac{2\pi d^2}{1 - j2Bd^2}} \exp \left\{ \frac{2d^2}{4(1 - j2Bd^2)} \right. \\
& \quad \left. \left( \frac{t^2}{d^4} - \frac{4\pi^2 f_g^2}{d^2} - D^2 - \frac{j4\pi f_g t}{d^3} + \frac{j2Dt}{d^2} + \frac{4\pi f_g D}{d} \right) \right\}
\end{aligned}$$

$$\begin{aligned}
&= d \exp(-jC) \sqrt{\frac{2\pi}{1-j2Bd^2}} \exp\left\{\frac{d^2}{2(1-j2Bd^2)}\right. \\
&\quad \left.\left(\frac{t^2}{d^4} - \left[\frac{j4\pi f_g}{d^3} - \frac{j2D}{d^2}\right]t - \frac{4\pi^2 f_g^2}{d^2} - D^2 + \frac{4\pi f_g D}{d}\right)\right\} \\
&= d \exp(-jC) \sqrt{\frac{2\pi}{1-j2Bd^2}} \exp\left\{\frac{1}{1-j2Bd^2}\right. \\
&\quad \left.\left(\frac{t^2}{2d^2} - \left[\frac{j2\pi f_g}{d} - jD\right]t - 2\pi^2 f_g^2 - \frac{D^2 d^2}{2} + 2\pi f_g Dd\right)\right\}. \tag{B3.3b}
\end{aligned}$$

In analogy, the third, the fourth, and the fifth integrals of Eq. (B3.2) becomes

$$\begin{aligned}
&\int_{-\infty}^{\infty} \exp\left[\frac{-x^2}{2d^2} + \left(\frac{t}{d^2} - \frac{j2\pi f_g}{d}\right)x - j(Bx^2 - Dx - C)\right] dx \\
&= d \exp(jC) \sqrt{\frac{2\pi}{1+j2Bd^2}} \exp\left\{\frac{1}{1+j2Bd^2}\right. \\
&\quad \left.\left(\frac{t^2}{2d^2} - \left[\frac{j2\pi f_g}{d} - jD\right]t - 2\pi^2 f_g^2 - \frac{D^2 d^2}{2} + 2\pi f_g Dd\right)\right\}, \tag{B3.3c}
\end{aligned}$$

$$\begin{aligned}
&\int_{-\infty}^{\infty} \exp\left[\frac{-x^2}{2d^2} + \left(\frac{t}{d^2} - \frac{j2\pi f_g}{d}\right)x + j(Bx^2 - Dx - C)\right] dx \\
&= d \exp(-jC) \sqrt{\frac{2\pi}{1-j2Bd^2}} \exp\left\{\frac{1}{1-j2Bd^2}\right. \\
&\quad \left.\left(\frac{t^2}{2d^2} - \left[\frac{j2\pi f_g}{d} + jD\right]t - 2\pi^2 f_g^2 - \frac{D^2 d^2}{2} - 2\pi f_g Dd\right)\right\}, \tag{B3.3d}
\end{aligned}$$

and

$$\begin{aligned}
&\int_{-\infty}^{\infty} \exp\left[\frac{-x^2}{2d^2} + \left(\frac{t}{d^2} - \frac{j2\pi f_g}{d}\right)x - j(Bx^2 + Dx - C)\right] dx \\
&= d \exp(jC) \sqrt{\frac{2\pi}{1+j2Bd^2}} \exp\left\{\frac{1}{1+j2Bd^2}\right.
\end{aligned}$$

$$\left( \frac{t^2}{2d^2} - \left[ \frac{j2\pi f_g}{d} + jD \right] t - 2\pi^2 f_g^2 - \frac{D^2 d^2}{2} - 2\pi f_g Dd \right) \Bigg\}, \quad (\text{B3.3e})$$

respectively. Substitution of Eqs. (B3.3) into Eq. (B3.2) yields

$$\begin{aligned} W(t, d) = & \frac{1}{\sqrt{d}} \exp\left(\frac{-t^2}{2d^2} + \frac{j2\pi f_g t}{d}\right) \left[ \sqrt{2\pi d} \exp\left(\frac{t^2}{2d^2} - \frac{j2\pi f_g t}{d} - 2\pi^2 f_g^2\right) \right. \\ & - \frac{Ad}{4} \exp(-jC) \sqrt{\frac{2\pi}{1-j2Bd^2}} \exp\left\{ \frac{1}{1-j2Bd^2} \right. \\ & \left. \left( \frac{t^2}{2d^2} - \left[ \frac{j2\pi f_g}{d} - jD \right] t - 2\pi^2 f_g^2 - \frac{D^2 d^2}{2} + 2\pi f_g Dd \right) \right\} \\ & - \frac{Ad}{4} \exp(jC) \sqrt{\frac{2\pi}{1+j2Bd^2}} \exp\left\{ \frac{1}{1+j2Bd^2} \right. \\ & \left. \left( \frac{t^2}{2d^2} - \left[ \frac{j2\pi f_g}{d} - jD \right] t - 2\pi^2 f_g^2 - \frac{D^2 d^2}{2} + 2\pi f_g Dd \right) \right\} \\ & - \frac{Ad}{4} \exp(-jC) \sqrt{\frac{2\pi}{1-j2Bd^2}} \exp\left\{ \frac{1}{1-j2Bd^2} \right. \\ & \left. \left( \frac{t^2}{2d^2} - \left[ \frac{j2\pi f_g}{d} + jD \right] t - 2\pi^2 f_g^2 - \frac{D^2 d^2}{2} - 2\pi f_g Dd \right) \right\} \\ & \left. - \frac{Ad}{4} \exp(jC) \sqrt{\frac{2\pi}{1+j2Bd^2}} \exp\left\{ \frac{1}{1+j2Bd^2} \right. \right. \\ & \left. \left. \left( \frac{t^2}{2d^2} - \left[ \frac{j2\pi f_g}{d} + jD \right] t - 2\pi^2 f_g^2 - \frac{D^2 d^2}{2} - 2\pi f_g Dd \right) \right\} \right]. \quad (\text{B3.4}) \end{aligned}$$

The first term of Eq. (B3.4) is

$$\begin{aligned} & \frac{\sqrt{2\pi d}}{\sqrt{d}} \exp\left(\frac{-t^2}{2d^2} + \frac{j2\pi f_g t}{d}\right) \exp\left(\frac{t^2}{2d^2} - \frac{j2\pi f_g t}{d} - 2\pi^2 f_g^2\right) \\ & = \sqrt{2\pi d} \exp(-2\pi^2 f_g^2). \quad (\text{B3.5a}) \end{aligned}$$

The second term of Eq. (B3.4) is

$$\begin{aligned}
& \frac{1}{\sqrt{d}} \exp\left(\frac{-t^2}{2d^2} + \frac{j2\pi f_g t}{d}\right) \left[ -\frac{Ad}{4} \exp(-jC) \sqrt{\frac{2\pi}{1-j2Bd^2}} \right. \\
& \left. \exp\left\{ \frac{1}{1-j2Bd^2} \left( \frac{t^2}{2d^2} - \left[ \frac{j2\pi f_g}{d} - jD \right] t - 2\pi^2 f_g^2 - \frac{D^2 d^2}{2} + 2\pi f_g Dd \right) \right\} \right] \\
& = \frac{-Ad}{4\sqrt{d}} \exp(-jC) \sqrt{\frac{2\pi}{1-j2Bd^2}} \exp\left( \frac{1}{1-j2Bd^2} \left\{ \frac{t^2}{2d^2} \right. \right. \\
& \quad \left. \left. - \left[ \frac{j2\pi f_g}{d} - jD \right] t - 2\pi^2 f_g^2 - \frac{D^2 d^2}{2} + 2\pi f_g Dd \right\} - \frac{t^2}{2d^2} + \frac{j2\pi f_g t}{d} \right) \\
& = \frac{-A}{4} \exp(-jC) \sqrt{\frac{2\pi d}{1-j2Bd^2}} \exp\left( \frac{1}{1-j2Bd^2} \left\{ \frac{t^2}{2d^2} - \frac{j2\pi f_g t}{d} + jDt \right. \right. \\
& \quad \left. \left. - 2\pi^2 f_g^2 - \frac{D^2 d^2}{2} + 2\pi f_g Dd - (1-j2Bd^2) \frac{t^2}{2d^2} + (1-j2Bd^2) \frac{j2\pi f_g t}{d} \right\} \right) \\
& = \frac{-A}{4} \exp(-jC) \sqrt{\frac{2\pi d}{1-j2Bd^2}} \exp\left( \frac{1}{1-j2Bd^2} \left\{ \frac{t^2}{2d^2} [1-(1-j2Bd^2)] \right. \right. \\
& \quad \left. \left. - \frac{j2\pi f_g t}{d} [1-(1-j2Bd^2)] + jDt - 2\pi^2 f_g^2 - \frac{D^2 d^2}{2} + 2\pi f_g Dd \right\} \right) \\
& = \frac{-A}{4} \exp(-jC) \sqrt{\frac{2\pi d}{1-j2Bd^2}} \exp\left( \frac{1}{1-j2Bd^2} \left\{ \frac{t^2}{2d^2} (j2Bd^2) \right. \right. \\
& \quad \left. \left. - \frac{j2\pi f_g t}{d} (j2Bd^2) + jDt - 2\pi^2 f_g^2 - \frac{D^2 d^2}{2} + 2\pi f_g Dd \right\} \right) \\
& = \frac{-A}{4} \exp(-jC) \sqrt{\frac{2\pi d}{1-j2Bd^2}} \exp\left( \frac{1}{1-j2Bd^2} \left\{ jBt^2 \right. \right. \\
& \quad \left. \left. + 4\pi f_g Bdt + jDt - 2\pi^2 f_g^2 - D^2 d^2/2 + 2\pi f_g Dd \right\} \right) \\
& = \frac{-A}{4} \exp(-jC) \sqrt{\frac{2\pi d}{1-j2Bd^2}} \exp\left( \frac{1}{1-j2Bd^2} \left[ \frac{1+j2Bd^2}{1+j2Bd^2} \right] \right)
\end{aligned}$$

$$\begin{aligned}
& \left\{ jBt^2 + 4\pi f_g Bdt + jDt - 2\pi^2 f_g^2 - D^2 d^2 / 2 + 2\pi f_g Dd \right\} \\
&= \frac{-A}{4} \exp(-jC) \sqrt{\frac{2\pi d}{1-j2Bd^2}} \exp\left( \frac{1+j2Bd^2}{1+4B^2d^4} \left\{ jBt^2 \right. \right. \\
&\quad \left. \left. + 4\pi f_g Bdt + jDt - 2\pi^2 f_g^2 - D^2 d^2 / 2 + 2\pi f_g Dd \right\} \right) \\
&= \frac{-A}{4} \exp(-jC) \sqrt{\frac{2\pi d}{1-j2Bd^2}} \exp\left( \frac{1}{1+4B^2d^4} \left\{ jBt^2 + 4\pi f_g Bdt \right. \right. \\
&\quad \left. \left. + jDt - 2\pi^2 f_g^2 - D^2 d^2 / 2 + 2\pi f_g Dd - 2B^2 d^2 t^2 + j8\pi f_g t B^2 d^3 \right. \right. \\
&\quad \left. \left. - 2BDtd^2 - j4\pi^2 f_g^2 B d^2 - jBD^2 d^4 + j4\pi f_g B D d^3 \right\} \right) \\
&= \frac{-A}{4} \exp(-jC) \sqrt{\frac{2\pi d}{1-j2Bd^2}} \exp\left( \frac{1}{1+4B^2d^4} \right. \\
&\quad \left. \left\{ - \left[ 2B^2 d^2 t^2 + 2BDtd^2 - 4\pi f_g Bdt - 2\pi f_g Dd + D^2 d^2 / 2 + 2\pi^2 f_g^2 \right] \right. \right. \\
&\quad \left. \left. + j \left[ Bt^2 + Dt + 8\pi f_g t B^2 d^3 - 4\pi^2 f_g^2 B d^2 - BD^2 d^4 + 4\pi f_g B D d^3 \right] \right\} \right) \\
&= \frac{-A}{4} \exp(-jC) \sqrt{\frac{2\pi d}{1-j2Bd^2}} \exp\left( \frac{1}{1+4B^2d^4} \right. \\
&\quad \left. \left\{ - \left[ \sqrt{2} Bdt - \left( \sqrt{2}\pi f_g - \frac{Dd}{\sqrt{2}} \right) \right]^2 + j \left[ Bt^2 + Dt \right. \right. \right. \\
&\quad \left. \left. \left. + 8\pi f_g t B^2 d^3 - 4\pi^2 f_g^2 B d^2 - BD^2 d^4 + 4\pi f_g B D d^3 \right] \right\} \right). \tag{B3.5b}
\end{aligned}$$

The third term of Eq. (B3.4) is

$$\begin{aligned}
& \frac{1}{\sqrt{d}} \exp\left( \frac{-t^2}{2d^2} + \frac{j2\pi f_g t}{d} \right) \left[ -\frac{Ad}{4} \exp(jC) \sqrt{\frac{2\pi}{1+j2Bd^2}} \exp\left\{ \frac{1}{1+j2Bd^2} \right. \right. \\
& \left. \left. \left( \frac{t^2}{2d^2} - \left[ \frac{j2\pi f_g}{d} - jD \right] t - 2\pi^2 f_g^2 - \frac{D^2 d^2}{2} + 2\pi f_g Dd \right) \right\} \right]
\end{aligned}$$

$$\begin{aligned}
&= \frac{-Ad}{4\sqrt{d}} \exp(jC) \sqrt{\frac{2\pi}{1+j2Bd^2}} \exp\left(\frac{1}{1+j2Bd^2} \left\{ \frac{t^2}{2d^2} \right. \right. \\
&\quad \left. \left. - \left[ \frac{j2\pi f_g}{d} - jD \right] t - 2\pi^2 f_g^2 - \frac{D^2 d^2}{2} + 2\pi f_g Dd \right\} - \frac{t^2}{2d^2} + \frac{j2\pi f_g t}{d} \right) \\
&= \frac{-A}{4} \exp(jC) \sqrt{\frac{2\pi d}{1+j2Bd^2}} \exp\left(\frac{1}{1+j2Bd^2} \left\{ \frac{t^2}{2d^2} - \frac{j2\pi f_g t}{d} + jDt \right. \right. \\
&\quad \left. \left. - 2\pi^2 f_g^2 - \frac{D^2 d^2}{2} + 2\pi f_g Dd - (1+j2Bd^2) \frac{t^2}{2d^2} + (1+j2Bd^2) \frac{j2\pi f_g t}{d} \right\} \right) \\
&= \frac{-A}{4} \exp(jC) \sqrt{\frac{2\pi d}{1+j2Bd^2}} \exp\left(\frac{1}{1+j2Bd^2} \left\{ \frac{t^2}{2d^2} [1 - (1+j2Bd^2)] \right. \right. \\
&\quad \left. \left. - \frac{j2\pi f_g t}{d} [1 - (1+j2Bd^2)] + jDt - 2\pi^2 f_g^2 - \frac{D^2 d^2}{2} + 2\pi f_g Dd \right\} \right) \\
&= \frac{-A}{4} \exp(jC) \sqrt{\frac{2\pi d}{1+j2Bd^2}} \exp\left(\frac{1}{1+j2Bd^2} \left\{ \frac{t^2}{2d^2} (-j2Bd^2) \right. \right. \\
&\quad \left. \left. - \frac{j2\pi f_g t}{d} (-j2Bd^2) + jDt - 2\pi^2 f_g^2 - \frac{D^2 d^2}{2} + 2\pi f_g Dd \right\} \right) \\
&= \frac{-A}{4} \exp(jC) \sqrt{\frac{2\pi d}{1+j2Bd^2}} \exp\left(\frac{1}{1+j2Bd^2} \left\{ -jBt^2 \right. \right. \\
&\quad \left. \left. - 4\pi f_g Bdt + jDt - 2\pi^2 f_g^2 - D^2 d^2/2 + 2\pi f_g Dd \right\} \right) \\
&= \frac{-A}{4} \exp(jC) \sqrt{\frac{2\pi d}{1+j2Bd^2}} \exp\left(\frac{1}{1+j2Bd^2} \left[ \frac{1-j2Bd^2}{1-j2Bd^2} \right] \right. \\
&\quad \left. \left\{ -jBt^2 - 4\pi f_g Bdt + jDt - 2\pi^2 f_g^2 - D^2 d^2/2 + 2\pi f_g Dd \right\} \right) \\
&= \frac{-A}{4} \exp(jC) \sqrt{\frac{2\pi d}{1+j2Bd^2}} \exp\left(\frac{1-j2Bd^2}{1+4B^2d^4} \left\{ -jBt^2 \right. \right.
\end{aligned}$$

$$\begin{aligned}
& -4\pi f_g Bdt + jDt - 2\pi^2 f_g^2 - D^2 d^2/2 + 2\pi f_g Dd \} \\
& = \frac{-A}{4} \exp(jC) \sqrt{\frac{2\pi d}{1+j2Bd^2}} \exp\left(\frac{1}{1+4B^2 d^4} \left\{ -jBt^2 - 4\pi f_g Bdt \right. \right. \\
& \quad \left. \left. + jDt - 2\pi^2 f_g^2 - D^2 d^2/2 + 2\pi f_g Dd - 2B^2 d^2 t^2 + j8\pi f_g t B^2 d^3 \right. \right. \\
& \quad \left. \left. + 2BDtd^2 + j4\pi^2 f_g^2 B d^2 + jBD^2 d^4 - j4\pi f_g B D d^3 \right\} \right) \\
& = \frac{-A}{4} \exp(jC) \sqrt{\frac{2\pi d}{1+j2Bd^2}} \exp\left(\frac{1}{1+4B^2 d^4} \right. \\
& \quad \left. \left\{ -\left[ 2B^2 d^2 t^2 - 2BDtd^2 + 4\pi f_g Bdt - 2\pi f_g Dd + D^2 d^2/2 + 2\pi^2 f_g^2 \right] \right. \right. \\
& \quad \left. \left. + j\left[ -Bt^2 + Dt + 8\pi f_g t B^2 d^3 + 4\pi^2 f_g^2 B d^2 + BD^2 d^4 - 4\pi f_g B D d^3 \right] \right\} \right) \\
& = \frac{-A}{4} \exp(jC) \sqrt{\frac{2\pi d}{1+j2Bd^2}} \exp\left(\frac{1}{1+4B^2 d^4} \right. \\
& \quad \left. \left\{ -\left[ \sqrt{2}Bdt + \left( \sqrt{2}\pi f_g - \frac{Dd}{\sqrt{2}} \right) \right]^2 + j\left[ -Bt^2 + Dt \right. \right. \right. \\
& \quad \left. \left. \left. + 8\pi f_g t B^2 d^3 + 4\pi^2 f_g^2 B d^2 + BD^2 d^4 - 4\pi f_g B D d^3 \right] \right\} \right). \tag{B3.5c}
\end{aligned}$$

The fourth term of Eq. (B3.4) is

$$\begin{aligned}
& \frac{1}{\sqrt{d}} \exp\left(\frac{-t^2}{2d^2} + \frac{j2\pi f_g t}{d}\right) \left[ -\frac{Ad}{4} \exp(-jC) \sqrt{\frac{2\pi}{1-j2Bd^2}} \exp\left\{\frac{1}{1-j2Bd^2} \right. \right. \\
& \quad \left. \left. \left( \frac{t^2}{2d^2} - \left[ \frac{j2\pi f_g}{d} + jD \right] t - 2\pi^2 f_g^2 - \frac{D^2 d^2}{2} - 2\pi f_g Dd \right) \right\} \right] \\
& = \frac{-Ad}{4\sqrt{d}} \exp(-jC) \sqrt{\frac{2\pi}{1-j2Bd^2}} \exp\left(\frac{1}{1-j2Bd^2} \left\{ \frac{t^2}{2d^2} \right. \right. \\
& \quad \left. \left. - \left[ \frac{j2\pi f_g}{d} + jD \right] t - 2\pi^2 f_g^2 - \frac{D^2 d^2}{2} - 2\pi f_g Dd \right\} - \frac{t^2}{2d^2} + \frac{j2\pi f_g t}{d} \right)
\end{aligned}$$

$$\begin{aligned}
&= \frac{-A}{4} \exp(-jC) \sqrt{\frac{2\pi d}{1-j2Bd^2}} \exp\left(\frac{1}{1-j2Bd^2} \left\{ \frac{t^2}{2d^2} - \frac{j2\pi f_g t}{d} - jDt \right. \right. \\
&\quad \left. \left. - 2\pi^2 f_g^2 - \frac{D^2 d^2}{2} - 2\pi f_g Dd - (1-j2Bd^2) \frac{t^2}{2d^2} + (1-j2Bd^2) \frac{j2\pi f_g t}{d} \right\}\right) \\
&= \frac{-A}{4} \exp(-jC) \sqrt{\frac{2\pi d}{1-j2Bd^2}} \exp\left(\frac{1}{1-j2Bd^2} \left\{ \frac{t^2}{2d^2} [1-(1-j2Bd^2)] \right. \right. \\
&\quad \left. \left. - \frac{j2\pi f_g t}{d} [1-(1-j2Bd^2)] - jDt - 2\pi^2 f_g^2 - \frac{D^2 d^2}{2} - 2\pi f_g Dd \right\}\right) \\
&= \frac{-A}{4} \exp(-jC) \sqrt{\frac{2\pi d}{1-j2Bd^2}} \exp\left(\frac{1}{1-j2Bd^2} \left\{ \frac{t^2}{2d^2} (j2Bd^2) \right. \right. \\
&\quad \left. \left. - \frac{j2\pi f_g t}{d} (j2Bd^2) - jDt - 2\pi^2 f_g^2 - \frac{D^2 d^2}{2} - 2\pi f_g Dd \right\}\right) \\
&= \frac{-A}{4} \exp(-jC) \sqrt{\frac{2\pi d}{1-j2Bd^2}} \exp\left(\frac{1}{1-j2Bd^2} \left\{ jBt^2 \right. \right. \\
&\quad \left. \left. + 4\pi f_g Bdt - jDt - 2\pi^2 f_g^2 - D^2 d^2/2 - 2\pi f_g Dd \right\}\right) \\
&= \frac{-A}{4} \exp(-jC) \sqrt{\frac{2\pi d}{1-j2Bd^2}} \exp\left(\frac{1}{1-j2Bd^2} \left[ \frac{1+j2Bd^2}{1+j2Bd^2} \right] \right. \\
&\quad \left. \left\{ jBt^2 + 4\pi f_g Bdt - jDt - 2\pi^2 f_g^2 - D^2 d^2/2 - 2\pi f_g Dd \right\}\right) \\
&= \frac{-A}{4} \exp(-jC) \sqrt{\frac{2\pi d}{1-j2Bd^2}} \exp\left(\frac{1+j2Bd^2}{1+4B^2 d^4} \left\{ jBt^2 \right. \right. \\
&\quad \left. \left. + 4\pi f_g Bdt - jDt - 2\pi^2 f_g^2 - D^2 d^2/2 - 2\pi f_g Dd \right\}\right) \\
&= \frac{-A}{4} \exp(-jC) \sqrt{\frac{2\pi d}{1-j2Bd^2}} \exp\left(\frac{1}{1+4B^2 d^4} \left\{ jBt^2 + 4\pi f_g Bdt \right. \right. \\
&\quad \left. \left. - jDt - 2\pi^2 f_g^2 - D^2 d^2/2 - 2\pi f_g Dd - 2B^2 d^2 t^2 + j8\pi f_g t B^2 d^3 \right\}\right)
\end{aligned}$$

$$\begin{aligned}
& +2BDtd^2 - j4\pi^2 f_g^2 Bd^2 - jBD^2d^4 - j4\pi f_g BDd^3 \}) \\
& = \frac{-A}{4} \exp(-jC) \sqrt{\frac{2\pi d}{1-j2Bd^2}} \exp\left(\frac{1}{1+4B^2d^4}\right. \\
& \quad \left. \left\{ -\left[ 2B^2d^2t^2 - 2BDtd^2 - 4\pi f_g Bdt + 2\pi f_g Dd + D^2d^2/2 + 2\pi^2 f_g^2 \right] \right. \right. \\
& \quad \left. \left. + j\left[ Bt^2 - Dt + 8\pi f_g tB^2d^3 - 4\pi^2 f_g^2 Bd^2 - BD^2d^4 - 4\pi f_g BDd^3 \right] \right\} \right) \\
& = \frac{-A}{4} \exp(-jC) \sqrt{\frac{2\pi d}{1-j2Bd^2}} \exp\left(\frac{1}{1+4B^2d^4}\right. \\
& \quad \left. \left\{ -\left[ \sqrt{2}Bdt - \left( \sqrt{2}\pi f_g - \frac{Dd}{\sqrt{2}} \right) \right]^2 + j\left[ Bt^2 - Dt \right. \right. \right. \\
& \quad \left. \left. \left. + 8\pi f_g tB^2d^3 - 4\pi^2 f_g^2 Bd^2 - BD^2d^4 - 4\pi f_g BDd^3 \right] \right\} \right). \tag{B3.5d}
\end{aligned}$$

The fifth term of Eq. (B3.4) is

$$\begin{aligned}
& \frac{1}{\sqrt{d}} \exp\left(\frac{-t^2}{2d^2} + \frac{j2\pi f_g t}{d}\right) \left[ \frac{-Ad}{4} \exp(jC) \sqrt{\frac{2\pi}{1+j2Bd^2}} \exp\left\{\frac{1}{1+j2Bd^2}\right. \right. \\
& \quad \left. \left. \left( \frac{t^2}{2d^2} - \left[ \frac{j2\pi f_g}{d} + jD \right] t - 2\pi^2 f_g^2 - \frac{D^2d^2}{2} - 2\pi f_g Dd \right) \right\} \right] \\
& = \frac{-Ad}{4\sqrt{d}} \exp(jC) \sqrt{\frac{2\pi}{1+j2Bd^2}} \exp\left(\frac{1}{1+j2Bd^2}\right) \left\{ \frac{t^2}{2d^2} \right. \\
& \quad \left. - \left[ \frac{j2\pi f_g}{d} + jD \right] t - 2\pi^2 f_g^2 - \frac{D^2d^2}{2} - 2\pi f_g Dd \right\} - \frac{t^2}{2d^2} + \frac{j2\pi f_g t}{d} \\
& = \frac{-A}{4} \exp(jC) \sqrt{\frac{2\pi d}{1+j2Bd^2}} \exp\left(\frac{1}{1+j2Bd^2}\right) \left\{ \frac{t^2}{2d^2} - \frac{j2\pi f_g t}{d} - jDt \right. \\
& \quad \left. - 2\pi^2 f_g^2 - \frac{D^2d^2}{2} - 2\pi f_g Dd - (1+j2Bd^2) \frac{t^2}{2d^2} + (1+j2Bd^2) \frac{j2\pi f_g t}{d} \right\}
\end{aligned}$$

$$\begin{aligned}
&= \frac{-A}{4} \exp(jC) \sqrt{\frac{2\pi d}{1+j2Bd^2}} \exp\left(\frac{1}{1+j2Bd^2} \left\{ \frac{t^2}{2d^2} [1-(1+j2Bd^2)] \right. \right. \\
&\quad \left. \left. - \frac{j2\pi f_g t}{d} [1-(1+j2Bd^2)] - jDt - 2\pi^2 f_g^2 - \frac{D^2 d^2}{2} - 2\pi f_g Dd \right\}\right) \\
&= \frac{-A}{4} \exp(jC) \sqrt{\frac{2\pi d}{1+j2Bd^2}} \exp\left(\frac{1}{1+j2Bd^2} \left\{ \frac{t^2}{2d^2} (-j2Bd^2) \right. \right. \\
&\quad \left. \left. - \frac{j2\pi f_g t}{d} (-j2Bd^2) - jDt - 2\pi^2 f_g^2 - \frac{D^2 d^2}{2} - 2\pi f_g Dd \right\}\right) \\
&= \frac{-A}{4} \exp(jC) \sqrt{\frac{2\pi d}{1+j2Bd^2}} \exp\left(\frac{1}{1+j2Bd^2} \left\{ -jBt^2 \right. \right. \\
&\quad \left. \left. - 4\pi f_g Bdt - jDt - 2\pi^2 f_g^2 - D^2 d^2/2 - 2\pi f_g Dd \right\}\right) \\
&= \frac{-A}{4} \exp(jC) \sqrt{\frac{2\pi d}{1+j2Bd^2}} \exp\left(\frac{1}{1+j2Bd^2} \left[ \frac{1-j2Bd^2}{1-j2Bd^2} \right] \right. \\
&\quad \left. \left\{ -jBt^2 - 4\pi f_g Bdt - jDt - 2\pi^2 f_g^2 - D^2 d^2/2 - 2\pi f_g Dd \right\}\right) \\
&= \frac{-A}{4} \exp(jC) \sqrt{\frac{2\pi d}{1+j2Bd^2}} \exp\left(\frac{1-j2Bd^2}{1+4B^2 d^4} \left\{ -jBt^2 \right. \right. \\
&\quad \left. \left. - 4\pi f_g Bdt - jDt - 2\pi^2 f_g^2 - D^2 d^2/2 - 2\pi f_g Dd \right\}\right) \\
&= \frac{-A}{4} \exp(jC) \sqrt{\frac{2\pi d}{1+j2Bd^2}} \exp\left(\frac{1}{1+4B^2 d^4} \left\{ -jBt^2 - 4\pi f_g Bdt \right. \right. \\
&\quad \left. \left. - jDt - 2\pi^2 f_g^2 - D^2 d^2/2 - 2\pi f_g Dd - 2B^2 d^2 t^2 + j8\pi f_g t B^2 d^3 \right. \right. \\
&\quad \left. \left. - 2BDtd^2 + j4\pi^2 f_g^2 B d^2 + jBD^2 d^4 + j4\pi f_g B D d^3 \right\}\right) \\
&= \frac{-A}{4} \exp(jC) \sqrt{\frac{2\pi d}{1+j2Bd^2}} \exp\left(\frac{1}{1+4B^2 d^4} \right. \\
&\quad \left. \left\{ -[2B^2 d^2 t^2 + 2BDtd^2 + 4\pi f_g Bdt + 2\pi f_g Dd + D^2 d^2/2 + 2\pi^2 f_g^2] \right\}\right)
\end{aligned}$$

$$\begin{aligned}
& + j \left[ -Bt^2 - Dt + 8\pi f_g t B^2 d^3 + 4\pi^2 f_g^2 B d^2 + B D^2 d^4 + 4\pi f_g B D d^3 \right] \Big\} \Big) \\
& = \frac{-A}{4} \exp(jC) \sqrt{\frac{2\pi d}{1+j2Bd^2}} \exp\left(\frac{1}{1+4B^2d^4}\right. \\
& \quad \left. \left\{ - \left[ \sqrt{2} B d t + \left( \sqrt{2\pi} f_g + \frac{D d}{\sqrt{2}} \right) \right]^2 + j \left[ -Bt^2 - Dt \right. \right. \right. \\
& \quad \left. \left. \left. + 8\pi f_g t B^2 d^3 + 4\pi^2 f_g^2 B d^2 + B D^2 d^4 + 4\pi f_g B D d^3 \right] \right\} \right). \tag{B3.5e}
\end{aligned}$$

Substitution of Eqs. (B3.5) into Eq. (B3.4) yields

$$\begin{aligned}
W(t, d) & = \sqrt{2\pi d} \exp(-2\pi^2 f_g^2) \\
& - \frac{A \exp(-jC)}{4} \sqrt{\frac{2\pi d}{1-j2Bd^2}} \exp\left[\frac{1}{1+4B^2d^4} \left\{ - \left[ \sqrt{2} B d_0 t - \left( \sqrt{2\pi} f_g - \frac{D d}{\sqrt{2}} \right) \right]^2 \right. \right. \\
& \quad \left. \left. + j \left( B t^2 + D t + 8\pi f_g B^2 d^3 t - 4\pi^2 f_g^2 B d^2 - B D^2 d^4 + 4\pi f_g B D d^3 \right) \right\} \right] \\
& - \frac{A \exp(jC)}{4} \sqrt{\frac{2\pi d}{1+j2Bd^2}} \exp\left[\frac{1}{1+4B^2d^4} \left\{ - \left[ \sqrt{2} B d t + \left( \sqrt{2\pi} f_g - \frac{D d}{\sqrt{2}} \right) \right]^2 \right. \right. \\
& \quad \left. \left. + j \left( -B t^2 + D t + 8\pi f_g B^2 d^3 t + 4\pi^2 f_g^2 B d^2 + B D^2 d^4 - 4\pi f_g B D d^3 \right) \right\} \right] \\
& - \frac{A \exp(-jC)}{4} \sqrt{\frac{2\pi d}{1-j2Bd^2}} \exp\left[\frac{1}{1+4B^2d^4} \left\{ - \left[ \sqrt{2} B d t - \left( \sqrt{2\pi} f_g + \frac{D d}{\sqrt{2}} \right) \right]^2 \right. \right. \\
& \quad \left. \left. + j \left( B t^2 - D t + 8\pi f_g B^2 d^3 t - 4\pi^2 f_g^2 B d^2 - B D^2 d^4 - 4\pi f_g B D d^3 \right) \right\} \right] \\
& - \frac{A \exp(jC)}{4} \sqrt{\frac{2\pi d}{1+j2Bd^2}} \exp\left[\frac{1}{1+4B^2d^4} \left\{ - \left[ \sqrt{2} B d t + \left( \sqrt{2\pi} f_g + \frac{D d}{\sqrt{2}} \right) \right]^2 \right. \right. \\
& \quad \left. \left. + j \left( -B t^2 - D t + 8\pi f_g B^2 d^3 t + 4\pi^2 f_g^2 B d^2 + B D^2 d^4 + 4\pi f_g B D d^3 \right) \right\} \right] \tag{B3.6}
\end{aligned}$$

Equation (B3.6) consists of five terms. The first term is constant, while the other terms are the multiplication of a Gaussian function and a complex exponential function. The amplitude of each terms is determined by the Gaussian function which acts as an envelope function. Figure A6 shows the plots the first term and the

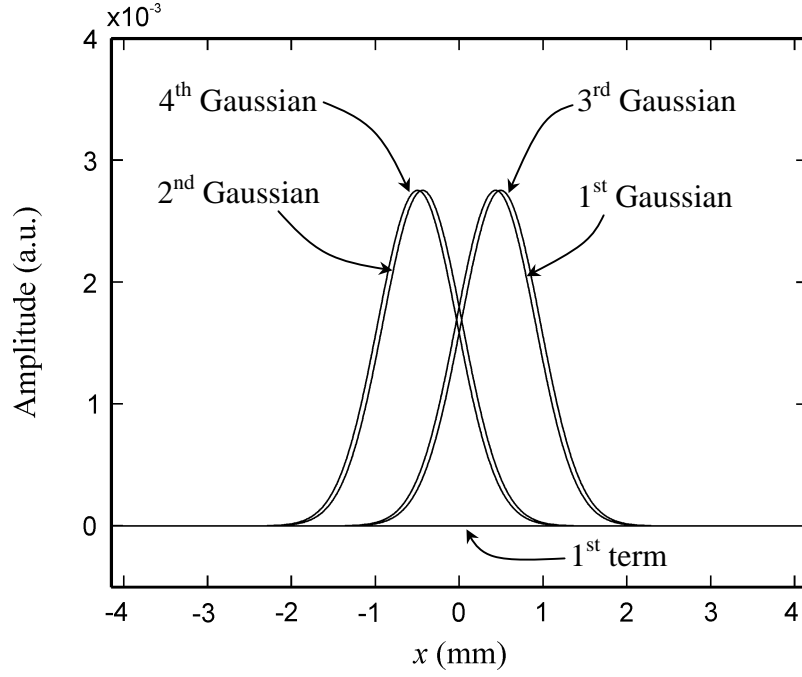


**Figure A6** Plots of the first term and the Gaussian functions of the other four terms of the Eq. (B3.6) at the dilation  $d_0$ .

Gaussian function of the other four terms of the Eq. (B3.6) along the dilation  $d_0 = 1.05\sqrt{\lambda z}$ . It is found that the amplitude of the first term which is in the order of  $10^{-10}$  is much smaller than those of the other four terms which are in the order of  $10^{-3}$ . Thus, the first term can be neglected and Eq. (B3.6) reduces to

$$\begin{aligned}
 W(t, d) = & -\frac{A \exp(-jC)}{4} \sqrt{\frac{2\pi d}{1-j2Bd^2}} \exp \left[ \frac{1}{1+4B^2d^4} \left\{ -\left[ \sqrt{2}Bd_0t - \left( \sqrt{2}\pi f_g - \frac{Dd}{\sqrt{2}} \right) \right]^2 \right. \right. \\
 & \left. \left. + j(Bt^2 + Dt + 8\pi f_g B^2 d^3 t - 4\pi^2 f_g^2 B d^2 - B D^2 d^4 + 4\pi f_g B D d^3) \right\} \right] \\
 & -\frac{A \exp(jC)}{4} \sqrt{\frac{2\pi d}{1+j2Bd^2}} \exp \left[ \frac{1}{1+4B^2d^4} \left\{ -\left[ \sqrt{2}Bdt + \left( \sqrt{2}\pi f_g - \frac{Dd}{\sqrt{2}} \right) \right]^2 \right. \right. \\
 & \left. \left. + j(-Bt^2 + Dt + 8\pi f_g B^2 d^3 t + 4\pi^2 f_g^2 B d^2 + B D^2 d^4 - 4\pi f_g B D d^3) \right\} \right] \\
 & -\frac{A \exp(-jC)}{4} \sqrt{\frac{2\pi d}{1-j2Bd^2}} \exp \left[ \frac{1}{1+4B^2d^4} \left\{ -\left[ \sqrt{2}Bdt - \left( \sqrt{2}\pi f_g + \frac{Dd}{\sqrt{2}} \right) \right]^2 \right. \right.
 \end{aligned}$$

$$\begin{aligned}
& + j \left( Bt^2 - Dt + 8\pi f_g B^2 d^3 t - 4\pi^2 f_g^2 B d^2 - B D^2 d^4 - 4\pi f_g B D d^3 \right) \Big\} \Big] \\
& - \frac{A \exp(jC)}{4} \sqrt{\frac{2\pi d}{1 + j2Bd^2}} \exp \left[ \frac{1}{1 + 4B^2 d^4} \left\{ - \left[ \sqrt{2} B d t + \left( \sqrt{2} \pi f_g + \frac{D d}{\sqrt{2}} \right) \right]^2 \right. \right. \\
& \left. \left. + j \left( -B t^2 - D t + 8\pi f_g B^2 d^3 t + 4\pi^2 f_g^2 B d^2 + B D^2 d^4 + 4\pi f_g B D d^3 \right) \right\} \right]. \quad (\text{B3.7})
\end{aligned}$$

## CURRICULUM VITAE

FIRST NAME: Siritwat

LAST NAME: Soontaranon

GENDER: Male

NATIONALITY: Thai

DATE OF BIRTH: April 22, 1978

EDUCATION BACKGROUND:

- Bachelor of Engineering in Telecommunication Engineering  
May 29, 1995 – April 3, 1999  
Suranaree University of Technology, Thailand.

PUBLICATIONS:

- S. Soontaranon, J. Widjaja, and T. Asakura. (2002). Direct analysis of in-line particle holograms by using wavelet transform and envelope reconstruction method. **Optik**. 113(11): 489-494.
- S. Soontaranon, J. Widjaja, and T. Asakura. (2004). Improved holographic particle sizing by using absolute values of the wavelet transform. **Optics Communications**. 240: 253-260.

SCHOLARSHIP:

- Royal Golden Jubilee Ph.D. program, 2000-2004.